

Imaging system for the characterization of skin layers using diffuse reflectance

Nils Petitdidier

▶ **To cite this version:**

Nils Petitdidier. Imaging system for the characterization of skin layers using diffuse reflectance. Optics / Photonic. Université de Strasbourg, 2018. English. NNT : 2018STRAD048 . tel-02180958

HAL Id: tel-02180958

https://theses.hal.science/tel-02180958

Submitted on 11 Jul 2019

HAL is a multi-disciplinary open access archive for the deposit and dissemination of scientific research documents, whether they are published or not. The documents may come from teaching and research institutions in France or abroad, or from public or private research centers.

L'archive ouverte pluridisciplinaire **HAL**, est destinée au dépôt et à la diffusion de documents scientifiques de niveau recherche, publiés ou non, émanant des établissements d'enseignement et de recherche français ou étrangers, des laboratoires publics ou privés.

UNIVERSITÉ DE STRASBOURG

ÉCOLE DOCTORALE MSII

Laboratoire ICube UMR 7357

THÈSE présentée par :

Nils PETITDIDIER

soutenue le : **27 Novembre 2018**

pour obtenir le grade de : **Docteur de l'université de Strasbourg**

Discipline/ Spécialité : Mathématiques, Sciences de l'Information et de l'Ingénieur / SIAR – imagerie physique

Système d'imagerie pour la caractérisation en couches de la peau par réflectance diffuse

THÈSE dirigée par :

M. GIOUX Sylvain	Professeur, Université de Strasbourg, Strasbourg

RAPPORTEURS :

M. BLONDEL Walter	Professeur, Université de Lorraine, Nancy
M. MONTCEL Bruno	Maître de conférences, HDR, Université Claude Bernard, Lyon 1

AUTRES MEMBRES DU JURY :

M. PIFFERI Antonio	Professeur, Politecnico di Milano, Milan, Italie
Mme. KOENIG Anne	Ingénieur Chercheur, HDR, CEA-Leti, Grenoble

Résumé de la thèse en français

1. Introduction

La connaissance des propriétés optiques de la peau constitue un enjeu majeur dans la prise en charge des patients pour un grand nombre de pathologies. Des instruments capables de mesurer ces propriétés *in vivo* et de manière non invasive font l'objet d'une forte demande à la fois de la part du corps médical et de l'industrie cosmétique.

Dans ce contexte, les méthodes d'imagerie optiques ont connu un essor grandissant ces dernières années du fait de leur capacité à assister le praticien dans de nombreux processus cliniques en sondant les propriétés du tissu de manière fiable et objective. Ces techniques sont fondées sur l'interaction de la lumière visible et proche infra-rouge avec les constituants de la peau afin de déterminer ses propriétés biochimiques et morphologiques. Ces propriétés pouvant à leur tour être reliées à des paramètres fonctionnels utiles au praticien.

La Spectroscopie de Réflectance Diffuse (DRS) consiste à illuminer la surface du tissu et à analyser le spectre de la lumière rétrodiffusée, dénommée réflectance diffuse, dans lequel la signature de diverses espèces biochimiques peut être identifiée. La DRS informe sur les propriétés d'absorption et de diffusion du tissu en profondeur (jusqu'à 2-3 cm dans certains cas) et de manière quantitative. En outre, cette technique peut être mise en œuvre au travers d'instruments compacts et relativement peu coûteux, ce qui constitue un net avantage dans de nombreuses applications. Toutefois, la translation clinique de cette technologie reste freinée par certaines difficultés. Celles-ci concernent notamment la miniaturisation des instruments DRS et leur intégration dans les procédures de routine hospitalière, ainsi que leur capacité à s'adapter à la complexité et à la variété des tissus rencontrés *in vivo*. En particulier, la détermination des propriétés des couches individuelles de la peau (épiderme, derme) peut s'avérer nécessaire pour de nombreuses applications telles que le diagnostic de cancers, le monitorage de l'oxygénation des tissus ou encore le suivi de la pénétration d'actifs en profondeur.

La Spectroscopie de Réflectance Diffuse résolue spatialement (srDRS) est une modalité particulière de la DRS consistant à analyser le profil spatial de la réflectance diffuse produite par une illumination à géométrie contrôlée. La lumière rétrodiffusée à différentes distances du point d'excitation étant sensible aux propriétés du tissu à différentes profondeurs, la

srDRS possède un potentiel pour la caractérisation de la peau couche par couche. Cependant, les instruments existants reposant sur l'utilisation de sondes fibrées ou de photodiodes placées en contact avec la peau ne permettent généralement pas cette séparation des propriétés optiques en couches du fait de leur faible résolution spatiale de détection.

L'objectif de ces travaux est d'établir les bases du développement d'une nouvelle génération d'instruments DRS à la fois bas coûts, potentiellement portés sur la personne et capables de fournir une mesure quantitative des propriétés de la peau en couches. Notre approche repose sur l'utilisation d'un capteur d'images matriciel à haute résolution spatiale placé en contact avec le tissu. La haute résolution de détection de ce type de capteur comparé à celle fournie par les instruments fibrés et à photodiodes existants accroît significativement le potentiel de la srDRS pour la caractérisation de la peau en couches. Nous proposons de mettre en œuvre cette approche à partir de technologies portables et bas coûts, incluant un capteur CMOS (Complementary Metal Oxide Semiconductor) associé à une illumination par LEDs (Light-Emitting Diode) afin de limiter au maximum l'impact de l'instrument en termes de coût et d'encombrement.

Les travaux réalisés au cours de ce projet comprennent :

- La spécification d'une architecture système adéquate permettant la mise en œuvre de la srDRS selon l'approche proposée et la validation de cette architecture pour la caractérisation de fantômes de peau liquides.
- Le développement d'un système optimisé, basé sur l'architecture proposée et porté sur la personne, et la validation de ce système pour la caractérisation de fantômes de peau solides.
- L'évaluation du système développé pour le suivi en continu de l'oxygénation de la peau *in vivo*.

2. Etat de l'art et proposition

La majorité des instruments srDRS existants reposent sur l'utilisation d'une sonde fibrée placée en contact avec le tissu. La sonde est typiquement composée d'une fibre d'illumination centrale et d'un nuage de fibres de collections disposées de manière concentrique autour de l'excitation, comme décrit Fig. 1(a). Les fibres de collections sont placées à différentes distances de l'illumination afin de détecter le profil spatial de la réflectance diffuse. Une source à large spectre en entrée de la sonde associée à un

spectrophotomètre en sortie permet de mesurer les propriétés du tissu sur une large gamme de longueurs d'ondes et avec une haute résolution spectrale. Cependant, ce type de système possède plusieurs inconvénients en termes de géométrie et d'efficacité de détection. L'ouverture numérique des fibres (typiquement égale à 0.22) est limitée, ce qui impose généralement d'utiliser des fibres de 100 ou 200 microns de diamètre et de ce fait limite la résolution spatiale de détection. La résolution est de plus limitée par le cladding des fibres, qui réduit également le facteur de remplissage et donc l'efficacité de collection de la lumière. En conséquence, les systèmes fibrés comportent généralement moins d'une dizaine de distances source-détecteur typiquement comprises entre 0.1 et 2-3 millimètres avec une résolution de l'ordre de la centaine de microns.

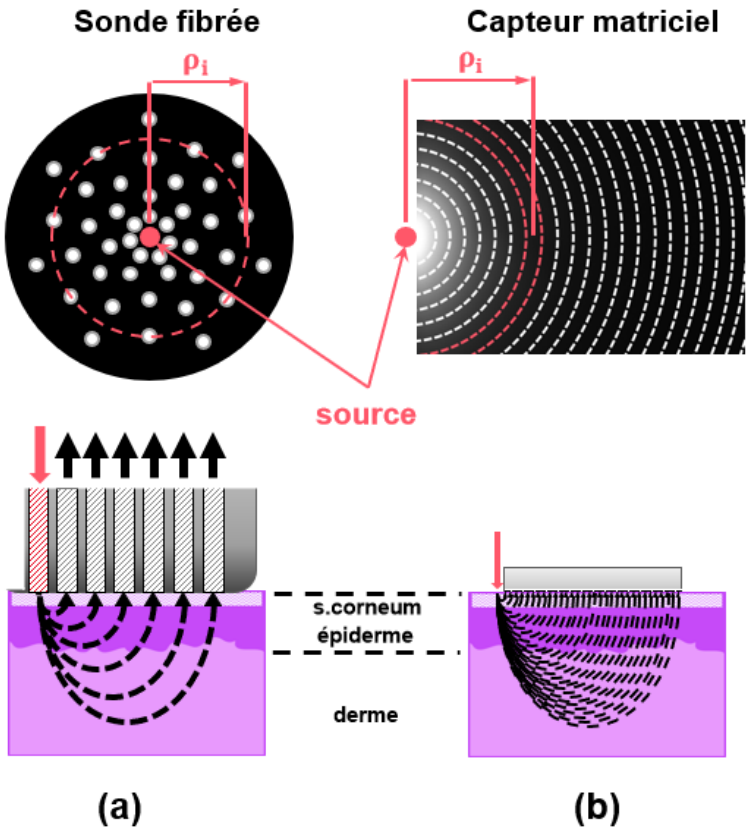


Fig. 1 Géométries de détection de sonde fibrée (a) et de capteur matriciel (b) pour la srDRS. (Haut) vue axiale. (Bas) vue transversale. La réflectance diffuse est moyennée sur des couronnes à distance ρ_i de la source (ligne rouge pointillée).

Outre les systèmes fibrés, des systèmes basés sur la détection de la réflectance diffuse par des photodiodes ont été développés. Ce type d'architecture permet de fabriquer des systèmes compacts, potentiellement portés sur la personne et dont l'efficacité de collection est supérieure à celle des instruments fibrés (en termes d'ouverture numérique de détection et de facteur de remplissage). La contrepartie est que l'information spectrale fournie est moins

riche. Dans les systèmes existants, la détection reste le plus souvent limitée à une seule distance source-détecteur. Des travaux récents portant sur le développement de capteurs composés de photodiodes annulaires concentriques ont permis d'accroître le potentiel de cette architecture pour la caractérisation de milieux en couches. Toutefois, cette approche nécessite le développement de circuits optoélectroniques dédiés.

Afin de dépasser les limitations des systèmes srDRS existants, nous proposons de développer un instrument comprenant un capteur matriciel placé en contact avec le tissu (Fig. 1(b)). Ce type de capteur fournit une géométrie de détection optimisée à la fois en termes de résolution spatiale et d'efficacité de collection (facteur de remplissage et ouverture numérique). Notre approche repose sur l'utilisation d'un capteur CMOS du commerce et de LEDs afin de développer un instrument portable et bas coût.

3. Spécification de l'architecture système et preuve de concept

La première phase du projet a été dédiée à la spécification de l'architecture système adéquate permettant de mettre en œuvre notre approche. En effet, l'implémentation d'un système srDRS performant à partir d'un capteur CMOS standard fait face à plusieurs limitations principalement liées au packaging du capteur. En particulier, la vitre de protection en verre induit un espacement non désiré entre le tissu et la surface photosensible du capteur, ce qui entraîne une chute du contraste sur les images de réflectances. Ceci a pour effet de réduire la capacité du système à détecter les variations de profils de réflectance sur de faibles gammes de distances, en particulier proches de la source, et donc à caractériser le tissu couche par couche. D'autre part, la présence des bondings autour de la zone photosensible rend impossible le placement d'une source de lumière suffisamment proche du premier point de détection. En effet, une séparation efficace de l'influence des propriétés d'absorption et de diffusion sur les signaux mesurés nécessite de détecter la réflectance diffuse à des distances à la fois proches (typiquement moins d'un millimètre) et plus éloignées de la source. Or, les bondings s'étendent généralement sur plusieurs millimètres. De plus, leur fragilité impose de les encapsuler dans un matériau plastique. Un éventuel retrait de ce matériau pour placer une source sur les bondings ne peut se faire sans risquer d'endommager le capteur.

L'architecture que nous avons développée (Fig. 2(a)) vise à contourner ce problème en déportant l'aire d'imagerie du système au-delà de l'encapsulation du CMOS afin de placer les sources de lumière au plus proche de la zone de détection. Concrètement, une plaque de

fibres optiques (FOP) est utilisée pour transposer l'image de la zone photosensible du CMOS vers la surface du tissu analysé avec une conjugaison 1 :1. Il devient alors possible de placer une source directement contre les bords du FOP, eux-mêmes alignés avec les bords de la zone photosensible (ou à l'intérieur de celle-ci). L'architecture du système reste compacte moyennant l'utilisation de sources de faibles dimensions. De plus, les possibilités des FOPs du commerce en termes de transmission (~60% en éclairement Lambertien) et de résolution spatiale (jusqu'à 160 lp/mm)) permettent de conserver les avantages offerts par notre approche.

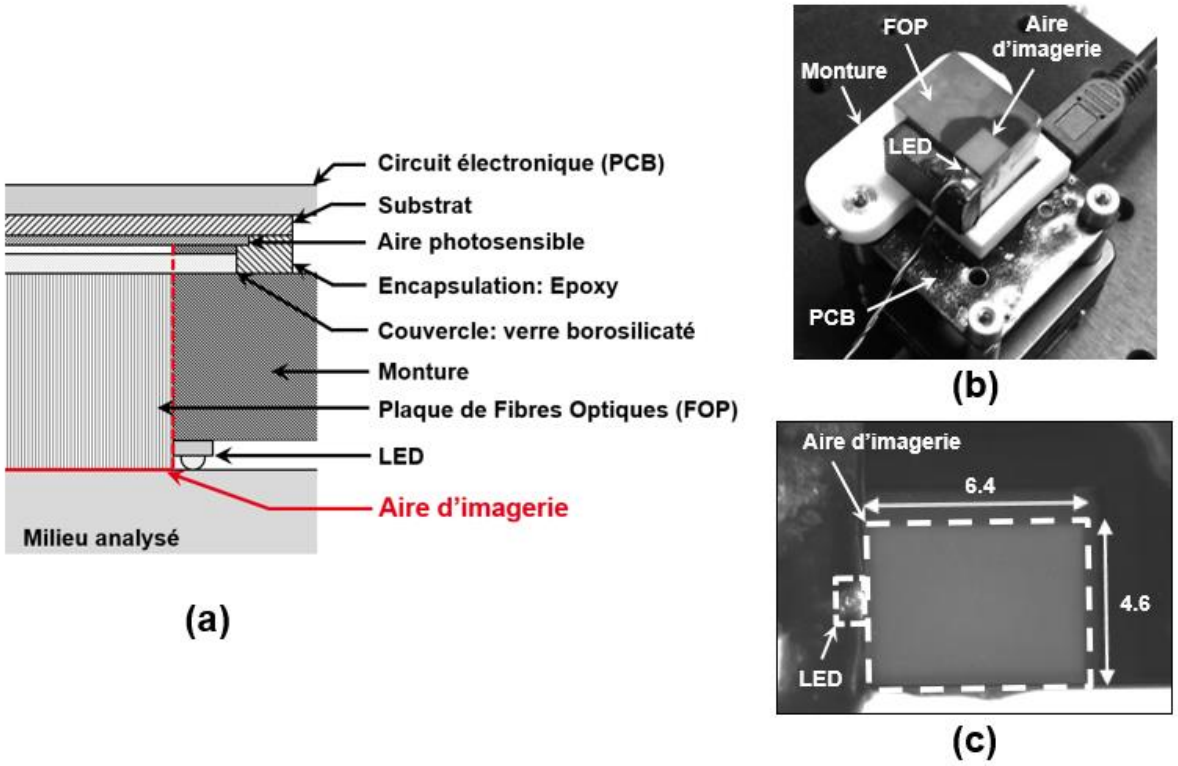


Fig. 2 (a) Structure schématique du système proposée pour l'imagerie de réflectance diffuse en contact. L'aire d'imagerie (ligne rouge) est déportée depuis l'aire photosensible du CMOS vers la surface du milieu analysé. (b) Photographie du prototype implémenté pour preuve de concept (c) Vue axiale du prototype. Les dimensions sont données en millimètres. L'aire d'imagerie délimitée par la ligne pointillée est vue à travers la plaque de fibres optiques (FOP).

Afin de valider l'architecture proposée, un premier prototype a été fabriqué (Fig. 2(b) et (c)). Les performances de ce prototype ont été évaluées pour la caractérisation de fantômes de peau liquides. Dans un premier temps, les méthodes de traitement de l'information nécessaires à l'estimation des propriétés optiques ont été mises en place. Chaque image de réflectance diffuse acquise par la caméra est traitée afin de calculer le profil radial de décroissance du signal en fonction de la distance à la source de lumière. La courbe obtenue est ensuite comparée à une table de profils théoriques calculés à partir de simulations Monte

Carlo pour une gamme de propriétés optiques étendue. Le processus d'estimation des propriétés optiques passe par une correction de la réponse instrumentale. Celle-ci est fournie par une mesure de référence réalisée sur un fantôme aux propriétés optiques connues, dénommé ici fantôme de calibration. Suivant cette méthode, les coefficients d'absorption (μ_a) et de diffusion réduit (μ_s') des fantômes ont été mesurés avec le prototype srDRS développé et comparés aux valeurs attendues (valeurs fournies par la théorie de Mie pour μ_s' et par mesures préalables au spectrophotomètre à transmission pour μ_a). Les coefficients d'absorption (μ_a) et de diffusion réduit (μ_s') des fantômes ont été quantifiés avec une précision moyenne de 4.2±3.5% et 7.0±4.6%, respectivement (Fig. 3).

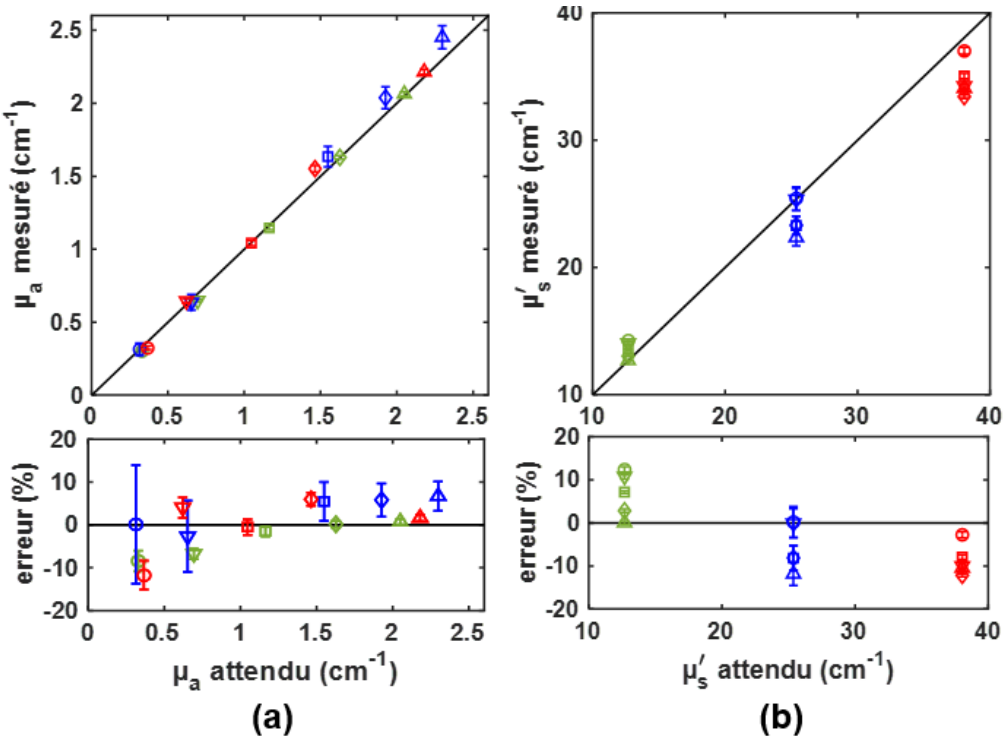


Fig. 3 Résultats sur fantômes liquides. Propriétés optiques mesurées pour différents niveaux de diffusion et d'absorption des fantômes. (Haut) valeurs absolues. (Bas) erreur relative entre les propriétés mesurées et attendues. Les barres d'erreur correspondent à l'écart-type entre différentes mesures d'un même fantôme.

Cette première étude de preuve de concept a permis de valider l'architecture proposée pour la quantification précise des coefficients d'absorption et de diffusion réduit de milieux homogènes. Toutefois, plusieurs limitations restent associées à cette étude. Ces limitations sont notamment liées à l'utilisation de fantômes liquides, rendant difficile la modélisation des conditions d'illumination du milieu dans les simulations Monte Carlo et ne permettant pas d'appréhender l'impact potentiel du couplage entre le capteur et la peau. D'autre part, la vitre protectrice du capteur CMOS n'a pas été retirée pour cette première implémentation de notre

approche, ce qui induit un brouillage de la réflectance diffuse et de ce fait limite le potentiel du système pour l'analyse de milieux en couches.

4. Implémentation d'un instrument srDRS bas coût et porté sur la personne

L'architecture spécifiée précédemment a conduit à l'implémentation d'un système srDRS compact pouvant être porté sur la personne (Fig. 4(b)) et conçu pour le suivi en continu de l'oxygénation des tissus et l'analyse de milieux en couches. Le système comprend le capteur CMOS utilisé lors de l'étude précédente associé à un ensemble de sources à plusieurs longueurs d'ondes (515, 611 et 660 nm) afin d'apporter l'information spectrale nécessaire à la mesure d'oxygénation des tissus.

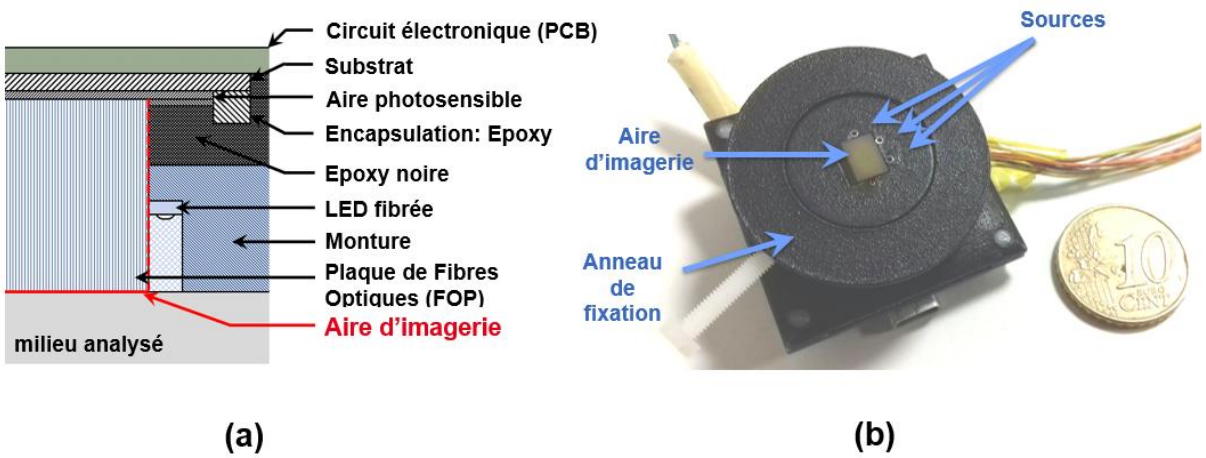


Fig. 4 (a) Structure schématique et (b) photographie du système srDRS porté sur la personne.

Afin de dépasser limitations évoquées précédemment, l'architecture du système a été modifiée en plusieurs points (Fig. 4(a)). Selon un protocole disponible dans la littérature et adapté à notre étude, la vitre protectrice du capteur CMOS a été retirée afin de placer le FOP directement contre la surface photosensible du capteur. La résolution spatiale offerte par ce nouveau prototype a été estimée à 9.8 µm (Fig. 5), correspondant à un gain d'un facteur 50 par rapport à la version précédente du système. De plus, l'une des deux sources émettant à 515 nm a été intégrée de manière à produire une illumination du tissu inclinée de 35° par rapport à la normale. Plusieurs études ont en effet démontré que cette approche permet d'augmenter la sensibilité de la réflectance diffuse aux propriétés du tissus à faibles profondeurs et ainsi d'accroître le potentiel de la srDRS pour la séparation des propriétés en

couches (épiderme et derme). Enfin, les sources et le FOP sont packagées au sein d'un module spécialement conçu et associé à un anneau de fixation permettant d'attacher le capteur à la peau du sujet lors d'expérimentations *in vivo*.

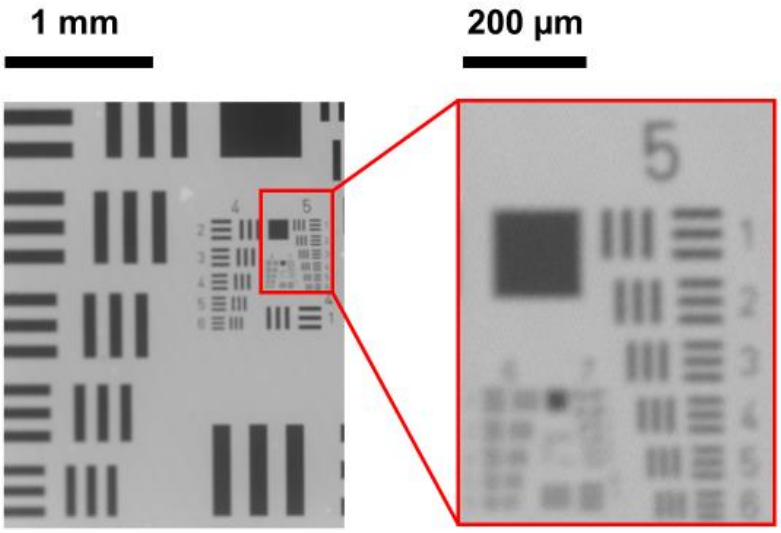


Fig. 5 Image de mire USAF-1951 positive enregistrée avec le système srDRS porté sur la personne après retrait de la vitre de protection en verre.

La capacité du système développé à fournir une mesure quantitative des propriétés de la peau a été évaluée sur fantômes optiques solides. Pour cela, une gamme de fantômes en poly(dimethylsiloxane) (PDMS) a été développée. Le protocole de fabrication de ces fantômes a été établi conjointement entre le laboratoire d'accueil au CEA (Commissariat à l'Energie Atomique et aux Energies Alternatives, Grenoble) et le laboratoire ICube (Laboratoire des sciences de l'Ingénieur, de l'Informatique et de l'Imagerie, UMR 7357, Strasbourg). Cette approche présente plusieurs avantages par rapport à l'étude précédente. Tout d'abord, l'utilisation de fantômes solides permet d'évaluer l'impact du coupage entre le capteur et la peau. De plus, alors que les fantômes liquides ont une durée de vie d'une semaine au mieux, les fantômes PDMS peuvent être conservés plusieurs années, ce qui permet de les caractériser suivant plusieurs méthodes et dans des laboratoires différents afin de réaliser des études comparatives. Enfin, l'état de surface et la structure de ces fantômes peuvent être contrôlés. En particulier, le protocole développé pourra servir à la fabrication de fantômes multicouches permettant d'évaluer plus finement les performances de notre système. Ce protocole ne permet toutefois pas de contrôler de façon sûre les propriétés d'absorption et de diffusion des fantômes. La caractérisation de ces fantômes s'est donc basée sur une mesure de référence par la méthode SFDI (Spatial Frequency Domain Imaging) développé au sein de l'équipe Instrumentation Photonique pour la Santé à ICube. Les

propriétés des fantômes développés au CEA et au laboratoire ICube et utilisés pour cette étude sont données Fig. 6. Une large gamme de propriétés représentatives de la peau est couverte. Les propriétés sont échantillonnées de manière fine sur la gamme [0 ;1] cm^{-1} en absorption et [7 ;20] cm^{-1} en diffusion, qui correspond aux valeurs les plus représentatives de peaux claires et du derme. Le reste des fantômes vient compléter la gamme de propriétés considérée vers des niveaux plus élevées d'absorption et de diffusion qui se rapprochent notamment des propriétés observées pour les peaux foncées ou l'épiderme.

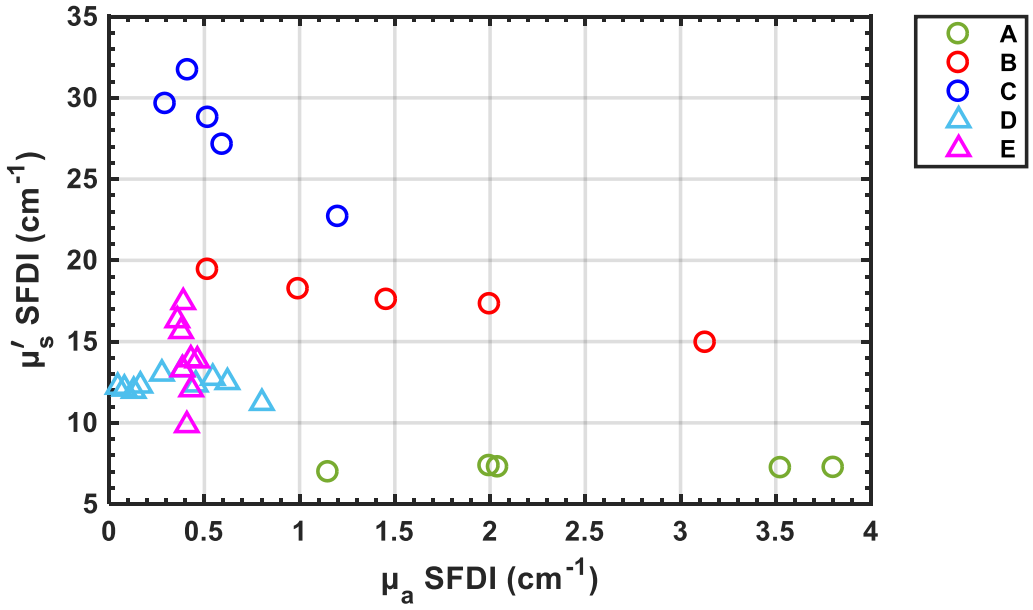


Fig. 6 Propriétés des fantômes PDMS mesurées en SFDI à 665 nm.

Les propriétés des fantômes fabriqués ont été mesurées avec le système srDRS développé et comparées aux valeurs données par la SFDI. Les résultats sont fournis Fig. 7.

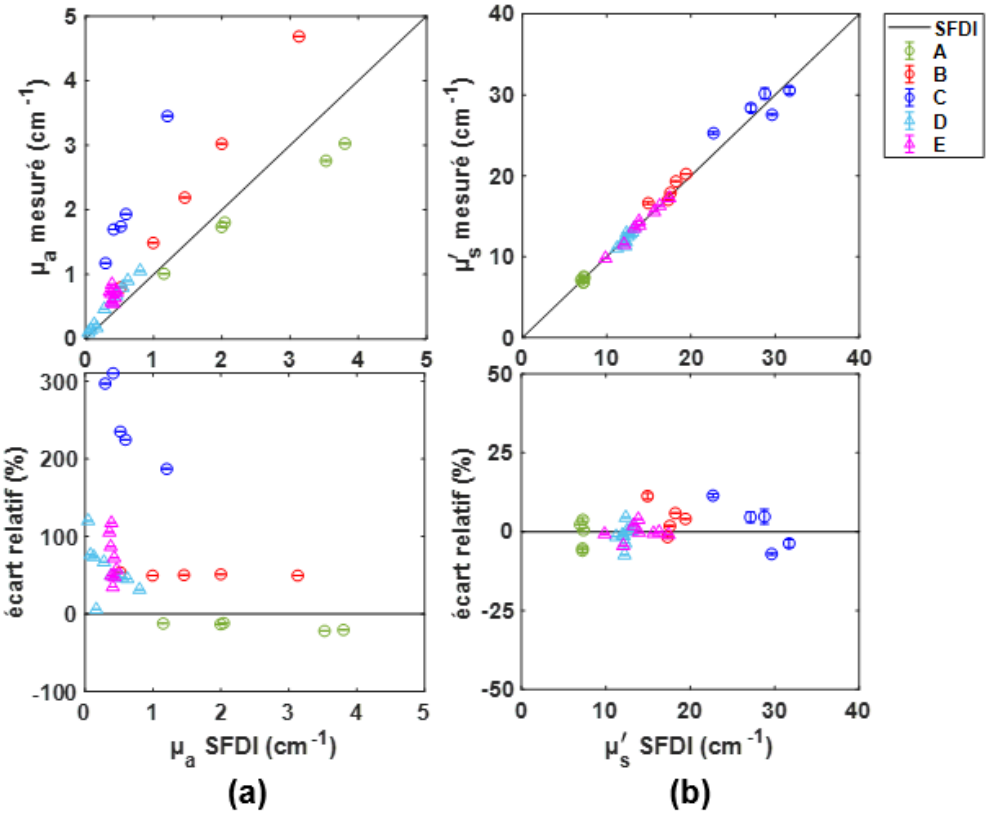


Fig. 7 Comparaison entre les propriétés optiques des fantômes PDMS mesurées en SFDI et avec le système srDRS développé. (a) Coefficients d'absorption. (b) Coefficients de diffusion réduits. (Haut) Valeurs absolues. (Bas) Ecarts relatifs entre srDRS et SFDI. Chaque couleur est associée à un groupe de fantômes.

La capacité du système à mesurer précisément le coefficient de diffusion réduit des fantômes semble confirmée par l'accord obtenu entre les mesures SFDI et srDRS pour ce paramètre. L'écart relatif moyen entre les deux systèmes est de 3.3±3.0%, avec un coefficient de corrélation R^2 = 0.983. A l'inverse, de très grandes disparités sont observées dans les coefficients d'absorption mesurés par les deux systèmes, avec des écarts de quantification atteignent 300% pour certains fantômes. Toutefois, une structure se dégage nettement de ces écarts. Notamment, pour une gamme de fantômes à niveau de diffusion constant, la variation relative d'absorption entre les fantômes est respectée. De plus, l'écart relatif en μ_a mesurés par les deux systèmes semble être dépendant de l'intervalle entre les niveaux de diffusion du fantôme considéré et du fantôme utilisé pour la calibration du système srDRS. En effet, les coefficients d'absorption mesurés en srDRS sont soit sous-estimés soit surestimés selon que le coefficient de diffusion réduit du fantôme considéré est plus faible, respectivement plus important que celui du fantôme de calibration. Cette observation nous a amené à proposer une approche empirique permettant de corriger l'erreur de quantification de l'absorption par srDRS. Pour cela, nous supposons une dépendance linéaire de l'écart relatif entre les

coefficients d'absorption mesurés en srDRS et en SFDI en fonction du coefficient de diffusion réduit des fantômes (Fig. 8(a)). Etant donné l'accord observé entre les coefficients μ_s' mesurés par les deux systèmes, cette approche se base uniquement sur les mesures srDRS sans a priori sur les propriétés des fantômes. La relation suivante de correction de l'absorption mesurée par srDRS peut alors être établie à partir des paramètres du fit linéaire :

$$\mu_a^{cor} = \frac{\mu_a}{1 + (11.45 \times \mu_s' - 97.03)/100}$$

où μ_a et μ_s' sont les coefficients d'absorption et de diffusion réduit estimés initialement par le système et μ_a^{cor} est le coefficient d'absorption corrigé. Les résultats de comparaison entre srDRS et SFDI une fois l'absorption mesurée en srDRS corrigée sont donnés Fig. 8(b). Après correction, un écart relatif moyen de 12.9±14.3% entre les coefficients d'absorption mesurés en srDRS et SFDI est obtenu, avec un coefficient de corrélation $R^2 = 0.965$.

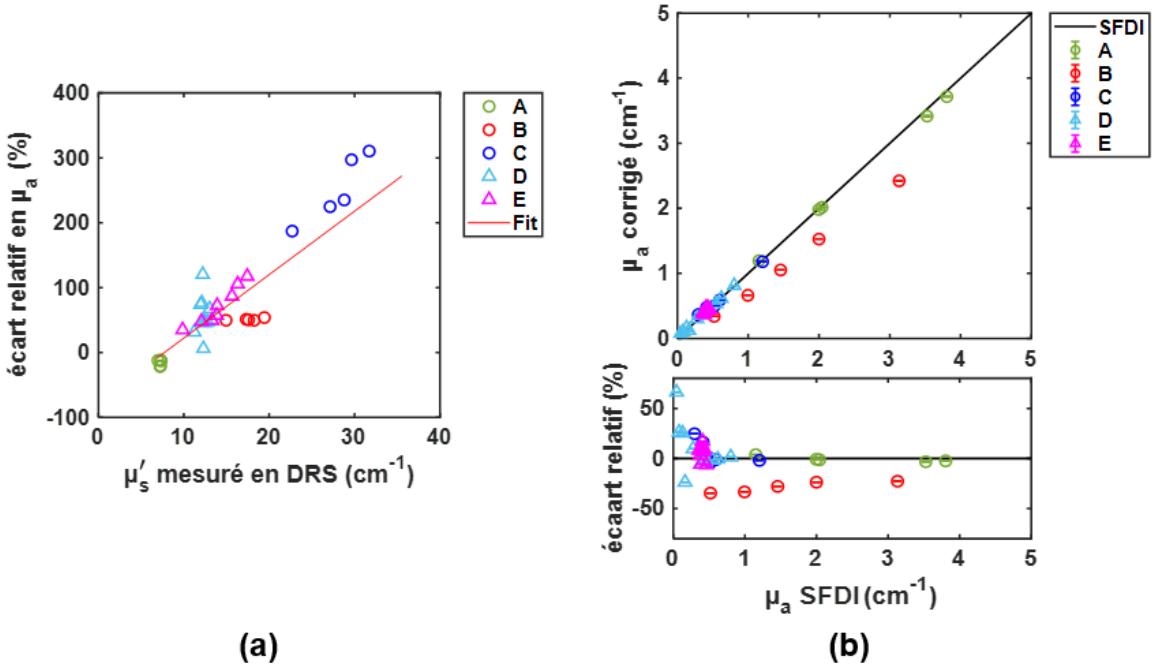


Fig. 8 (a) Ecart relatif de quantification du coefficient d'absorption entre srDRS et SFDI en fonction du coefficient de diffusion réduit des fantômes mesuré en srDRS. Le fit linéaire est représenté par la droite rouge. (b) Coefficients d'absorption mesurés en srDRS après correction en fonction des valeurs données par la SFDI. (Haut) Valeurs absolues. (Bas) écart relatif entre srDRS et SFDI.

Bien que cette approche permette de réduire significativement l'écart de quantification de l'absorption par notre système srDRS et la SFDI, il semble que les valeurs corrigées restent fortement sensibles à un éventuel écart d'estimation du coefficient μ_s' entre les deux instruments. Cela pourrait notamment expliquer les différences importantes observées pour la

gamme B (de l'ordre de 25%) après correction, étant donné que pour cette gamme le coefficient de diffusion réduit est systématiquement surestimé par rapport à la valeur donnée en SFDI. D'autre part, la faible corrélation entre l'écart relatif de quantification de l'absorption par les deux systèmes et le niveau de diffusion des fantômes ($R^2 = 0.814$) suggère la présence d'autres biais de mesure ne pouvant pas être corrigés selon cette approche. Une étude plus approfondie serait à mener pour confirmer nos observations et valider la méthode de correction proposée.

5. Evaluation du capteur pour le suivi d'oxygénation des tissus *in vivo*

L'approche proposée au cours de ce projet peut s'avérer pertinente dans le cadre du suivi de la viabilité de lambeaux superficiels en phase post-opératoire de chirurgie reconstructrice. En effet, le greffon de peau transféré sur la zone à reconstruire nécessite une inspection régulière par l'équipe médicale afin d'optimiser ses chances de survie. Notre approche possède un potentiel pour informer sur l'état d'oxygénation du tissu de manière continue et autonome à partir d'un instrument à faible coût, optimisant ainsi les chances de survie du lambeau tout en mobilisant un minimum de ressources humaines et matérielles.

Le potentiel de notre système pour le suivi en continu de l'oxygénation de la peau a donc été évalué au travers d'expérimentations *in vivo*. Afin de mener ces expérimentations, le système srDRS développé comprend une bague de fixation attachée à la peau du sujet à l'aide de rubans adhésifs médicaux (Fig. 9(a)). Le système vient s'insérer dans la bague avant d'être fixé par une vis de sorte à appliquer une pression stable sur le tissu pendant toute la durée de la mesure (Fig. 9(b)). L'effet de la pression appliquée par le système de mesure sur les propriétés optiques estimées a été mis en évidence par plusieurs auteurs. Nous avons donc étudié la répétabilité des signaux obtenus entre différents positionnements du capteur srDRS. Une série de mesures a été réalisées en un même point du tissu (sans déplacer la bague de fixation) avec retrait et repositionnement du capteur dans la bague entre chaque mesure. L'écart-type calculé entre les mesures est de 16.6% pour μ_a et 2.8% pour μ_s'.

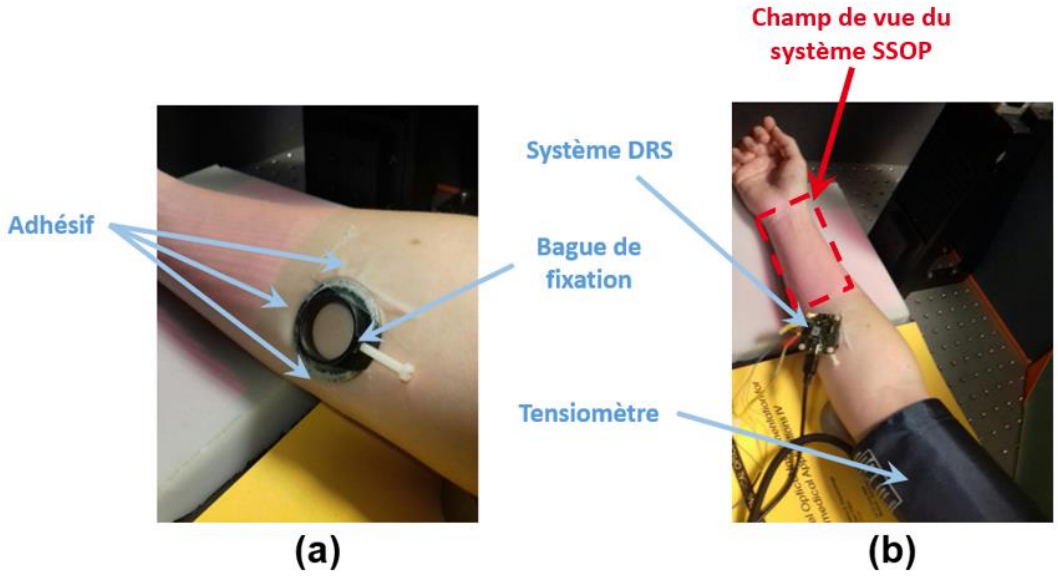


Fig. 9 Expérimentations pour le suivi d'oxygénation *in vivo*. L'avant-bras d'un volontaire sain est placé dans le champ de vue du système SSOP, repéré par le rectangle pointillé. Le système srDRS est attaché au bras du volontaire en dehors de champ d'illumination de la SSOP. Le système est fixé au moyen d'une bague attaché au tissue à l'aide de rubans adhésifs médicaux.

Afin de simuler les conditions d'une complication vasculaire au sein du greffon de peau, une occlusion veineuse a été réalisée au bras d'un sujet sain à l'aide d'un brassard tensiomètre médical. Les propriétés optiques ont été mesurées à l'avant-bras en continu avant, pendant et après l'occlusion simultanément avec le système srDRS et une modalité temps-réel de la SFDI, dénommée SSOP (Single Snapshot of Optical Properties). Les coefficients d'absorption et de diffusion réduits mesurés sont donnés Fig. 10.

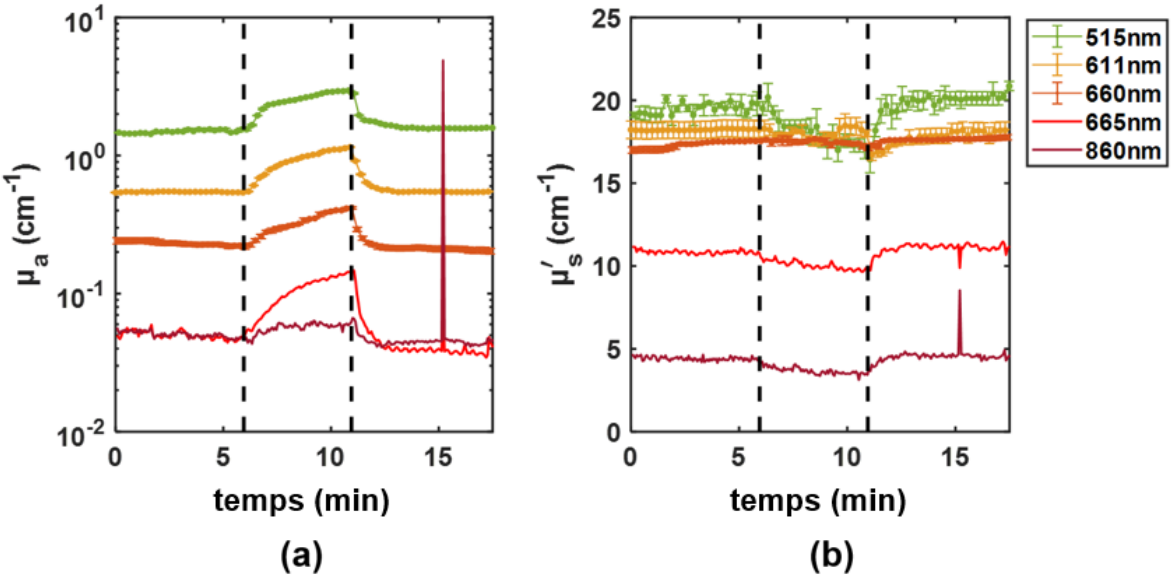


Fig. 10 Coefficients d'absorption (a) et de diffusion réduits (b) mesurés pendant l'expérience d'occlusion avec les systèmes srDRS (515, 611 et 660 nm) et SSOP (665 et 860 nm). Les barres d'erreur correspondent à l'écart-type entre les valeurs obtenues à partir de différentes mesures du fantôme de calibration.

Une augmentation progressive de l'absorption pendant l'occlusion a été détectée à toutes les longueurs d'onde, avec un retour rapide aux valeurs normales après que la pression soit relâchée. Les coefficients de diffusion mesurés sont dans l'ensemble peu sensibles à l'occlusion et restent stables pendant toute la durée de l'expérience, avec des changements observés pendant l'occlusion inférieurs à 10%. Les coefficients mesurés respectent donc qualitativement le comportement attendu pour ce type de protocole. Cependant, des disparités importantes sont observées entre les résultats fournis par le système srDRS et la méthode SSOP. Le coefficient d'absorption mesuré à 660 nm par srDRS est surestimé par rapport à la valeur donnée en SSOP à 665 nm, en accord avec ce que nous avons observé sur fantômes PDMS. En revanche, les coefficients de diffusion mesurés montrent une différence significative entre les deux systèmes pour ces mêmes longueurs d'onde. Ces différences sont potentiellement liées aux différences intrinsèques entre les systèmes srDRS et SFDI. Notamment, les propriétés optiques mesurées peuvent être altérées du fait de la pression appliquée par notre capteur sur le tissu. De plus, les propriétés mesurées en SFDI sont potentiellement sensibles aux réflexions spéculaires à la surface de la peau, ce qui n'est pas le cas de l'instrument srDRS.

Le paramètre de saturation tissulaire en oxygène S du tissu a été calculé selon une relation basée sur la différence des coefficients d'absorption mesurés à deux longueurs d'onde $\Delta\mu_a$:

$$S = \frac{\Delta\mu_a - \Delta\mu_{a,deoxy}}{\Delta\mu_{a,oxy} - \Delta\mu_{a,deoxy}}$$

où $\Delta\mu_{a,oxy}$ et $\Delta\mu_{a,deoxy}$ sont déterminés à partir de spectres tabulés de l'absorption du sang oxygéné et désoxygéné. Les mesures à 611 nm et 660 nm sont considérées pour le système srDRS, tandis que les mesures à 660 nm et 860 nm sont utilisées en SSOP. Les résultats obtenus (Fig. 11) démontrent la capacité du système srDRS à détecter la baisse de saturation produite par l'occlusion. D'un point de vue quantitatif, de grandes disparités sont toutefois observées entre les mesures srDRS et les signaux générés en SSOP. Les valeurs de saturation mesurées en SSOP sont globalement conformes aux résultats attendus. Des études réalisées par le passé ont en effet établi que la saturation se situe dans la gamme [70-80]% en conditions normales et ne chute pas au-delà de 50% dans le cas d'une occlusion de quelques minutes telle que celle réalisée ici. L'utilisation de la SSOP comme méthode de référence a ainsi pu être validée. La saturation mesurée par le système srDRS est cependant fortement

surestimée et atteint des valeurs peu réalistes aussi bien avant (~90%) que pendant l'occlusion (~22%). Diverses pistes ont été proposées afin d'expliquer les écarts observés et de les corriger. Celles-ci concernent en particulier le choix des sources implémentées dans le système srDRS. La relation utilisée pour le calcul de la saturation repose notamment sur l'approximation que seul le sang oxygéné et désoxygéné contribue à la différence d'absorption mesurée entre les deux longueurs d'ondes considérées. Il est probable que cette approximation ne soit pas vérifiée dans le cas de la mesure srDRS à 611 nm et 660 nm du fait de la contribution de la mélanine à l'absorption du tissu. Plusieurs auteurs ont établi que le choix d'un couple de longueurs d'onde optimal pour le suivi hémodynamique se situait typiquement dans la gamme [650-750] nm d'une part et [850-950] nm d'autre part. Suivant l'architecture proposée pour notre capteur, la nécessaire proximité des sources avec les bords de l'aire d'imagerie impose le choix de LEDs de faibles dimensions latérales (ici 0.8 mm). Dans la gamme d'émission à [850-950] nm, les LEDs disponibles sur le marché ne permettent pas de répondre à l'ensemble des contraintes liées à la fois à cette limitation, à la puissance d'émission nécessaire et à la faible sensibilité du capteur CMOS dans le domaine proche infra-rouge. De futurs travaux pourraient notamment s'attacher à la modification du packaging du système pour l'intégration d'un couple de sources aux longueurs d'ondes optimisées pour le suivi quantitatif de l'oxygénation des tissus. En parallèle, le modèle de peau et l'algorithme d'inversion associé pourraient être optimisés, notamment afin de prendre en contre la présence d'autres espèces moléculaires présentes dans le tissu telles que la mélanine.

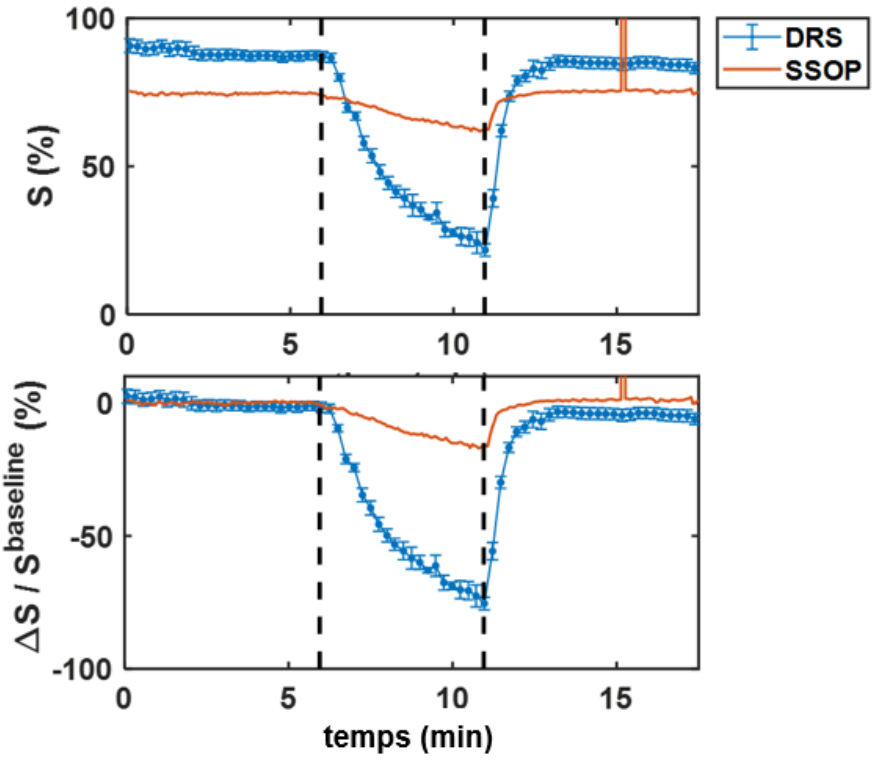


Fig. 11 Saturation tissulaire en oxygène (StO_2) mesurée pendant l'expérience d'occlusion avec les systèmes srDRS et SSOP. Les barres d'erreur correspondent à l'écart-type entre les valeurs obtenues à partir de différentes mesures du fantôme de calibration.

6. Perspectives pour la poursuite des travaux

Les perspectives ouvertes par ces travaux concernent principalement l'analyse de milieux en couche tels que la peau.

Dans un premier temps une validation plus complète du système développé devra être menée. Une telle validation nécessite le développement de fantômes de peau aux propriétés connues. Pour cette étude, nous nous somme reposés sur une caractérisation de ces fantômes par une méthode indépendante en SFDI. Toutefois cette approche présente des limitations liées aux différences intrinsèques entre la méthode SFDI et le système srDRS développé. Afin de renforcer notre étude, d'autres méthodes de référencement des propriétés optiques des fantômes pourraient être envisagées. C'est pourquoi une campagne de caractérisation de ces propriétés par un système DRS résolu en temps est notamment en cours au sein d'une équipe partenaire (Politecnico di Milano, Milan).

Afin d'évaluer les performances du système pour l'analyse de milieux en couches, le protocole de fabrication de fantômes établi pourra être exploité pour le développement de fantômes bicouche mimant par exemple l'épiderme et le derme.

Afin de séparer l'influence des couches superficielles (épiderme) d'une part et profondes d'autre part (derme) sur les propriétés optiques mesurées, la sensibilité du système aux propriétés du milieu à faibles profondeurs doit être maximisée. Dans ce but, une approche proposée par différents auteurs consistant à incliner l'illumination a été implémentée dans notre système. En parallèle, un algorithme de simulations Monte Carlo dans un milieu en couches précédemment développé au CEA a été étendu à la modélisation de sources inclinées. Ces outils pourront être mobilisés dans de futurs travaux.

Enfin, les travaux réalisés ici ont débouché sur le dépôt d'un protocole d'essai clinique en lien avec le CHU de Grenoble et une équipe partenaire de l'Inserm. Les essais, prévus pour le printemps 2019, incluent un panel de volontaires sains aux types de peau variés et soumis à une inhalation d'air hypoxique afin de générer une désaturation. Les données recueillies pourront notamment être exploitées pour spécifier le modèle de peau et l'algorithme d'inversion adéquats afin d'obtenir une mesure quantitative de la saturation tissulaire en oxygène.

7. Conclusion

Les travaux réalisés au cours de ce projet ont permis d'établir les bases du développement d'un capteur srDRS bas coût et potentiellement porté sur la personne pour l'analyse de la peau en couches. Notre approche repose sur l'utilisation d'un capteur matriciel placé en contact avec le tissu et permettant la détection de la réflectance diffuse à haute résolution spatiale afin d'optimiser le potentiel de la srDRS à fournir une mesure résolue en profondeur.

La première phase du projet a permis d'identifier les limitations associées à notre approche et de proposer une solution instrumentale innovante permettant de les contourner. La solution proposée a été implémentée au travers d'un premier prototype, dont les performances ont été validées sur fantômes de peau liquides. Les mesures réalisées avec ce prototype ont permis de quantifier les coefficients d'absorption (μ_a) et de diffusion réduit (μ_s') des fantômes avec une précision moyenne de 4.2±3.5% et 7.0±4.6%, respectivement.
Cette première étape de preuve de concept a mené à l'implémentation d'un capteur compact, porté sur la personne et optimisé pour l'analyse de milieux en couches et le suivi d'oxygénation de la peau *in vivo*. En particulier, la résolution d'images offerte par ce nouvel instrument a été multiplié par 25 par rapport au prototype précédent. Le système développé

permet ainsi de détecter des détails de l'ordre de 22 µm sur une large gamme de distances source-détecteur (approximativement entre 0.7 et 6.5 mm).

Afin d'évaluer les performances de ce système dans des conditions au plus proche de la mesure *in vivo*, une gamme de fantômes solides en PDMS a été développée. Les propriétés optiques des fantômes ont été caractérisées selon une approche par mesure de référence basée sur un système SFDI développé au sein d'un laboratoire partenaire (ICube, UMR 7357, Strasbourg). Ces propriétés ont ensuite été comparées à celles mesurées par le système srDRS que nous avons développé. L'accord entre les instruments srDRS et SFDI concernant l'estimation de μ_s' a pu être établi. Les écarts relatifs d'un instrument à l'autre étant en moyenne de 3.3±3.0%. De grandes disparités ont en revanche été observées concernant le coefficient d'absorption. Bien que les résultats obtenus concordent sur le plan qualitatif, une correspondance quantitative entre les deux instruments n'a pu être obtenue. En observant une nette corrélation entre l'écart relatif en absorption et le niveau de diffusion du fantôme considéré, nous avons proposé une approche empirique de correction des coefficients d'absorptions estimés par notre système. Le potentiel de cette approche a été évalué sur la gamme de fantômes PDMS fabriquée. L'écart de quantification de l'absorption entre les systèmes srDRS et SFDI a ainsi été significativement diminué sur l'ensemble des fantômes, passant en moyenne à 12.9±14.3%. Les résultats obtenus suggèrent toutefois que cette méthode ne permet pas de prendre en compte tous les biais de mesure existants entre notre capteur et le système SFDI. Des études plus approfondies seraient nécessaires afin d'identifier la source de ces écarts et de les corriger.

Enfin, les performances du système srDRS développé ont été évaluées pour le suivi d'oxygénation des tissus *in vivo*. Pour cela, une expérience d'occlusion au brassard tensiomètre a été menée sur un sujet sain afin de générer une chute de la saturation tissulaire en oxygène (StO_2). Les propriétés optiques ont été mesurées en continu avec notre système et une modalité temps-réel de la SFDI utilisées comme mesure de référence. La capacité du capteur srDRS à détecter la désaturation produite par l'occlusion a pu être démontrée. Cependant, une estimation précise et quantitative des valeurs de StO_2 en conditions normales et pendant l'occlusion n'a pu être obtenu. Afin d'atteindre ce but, plusieurs pistes d'améliorations ont été proposées et pourront être explorées dans de futures études. Ces améliorations concernent notamment la méthode de calibration de l'instrument, la modélisation du tissu, le choix des longueurs d'onde d'émission ainsi que la maîtrise du couplage entre le capteur et le tissu. L'architecture du système pourrait notamment être

adaptée afin de permettre l'intégration d'une combinaison optimale de sources. Par ailleurs, l'usage d'un gel de contact au propriétés adéquates pourrait être exploré.

Dans l'ensemble, les résultats confirment le potentiel de notre approche pour la quantification des propriétés optiques des tissus *in vivo*. Ces travaux ont permis de franchir une première étape vers le développement d'un instrument bas coût et compact pour l'analyse de la peau. Un tel instrument pourrait en particulier fournir un monitorage passif et en continu de la viabilité de lambeaux superficiels afin d'améliorer la prise en charge des patients en phase post-opératoire de chirurgie reconstructrice. Le système développé présente de plus un potentiel pour l'analyse du tissu résolue en couches, ce qui apporterait une forte plus-value dans de nombreuses applications aussi bien médicales que cosmétiques ou industrielles. Afin d'évaluer ce potentiel, plusieurs outils instrumentaux et algorithmiques ont été mis en place et pourront être mobilisés dans de futurs travaux.

Remerciements

Mes premiers remerciements vont aux membres du jury. Les rapporteurs Prof. Walter Blondel et Dr. Bruno Montcel pour leurs conseils avisés lors du comité de suivi et leur remarques constructives à la relecture du manuscrit. Je remercie également Prof. Antonio Pifferi pour sa disponibilité et ses commentaires sur mes travaux.

Je tiens ensuite à remercier mon directeur de thèse, Prof. Sylvain Gioux, pour m'avoir fait partager son expérience lors de nos échanges réguliers tout au long de cette thèse. Au-delà des compétences techniques et humaines que j'ai pu développer sous son encadrement, ses conseils et ses encouragements m'ont aidé à avancer et à rester positif dans nombre de moments où mon côté pessimiste reprenait le dessus. Je remercie chaleureusement mon encadrante au CEA, Dr. Anne Koenig, pour ses conseils, sa disponibilité, sa patience et son soutien sans failles qui m'ont permis de ne jamais me sentir seul pendant ces trois ans. Je remercie aussi Dr. Rémi Gerbelot pour ses remarques constructives qui m'ont aidé à avancer sur les aspects techniques. Ce projet n'aurait pas vu le jour sans Dr. Jean-Marc Dinten. Je le remercie ainsi que Dr. Sophie Morales et Dr. Pierre Jallon pour leurs conseils et le temps qu'ils ont pu me consacrer. Je dois également beaucoup à M. Henri Grateau qui a su transformer mes « vues d'artiste » en prototypes bien réels, ainsi qu'à MM. Thomas Bordy et Selimen Benhamed qui m'ont permis de les faire fonctionner. Je remercie également Dr. Blandine Roig et Keshia Badu pour leurs conseils concernant la fabrication des fantômes. J'ai aussi eu de nombreuses discussions avec Dr. Lionel Hervé, Dr. Anne Planat-Chrétien et M. Michel Berger qui m'ont permis d'avancer sur les aspects de modélisation et instrumentaux. Je tiens à remercier tout particulièrement Laurence Chassouant, qui prend grand soin de ses doctorants et sans qui nous sommes perdus tant elle nous facilite la vie, ainsi que Charlotte Emain pour sa bonne humeur communicative et son aide au quotidien et dans la fabrication de nos « précieux ». Ces travaux n'auraient pas pu se faire sans les moyens mis à disposition à ICube et la contribution de M. Fabrice Aguénounon. Je remercie également Manon, Aude, Swapnesh et Amir pour leur aide. Enfin je remercie tous mes collègues du LS2P et du LISA pour leur accueil et l'ambiance formidable dans laquelle j'ai évolué durant trois ans. Je pense notamment à mes compagnons thésard(es) Sophie, Judy, Veronica, Valentin, Anthony, Isaure, David, Stéphanie et Paul, mais aussi à Damien, Camille, Ondrej, Pierre, Cédric, Emmanuelle, Agathe, Romaric, Xavier, Emeric, Romain, Gaëlle, Yvon, Antoine, Alexis, et

les autres avec qui j'ai partagé d'excellents moments que ce soit au travail, en conférences, dans les pauses ou à l'extérieur. Je leur souhaite le meilleur pour l'avenir et espère les revoir très vite.

Enfin, j'ai une reconnaissance infinie envers ma famille, mes parents et mes frère et sœurs qui m'ont amené jusqu'ici et dont j'ai toujours ressenti le soutien infaillible même durant cette période où je n'ai pas été très disponible pour eux, et bien sûr Léa, à qui j'ai beaucoup demandé et dont la présence a été indispensable pour franchir cette étape.

Contents

Contents 24

Table of Figures 29

Table of Abbreviations 33

Introduction 38

Chapter 1 Context 44

1.1 Light-matter interactions in biological media 45

1.1.1 Reflection and refraction 45

1.1.2 Absorption 46

1.1.3 Elastic scattering 47

1.1.4 Raman scattering and fluorescence 50

1.2 Skin 51

1.2.1 Structure 51

1.2.1.1 Epidermis 53

1.2.1.2 Dermis 53

1.2.1.3 Hypodermis 54

1.2.2 Optical properties 54

1.2.2.1 Refractive index 54

1.2.2.2 Absorption parameters 56

1.2.2.3 Scattering parameters 59

1.3 Optical imaging for tissue diagnostics 60

1.3.1 Overview of optical imaging methods 60

1.3.2 Diffuse reflectance spectroscopy 63

1.4 Modeling the propagation of diffuse light in tissue 66

1.4.1 Transport theory 66

1.4.1.1 Assumptions 66

1.4.1.2 Notions of photometry 66

1.4.1.3 Radiative transfer equation 67

1.4.1.4 Limitations 69

1.4.2 Diffusion theory 70
1.4.2.1 Analytical approach 71
1.4.2.2 The diffusion approximation 71
1.4.2.3 Resolution of the diffusion equation 74
1.4.2.4 Domain of validity 78
1.4.2.5 The δP_1 approximation 78
1.4.3 Stochastic Model 80
1.4.4 Model comparison 82

Chapter 2 Specification of a compact, CMOS-based system architecture for contact, high resolution diffuse reflectance imaging 86
2.1 Introduction 87
2.1.1 Spatially resolved diffuse reflectance spectroscopy 87
2.1.2 State-of-the-art 88
2.1.3 Proposition 91
2.2 Proposed system architecture 91
2.2.1 Light sensor 92
2.2.2 Sensor-tissue coupling system 94
2.2.2.1 Technological limitation 94
2.2.2.2 Proposed solution 96
2.3 Proof of concept 98
2.3.1 Prototype srDRS device 98
2.3.1.1 Implementation 98
2.3.1.2 Characterization 101
2.3.2 Experiments and methods 105
2.3.2.1 Optical phantoms 105
2.3.2.2 Acquisition procedure 107
2.3.2.3 Data processing 108
2.3.3 Results 113
2.3.3.1 Model fit to data 113
2.3.3.2 Optical properties 113
2.3.3.3 Influence of minimal source-detector separation 115
2.3.4 Discussion 117
2.4 Conclusion 119

Chapter 3 Development of a low-cost, wearable srDRS system for skin condition diagnosis: validation study on solid phantoms 122
3.1 Instrument development 123
3.1.1 Sensor design 123
3.1.1.1 Packaging module 125
3.1.1.2 Lighting module 125
3.1.1.3 FOP-sensor coupling 127
3.1.2 Optical Characterization 129
3.2 Phantom validation 132
3.2.1 Development of solid phantoms 132
3.2.1.1 Motivation 132
3.2.1.2 Fabrication 133
3.2.1.3 SFDI Characterization 135
3.2.2 Materials and Methods 138
3.2.2.1 Experiments 138
3.2.2.2 Data Processing 139
3.2.3 Results 141
3.2.3.1 Validation of the experimental setup 141
3.2.3.2 Quantification of optical properties 143
3.2.3.3 Scaling of measured absorption coefficients 149
3.2.4 Discussion 151
3.3 Conclusion 154

Chapter 4 Low-cost, wearable srDRS system for skin condition diagnosis: evaluation for *in vivo* tissue oxygenation monitoring 156
4.1 Introduction 157
4.2 Materials and methods 159
4.2.1 Experiments 159
4.2.2 Data processing 161
4.2.2.1 Extraction of optical properties 161
4.2.2.2 Derivation of the tissue oxygen saturation (StO_2) 163
4.3 Results. 164
4.3.1 Measurement repeatability 164
4.3.2 Optical properties 166
4.3.3 Tissue oxygen saturation 169
4.4 Discussion 170
4.5 Conclusion 173

Chapter 5 Summary of results and future directions 176
5.1 Results summary 177
5.2 Future directions and perspectives 179
5.2.1 Analysis of layered media 179
5.2.2 Clinical trial 182

Conclusion 184

Appendix 188

A Convolution by the source beam profile 190

B Dynamic expansion algorithm 196
B.1 Principle 197
B.1.1 Initial data set 197
B.1.2 HDR reconstruction 198
B.2 Validation 199
B.2.1 Data simulation 199
B.2.2 Results 200

C Estimation of the blurring effect in contact CMOS-based imaging 204

Bibliography 208

Scientific communications 233

Table of Figures

Fig. 1-1 The Snell-Descartes law.....46

Fig. 1-2 Scattering event.....48

Fig. 1-3 Comparison between the Henyey-Greenstein and Mie phase function. 49

Fig. 1-4 Influence of scattering anisotropy g on the shape of the Henyey-Greenstein phase function. 50

Fig. 1-5 Epidermis and whole skin structures. 52

Fig. 1-6 Refractive index of skin as calculated from the water-protein and extended water-protein models.[11] 55

Fig. 1-7 Absorption coefficients of skin chromophores. 57

Fig. 1-8 Molar extinction coefficients of skin chromophores. 57

Fig. 1-9 Absorption spectra of skin layers as retrieved from Meglinski et al.[19].....58

Fig. 1-10 Sizes of skin constituents. 59

Fig. 1-11 Scattering coefficient of skin. 60

Fig. 1-12 Schematic display of various DRS modalities. 65

Fig. 1-13 Definition of the solid angle in spherical coordinates.....67

Fig. 1-14 Implications of the diffusion approximation on the source and scattering anisotropy. 74

Fig. 1-15 Graphical illustration of the extrapolated boundary condition. 76

Fig. 1-16 Image configuration in the extrapolated boundary condition. 76

Fig. 1-17 Flow-chart of the multilayer Monte Carlo algorithm developed at CEA.[125] 82

Fig. 1-18 Diffuse reflectance curves for various optical properties as derived from (blue) the standard diffusion approximation (SDA),[107] (red) the δP_1 approximation (δP_1)[109] and (black) Monte Carlo simulations (MC).[125].....84

Fig. 2-1 Detection schemes for fiber-based (a) and CMOS-based (b) srDRS instruments. 89

Fig. 2-2 Illustration of the Concentric Multi-Pixel Array (CMPA) probe developed by Senlik and Jokerst.[78].....90

Fig. 2-3 UI-1492-LE-M camera (IDS Imaging, Obersulm, Germany). 92

Fig. 2-4 Influence of shading compensation in contact imaging modality.....94

Fig. 2-5 Design of the experimental setup for the diffuse reflectance measurements reported by Schelkanova et al.: an axonometric view and a side view. 95

Fig. 2-6 Sensitivity of the diffuse reflectance to optical properties.....96

Fig. 2-7 Fiber-optic plates (commercial image from Ref. 143).....97

Fig. 2-8 Layout of the CMOS-based contact imaging system for spatially resolved diffuse reflectance spectroscopy. 98

Fig. 2-9 Photographs of the developed prototype CMOS-based contact imaging system. ...100

Fig. 2-10 Linearity measurement of the DRS prototype. 101

Fig. 2-11 Flat-field image recorded by the srDRS prototype. 103

Fig. 2-12 Source profile measurement.....104

Fig. 2-13 Impact of blurring in diffuse reflectance images. 105

Fig. 2-14 Photograph of liquid tissue-simulating phantoms.....106

Fig. 2-15 Flowchart of the data processing steps for optical properties quantification. 109

Fig. 2-16 Influence of the merit function on optical properties estimations. 112

Fig. 2-17 Measured calibrated reflectance of intralipid phantoms (dots) plotted against best fits of theoretical reflectance (solid lines).....113

Fig. 2-18 Results of phantom experiments. 115

Fig. 2-19 Influence of the minimal accessible SDS on optical properties estimates. 116

Fig. 2-20 Influence of the minimal source-detector separation on the merit function. 117

Fig. 3-1 Photograph of the wearable srDRS prototype.....124

Fig. 3-2 Layout of the wearable srDRS Prototype 124

Fig. 3-3 Digital model of the packaging module for the wearable srDRS prototype. 125

Fig. 3-4 Linearity curve of the wearable srDRS prototype. 129

Fig. 3-5 Positive USAF-1951 resolution test target imaged with the wearable srDRS system after glass lid removal. 130

Fig. 3-6 Lambertian flat-field images recorded (a) before and (b) after removal of the protective glass lid. 131

Fig. 3-7 Location of the FOP in the imaging area (a) before and (b) after removal of the protective glass lid. 132

Fig. 3-8 Photograph of manufactured PDMS phantoms. 135

Fig. 3-9 Optical properties of PDMS phantoms measured by SFDI at 665 nm. 136

Fig. 3-10 Experimental setup for phantom experiments before (a) and after (b) positioning of the PDMS phantom. 139

Fig. 3-11 Reproducibility of the pressure applied on phantoms: diffuse reflectance profiles. 141

Fig. 3-12 Reproducibility of the pressure applied on phantoms: optical property estimates. 142

Fig. 3-13 Influence of the wedge position on measured reflectance. 143

Fig. 3-14 Influence of the wedge position on measured optical properties. 143

Fig. 3-15 Comparison between optical properties measured with SFDI (black line) and the wearable srDRS system after glass removal. 145

Fig. 3-16 Comparison between two measured absorption (a) and reduced scattering (b) coefficients when considering n = 1 (red) or n = 1.5 (blue) in the exterior medium. 146

Fig. 3-17 Comparison between optical properties measured with the wearable srDRS device before (upward-pointing triangles) and after (circles) removal of the glass lid. 147

Fig. 3-18 Raw reflectance images of the rough (a) and flat (b) faces of phantom B1. 148

Fig. 3-19 Comparison between measurements performed on the rough (circles) or flat (downward-pointing triangles) surface of phantoms. 149

Fig. 3-20 Relation between relative errors in measured μa and reduced scattering coefficients of phantoms. 150

Fig. 3-21 Scaling of absorption coefficients measured with the srDRS device toward expected values. 151

Fig. 4-1 *In vivo* oxygenation measurement. 160

Fig. 4-2 Extrapolation of the calibration phantom absorption coefficient. 162

Fig. 4-3 Repeatability of reflectance profiles measured at 660 nm. 164

Fig. 4-4 Repeatability of (a) absorption and (b) reduced scattering coefficients measured at 660 nm. 165

Fig. 4-5 Measured absorption (a) and reduced scattering (b) coefficients. 166

Fig. 4-6 Measured (blue) and scaled (red) μ_a at 660 nm along with the SSOP measurement at 665 nm. 167

Fig. 4-7 Results from Single Snapshot of Optical Properties (SSOP) at 665 and 860 nm. ...168

Fig. 4-8 Measured tissue oxygen saturation (StO_2) during the cuff occlusion experiment. ..170

Fig. 5-1 Probability of photon visit as a function of (y,z) location in tissue for a 2 mm SDS and different source-detector combinations. 180

Fig. 5-2 Effect of the source and detector angles on the rate of photon propagation above various depths. 181

Fig. 5-3 Probability of photon visit as a function of (y,z) location in tissue for a 1 mm SDS and 45° angled source and detector. 181

Fig. A-1 Validation of the convolution algorithm for a circular flat beam. 192

Fig. A-2 Validation of the convolution algorithm for a Gaussian beam. 193

Fig. B-1 Example image set for reconstruction with expanded dynamic. 198

Fig. B-2 HDR image reconstruction. 199

Fig. B-3 Simulated image set. 200

Fig. B-4 Validation of the dynamic expansion algorithm. 201

Fig. C-1 Measurement of the srDRS prototype Edge Spread Function (ESF). 205

Table of Abbreviations

2-D **2-D**imensional

3-D **3-D**imensional

AFS **A**uto**F**luorescence **S**pectroscopy

CA **C**uring **A**gent

CARS **C**oherent **A**nti-Stockes **R**aman **S**pectroscopy

CLSM **C**onfocal **L**aser **S**canning **M**icroscopy

CMOS **C**omplementary **M**etal **O**xide **S**emiconductor

CMPA **C**oncentric **M**ulti-**P**ixel **A**rray

CPU **C**entral **P**rocessing **U**nit

CRA **C**hief **R**ay **A**ng**le**

DOI **D**iffuse **O**ptical **I**maging

DRS **D**iffuse **R**eflectance **S**pectroscopy

EMA **E**xtra **M**ural **A**bsorption

ESF **E**dge **S**pread **F**unction

fCLSM **f**luorescence **C**onfocal **L**aser **S**canning **M**icroscopy

FOP **F**iber **O**ptic **P**late

FOV **F**ield-**O**f-**V**iew

FWHM **F**ull **W**idth at **H**alf **M**aximum

GPU **G**raphics **P**rocessing **U**nit

HDR **H**igh **D**ynamic **R**ange

HHb deoxy**H**emoglobin

IR **I**nfra**R**ed

IRF **I**nstrument **R**esponse **F**unction

ISO **I**nternational **O**rganization for **S**tandardization

LED **L**ight-**E**mitting **D**iode

LSF **L**ine **S**pread **F**unction

LUT **L**ook-**U**p **T**able

MC **M**onte **C**arlo

MRI **M**agnetic **R**esonance **I**maging

MTF **M**odulation **T**ransfer **F**unction

NA **N**umerical **A**perture

Ng-EtOH **N**i**g**rosin-**Et**hyl**Alcohol**

NIR **N**ear **I**nfra**R**ed

NIRS **N**ear **I**nfra**R**ed **S**pectroscopy

O_2Hb **O**xy**H**emoglobin

OCT **O**ptical **C**oherence **T**omography

PCB **P**rinted **C**ircuit **B**oard

PD **P**hoto**D**iode

PDMS **P**oly(**D**i**M**ethyl**S**iloxane)

rCLSM **r**eflectance **C**onfocal **L**aser **S**canning **M**icroscopy

RGB **R**ed **G**reen **B**lue

ROI **R**egion Of **I**nterest

SDA **S**tandard **D**iffusion **A**pproximation

SDS **S**ource-**D**etector **S**eparation

SEM **S**lanted **E**dge **M**ethodology

SFDI **S**patial **F**requency **D**omain **I**maging

SHG **S**econd **H**armonic **G**eneration

SNR **S**ignal-to-**N**oise **R**atio

SORS **S**patially **O**ffset **R**aman **S**pectroscopy

srDRS **s**patially **r**esolved **D**iffuse **R**eflectance **S**pectroscopy

SSOP **S**ingle **S**napshot of **O**ptical **P**roperties

StO_2 **T**issue **Oxy**gen **S**aturation

THG **T**hird **H**armonic **G**eneration

TiO_2 **T**itanium **Dio**xide

TPEF **T**wo-**P**hoton **E**xcitation **F**luorescence

trDRS **t**ime **r**esolved **D**iffuse **R**eflectance **S**pectroscopy

UV **U**ltra**V**iolet

Introduction

Knowledge of the physiological properties of skin tissue is of critical importance for patient care management in a great number of pathologies. Instruments capable of characterizing these properties *in vivo* are of great interest both for the medical community and cosmetic industry.

In the past decades, optical imaging has emerged as an efficient tool to provide reliable information about the tissue status and assist clinicians in various diagnostic and therapeutic procedures. These techniques rely on the interaction of light with tissue to infer both biochemical and morphological properties of tissue that may be related to important functional parameters.

Diffuse reflectance spectroscopy (DRS) is a particular optical imaging modality that consists in illuminating the tissue and studying the properties of the backscattered light, referred to as diffuse reflectance, to identify the spectral signatures of various biochemical species. DRS provides non-invasive, quantitative characterization of tissue physiology in depth while relying on inexpensive and compact technology, making it a suitable candidate for various biomedical and cosmetic applications at the point of care.

Translation of DRS into clinical instruments raises difficulties notably concerning the miniaturization of devices, integration of these into the medical workflow of the hospital as well as their ability to provide reliable information over a wide range of tissue types. Notably, dealing with the stratified structure of skin (epidermis, dermis, fat) constitutes a significant challenge that must be met in order to address a variety of applications including early cancer detection, oxygenation monitoring and drug permeation follow-up.

Spatially resolved diffuse reflectance spectroscopy (srDRS) is a particular modality of DRS that analyzes the spatial dependence of diffuse reflectance spectra produced by an illumination with a controlled geometry. By collecting the diffuse reflectance at multiple distances from the source, srDRS has the potential to probe various depths in order to achieve the characterization of tissue with layer specificity. However, current instruments involving fiber components or photodiodes to collect the backscattered photons have difficulties achieving this goal due to limitations in terms of spatial resolution and light collection efficiency.

The objective of this doctoral thesis is to develop a new generation of instruments capable of addressing the characterization of skin with layer specificity while having minimal impact on the patient and medical staff in terms of cost, time and footprint. For this purpose, we propose to implement the srDRS technique using a high resolution multi-pixel sensor placed

in contact with the tissue. Compared to existing fiber optic and photodiode-based devices, such sensor provides enhanced spatial resolution and light collection efficiency, thereby having a significant potential for the layer-specific analysis of tissue. We propose to investigate the use of low-cost, compact technology including a Complementary Metal Oxide Semiconductor (CMOS) imager and surface mounted light emitting diodes (LED). Thereby, our approach is fully relevant for the development of wearable devices for point of care applications.

The project was divided into three stages:

- The specification of the adequate system architecture to perform srDRS measurements using a CMOS sensor in a contact imaging modality and the validation of this architecture for the characterization of tissue-simulating liquid phantoms
- The development of an optimized system based on the proposed architecture and validation of this system for the characterization of solid phantoms.
- The evaluation of the developed device for the continuous monitoring of tissue oxygenation *in vivo*.

Chapter 1 provides the contextual elements necessary to apprehend the project. In the first section, light-matter interactions in biological media are introduced and a description of skin structure and optical properties is given. Then, the clinical motivation for skin optical characterization and the potential of diffuse optical methods to address this issue are discussed. Following this discussion, diffuse reflectance spectroscopy is presented in further detail. Finally, the mathematical modeling of light propagation in turbid media is presented. During the first months of the PhD program, different models of light propagation have been studied in the literature. Several models were implemented, including a stochastic approach involving numerical calculations of photon paths through Monte Carlo simulations, as well as an analytical approach referred to as diffusion theory and an improvement of this approach denoted as the δP_1 approximation. In the end, a comparison between these models and their limits of validity is made.

Chapter 2 introduces the system architecture that was specified to carry out spatially resolved diffuse reflectance imaging in contact using a standard high resolution image sensor. In the first section, a detailed presentation of spatially resolved diffuse reflectance spectroscopy and state of the art of the method is provided. Then, the main limitations

associated to our approach are discussed and the system design that was developed to overcome these limitations is described. Finally, validation of the system's performance on tissue-simulating liquid phantoms is presented.

In Chapter 3, we report on the implementation of the proposed architecture into a compact, wearable prototype designed toward layer-specific and *in vivo* tissue analysis. First, the development of solid tissue-simulating phantoms is presented. Then, the performance of the developed prototype for the characterization of these phantoms is analyzed in comparison with Spatial Frequency Domain Imaging (SFDI), an imaging method developed at a partner institution (Laboratoire des sciences de l'Ingénieur, de l'Informatique et de l'Imagerie, ICube UMR 7357, Strasbourg, France).

In Chapter 4, the ability of our prototype to characterize oxygenation changes in tissue is evaluated. As an introduction to this chapter, the problematic of free flaps viability monitoring is presented and the potential of our approach for this application is discussed. Then, we report on *in vivo* experiments performed with the developed srDRS prototype and a real-time SFDI acquisition system. Notably, continuous oxygenation readings provided by the two systems on the forearm of a healthy volunteer during cuff occlusion are compared and discussed.

Chapter 5 provides a summary of obtained results as well as short-term and long-term perspectives opened by this work concerning the *in vivo* evaluation of the device and the analysis of layered media.

Finally, the last part of the manuscript discusses the main conclusions drawn from this project.

Chapter 1

Context

In this chapter, we introduce the scientific context of the doctoral work. Sec. 1.1 introduces the light-matter interactions most significant for our study. Sec. 1.2 describes the main properties of skin tissue and their physical modeling. In Sec. 1.3, a review of current imaging techniques and their application for tissue analysis is provided. Finally, Sec. 1.4 provides an outlook of current approaches to model the propagation of light in biological media and the diffuse reflectance from tissue.

1.1 Light-matter interactions in biological media

During its propagation in a biological medium, light interacts with the constituents of the medium through various processes. In this work, we are only interested in the following processes:

- Reflection and refraction
- Absorption
- Scattering

In this section, we describe the physical origin of these phenomena and their mathematical modeling.

1.1.1 Reflection and refraction

The first light-matter interactions to be considered are reflection and refraction, which occur at the point where an incident light beam enters the biological tissue, and more generally at the interface between two media with distinct refractive indices.

Refraction is governed by the Snell-Descartes law for refraction, as depicted in Fig. 1-1. An incident light beam propagating along an angle θ_{out} relatively to the normal of the interface is deviated towards an angle θ_{in} inside the medium. The incident and refraction angles are related to the refractive index mismatch between media, according to Eq. (1.1):

$$n_{in} \sin \theta_{in} = n_{out} \sin \theta_{out} \tag{1.1}$$

A part of the incident beam's energy is not transmitted through the interface and emanates in a second beam which is reflected in the opposite direction relatively to the normal of the interface. This process is referred to as specular reflection. The energy distribution between the specular reflected and refractive beams can be derived using Fresnel's law for reflection.

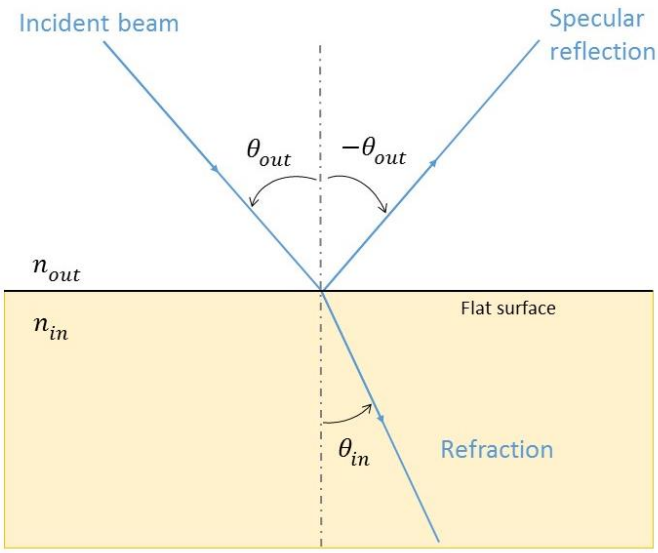


Fig. 1-1 The Snell-Descartes law. The incident beam makes an angle θ_{out} with the normal of the medium-exterior interface. After interaction at the interface, the incident beam energy is divided into a specular reflected beam and a refracted beam, which make an angle $-\theta_{out}$ and θ_{in} with the normal.

The previous relations hold in the case where the interface between media is perfectly planar. In general, and particularly for biological tissue, this is not true. In this case, the angle of propagation of the reflected and refracted beams are randomly distributed, according to a probability function which depends on the size and shape of the surface heterogeneities. However, this finer behavior is disregarded in our study.

1.1.2 Absorption

Absorption is the process in which the incident light propagating in the tissue transfers a part of its energy to a molecular species. This results in a transition of the molecule to a higher energy level. Absorption is particularly interesting for diagnostic applications since transitions between two energy levels are only possible at specific wavelengths, which depend on the nature of the molecule. Therefore, the quantification of absorption in a biological tissue directly informs about the tissue biochemical content.

The absorption mechanism is also at the basis of laser treatment procedures, in which the extraction of light energy by the tissue is used to produce therapeutic effects.

The absorption property of a medium is characterized by its absorption coefficient μ_a, defined as the probability of a photon to be absorbed per unit path length. As it propagates in an absorbing-only medium, light attenuates according to the following relation:

$$\frac{dI}{I} = -\mu_a dl \tag{1.2}$$

where I is the light intensity and l is the path length. Eq. (1.2) leads to the well-known Beer-Lambert law:

$$I(l) = I_0 \exp(-\mu_a l) \tag{1.3}$$

where I_0 is the light intensity at $l = 0$. From the absorption coefficients, one defines the absorption mean free path $l_a = 1/\mu_a$ as the average distance covered by a photon before experiencing absorption.

Provided that the photon pathlength is known, the measurement of the light attenuation in the medium directly yields the absorption coefficient. This parameter can in turn be linked to the tissue composition, as will be discussed in Sec. 1.3.

1.1.3 Elastic scattering

Scattering occurs when a photon incident on a tissue component along a certain direction is deviated towards another direction. Elastic scattering refers to the particular case in which the wavelengths of the incident and scattered photons are the same. In this manuscript, the terms ‘scattering’ and ‘elastic scattering’ are equivalently used for the sake of simplicity. Scattering results from the refractive index mismatch between the tissue component and its environment, inducing multiple reflection and refraction processes at the microscopic level. At the macroscopic level, a light signal incident on a scattering medium along a given direction is distributed over a range of angles, which depends on the size, shape and distribution of scatterers in the medium.

As for absorption, one defines the scattering coefficient μ_s as the probability for a photon to be scattered per unit length. The average distance covered by a photon before it undergoes a scattering event is referred to as the scattering mean free path $l_s = 1/\mu_s$.

The analogy between μ_a and μ_s leads to the definition of the total attenuation coefficient (or total interaction coefficient) $\mu_t = \mu_a + \mu_s$ and the associated mean free path $l_t = 1/\mu_t$ as the average distance covered by photons between interactions. For a medium with higher absorption than scattering, the modified Beer-Lambert law can be written as:

$$I(l) = I_0 \exp(-\mu_t l) \tag{1.4}$$

Eq. (1.4) only holds when considering the light transmitted by the medium in the same direction as the incident direction. This configuration is associated to the collimated transmission method, in which the modified Beer-Lambert law is used to extract the total attenuation coefficient of a turbid medium.[1] However, many applications including the one discussed in this manuscript involve the collection of the light reflected back from the tissue after interaction with its internal constituents. In such configurations, the angular distribution of scattering angles plays a crucial role on the shape of the collected signal. This angular distribution is parameterized by the scattering phase function $p(\hat{\boldsymbol{s}}, \hat{\boldsymbol{s}}')$, which describes the probability for a photon undergoing a scattering event with initial direction $\hat{\boldsymbol{s}}$ to be scattered along a direction $\hat{\boldsymbol{s}}'$ (see Fig. 1-2).

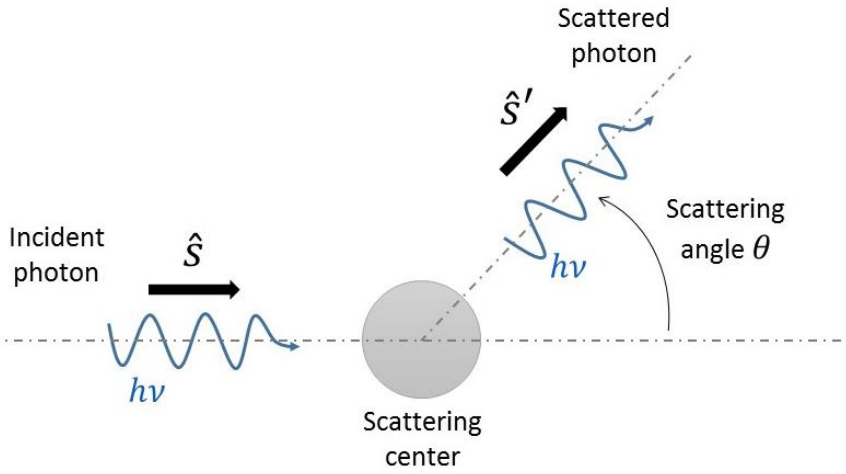


Fig. 1-2 Scattering event. A photon incident on a scattering center with a direction $\hat{\boldsymbol{s}}$ is deviated toward a direction $\hat{\boldsymbol{s}}'$ making an angle $\boldsymbol{\theta}$ with the initial direction.

From now on, we make the assumption that all scatterers are spherical. In this case, the scattering phase function only depends on the relative angle between the incident and exit direction, $\theta = \hat{\boldsymbol{s}} . \hat{\boldsymbol{s}}'$. The anisotropy factor g is defined as the average cosine of the scattering angle θ:

$$g = < \cos\theta > \tag{1.5}$$

The anisotropy factor is an expression of the directionality of scattering in the medium. Its value ranges from -1 to 1 for exclusively back-scattering, respectively forward-scattering media, $g = 0$ corresponding to isotropic scattering. The value of g is related to the scatterer size a and the wavelength λ of the incident light beam. Depending on these parameters, two regimes are distinguished:

- Mie scattering, which predominates when a is comparable to λ and corresponds to mainly anisotropic scattering with $g > 0$. Note that Mie theory is derived under the assumption that scattering particles are spherical.
- Rayleigh scattering, corresponding to a limit case of Mie theory for small particles (i.e. for $a \ll \lambda$), The Rayleigh regime is associated to isotropic scattering with $g = 0$.

As illustrated in Fig. 1-10, skin tissue is composed of various scatterers with different sizes, ranging from 0.01 µm for cell membranes to 10 µm and more for cells.

Therefore, both Mie and Rayleigh scattering influence the angular distribution of light in skin. The most commonly used phase function is the Henyey-Greenstein phase function:[2]

$$p_{HG}(\theta) = \frac{1}{4\pi} \frac{1 - g_{HG}^2}{(1 - 2g_{HG}\cos\theta + g_{HG}^2)^{3/2}} \tag{1.6}$$

This phase function is a good approximation of Mie theory provided that the medium under consideration is sufficiently thick[3] (see Fig. 1-3). Fig. 1-4 depicts the angular distribution of scattering angles when considering the Henyey-Greenstein phase function with various values of g.

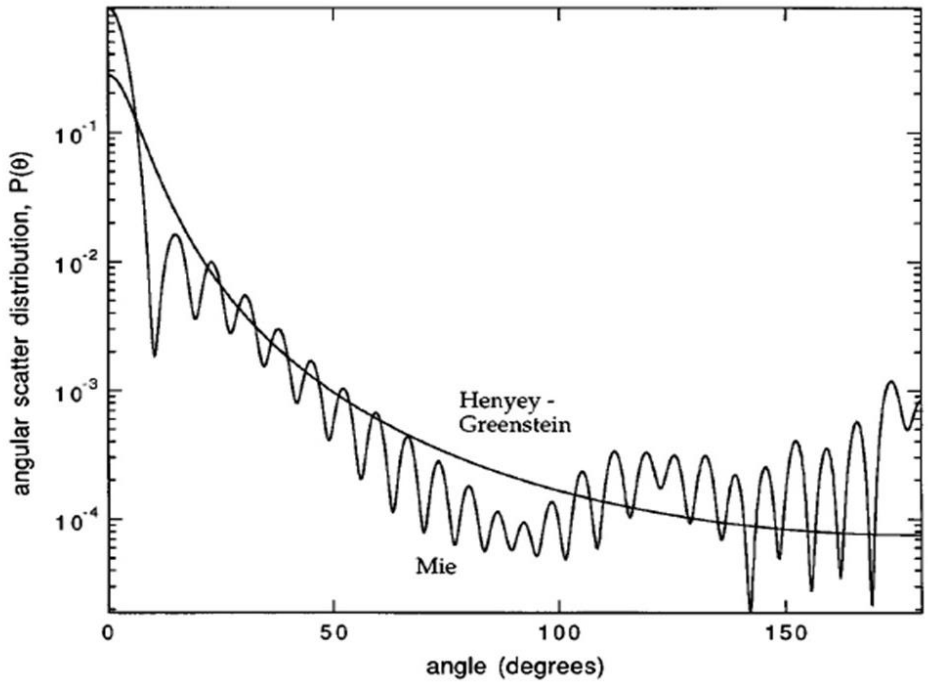


Fig. 1-3 Comparison between the Henyey-Greenstein and Mie phase function. Figure retrieved from Mourant et al.[3]

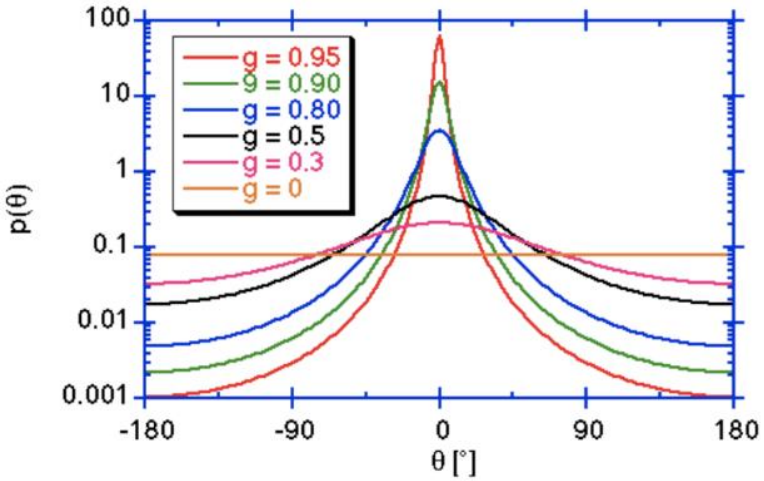


Fig. 1-4 Influence of scattering anisotropy g on the shape of the Henyey-Greenstein phase function. Figure retrieved from Ref. 4.

Biological tissues are characterized by a high probability of scattering with respect to absorption. This property is referred to as turbidity. In a turbid medium, light propagation rapidly becomes isotropic at the macroscopic scale. To this extent, the scattering coefficient and anisotropy factor are commonly gathered in a single parameter, referred to as the reduced scattering coefficient:

$$\mu_s' = \mu_s(1 - g) \tag{1.7}$$

The physical interpretation of μ_s' is further discussed in Sec. 1.4.2.

1.1.4 Raman scattering and fluorescence

Raman scattering occurs when a scattering event results in the generation of a photon of lower energy than the incident photon (inelastic scattering).

Fluorescence is the generation of a photon after the decay of a molecule from a higher energy state to a lower energy state. It differs from Raman scattering, in which the molecule is transferred to a virtual higher energy state before re-emitting a photon. Fluorescence can be generated by an external source of photons (exogenous fluorescence) or by internal processes (endogenous fluorescence).

In the next chapters, both fluorescence and Raman scattering are disregarded as they are involved in less than on in a million absorption events.[5] Several imaging techniques have been developed to provide enhanced sensitivity to Raman and fluorescence emissions for improved biochemical contrast. These are discussed in Sec. 1.3.1.

1.2 Skin

Skin is the most extensive organ of the human body. It provides a bidirectional exchange between the body and its environment, ensuring multiple functions, among which:

- Temperature regulation of the body via sweat glands, hair and blood circulation
- Protection barrier from external aggression (mechanical impact, temperature variation, biological or chemical agent)
- Sensation through nerve cell receptors

Skin tissue exhibits a heterogeneous structure of multiple layers with individual mechanical and optical properties. In this section, we present the function and histological structure of skin. The components contained in skin tissue are listed and their impact on skin optical properties are described.

1.2.1 Structure

Skin is composed of three elementary layers, from top to bottom: epidermis, dermis and hypodermis. Graphical displays of the histological structures of skin are given in Fig. 1-5.

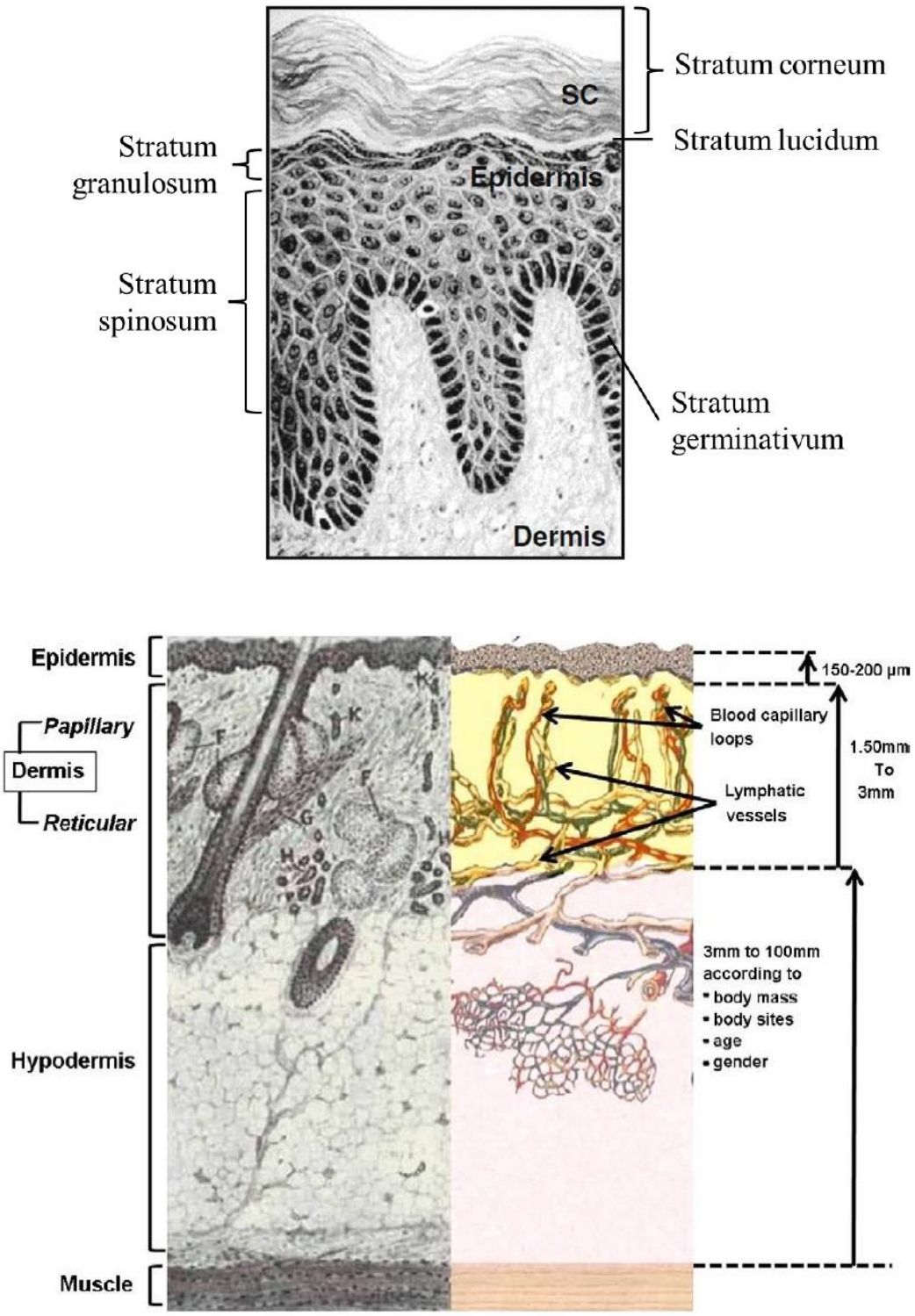


Fig. 1-5 Epidermis and whole skin structures. Figures retrieved from Refs. 6 and 7, respectively.

1.2.1.1 Epidermis

Epidermis is the superficial layer of skin, which acts as a barrier against external stresses. In the human body, its thickness ranges from 150 to 200 microns depending on the body site and age.[6] The epidermis itself can be divided into five sub-layers: the basal layer (or stratum germinativum), the prickle layer (or stratum spinosum), the granule layer (or stratum granulosum), the transition layer (or stratum lucidum) and the keratinized squamous layer (or stratum corneum).

The basal layer is where the keratinocytes (or epithelial cells) and melanocytes are synthesized. The birth of new epithelial cells forces the ascension of older ones through the prickle, granule and transition layers. During this process, keratinocytes progressively change shape until they reach the stratum corneum, in which they are reduced to flattened dead cells, densely filled with keratin.[8] This continuous regeneration of epithelial cells sustains the protection faculty of the epidermis.

The stratum corneum protects from damages due to mechanical abrasion or temperature change, prevents from invasion by micro-organisms and participates in the control of hydration. The melanocytes contained in the basal layer produce melanin granules, which absorb harmful UV radiation. These cells will naturally respond to an increase of UV radiation by increasing their production of melanin, giving rise to the well-known tanning effect.

1.2.1.2 Dermis

The dermal layer is separated from the epidermis by the basal membrane. The dermis thickness ranges from 1 to 3 millimeters in human skin. The dermis contains nerves and sweat glands for sensation and thermoregulation, arterial and venous vessels for blood supply, and a network of fibroblast cells. Fibroblasts synthesize the collagen and elastin fibers, which provide skin with its mechanical integrity and elasticity. The dermis is divided into two sub-layers: the papillary dermis, which makes the junction with the epidermis, and the reticular dermis.

The papillary dermis is composed of numerous capillary vessels contained in a loose fibrous network. It notably ensures blood provision to the epidermis. The reticular dermis is filled with a dense network of larger blood vessels contained in a denser and irregular fibrous network.

The dermis is the most vascularized layer of skin, responsible for 10% of the total blood flow in the body. It is the place where most of the exchanges between blood, skin and the environment occur.

1.2.1.3 Hypodermis

The hypodermis is situated underneath the dermis and makes the junction between skin and muscles. It principally contains adipose tissue, sweat glands and blood vessels. The adipose tissue synthesizes the lipids, which are involved in thermoregulation processes and in the production of vitamin D. The hypodermis thickness depends on the body site. It can reach up to 10 centimeters and highly varies among people.

1.2.2 Optical properties

1.2.2.1 Refractive index

Skin is composed of various components with individual refractive indices. Jacques et al.[9] proposed a model which takes account on the influence of water content on the refractive index value:

$$n_{skin}(\lambda) = n_{dry} - \left(n_{dry} - n_{water}(\lambda)\right) W \tag{1.8}$$

where W is the proportion of water in the tissue. $n_{dry} = 1.514$ is the refractive index of dry tissue as calculated from MRI measurements[10] and is considered as independent on wavelength.

A similar approach developed by Bashkatov et al.[11] considers the fraction of protein versus water content which the authors set at 70/30:

$$n_{skin}(\lambda) = 0.7 \times n_{protein} + 0.3 \times n_{water}(\lambda) \tag{1.9}$$

As for n_{dry}, the refractive index of proteins is assumed to be independent on wavelength with $n_{protein} = 1.5$. The refractive index of water is calculated from the following empirical formula:[11]

$$\begin{aligned} n_{water} = 1.58 - 8.45 \times 10^{-4}\lambda + 1.1 \times 10^{-6}\lambda^2 - 7.19 \times 10^{-10}\lambda^3 \\ + 2.32 \times 10^{-13}\lambda^4 - 2.98 \times 10^{-17}\lambda^5 \end{aligned} \tag{1.10}$$

where λ is expressed in nanometers. Alternatively, the authors proposed a finer model taking account on other tissue constituents such as collagen:

$$n_{skin} = 1.309 - 4.346 \times 10^{2}\lambda^{-2} + 1.6065 \times 10^{9}\lambda^{-4} - 1.2811 \times 10^{14}\lambda^{-6} \qquad (1.11)$$

Fig. 1-6 displays the refractive index of skin as calculated from Eqs. (1.10) and (1.11). Both models exhibit the same wavelength dependence that is the one of water. Practically, most publications assume a wavelength-independent refractive index of 1.4,[9] 1.36[12] or 1.37.[11,13,14] These values are in good agreement with the models developed by Bashkatov et al.[11] In addition, the refractive index is supposed no to vary from one layer to another.

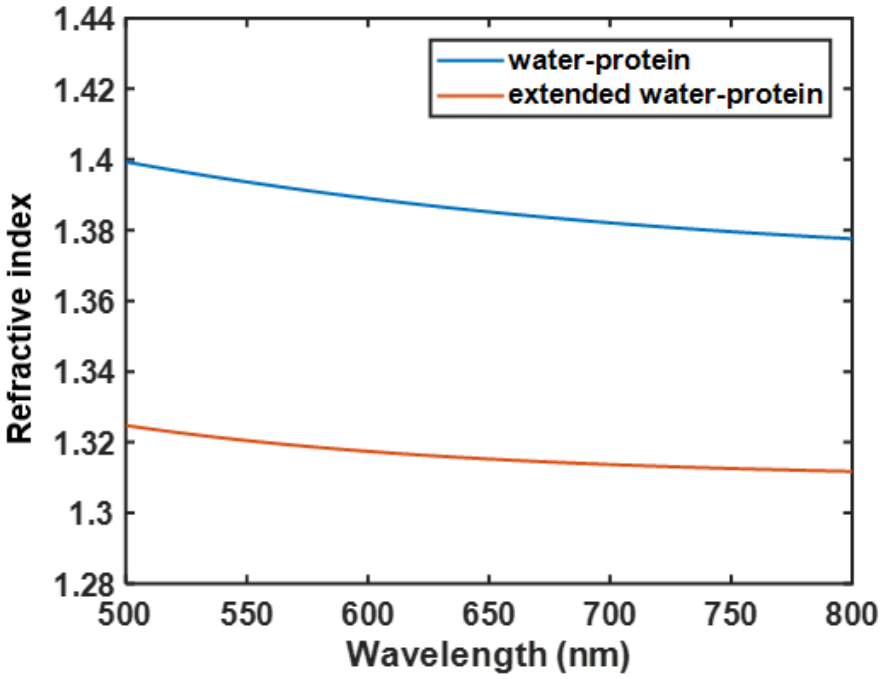


Fig. 1-6 Refractive index of skin as calculated from the water-protein and extended water-protein models.[11]

Some experimental studies report differences in refractive indices between layers, with a slightly higher refractive index in epidermis (stratum corneum included) than in dermis.[11,15–17] Except for the values reported by Tuchin,[17] measurements were not made in the visible spectrum. In addition, the differences between the recovered epidermal and dermal refractive indices in each study is on the order of the differences between values recovered for the same layer from one study to another. More data is needed to establish a clear difference between epidermal and dermal refractive indices.

1.2.2.2 Absorption parameters

The color of skin is principally influenced by its absorption properties. Fig. 1-7 displays the absorption spectra of the principal constituents of skin, referred to as chromophores. Each of these constituents exhibits a specific absorption spectrum which acts as a signature. In the visible domain, absorption is dominated by four chromophores: melanin, hemoglobin, bilirubin and carotene. Melanin pigments are characterized by their brown-black color which gives the different tones of human skin. Hemoglobin is responsible for the red tint of tissue while bilirubin and carotene exhibit a yellow-orange color. Hemoglobin can be found in various forms associated to individual absorption spectra. Among these, oxyhemoglobin is the carrier of oxygen in the body, while deoxyhemoglobin is the main deoxygenated form of hemoglobin (other forms such as carboxyhemoglobin and methemoglobin are found with lower concentration). Lipids and water have a significant impact at longer wavelengths and thereby should be taken into account in NIR and IR spectroscopy. Collagen absorbs light in the IR range while other proteins such as keratin absorb light in the UV spectrum. The absorption coefficient is directly related to the chromophore concentrations in tissue by the following formula:

$$\mu_a = \ln(10) \sum_i \varepsilon_i \, C_i \tag{1.12}$$

where ε_i and C_i denote the molar extinction coefficient and molar concentration, respectively, of chromophore i. The molar extinction spectra of the principle chromophores are shown in Fig. 1-8. In Fig. 1-7 and Fig. 1-8, a part of the visible spectrum can be distinguished where absorption (or extinction) is minimal and almost exclusively governed by melanin and hemoglobin. Inside this domain, light penetrates deeply into tissue and carries information about the blood and melanin content of skin, which are of great interest for biomedical application (see Sec. 1.3). For this reason, it is often referred to as the “biological window” or “therapeutic window”. The contribution of bilirubin and carotene to skin absorption is only significant at wavelengths lower than 500 nm and thereby is disregarded in this study.

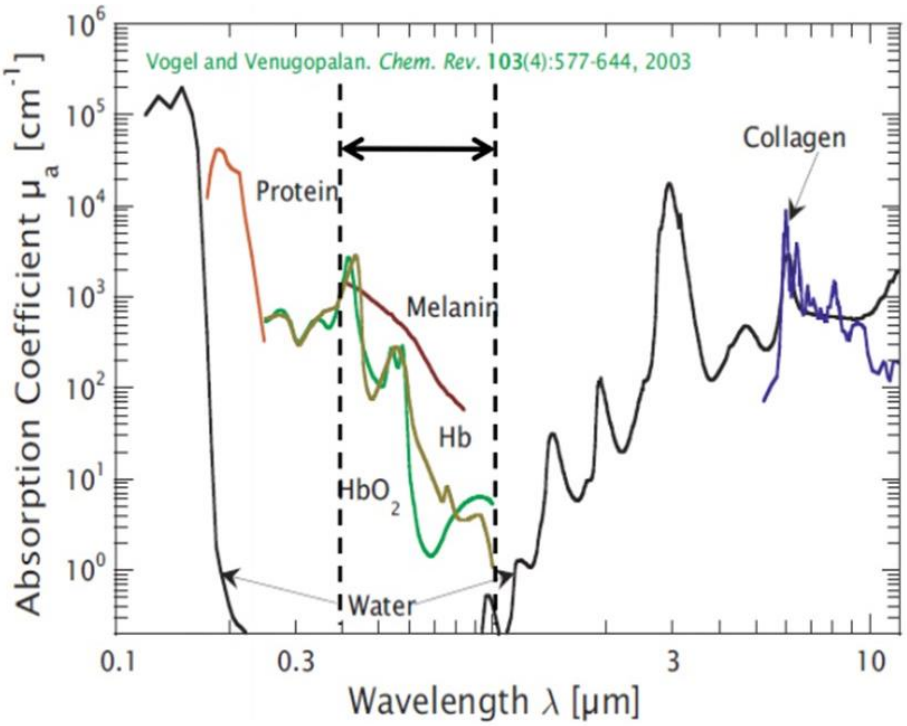


Fig. 1-7 Absorption coefficients of skin chromophores. Figure retrieved from Ref. 18.

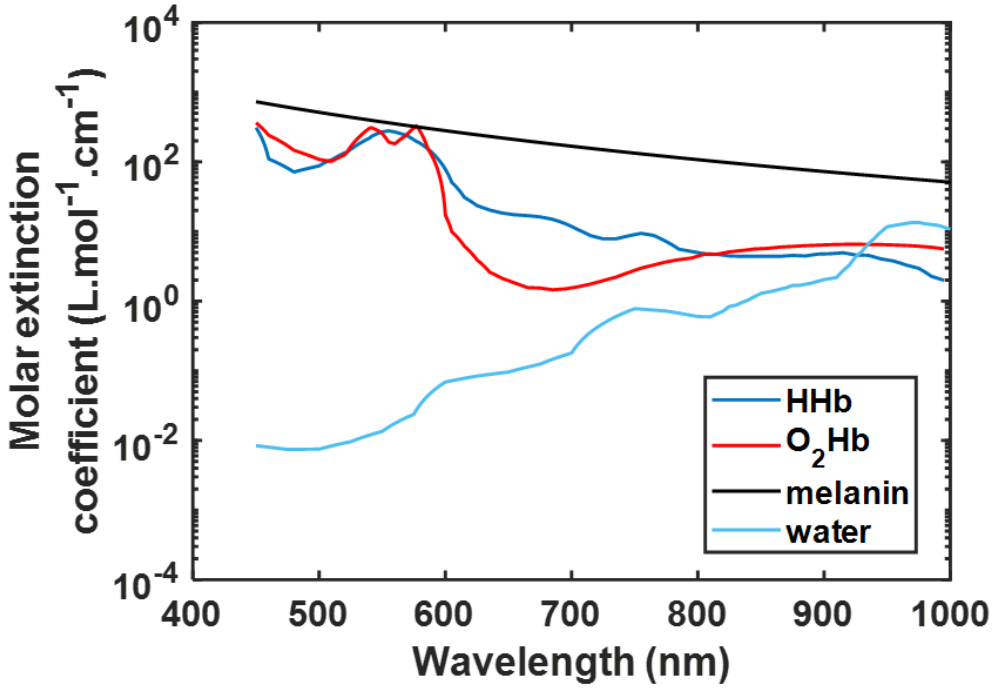


Fig. 1-8 Molar extinction coefficients of skin chromophores.

As discussed in Sec. 1.2.1, melanin is the only absorbing agent present in the epidermis. Conversely, the dermis does not contain melanin but hosts a network of blood vessels filled with hemoglobin. Bilirubin and carotene are also contained in the dermis while lipids mostly populate the hypodermis. Eventually, water is present in all layers except the stratum corneum. In particular, this means that absorption spectra are not the same from layer to layer. Meglinski et al.[19] used an 8-layer structure to model skin. The absorption spectrum of each layer is illustrated in Fig. 1-9. The characteristic shape of the hemoglobin spectrum is clearly visible in all layers but the epidermis and stratum corneum, which do not contain blood. Besides, the exponential decrease of melanin absorption can be observed in the epidermis spectrum.

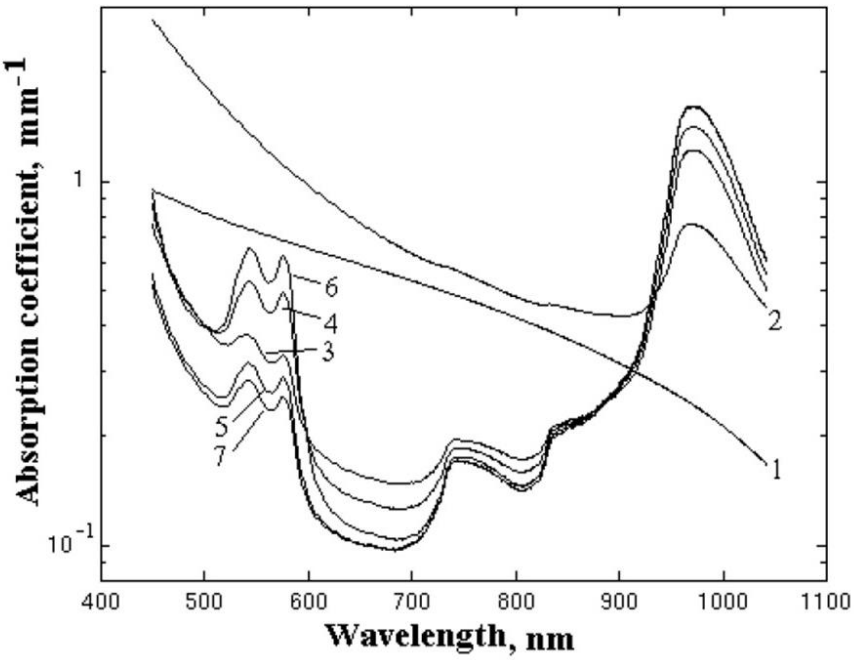


Fig. 1-9 Absorption spectra of skin layers as retrieved from Meglinski et al.[19] 1- stratum corneum, 2-living epidermis, 3-papillary dermis, 4-upper blood net dermis, 5-reticular dermis, 6-deep blood net dermis, 7-subcutaneous fat.

This layer to layer dependence of absorption in skin can be beneficial for many biomedical applications. Indeed, targeting a particular layer makes it possible to target a specific chromophore without being influenced by the pigments contained in surrounding layers. This is of high interest when it comes to pathologies associated to a specific chromophore such as melanin or bilirubin. For this reason, the development of instruments capable of performing measurements with layer to layer specificity constitutes an active research field.

1.2.2.3 Scattering parameters

In the visible domain, scattering is dominated by collagen, elastin and keratin. Collagen and elastin are responsible for the scattering property of dermis while scattering in epidermis originates from keratin. The contribution of melanin to the epidermis scattering has been suggested by the study of Tseng et al.[20], who retrieved higher scattering coefficients on African skin types, but was contested by the results reported in Ref. 12. Scattering centers of skin have various sizes, ranging from 10 nm for cell membranes to 10 µm and more for cells (see Fig. 1-10). Collagen and elastin are of the order of 100 nm and are organized in fiber bundles reaching up to 8 µm, meaning that both Mie and Rayleigh regimes are generated.[11] Therefore, the reduced scattering coefficient is commonly modeled by a power law on the wavelength, with separate contributions of Rayleigh and Mie scattering:[9,11,21]

$$\mu'_{s,skin}(\lambda) = \mu'_{s,skin}(\lambda_0)\left[f_{Ray}\left(\frac{\lambda}{\lambda_0}\right)^{-4} + \left(1 - f_{Ray}\right)\left(\frac{\lambda}{\lambda_0}\right)^{-b_{Mie}}\right] \tag{1.13}$$

where λ_0 is an arbitrary wavelength used for scaling of experimental data. The factor f_{Ray} is the part of scattering following the Rayleigh regime while the factor $(1 - f_{Ray})$ corresponds to the Mie regime. The coefficient b_{Mie} depends on the average size of scatterers in the medium under consideration. A review of experimental values of theses parameters was provided by Jacques et al.[9] Fig. 1-11 illustrates the prevalence of Mie, respectively Rayleigh scattering to skin scattering properties at longer, respectively shorter wavelengths.

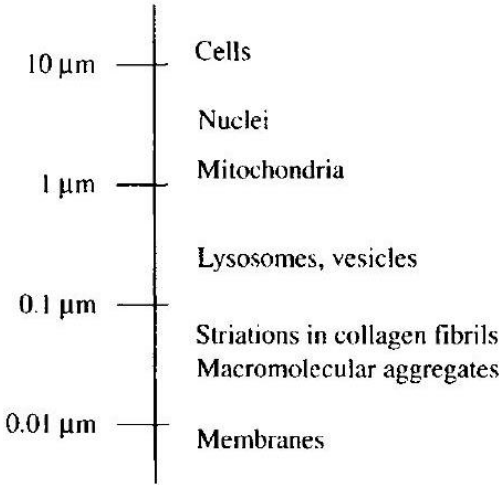


Fig. 1-10 Sizes of skin constituents. Figure retrieved from Ref. 1.

Reviews of absorption and reduced scattering coefficients of biological tissue measured in vitro and *in vivo* can be found in Refs. 9, 11 and 22. Retrieved μ'_s values for skin tissue are

comprised between 40 and 55 cm^{-1} at $\lambda = 500\,nm$. Bashkatov et al.[11] reported a lower value of 36.4 cm^{-1}. As for absorption, a distinction between epidermal and dermal scattering properties can be made. In particular, authors reported a higher value of scattering coefficient in the epidermis than in the dermis.[23,24] More data is needed to confirm this result.

As discussed in Sec. 1.1.3, scattering is also parameterized by its anisotropy. Jacques et al.[25] and van Gemert et al.[26] derived empirical formulae for the anisotropy factor of skin. In both studies, the predicted g value ranges from 0.75 to 0.85 in the visible spectrum. Skin is thus characterized by a strongly forward scattering behavior.

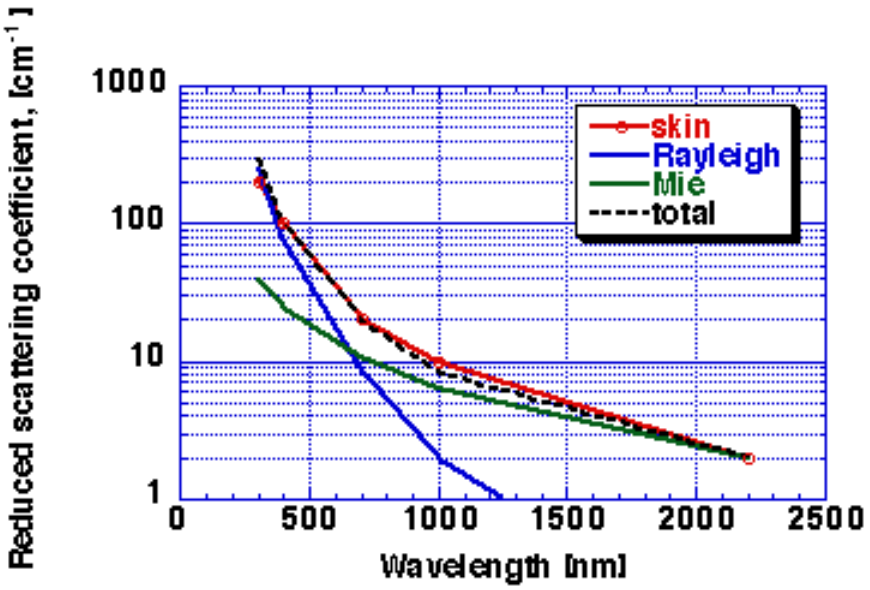


Fig. 1-11 Scattering coefficient of skin. Figure retrieved from Ref. 27. Reduced scattering coefficients were calculated using Mie (green) and Rayleigh (blue) theory. The total contribution of Mie and Rayleigh scattering (black) as calculated from Eq. (1.13) matches well the *in vivo* data (red).

1.3 Optical imaging for tissue diagnostics

1.3.1 Overview of optical imaging methods

In recent years, optical imaging techniques have emerged as a new powerful tool for *in vivo* tissue diagnostics. In the visible and near infrared domain, most biological tissues are characterized by strong scattering and weak absorption, the latter being dominated by blood, water and, for skin, melanin. In these conditions, photons can penetrate up to several centimeters in depth before being scattered back to the tissue surface, where they can be detected. The interaction of light with the constituents of tissue may then be used to generate

subsurface images with chemical and/or morphological contrast. Unlike X-ray imaging, optical imaging only involves nonionizing radiation being harmless to the patient and medical staff. Furthermore, optical imaging techniques can be conducted using relatively inexpensive instrumentation compared to Magnetic Resonance Imaging (MRI).

Various optical imaging methods have been developed for biomedical applications. These include Optical Coherence Tomography (OCT), Confocal Laser Scanning Microscopy (CLSM), nonlinear microscopy and Diffuse Optical Imaging (DOI), and can in some cases be combined with the detection of fluorescence or Raman emission to provide more detailed information about the biochemical composition of tissue. Optical imaging techniques differ in terms of spatial resolution, penetration depth, acquisition rate and accessible information (spectroscopic, morphological, biochemical, functional…). In the following we give a brief outlook of these techniques and their main features.

Optical Coherence Tomography (OCT) is an interferometric method that studies the morphological properties of tissue in real-time. The backscattered light that originates from a small volume of tissue corresponding to an individual coherence gate is selected. The method is based on the use of a broadband source (hence with a short coherence length) to reduce the size of the coherence gate and thereby the sampled volume of tissue. 2-D or 3-D images are formed by transverse scanning across the sample. OCT systems provide images up to 1-2 mm in depth and with 1-10 µm resolution.[1] Current OCT systems only provide structural information, although the extraction of metabolic contrast has been investigated in recent studies.[28] The most significant applications include skin cancer detection[29] and imaging of ocular tissue.[30] Most recent studies investigated the addition of metabolic contrast.

In Confocal Laser Scanning Microscopy (CLSM), optical sectioning of photons is performed by focusing both the illumination and detection beams on the same portion of tissue, referred to as the confocal volume. 3-D imaging is then obtained by transverse scanning of the confocal volume across the sample. CLSM images reach higher resolution than OCT images, but with reduced framerate and field-of-view. In reflectance CLSM (rCLSM), only morphological contrast is provided.[31,32] For biochemical characterization of tissue, CLSM can be combined either with fluorescence detection (fCLSM)[33] or Raman transition identification (Raman CLSM).[34] However, signal-to-noise ratios decrease rapidly with depth due to the unwanted contribution of multiple elastic scattering. This method is therefore restricted to shallow tissue depths not exceeding 300 µm.

Nonlinear microscopy methods have been developed to further push both the imaging depth and the spatial resolution. These include Two-Photon Excitation Fluorescence (TPEF),[35] Second and Third Harmonic Generation (SHG and THG, respectively),[36] and Coherent Anti-Stockes Raman Spectroscopy (CARS).[37] In TPEF, the simultaneous absorption of two photons produces the fluorescence signal. This technique provides biochemical contrast and spectroscopic information with high resolution and up to a few hundreds of microns. SHG, THG and CARS use multiphoton absorption to generate either fluorescence (for SHG and THG) or Raman emission signals (for CARS). The wavelengths of sources must be adjusted to a predetermined fluorescence or Raman emission to detect the presence of specific molecular species. Hence spectroscopic characterization is not provided.

Previously mentioned methods involve the imaging of ballistic light, which refers to photons that undergo only one or a few scattering events during their propagation through the tissue. Photons experiencing multiple scattering generate a diffuse light signal that increases with the imaging depth due to the strong scattering property of biological tissue. Although ballistic light imaging makes it possible to achieve extremely high spatial resolution, the imaging depth does not exceed a few hundreds of microns, except in OCT, which does however not provide biochemical contrast. Therefore, these techniques are not fully adequate for the analysis of deeper media (such as stromal, fat or muscle tissue). Besides, the cost and complexity of the instrumentation used in nonlinear microscopy techniques (high power, ultra-fast laser sources, high-end focusing optics) may be prohibitive for their implementation in the clinic.

Diffuse optical imaging is based on the detection and analysis of diffuse light signals to characterize the tissue content. In the diffusive regime, photon paths at the microscopic scale are treated as random and only macroscopic parameters are measured. Tissue images with biochemical and/or morphological contrast are reconstructed by a computer using analytical or numerical models of light propagation in the medium. Diffuse optical imaging comprises different techniques:

Diffuse Reflectance Spectroscopy (DRS) measures the elastically backscattered light to yield absorption and scattering properties of the tissue. Spectroscopic analysis of tissue absorption may yield the concentration of various molecular species (oxy and

deoxyhemoglobin, melanin, water, bilirubin, β-carotene…) while scattering parameters inform about the tissue morphology (thickness of layers, structure of collagen fibers…).

AutoFluorescence Spectroscopy (AFS) follows a similar principle as DRS except that it detects the tissue endogenous fluorescence.[38] This method makes it possible to measure the concentration of specific molecular compounds (including various enzymes, porphyrins, lipids, elastin, collagen and keratin) that cannot be accessed with DRS, which is why bimodal AFS-DRS systems have been developed.[39]

Spatially Offset Raman Spectroscopy (SORS) involves a laser illumination and the measurement of Raman emission spectra at multiple distances to the source for biochemical characterization of the tissue.[40]

Diffuse optical imaging does not compete with ballistic imaging in the field of spatial resolution. Current systems achieve image resolution of the order of the millimeter at the best. The main advantage of diffuse optical imaging is its ability to provide quantitative analysis of biological changes up to several centimeters in depth that are invisible to ballistic imaging systems. Thereby, *in vivo* functional imaging of deep media such as muscle, breast or brain tissue becomes possible. Diffuse optical imaging can be conducted at moderate cost using portable instruments and at high rate of acquisitions. Thereby, this technique has a great potential for rapid, non-invasive, *in vivo* tissue diagnostics and implementation in the clinic. The most significant applications include per and post-operative monitoring of tissue oxygenation and hemodynamics,[41–47] cancer detection,[48–53] jaundice diagnosis,[54] wound analysis,[55–57] pharmacokinetics[58] and treatment evaluation.[59,60] In the next section, we focus on diffuse reflectance spectroscopy.

1.3.2 Diffuse reflectance spectroscopy

Diffuse Reflectance Spectroscopy (DRS) is founded on the analysis of the backscattered light signal produced by a controlled illumination of the tissue surface. This signal, referred to as diffuse reflectance, is sensitive to absorption and scattering properties of the tissue, being themselves related to relevant biochemical and morphological parameters. Depending on the type of sources and detectors that are used, spatial, spectral or temporal reconstruction of these parameters is performed computationally by comparing the observed signal with theoretical predictions. These predictions are calculated using analytical or numerical models of light propagation in tissue for various combinations of optical properties (see Sec. 1.4).

The diffuse reflectance is measured as a function of time or space with or without modulation of the illumination, giving rise to various implementations of DRS (see Fig. 1-12).

In time resolved DRS (trDRS), an ultra-short laser pulse is employed for illumination of the tissue. The produced diffuse reflectance is detected using a time-correlated single photon counter (or a streak camera) to measure the time of flight of the backscattered photons.[46,47,61–66] Instead of short pulses, temporal modulation of the source can be used to measure the diffuse reflectance in the frequency domain, which is related to the real domain via Fourier transform.[67,68]

Alternatively, the spatial profile of the diffuse reflectance produced by a continuous-wave illumination with controlled geometry can be measured. The diffuse reflectance is recorded either with a camera,[42,59,69–75] photodiodes[76–81] or a fiber-based system.[49,82–91] In spatially resolved DRS (srDRS), a narrow beam illumination is produced, and the diffuse reflectance is measured at multiple distances to the source. This modality measures tissue properties on a single point underneath the sensing area. Therefore, lateral scanning is required to produce 2-D images. However, srDRS has a significant potential to discriminate between properties of individual tissue layers.[92] In analogy with time-domain DRS, spatial-domain measurements can be performed either in real[71–74,82–91] or frequency space.[42,59,70,75] In the latter case, referred to as Spatial Frequency Domain Imaging (SFDI), a spatially structured illumination (typically with sinusoidal or square intensity variation) is projected onto the tissue surface. The spatial frequency of illumination is modulated to produce 2-D images of the diffuse reflectance in the spatial frequency domain. In this manner, SFDI can perform tissue analysis in 2-D and in real-time.[70]

Time-domain modalities of DRS provide the highest penetration depth (typically a few centimeters) and are thereby most adapted to the functional imaging of cerebral and mammary tissue,[46,47,50] with resolution of the order of the centimeter. Conversely, spatial-domain DRS characterizes tissue at smaller depths (up to a few millimeters) but with higher resolution (~1 mm). Moreover, they can be implemented at low cost compared to time-domain methods.

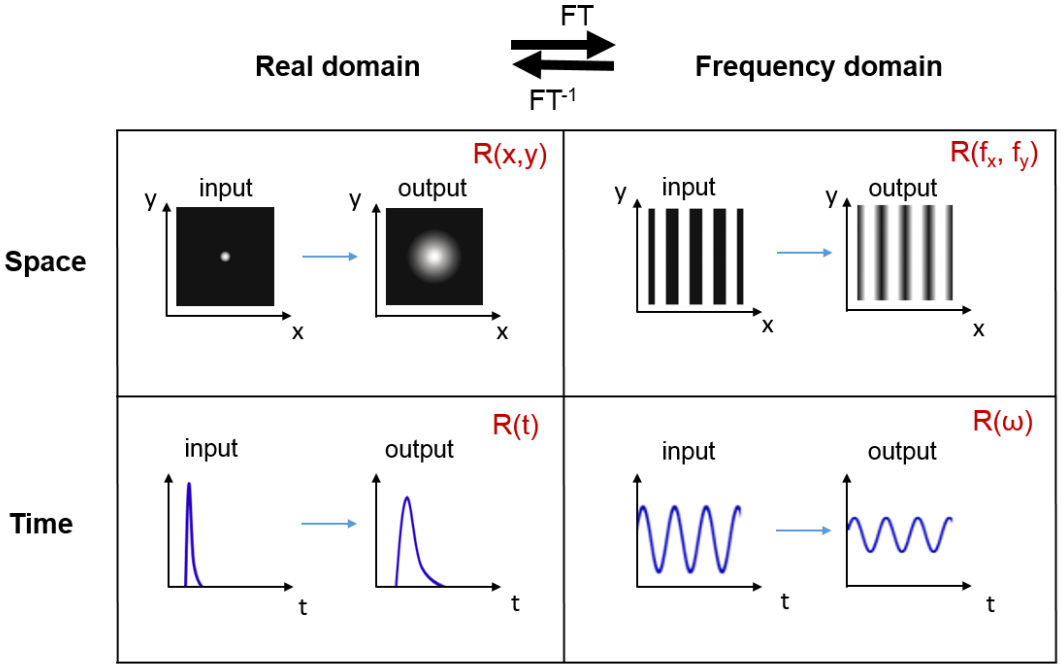


Fig. 1-12 Schematic display of various DRS modalities. The input beam illuminates the analyzed medium while the output light or diffuse reflectance R is detected after propagation in the medium. The diffuse reflectance can be measured in space (top) or time (bottom). Spatial/temporal modulation of the illumination can be employed to measure the frequency domain reflectance, which is related to the real domain reflectance by Fourier transform.

Through its different modalities, DRS has proven a valuable tool in a variety of situations including oxygenation monitoring,[41–47] investigation of melanin content,[93,94] breast and colon cancer detection,[47,50,51,53] tumor margin assessment in epithelium,[48,49,52] pharmacokinetics,[58] jaundice diagnostics in new-born skin,[54] skin ageing study,[95] skin test readings,[96] wound analysis[55–57] and treatment evaluation evaluation.[59,85] Several challenges remain that are subject to active research. These notably concern the translation of DRS technologies into clinical instruments (miniaturization, 2-D and 3-D measurements, real-time capabilities) and the depth resolved analysis of tissue. In the frame of cutaneous tissue analysis, recent studies have notably focused on the sectioning of photons propagating in the skin upper layers for carcinoma detection[48] or oppositely on the correction of *in vivo* oxygenation readings from the influence of epidermal properties.[43,75]

1.4 Modeling the propagation of diffuse light in tissue

In this section, we introduce two approaches for the description of light propagation in tissue. These methods lie in the frame of transport theory, which is presented in Sec. 1.4.1. In Sec. 1.4.2, we present two analytical approaches of the light transport model derived from diffusion theory. Then, we focus on a stochastic approach based on the use of the Monte Carlo method (Sec. 1.4.3). A comparison between these models is provided in Sec. 1.4.4.

1.4.1 Transport theory

Transport theory leads to the derivation of the Radiative Transfer Equation (RTE), which is commonly employed to describe the propagation of photons in biological media. In this section, we describe the main principles associated to transport theory and the derivation of the time-independent RTE.

1.4.1.1 Assumptions

In transport theory, the ballistic model of light is employed, in which photons propagating the medium are treated as single particles. Therefore, wave effects due to coherence of light and a fortiori quantum effects, which dominate at small length scales, are neglected. Polarization of light is also not considered here, although it can in some extent be included in the models presented in the following sections.

1.4.1.2 Notions of photometry

In this section, we use the spherical coordinates system with the notations of Fig. 1-13. The elementary solid angle made by an area element dA placed at a distance ρ from the origin is defined as follows:

$$d\Omega = \frac{dA}{\rho^2} \tag{1.14}$$

with

$$d\Omega = \sin\theta \, d\theta \, d\phi \tag{1.15}$$

In diffuse optics, the quantity of interest is the radiance L, expressed in $[W.sr^{-1}.m^{-2}]$. With the notations of Fig. 1-13, the elementary radiance generated by a flux dP traversing an area element dA and propagating in a solid angle element $d\Omega$ making a relative angle θ with this area writes as follows:

$$dL = \frac{dP}{dG} \tag{1.16}$$

where

$$dG = \cos\theta \, d\Omega \, dA \tag{1.17}$$

Eq. (1.17) defines the geometrical etendue associated with the light beam under consideration. A very convenient property of this quantity is that it is conserved during light propagation in free space and upon refraction or reflection processes. Consequently, the radiance must be conserved throughout the beam's propagation in order to respect energy conservation.

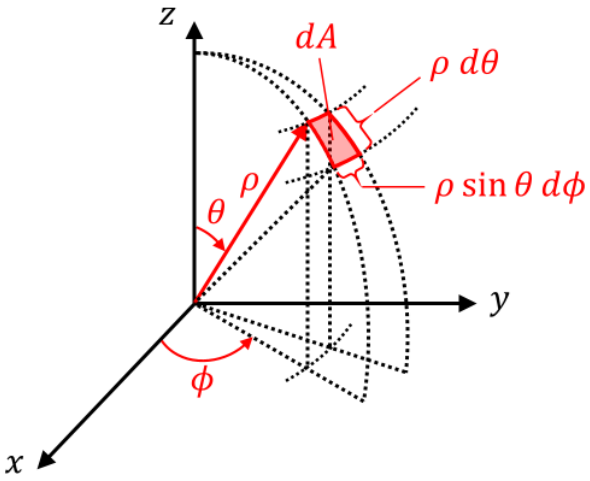


Fig. 1-13 Definition of the solid angle in spherical coordinates.

1.4.1.3 Radiative transfer equation

The behavior of light in turbid media is described by the radiative transfer equation, which was first derived by Chandrasekhar.[97] The RTE is heuristically built from a balance between losses and gains of radiance propagating along a unit vector $\hat{\boldsymbol{s}}$ throughout a volume element

dV of the medium. As discussed in Sec. 1.4.1.2, the RTE is therefore an energy conservation equation. Let us consider a volume element dV with coordinate vector $\boldsymbol{r}$ of a turbid medium.

Divergence of the beam

Unless the local photon beam is collimated, the beam's divergence has to be taken into account. The associated loss of energy writes as follows:

$$dP_{div} = \frac{\partial L(\boldsymbol{\rho}, \hat{\boldsymbol{s}}, t)}{\partial s} d\Omega \, dV = \hat{\boldsymbol{s}} \,.\, \boldsymbol{\nabla} L(\boldsymbol{\rho}, \hat{\boldsymbol{s}}, t) \, d\Omega \, dV \tag{1.18}$$

Note that this contribution can either be positive or negative whether the beam is diverging, respectively converging.

Loss by extinction

Another contribution to the energy change is the loss due to absorption of light within the volume element and scattering of photons toward a direction other than the incident direction $\hat{\boldsymbol{s}}$. The energy loss associated with this contribution writes:

$$dP_{ext} = -\mu_t \, ds \, L(\boldsymbol{\rho}, \hat{\boldsymbol{s}}, t) \, dA \, dV = -\mu_t \, L(\boldsymbol{\rho}, \hat{\boldsymbol{s}}, t) \, d\Omega \, dV \tag{1.19}$$

where $\mu_t = \mu_a + \mu_s$ is the total attenuation coefficient.

Gain by scattering

In a scattering medium, the gain of energy due to photons scattered from any direction $\hat{\boldsymbol{s}}'$ towards direction $\hat{\boldsymbol{s}}$ within $d\Omega$ has to be considered. The probability for a photon incident along direction $\hat{\boldsymbol{s}}'$ to be scattered toward a direction $\hat{\boldsymbol{s}}$ within $d\Omega$ writes as follows:

$$P(\hat{\boldsymbol{s}}, \hat{\boldsymbol{s}}') = \mu_s \, ds \, p(\hat{\boldsymbol{s}}, \hat{\boldsymbol{s}}') \, dA \, d\Omega = \mu_s \, p(\hat{\boldsymbol{s}}, \hat{\boldsymbol{s}}') \, d\Omega \, dV \tag{1.20}$$

where $p(\hat{\boldsymbol{s}}, \hat{\boldsymbol{s}}')$ is the scattering phase function defined in Sec. 1.1.3. Note that we have used the assumption that all scatterers are spherical, which means that the scattering phase function is only dependent on the relative angle between the incident and outgoing directions:

$$p(\hat{\boldsymbol{s}}, \hat{\boldsymbol{s}}') = p(\hat{\boldsymbol{s}} \,.\, \hat{\boldsymbol{s}}') \tag{1.21}$$

Making the sum of contributions of photons coming from all directions gives

$$dP_{scat} = \iint_{4\pi} L(\boldsymbol{\rho}, \hat{\boldsymbol{s}}, t) \, P(\hat{\boldsymbol{s}} \,.\, \hat{\boldsymbol{s}}') \, d\Omega' \tag{1.22}$$

From Eq. (1.22), this term can be rewritten as

$$dP_{scat} = \mu_s \iint_{4\pi} L(\boldsymbol{\rho}, \hat{\boldsymbol{s}}, t)\, p(\hat{\boldsymbol{s}} \,.\, \hat{\boldsymbol{s}}')\, d\Omega' d\Omega\, dV \tag{1.23}$$

Gain from sources

Finally, light sources can be present in the medium. The contribution of energy produced by a light source along direction $\hat{\boldsymbol{s}}$ within $d\Omega$ in the volume element dV can be written as

$$dP_{source} = S(\boldsymbol{\rho}, \hat{\boldsymbol{s}}, t)\, d\Omega\, dV \tag{1.24}$$

where S is expressed in $[W.sr^{-1}.m^{-3}]$. This source term can be introduced to model an excitation light beam injected in the medium or fluorescence emissions, which are not considered in this study.

Energy conservation

The variation of energy per unit time in direction $\hat{\boldsymbol{s}}$ within $d\Omega$ inside the volume element expresses as follows:

$$dP = \frac{\partial L(\boldsymbol{\rho}, \hat{\boldsymbol{s}}, t)/c}{\partial t} d\Omega\, dV \tag{1.25}$$

Energy conservation requires

$$dP = -dP_{div} - dP_{ext} + dP_{scat} + dP_{source} \tag{1.26}$$

In the following, only time-invariant media and continuous-wave sources are considered, meaning that

$$dP = 0 \tag{1.27}$$

Substituting all terms in Eq. (1.26), we obtain the time-independent RTE:

$$\hat{\boldsymbol{s}} \,.\, \boldsymbol{\nabla} L(\boldsymbol{\rho}, \hat{\boldsymbol{s}}, t) = -\mu_t\, L(\boldsymbol{\rho}, \hat{\boldsymbol{s}}) + \mu_s \iint_{4\pi} L(\boldsymbol{\rho}, \hat{\boldsymbol{s}}, t)\, p(\hat{\boldsymbol{s}} \,.\, \hat{\boldsymbol{s}}')\, d\Omega' + S(\boldsymbol{\rho}, \hat{\boldsymbol{s}}) \tag{1.28}$$

1.4.1.4 Limitations

Several assumptions are related to this equation. First, the medium's geometry is approximated by an infinite plane-parallel slab of finite thickness.[98] Practically, this condition requires that the excitation beam's width be small in front of the medium's expanse in lateral directions. Secondly, the optical properties are assumed to be homogeneous, meaning that the

index of refraction, absorption coefficient and scattering coefficient are considered to be space-invariant inside the medium. This assumption is respected provided that local heterogeneities in optical properties occur at length scales sufficiently small compared to the slab thickness.

Two important points have to be mentioned concerning scattering in the medium. First, the derivation of the RTE requires that each scattering event be not affected by other interactions occurring in its vicinity. This is equivalent to say that scatterers and absorbers are sparsely distributed in the tissue. The second point is that the RTE holds considering that every scattering event can be described by a unique phase function. In principle, this is only true if scatterers are all identical. These two requirements are clearly not fulfilled in biological media such as skin, where scattering centers exhibit various shapes and sizes and can be in contact with absorbing particles.

Despite of its crudeness relatively to the actual complexity of biological tissues, the radiative transport equation has provided a satisfying description of light transport in tissue for many applications.

In this chapter, the medium is modeled by an infinite plane-parallel slab of infinite thickness with a smooth surface. The medium is filled with randomly positioned identical absorbing and scattering particles with a sparse distribution. Optical properties are assumed to be homogeneous and the behavior of light at the interface between the medium and its environment is governed by Snell and Fresnel laws. Note that generalization to layered media is possible.[99,100]

Various approaches have been developed to derive the fluence rate in the medium, including numerical,[72,98,101–103] empirical[104] and analytical[92,105–109] methods. For an extensive review of these methods, one can refer to Ref. 110. In Sec. 1.4.3, we focus on a stochastic approach based on the Monte Carlo method. In Sec. 1.4.2, we describe the analytical approach referred to as the diffusion theory. A comparison of diffusion theory with Monte Carlo predictions is given in Sec. 1.4.4.

1.4.2 Diffusion theory

A possible approach for the description of light transport in tissue consists in making several simplifications in order to derive a new form of the RTE that admits analytical solutions. This approach, known as diffusion theory, leads to the derivation of the well-known diffusion

equation, which has been used in a variety of contexts to derive the optical properties of turbid media.

1.4.2.1 Analytical approach

The preliminary step in the derivation of diffusion theory is the separation of scattered from primary photons in the description of the radiance:

$$L(\boldsymbol{\rho}, \hat{\boldsymbol{s}}) = L_s(\boldsymbol{\rho}, \hat{\boldsymbol{s}}) + L_p(\boldsymbol{\rho}, \hat{\boldsymbol{s}}) \tag{1.29}$$

Photons propagating in the tissue without undergoing any scattering event are referred to as primary photons and contribute to the L_p term in Eq. (1.29). Once an incident photon experiences a scattering event, its contribution is transferred from L_p to L_s, denoted as the scattered radiance. In diffuse reflectance spectroscopy, light is collected after being scattered back from the tissue. Therefore, the quantity of interest is the scattered radiance.

From there, the scattered radiance is expanded into its spherical harmonic expansion:

$$L_s(\boldsymbol{\rho}, \hat{\boldsymbol{s}}) = \sum_{n=0}^{N} \sum_{m=-n}^{n} L_{n,m}(\boldsymbol{\rho})\, Y_{n,m}(\hat{\boldsymbol{s}}) \tag{1.30}$$

where $L_{n,m}$ are the expansion coefficients and $Y_{n,m}$ are the spherical harmonics expressed as a function of Legendre polynomials. This decomposition gives rise to a family of approximations called the P_N approximations, N referring to the maximum order to which the radiance is expanded. Note that the spherical harmonics expansion of L_s implies that spherical symmetry is respected in the medium. The limitations associated with this underlying assumption are further discussed in Sec. 1.4.2.4.

1.4.2.2 The diffusion approximation

The diffusion approximation is a popular approach of the transport model that has been applied in many studies.[71,72,111] This method allows the derivation of a simplified version of the RTE, namely the diffusion equation, that admits simple analytical solutions. In this section, we first describe the consecutive steps towards the derivation of the diffusion equation and its solution. Then, the limitations associated to this approach are discussed.

The diffusion approximation is based on the use of a particular phase function: the Eddington phase function.

$$p_E(\theta) = \frac{1}{4\pi}(1 + 3g\cos\theta) \tag{1.31}$$

This phase function makes it possible to separate the scattered radiance from the collimated radiance in the RTE. From there, an equation is derived for the scattered radiance.

In the diffusion approximation, the scattered radiance is expanded to the first order, which gives:[1]

$$L_s(\boldsymbol{\rho}, \hat{\boldsymbol{s}}) = \frac{1}{4\pi}\varphi_s(\boldsymbol{\rho}) + \frac{3}{4\pi}\boldsymbol{J}(\boldsymbol{\rho}) \,.\, \hat{\boldsymbol{s}} \tag{1.32}$$

In Eq. (1.32), two important quantities have been introduced: the scattered photon density or fluence rate φ_s and the photon current density $\boldsymbol{J}$, with

$$\varphi_s(\boldsymbol{\rho}) = \iint_{4\pi} L_s(\boldsymbol{\rho}, \hat{\boldsymbol{s}})\, d\Omega \tag{1.33}$$

$$\boldsymbol{J}(\boldsymbol{\rho}) = \iint_{4\pi} L_s(\boldsymbol{\rho}, \hat{\boldsymbol{s}}) \,.\, \hat{\boldsymbol{s}}\, d\Omega \tag{1.34}$$

L_s is therefore a combination of an isotropic term proportional the fluence rate and an anisotropic term proportional to the photon current density. From the time-independent RTE, the following equation can be derived:[1]

$$\boldsymbol{\nabla}.\boldsymbol{J}(\boldsymbol{\rho}) = -\mu_a\varphi_s(\boldsymbol{\rho}) + S(\boldsymbol{\rho}) \tag{1.35}$$

As for the scattered radiance, the spherical harmonic expansion of S is used. The main condition associated to the diffusion approximation is that this term is assumed to be isotropic. Consequently, all orders equal to or larger than 1 are neglected in the source harmonic expansion. In this case, the fluence rate and photon current density are related using Fick's law:[112]

$$\boldsymbol{J}(\boldsymbol{\rho}) = -D\nabla\varphi_s(\boldsymbol{\rho}) \tag{1.36}$$

where the diffusion constant D is introduced:

$$D = \frac{1}{3\mu_{tr}} \tag{1.37}$$

$$\mu_{tr} = \mu_a + \mu_s' \tag{1.38}$$

Remark that $\mu_s' = \mu_s(1-g)$ is the reduced scattering coefficient introduced in Sec. 1.1.3. Since the moment of order 1 is neglected in the source harmonic expansion, the diffusion approximation is more restrictive than the P_1 approximation. However, a derivation of the

diffusion equation which takes account of S_1 has been proposed by several authors.[98,105,112] Inserting Fick's law in Eq. (1.36) gives

$$\boldsymbol{\nabla}.\left(-D\nabla\varphi_s(\boldsymbol{\rho})\right) = -\mu_a\varphi_s(\boldsymbol{\rho}) + S_0(\boldsymbol{\rho}) \tag{1.39}$$

where S_0 is the 0-order term in the spherical harmonic expansion of the source. Since the optical properties of the medium are assumed to be invariant in space, Eq. (1.39) rewrites

$$\nabla^2\varphi_s(\boldsymbol{\rho}) - \frac{\mu_a}{D}\varphi_s(\boldsymbol{\rho}) = -\frac{S_0(\boldsymbol{\rho})}{D} \tag{1.40}$$

which is the so-called the *diffusion equation*.

While the RTE governs the behavior of the radiance, the diffusion equation only predicts the distribution of the fluence rate, which is no longer dependent on direction $\hat{\boldsymbol{s}}$. Additionally, a degeneracy appears between the scattering coefficient μ_s and the scattering anisotropy g, which are now combined into a single coefficient μ_s'. In the frame of the diffusion approximation, two media with different μ_s and g values lead to the same fluence rate distribution if their reduced scattering coefficients are respectively equal. This property is referred to as the similarity relation,[113] and is directly linked to the modeling of the source. Indeed, the similarity relation implies that a medium having a scattering coefficient μ_s and anisotropy $g > 0$ can be assimilated to a medium with scattering coefficient μ_s' and anisotropy 0.

The left side of Fig. 1-14 illustrates the implications relative to the diffusion approximation. Consider a collimated pencil beam incident on the surface of a medium characterized by its optical properties n, μ_a, μ_s and $g > 0$. In this configuration the source is problematic because it is collimated, hence highly anisotropic. The diffusion equation only governs scattered photons, which are separated from primary photons. Therefore, the source term of Eq. (1.36) can be modeled by a virtual secondary source of scattered photons placed a depth $l_s = 1/\mu_s$ from the surface, where it can reasonably be assumed that all photons have been scattered at least once. Yet at this stage the requirements of Eq. (1.40) are not fulfilled if scattering inside the medium is anisotropic, which is especially the case in skin tissues. In fact, after only one scattering event, photons are still mostly directed towards the incident beam's direction and the virtual secondary source cannot be qualified as isotropic. In the frame of the diffusion equation, the secondary virtual source is placed at a distance $l_s' = 1/\mu_s'$. At this distance, it can be shown that photons coming from the source have undergone enough scattering events to have completely lost the memory of their initial direction.

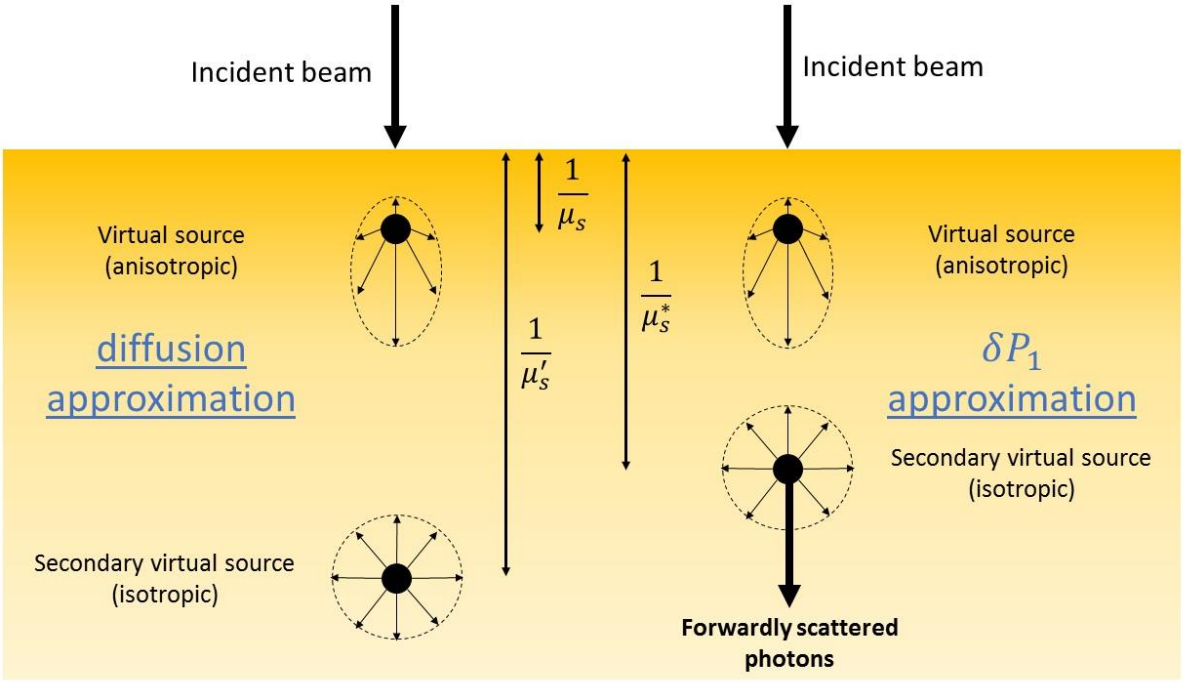


Fig. 1-14 Implications of the diffusion approximation on the source and scattering anisotropy.

1.4.2.3 Resolution of the diffusion equation

Various attempts have been made to derived analytical expressions of the fluence rate from the diffusion equation, both for vertical[106,107,112,114] and oblique[115,116] illumination. Following the approach of Kienle et al.[107], we derive the solution of the diffusion equation for a semi-infinite homogeneous medium illuminated by a pencil beam vertically incident on the medium's surface.

Source term

The derivation of the diffusion equation leads to the exponential source term (with order 1 neglected):

$$S_0(\rho, z) = \mu_s' \, \delta(\rho) \exp(-\mu_t' \, z), \tag{1.41}$$

where $\mu_t' = \mu_a + \mu_s'$. The source term in Eq. (1.41) can be viewed as an exponential decay of isotropic point sources. A simpler approach is generally used, which consists in modeling the source by a punctual isotropic source located at one scattering mean free path from the boundary:[106,107]

$$S_0(\rho, z) = \delta(\rho) \, \delta(z - z'), \tag{1.42}$$

with $z' = 1/\mu_s'$.

Green's function

The Green's function for a punctual source located at the origin of an infinite medium writes

$$G(\rho) = \frac{1}{4\pi D\rho} \exp\left(-\sqrt{\frac{\mu_a}{D}}\rho\right) \tag{1.43}$$

Provided that illumination is vertical, the linearity of the diffusion equation makes it possible to calculate the fluence rate for any source profile $S(\rho)$ by performing convolution.

Boundary conditions

Boundary conditions at the interface between the medium and its environment (usually glass or air) have to be applied to derive the expression of φ_s in a semi-infinite medium. Various types of conditions can be found in the litterature. The main ones are the zero-boundary conditions, the partial-current boundary condition and the extrapolated boundary condition. For an extensive study of these conditions and the associated limitations, one can refer to Refs. 107, 114 and 117.

The partial-current boundary condition consists in ensuring the conservation of φ_s at the interface. Using Fick's law, it can be shown that this is equivalent to the following relation:[112]

$$[\varphi_s(\boldsymbol{\rho}) - 2AD\boldsymbol{\nabla}\varphi_s(\boldsymbol{\rho}) \,.\, \hat{\boldsymbol{z}}]|_{z=0} = 0 \tag{1.44}$$

where factor A carries the influence of Fresnel reflections at the boundary:

$$A = \frac{1 + R_J}{1 - R_\varphi} \tag{1.45}$$

with

$$R_\varphi = \int_0^{\frac{\pi}{2}} 2 \sin\theta \cos\theta \, R_{Fresnel}(\theta) \, d\theta \tag{1.46}$$

$$R_J = \int_0^{\frac{\pi}{2}} 3 \sin\theta \cos^2\theta \, R_{Fresnel}(\theta) \, d\theta \tag{1.47}$$

where $R_{Fresnel}(\theta)$ is the Fresnel reflection coefficient for a photon with incident angle θ relative to the normal to the interface.

Extrapolating the fluence rate outside the medium by the extension of its derivative according to $\hat{\boldsymbol{z}}$ at $z = 0$, Eq. (1.44) is equivalent to say that the fluence rate cancels on an

extrapolated boundary placed at a distance $z_b = 2AD$ from the interface, as illustrated in Fig. 1-15. This is known as the *extrapolated boundary condition*.

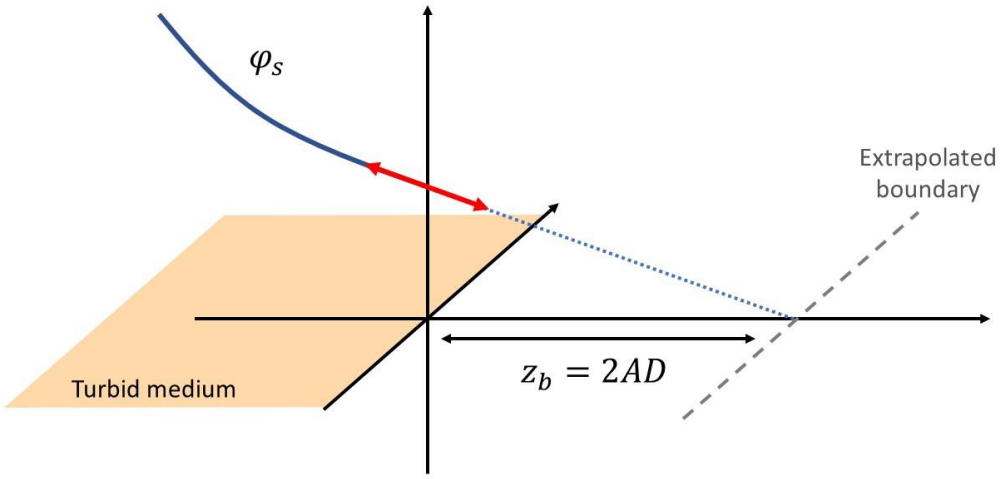


Fig. 1-15 Graphical illustration of the extrapolated boundary condition.

This condition is commonly used as it can easily be fulfilled using a method referred to as the method of images. In fact, an ingenious way of cancelling the fluence rate on the extrapolated boundary is to place a virtual negative source at a distance $z_- = -(1/\mu_s' + 4AD)$ from the physical boundary, as depicted in Fig. 1-16.

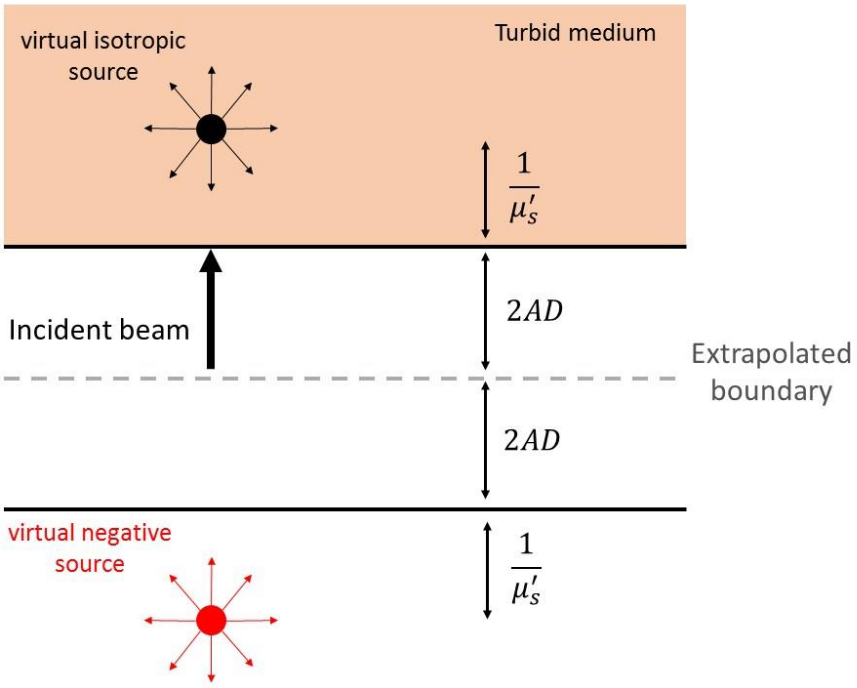


Fig. 1-16 Image configuration in the extrapolated boundary condition.

Expression of the solution

By linearity of the diffusion equation, the fluence rate in a semi-infinite medium expresses as the sum of the impulse responses to the virtual positive and negative sources displayed in Fig. 1-16. This yields:

$$\varphi_s(\rho,z) = \frac{1}{4\pi D}\left[\frac{1}{\rho_1}\exp\left(-\sqrt{\frac{\mu_a}{D}}\rho_1\right) - \frac{1}{\rho_2}\exp\left(-\sqrt{\frac{\mu_a}{D}}\rho_2\right)\right] \tag{1.48}$$

where

$$\rho_1 = \sqrt{(z-z')^2+\rho^2} \tag{1.49}$$

$$\rho_2 = \sqrt{(z+z'+4AD)^2+\rho^2} \tag{1.50}$$

By linearity of the equation, the solution for an exponential distribution of isotropic point sources writes

$$\varphi_s(\rho,z) = \frac{\mu_s'}{4\pi D}\int_0^\infty \left[\frac{1}{\rho_1}\exp\left(-\sqrt{\frac{\mu_a}{D}}\rho_1\right) - \frac{1}{\rho_2}\exp\left(-\sqrt{\frac{\mu_a}{D}}\rho_2\right)\right]\exp(-\mu_t' z')\,dz' \tag{1.51}$$

Notice that φ_s is function of the depth z in tissue, with the plane $z = 0$ being the surface of the medium, and of the distance to the source $\rho = \sqrt{x^2+y^2}$. The fluence rate and photon current thus exhibit a cylindrical symmetry around the source propagation axis.

Derivation of the diffuse reflectance

In diffuse reflectance spectroscopy, an expression of the diffuse reflectance R at the tissue surface is needed. Farrel et al.[106] calculated this quantity as the photon current density pointing towards the normal direction at the interface and used Fick's law to relate it to the fluence rate. A finer approach was developed by Haskell et al.[114], who took the contribution of the radiance along all directions at the boundary. In this case, the diffuse reflectance can be written

$$R(\rho) = \frac{1-R_\varphi}{4}\varphi_s(\rho,z=0) - \frac{1-R_J}{2}\boldsymbol{J}(\rho,z=0)\,.\,\hat{\boldsymbol{z}} \tag{1.52}$$

Making use of Eq. (1.36), we get

$$R(\rho) = \frac{1-R_\varphi}{4}\varphi_s(\rho,z=0) + \frac{1-R_J}{2}D\frac{\partial\varphi_s}{\partial z}(\rho,z=0) \tag{1.53}$$

1.4.2.4 Domain of validity

The derivation of the diffusion equation requires several simplifications of the source and medium's properties. Therefore, it should only be used under certain conditions in order to avoid significant errors in the predictions of light transport. A detailed discussion of the limitations and sources of errors related to the diffusion approximation can be found in Refs. 114 and 118. The generally accepted statement is that the diffusion equation holds for media exhibiting (1) a high albedo, hence when $\mu_s' \gg \mu_a$, (2) moderate scattering anisotropy ($g < 0.99$) and (3) far enough from collimated sources ($\rho > l'$) and boundaries. These conditions are clearly correlated. Since the diffusion equation assumes an isotropic source, large errors appear in the vicinity of the source where photons are mainly directed along the beam propagation direction. At a distance equal or larger to a few transport mean free paths, photons have globally lost the memory of their initial direction, and the isotropic modeling of the source closely matches the reality. In a medium with very high scattering anisotropy g the diffusion equation is a poor description since the propagation of photons remains anisotropic at large distances from the source. In an absorbing medium, photons only propagate within a few absorption mean free paths, where the diffusion approximation does not apply. Eventually, close to the boundary, light propagation is strongly anisotropic since photons tend to be directed towards the exterior.

In the following, the model presented in this section will be referred to as the *Standard Diffusion Approximation* (SDA).

1.4.2.5 The δP_1 approximation

The diffusion equation approximates the response of the medium to the first order, which induces the limitations listed in Sec. 1.4.2.4. In theory, these limitations can be overcome by the use of a higher order expansion of the radiance. Notably, Hull and Foster[119] developed a P_3 approximation of the RTE and demonstrated improved results compared to the classical diffusion approximation. This approach can be generalized to higher order approximations, yet at the expanse of computation efficiency. Prahl[98] and Star[112] independently proposed an ingenious way to improve the diffusion approximation while conserving its simplicity. This approach, referred to as the *δP_1 approximation*, is described in this section.

δ-Eddington phase function

The δP_1 approximation consists in employing a second order phase function while conserving a first order approximation of the radiance. In practice, the δ-Eddington phase function, first introduced by Joseph et al.[120] is used:

$$p_{\delta E}(\theta) = \frac{1}{4\pi}[2f\delta(1-\cos\theta) + (1-f)(1+3g^{*}cos\theta)] \tag{1.54}$$

The δ-Eddington phase function is the sum of two terms: one corresponding to scattering toward the beam direction and the other associated to scattering outside the beam. The second term is the classical Eddington phase function weighted by a factor f defining the contribution of scattering along the beam's direction. Thus, photons scattered along the incident beam's direction are treated separately from photons scattered outside the beam. The latter are described in the frame of the diffusion equation for propagation in a medium with reduced scattering coefficient μ_s^* and anisotropy g^*:

$$\nabla^2\varphi_s(\boldsymbol{\rho}) - \frac{\mu_a}{D^*}\varphi_s(\boldsymbol{\rho}) = -\frac{S_0^*(\boldsymbol{\rho})}{D^*} \tag{1.55}$$

with $D^* = 1/3\mu_t^*$, $\mu_t^* = \mu_a + \mu_s^*$ and $\mu_s^* = \mu_s(1-g^*)$. The δ-Eddington phase function is constructed so as the first and second order moments of its spherical harmonic expansion match the corresponding moments of the Henyey-Greenstein phase function. This results in the following formulae:[108,120]

$$\mathrm{g}^* = \frac{g_{HG}}{1+g_{HG}}; f = g_{HG}^2 \tag{1.56}$$

Consequently, the δ -Eddington phase function reduces the anisotropy of scattering that is described by the diffusion equation compared to the Eddington phase function. For a tissue with anisotropy $g_{HG} = 0.8$, which is representative of skin tissue, the anisotropy reduces to $g^* = 0.44$.

Since the diffusion approximation performs well for isotropic scattering, this results in better performance of the δP_1 approximation. Notably, the reduced scattering coefficient is decreased when compared to the standard diffusion approximation. Therefore, the δP_1 approximation may hold at distances closer to the source than the diffusion approximation (see Fig. 1-14 right side).

Source term

In the δP$_1$ approximation as derived by Prahl[98], the first order moment S_1 of the source term source term is taken into account in the diffusion equation. Here, we employ a simpler version of the approximation proposed by Seo et al.[109], who modeled the source by an exponential distribution of isotropic terms along the $\hat{\boldsymbol{z}}$ direction:

$$S_0^*(\rho, z) = \mu_s^* \, \delta(\rho) \exp(-\mu_t^* \, z) \tag{1.57}$$

Boundary conditions and solution

A similar approach as the one described in Sec. 1.4.2.3 is used to derive the fluence rate in the δP$_1$ approximation:

$$\varphi_s(\rho, z) = \frac{\mu_s^*}{4\pi D} \int_0^\infty \left[\frac{1}{\rho_1} \exp\left(-\sqrt{\frac{\mu_a}{D}} \rho_1 \right) - \frac{1}{\rho_2} \exp\left(-\sqrt{\frac{\mu_a}{D}} \rho_2 \right) \right] \exp(-\mu_t^* z') \, dz' \tag{1.58}$$

The partial-current boundary condition yields the following expression for the diffuse reflectance:[108]

$$R^*(\rho) = \frac{\varphi_s(\rho, z = 0)}{2A} \tag{1.59}$$

Improvements over the diffusion approximation

The δP$_1$ approximation reduces the anisotropy of light described by the diffusion equation. Consequently, the description of the fluence rate close to the source is improved compared to the diffusion approximation.[92,108,109] Contrarily to the diffusion approximation, the δP$_1$ model provides an accurate description of the fluence rate when $\mu_a \gg \mu_s'$.[92,108] However, this model fails to accurately describe the diffuse reflectance emitted from strongly absorbing media.

1.4.3 Stochastic Model

In this section, we focus on the Monte Carlo method, which was first applied to biological media by Prahl.[121] The Monte Carlo method is a stochastic approach of the light transport problem, which consists in simulating and recording photons trajectories as they are scattered and absorbed. Absorption and scattering events are randomly generated with probability laws corresponding to the optical properties of the medium. Scattering directions are computed using the Henyey-Greenstein phase function, which provides a good approximation of Mie

theory (see Fig. 1-3). Observable quantities are then calculated by averaging the contributions of individual photons. Provided that a sufficient number of photons is launched (typically 10^6 to 10^9), the Monte Carlo method provides accurate solutions of the RTE and has been applied with good efficacy in various studies.[72,102,103] Moreover, this method makes no prior assumption on the medium's properties or source geometry. In particular, strongly absorbing media can be accurately described by the Monte Carlo method.

However, this approach implies a trade-off between model complexity and computation efficiency. For instance, addressing an angled instead of vertical illumination is possible[122] but requires to store photon trajectories in 3 dimensions as the cylindrical symmetry is no longer fulfilled. Consequently, an increased number of photons is needed to generate sufficient statistics. Therefore, Monte Carlo approaches are usually restricted to vertically incident sources exhibiting cylindrical symmetry.

Similarly, calculations considering strongly absorbing media can become highly time-consuming, since only a few photons are scattered back to the tissue surface and contribute to the reflectance signal.

Finally, estimating the optical properties of unknown tissue requires that a large number of simulations be computed and stored beforehand. This number is dramatically increased when considering layered media. The associated calculation times and necessary storage capacity may not be suited to some applications.

This issue has been addressed by several groups who proposed accelerated Monte Carlo algorithms. Graaf et al.[123] developed a scaling method to derive diffuse reflectance profiles for various absorption and scattering properties from a single Monte Carlo simulation. Alternatively, Wang et al.[124] proposed a hybrid model mixing Monte Carlo calculations with the predictions of diffusion theory (see Sec. 1.4.2). Later, Liu and Ramanujam[103] extended the approach of Graaf et al.[123] to layered media.

In this study, we employ a Monte Carlo algorithm previously developed at the CEA.[125] The code was written according to the work of Wang et al.[101] and the approach of Liu and Ramanujam[103] for accelerated computation was implemented both on Central Processing Unit (CPU) and Graphics Processing Unit (GPU). The algorithm was then validated in comparison with the MCML code available online.[126] A flowchart of the algorithm is displayed in Fig. 1-17.

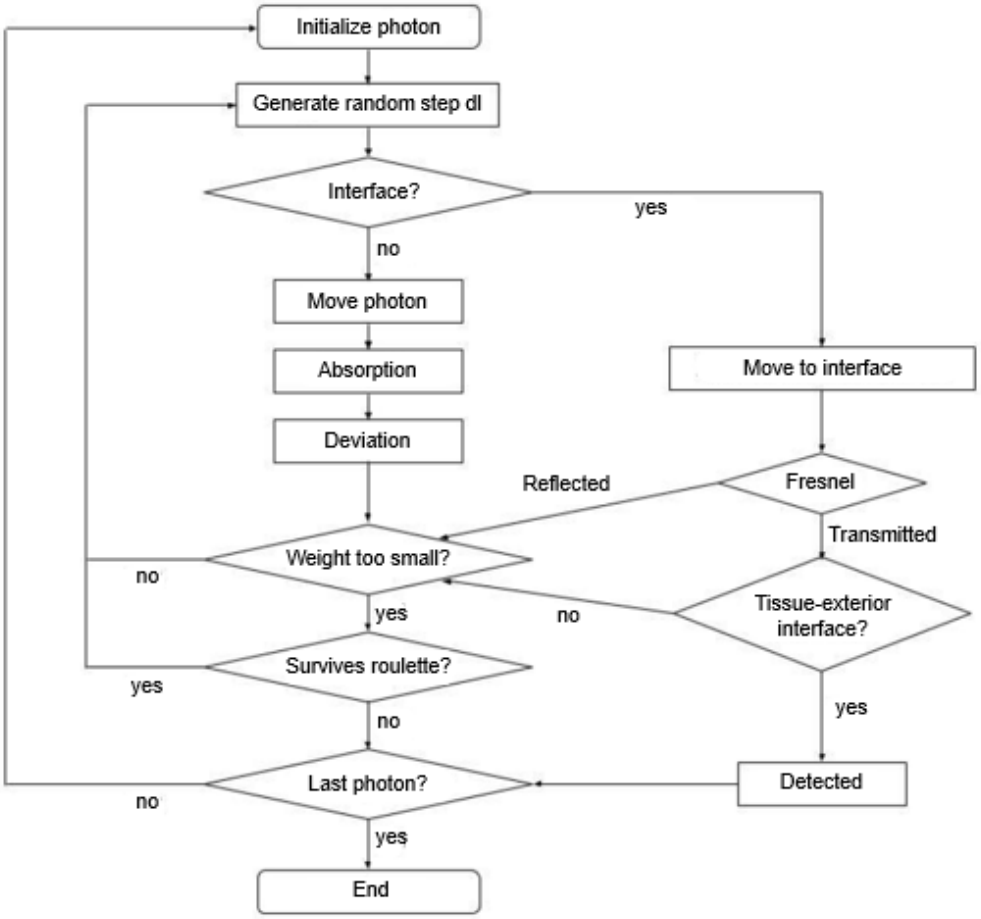


Fig. 1-17 Flow-chart of the multilayer Monte Carlo algorithm developed at CEA.[125]

1.4.4 Model comparison

We implemented the standard diffusion model and δP_1 model in Matlab (Mathworks Inc., Natick, MA). Fig. 1-18 displays the diffuse reflectance calculated according to these models for various μ_s'/μ_a with $\mu_a = 1\,cm^{-1}$ and $g = 0.8$. The corresponding Monte Carlo simulations are plotted as reference curves (see Sec. 1.4.3).

The limitations of diffusion theory described in Sec. 1.4.2.4 are clearly visible. Both SDA and δP_1 models fail to accurately describe media with low albedo. For higher μ_s'/μ_a ratios, the diffuse reflectance is well modeled at distances typically longer than a few transport mean free paths. The δP_1 model provides closer agreement with MC simulations than the standard diffusion approximation at short source-detector separations (SDS). However, the δP_1 approximation generates larger deviations from MC curves in the intermediate SDS range compared to the standard diffusion model. Besides, in weakly absorbing media, reflectance curves calculated from the SDA exhibit closer agreement with MC simulations than the δP_1

model. Therefore, depending on the SDS range used in measurements and the optical properties of the medium under test, it is not straightforward whether one or the other analytical model should preferably be used.

In the following chapters, only the stochastic model of light propagation is considered. Monte Carlo simulations were preferred considering the larger domain of validity of this approach and the last developments of our laboratory concerning the acceleration of simulations in GPU.

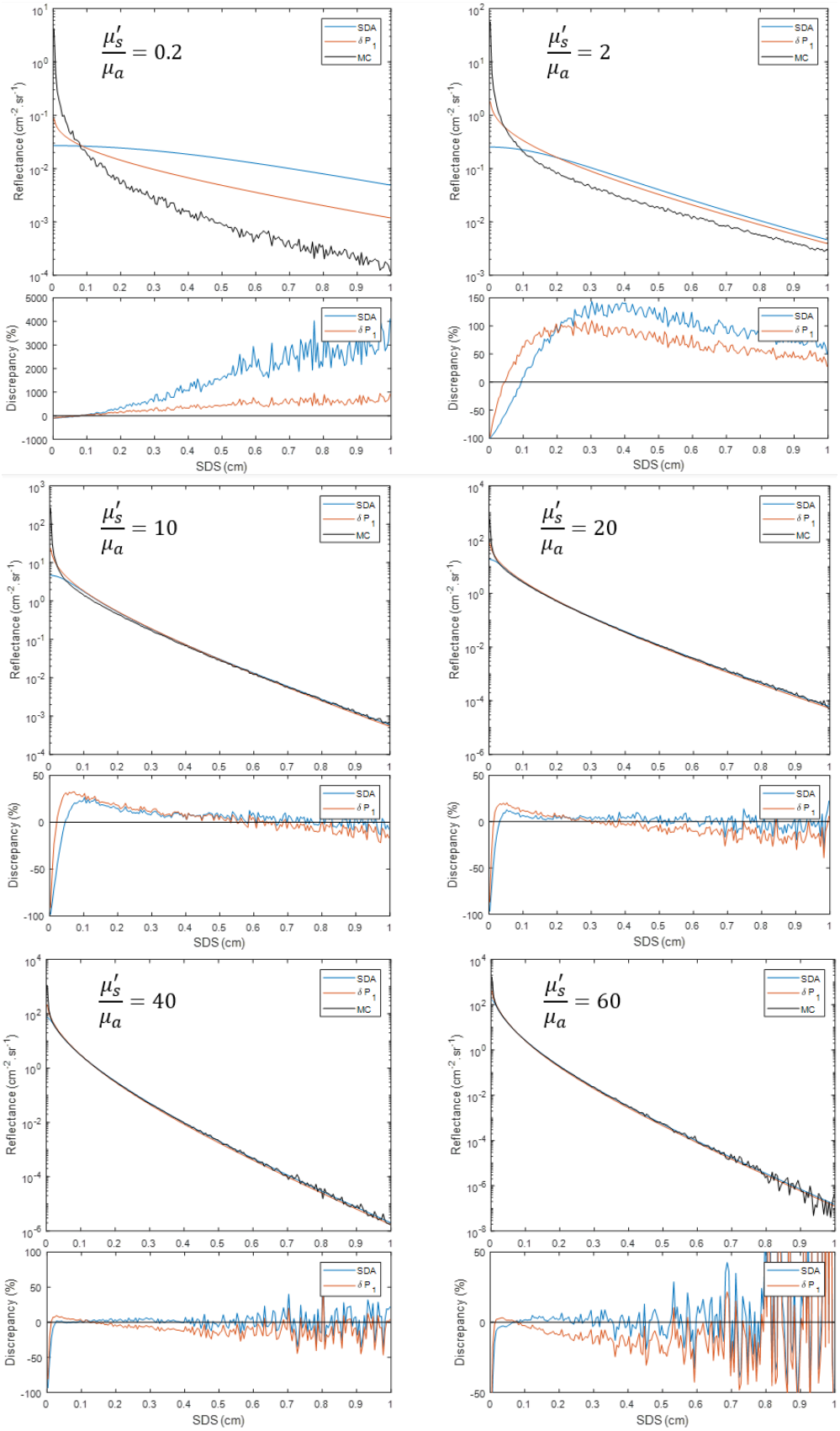


Fig. 1-18 Diffuse reflectance curves for various optical properties as derived from (blue) the standard diffusion approximation (SDA),[107] (red) the δP_1 approximation (δP_1)[109] and (black) Monte Carlo simulations (MC).[125]

Chapter 2

Specification of a compact, CMOS-based system architecture for contact, high resolution diffuse reflectance imaging

This chapter reports on the design and validation of a dedicated system architecture to perform the spatially resolved detection of the diffuse reflectance in contact with turbid media and with high spatial resolution. This work comprises both the instrumental developments leading to the proposed architecture and the associated algorithmic tools for data acquisition, processing and analysis. As a proof of concept, a first prototype is developed and qualified for the quantitative measurement of the optical properties of tissue-simulating homogeneous phantoms.

From these results, evolution of the system is engaged toward *in vivo* and layer specific tissue analysis, which are the scope of Chapter 4 and Chapter 5. The work presented here has been accepted for publication in the Journal of Biomedical Optics. A patent dedicated to the described architecture has been submitted and reviewed. The post-review version of the patent is under preparation.

2.1 Introduction

2.1.1 Spatially resolved diffuse reflectance spectroscopy

Diffuse reflectance spectroscopy (DRS) has been widely used to determine absorption and scattering properties of turbid media. When applied to biological tissue such as skin, DRS provides quantitative characterization of tissue composition for diagnostic purposes. The reduced scattering coefficient (μ_s') is sensitive to cells and tissue morphology, while the absorption coefficient (μ_a) relates to the bio-chemical content of tissue and may be used to infer the concentration of particular molecular species. In the visible and near-infrared domain, these notably include oxyhemoglobin (HHb), deoxyhemoglobin (O_2Hb), melanin and bilirubin, which are of great interest in a variety of clinical situations. Many groups have investigated DRS as a non-invasive tool to provide diagnostic criteria *in vivo*. Examples of application include tissue oxygenation monitoring,[41–47] tumor margin assessment in epithelium,[48,49,52] breast and colon cancer detection,[47,50,51,53] jaundice diagnosis in new-born skin,[54] pharmacokinetics[58] or port-wine stain treatment evaluation.[59]

Spatially resolved diffuse reflectance spectroscopy (srDRS) is a particular implementation of DRS that consists in analyzing the spatial dependence of diffuse reflectance profiles produced by a given arrangement of light sources and detectors. By exploiting the spatially-dependent influence of optical parameters on the diffuse reflectance

intensity, independent determination of absorption and scattering parameters can be achieved. Furthermore, the measurement of photons at multiple source-to-detector separations (SDS) provides a potential for depth-resolved analysis.[92] Translation of srDRS into the clinic necessitates an optimized combination of sources and detectors, as well as modeling of light transport in tissue and specific constraints related to the targeted application.

2.1.2 State-of-the-art

Various ways to implement srDRS have been reported in the literature.[42,49,59,69–79,82–91] Most common srDRS instruments involve a broadband source and a spectrophotometer, both coupled to a fiber-optic probe ensuring light delivery and collection. Unlike camera-based systems, fiber-based probes enable tissue characterization in contact modality without the need for focusing optics, reducing the cost and complexity of the device.[49,82–90] This approach has led to the development of portable instruments that have been deployed in a variety of clinical and pre-clinical studies.[49,60,85,87,88,95,96,127] Typical fiber-based probes consist of a concentric arrangement of multiple collection fibers around a central illumination fiber for maximization of signal-to-noise ratio (SNR),[49,82–84] as depicted in Fig. 2-1(a). However, the fill factor and light collection efficiency of the system are limited by the density of the fibers as well as the cladding and low numerical aperture (NA) of the fibers. As a result, typically less than 10 source-to-detector separations (SDS) can be used, limiting the ability of the instrument to achieve depth specific analysis of tissue.

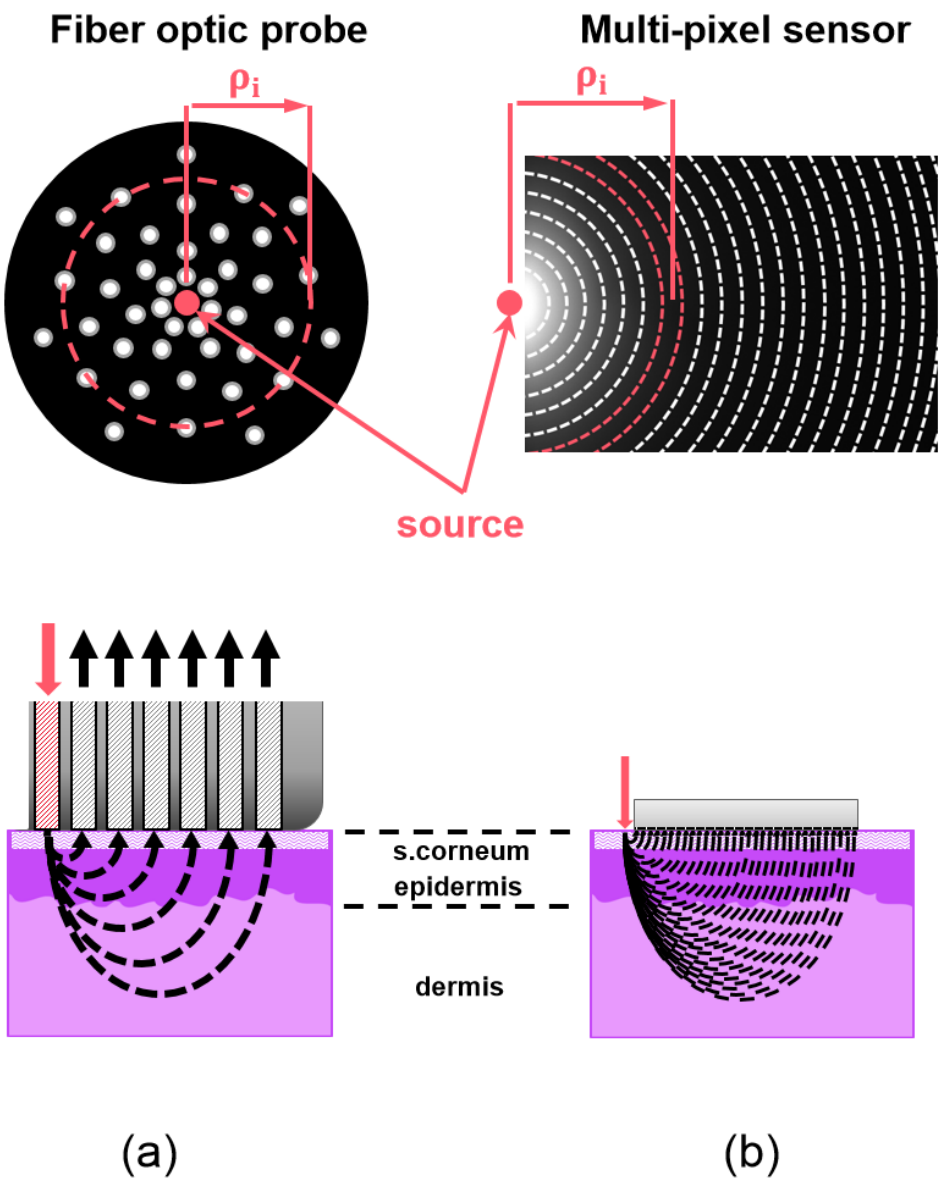


Fig. 2-1 Detection schemes for fiber-based (a) and CMOS-based (b) srDRS instruments. Views from the top (top) and side (bottom) of the instruments are shown. The diffuse reflectance at distance ρ_i to the source is radially averaged (red dotted lines).

Recently, alternative approaches have been investigated for further miniaturization of srDRS devices. Several groups used photodiodes (PD) in contact with tissue to collect the diffuse reflectance.[76–81] Yu et al.[76] and Lo et al.[77] used a fiber illumination system coupled to PDs for detection of the diffuse reflectance of turbid media with improved NA compared to classical fiber probes. Shokoufi et al.[79] developed an srDRS probe made up of four LED sources and two PDs for detection. The authors were able to perform dynamic measurements at the rate of 10 Hz and measure the optical properties of manufactured turbid media. Such

technology enables the production of source excitation and collection of the diffuse reflectance on a chip, paving the way for the development of wearable systems at minimal cost. Alternatively, several groups developed DRS systems based on annular photodiode sensors,[80,81] which benefit from the circular symmetry of the reflectance signal to further improve the light collection efficiency of the system. However, instruments reported in these studies only involved single PD-source pairs and thus did not exploit the spatial profile of diffuse reflectance spectra.

Later, this issue was addressed by Senlik and Jokerst, who developed a custom probe made of an array of multiple concentric annular PDs surrounding a central illumination aperture (Fig. 2-2).[78] Spatially resolved diffuse reflectance spectra were acquired at 24 SDS ranging from 400 to 3550 µm. Their approach may have a significant potential for the analysis of layered tissue using a wearable system. However, such solution involves the development of custom PD arrays, and restricts the detection of the spatially resolved diffuse reflectance to a particular geometry.

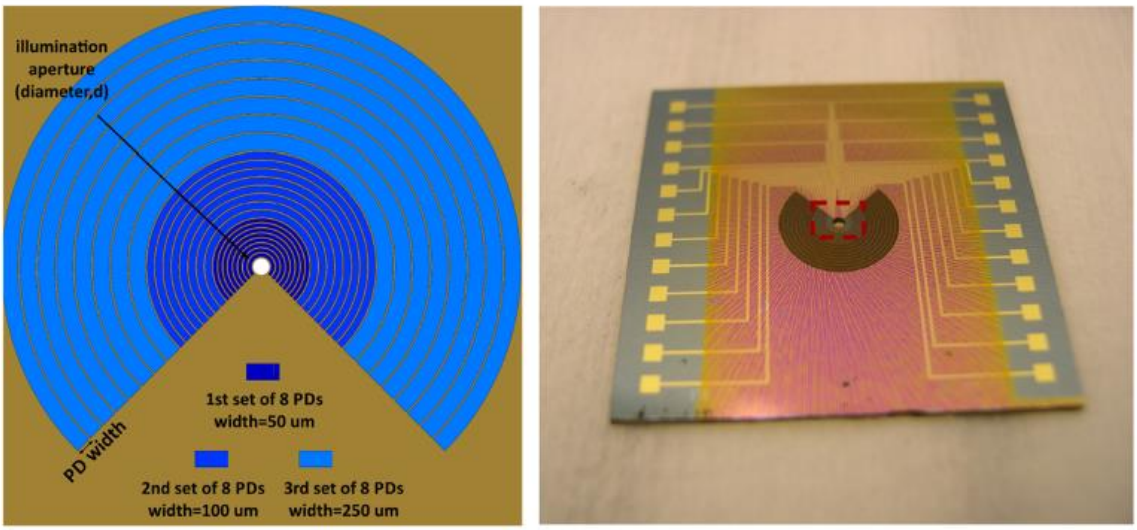


Fig. 2-2 Illustration of the Concentric Multi-Pixel Array (CMPA) probe developed by Senlik and Jokerst.[78] (a) Schematic structure. The probe contains three sets of photodiodes with annulus widths of 50, 100 and 250 µm. Each set is represented by different colors. The white circle in the middle represents the illumination aperture. (b) Photograph showing the entire CMPA array with PDs and wire pads. The illumination aperture is 750 µm. Figures and captions were retrieved from Ref. 78.

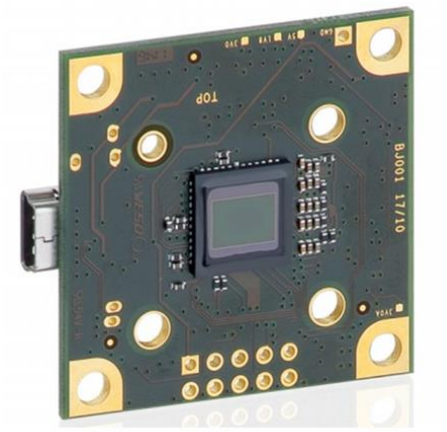
2.1.3 Proposition

In this chapter, we introduce an alternative approach based on the use of a standard high resolution multi-pixel image sensor to achieve spatially resolved diffuse reflectance imaging at a high resolution (see Fig. 2-1(b)). Commercial imaging sensors based on the complementary metal-oxide semiconductor (CMOS) technology are readily available at low cost and with constantly improving optical and electronical performance. We believe that there is opportunity to exploit this technology to address a new range of clinical situations requiring cost-effective, tightly-packed tissue characterization tools. In order to evaluate the potential of our approach for the quantitative characterization of tissue, a prototype instrument is designed and fabricated. The instrument is made of a commercially available CMOS sensor combined with a dedicated fiber-based coupling system. The coupling system employs a surface mounted light-emitting diode (LED) and a fiber-optic plate (FOP), which ensures efficient photons transfer onto the CMOS pixel array at high spatial resolution, thereby overcoming the limitations of current fiber-based and PD-based system. In the next sections, we describe the design of the instrument, introduce the developed prototype, and finally evaluate its performance on tissue-mimicking optical phantoms.

2.2 Proposed system architecture

In this section, an innovative system architecture for srDRS measurements is presented. This architecture is based on a high resolution imaging sensor (Sec. 2.2.1) used in combination with a dedicated sensor-tissue coupling system (Sec. 2.2.2).

2.2.1 Light sensor



Sensor type	CMOS Mono
Shutter	Rolling shutter
Sensor characteristic	Linear
Readout mode	Progressive scan
Pixel Class	UHD+
Resolution	10.55 Mpix
Resolution (h x v)	3840 x 2748 Pixel
Aspect ratio	4:3
ADC	12 bit
Color depth (camera)	8 bit
Optical sensor class	1/2"
Optical Size	6.413 mm x 4.589 mm
Optical sensor diagonal	7.89 mm (1/2.03")
Pixel size	1.67 µm
Manufacturer	ON Semiconductor
Sensor Model	MT9J003STM

Fig. 2-3 UI-1492-LE-M camera (IDS Imaging, Obersulm, Germany).

The spatial profile of the diffuse reflectance from tissue contains information related to the underlying optical properties with specificity in depth. In the case of layered tissue such as skin or cervix, this depth-specific information may provide important diagnostic criteria.[23,44,57,128–131] The potential of srDRS to achieve depth-resolved tissue analysis is increased when a high number of source-to-detector separations (SDS) are considered in the system. Therefore, the spatial resolution of the light sensor used for detection of the diffuse reflectance is a critical parameter in the design of srDRS systems.

An efficient way to detect scattered light at a high resolution is to use a multi-pixel image sensor, typically a charge-coupled device (CCD) or a CMOS. This approach was followed by several groups, who used camera-based systems to analyze the spatial dependence of diffuse reflectance spectra, either in real space[71–74,82–91] or frequency domain.[42,59,70,75] However, focusing optics are usually employed for remote collection of scattered photons, leading to increased costs and system complexity.

Recently, there has been significant interest in removing the focusing optics to achieve imaging of scattered light from turbid samples using a contact geometry.[132–140] Notably, Schelkanova et al. employed a color CMOS sensor directly coupled to silicon phantoms and combined with a broadband source. Using this system, the authors were able to visualize subsurface microfluidic patterns mimicking epithelial vascular structures, demonstrating the ability of their approach to achieve diffuse reflectance imaging at a high resolution.[139] Yet,

quantitative characterization of optical parameters could not be intended considering the broad bandwidth of the CMOS RGB channels.

For this study, an 8-bit monochrome CMOS camera was purchased from IDS Imaging Inc. (UI-1492-LE-M). Properties of the camera are reviewed in Fig. 2-3. The CMOS sensor had a 6.413 x 4.589 mm² active area with 1.67 µm pixel pitch. The relatively low dynamic range of detection is compensated by the use of a dynamic expansion procedure, which is detailed in Appendix B. When choosing the sensor, attention was paid to the Chief Ray Angle (CRA) property. In fact, most commercial sensors are equipped with a micro-lens array for fill factor optimization. During sensor fabrication, the lens array is often deliberately misaligned with respect to the pixel array so as to compensate for shading in images formed through the associated focusing lens.[141] However, such compensation should be avoided in our case because of the presence of the protective glass window usually mounted above the photon sensitive area. This glass lid induces an unwanted 550 microns spacing between the imaging plane and the sample surface. The effect of this spacing when considering the contact imaging modality is illustrated in Fig. 2-4. In particular, a pixel located near the borders of the imaging area would detect photons arising from the sample's surface at a location slightly shifted from the vertical projection of the pixel, which may result in distorted measurements of the reflectance, especially at short SDS. Therefore, a sensor with a CRA of 0° was chosen. In the next section, we describe the dedicated coupling system developed to produce and collect diffuse reflectance patterns in contact with samples. A layout of the sensor and coupling system architectures is displayed in Fig. 2-8.

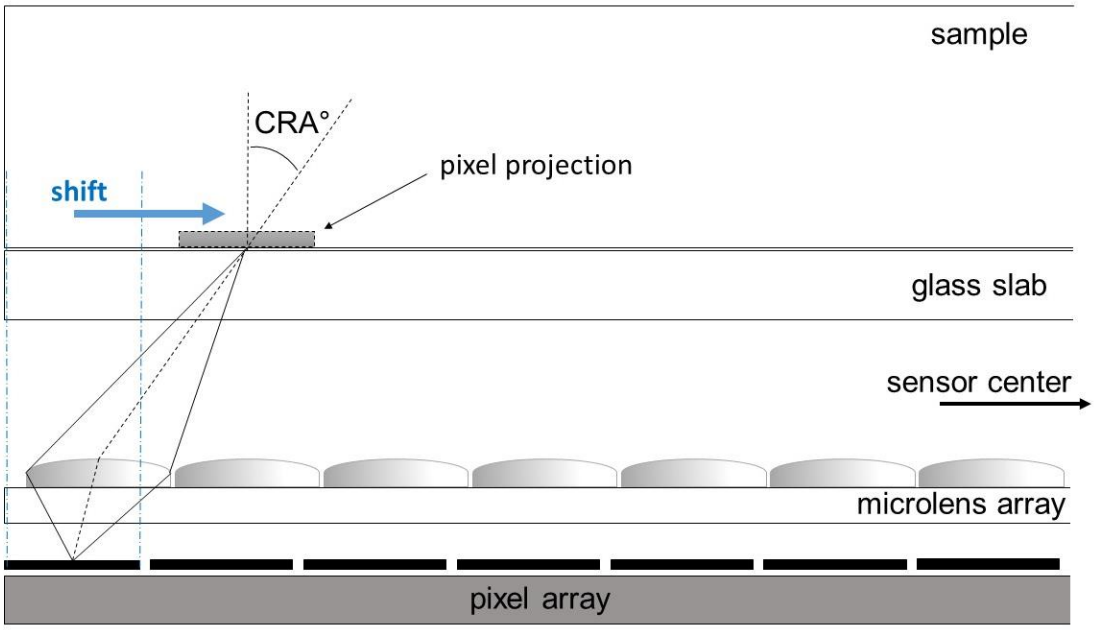


Fig. 2-4 Influence of shading compensation in contact imaging modality.

2.2.2 Sensor-tissue coupling system

2.2.2.1 Technological limitation

In the architecture considered in our study, the light emitter and receiver are positioned next to one another, in contact with the analyzed medium. Most intuitively, the CMOS sensor itself may be placed in contact with tissue to both collect and detect scattered photons, as proposed by Schelkanova et al.[139] (Fig. 2-5). In this study, the authors emulated the skin micro-vascular system by a linear arrangement of microfluidic channels, which were imaged with a CMOS sensor in contact modality.

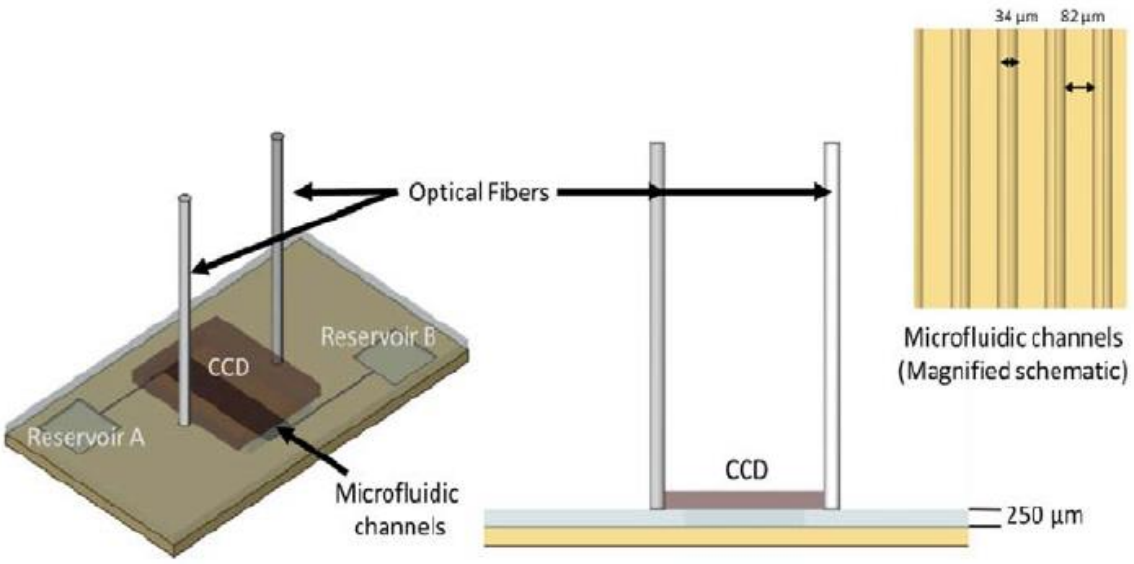


Fig. 2-5 Design of the experimental setup for the diffuse reflectance measurements reported by Schelkanova et al.: an axonometric view and a side view. The magnified schematic of the microfluidic channels shows an average value of the groove's width, 34 µm, and a separation of approximately 82 µm. Figure and caption were retrieved from Ref. 139.

In such configuration, the presence of wire bonds and protective encapsulant on every sides of the sensitive area prohibits the placement of a light source in close proximity to the sensor. Several studies have pointed out that spatially resolved diffuse reflectance from tissue was most sensitive to μ_s' at short distances to the illumination point, typically below 1 mm, while being both dependent on μ_a and μ_s' further away from the source,[92,142] as illustrated in Fig. 2-6. Moreover, a decrease, respectively increase, in signals measured at long SDS may be induced by a decrease, respectively increase, in either diffusion or absorption. As a consequence, access to both short and large source-to-detector separation (SDS) is necessary for accurate determination of absorption and scattering parameters. The packaging of commercial CMOS sensors thus constitutes a clear limitation toward the implementation of a performing srDRS device.

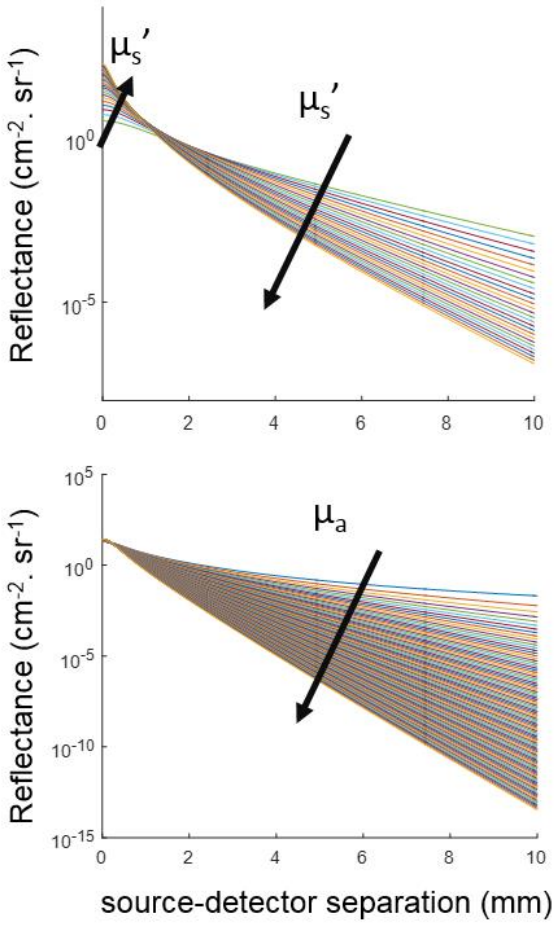


Fig. 2-6 Sensitivity of the diffuse reflectance to optical properties. Spatially resolved diffuse reflectance profiles were calculated for varying μ_s' and constant μ_a (top) or vice versa (bottom) using the Standard Diffusion Approximation (see Sec. 1.4.2.2). At short source-detector separations (typically below 1 mm), the diffuse reflectance is strongly sensitive to μ_s' while being weakly sensitive to μ_a. At longer SDS, both coefficients have strong influence on the reflectance. Moreover, a drop, respectively increase, in the measured signals may be induced by a drop, respectively increase, in either diffusion or absorption.

2.2.2.2 Proposed solution

In order to overcome this limitation, we propose to insert a fiber-optic plate (FOP) between the sensor and the analyzed medium. Fiber-optic plates (FOP) are formed by a network of micron-sized optical fibers densely packed into a glass or polymer material that performs image transfer between the top and bottom faces of the plate (Fig. 2-7). FOPs can support high resolution imaging up to 160 lp/mm and exceed 60% in diffused light transmittance.[143] They can be purchased with various shapes, numerical aperture and can be tapered to achieve magnification/demagnification.



Fig. 2-7 Fiber-optic plates (commercial image from Ref. 143)

FOP coupled CMOS/CCD imaging platforms are involved in both scientific and industrial applications, including x-ray imaging,[144] biosensing,[134,137,145] display screen enhancement and fingerprint reading.[143] In recent work, Schelkanova et al. evaluated the applicability of this architecture for diffuse reflectance imaging.[140] The authors emulated a 2-D fiber-optic grid by a single fiber scanning system for visualization of subsurface patterns in turbid phantoms. However, quantification of absorption and scattering parameters was not investigated.

In the present case, insertion of a FOP can be exploited to provide access to short source-to-detector separations (SDS). Dimensions and positioning of the FOP can be optimized to produce a 1:1 image conjugation between the CMOS sensitive area and the surface of tissue delimited by the FOP edges. In this manner, borders of the imaging area become physically accessible. The FOP thickness can be adapted to insert a light source between the CMOS chip and tissue, at the closest possible distance to the first detection point. For example, light-emitting diodes (LED) may be employed to generate the desired diffuse reflectance signals. LEDs are available at many wavelengths, can be highly miniaturized and are inexpensive, which may participate in the reduction of srDRS systems footprint and cost.

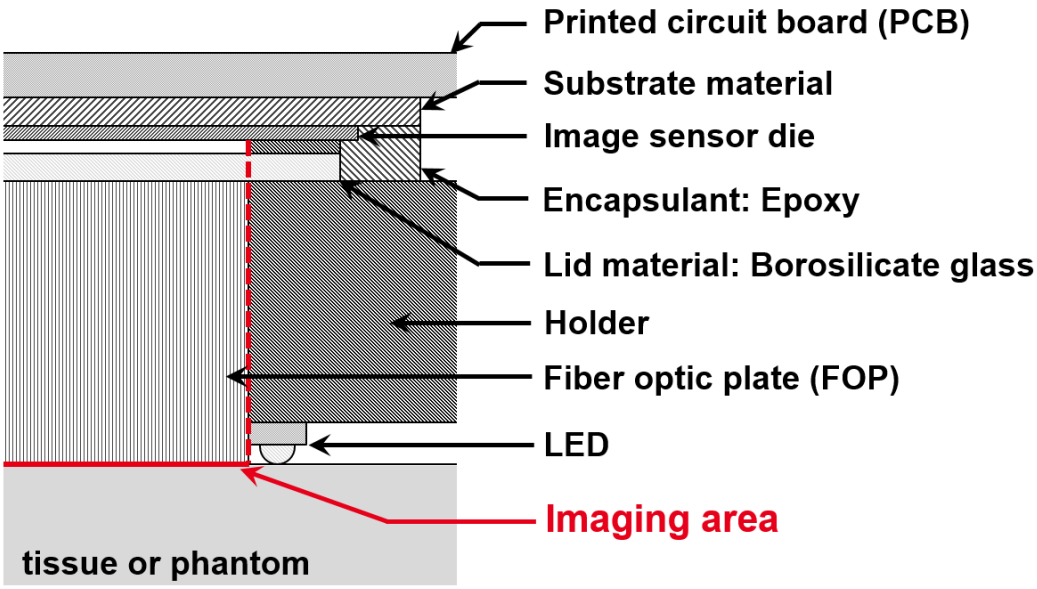


Fig. 2-8 Layout of the CMOS-based contact imaging system for spatially resolved diffuse reflectance spectroscopy. The imaging area (red line) is transported from the CMOS pixel area to the bottom face of the fiber optic plate, which is placed in contact with the analyzed sample.

2.3 Proof of concept

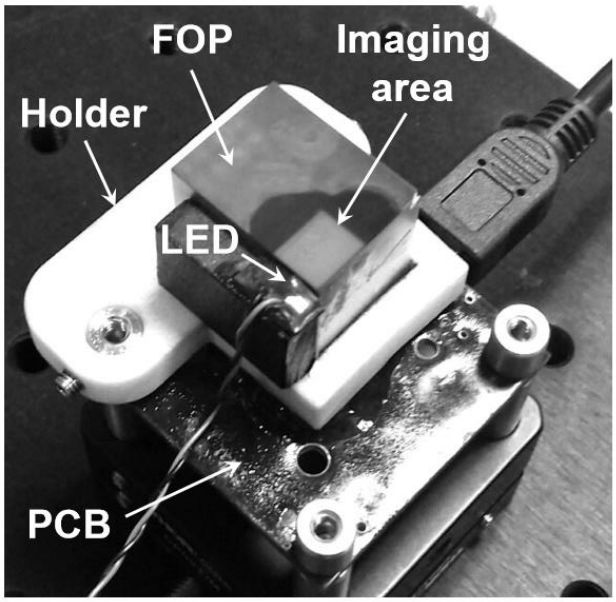
In order to demonstrate the potential of our approach for the characterization of tissue optical properties, a proof-of-concept study is conducted. In this section, we present the prototype srDRS system (Sec. 2.3.1) that was developed for this study. Sec. 2.3.2 describes the optical phantoms, experiments protocol and algorithmic methods that were used. Evaluation and discussion of the prototype's performance are provided in Secs. 2.3.3 and 2.3.4.

2.3.1 Prototype srDRS device

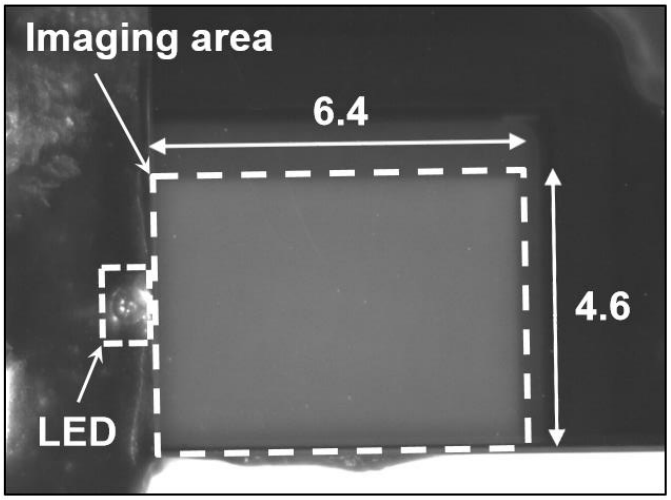
2.3.1.1 Implementation

A prototype CMOS-based srDRS device was fabricated according to the proposed architecture (see Fig. 2-8). Photographs of the system are provided in Fig. 2-9. A custom fiber-optic plate (FOP) with 6 µm unit fiber core diameter (OS-ST, SZPhoton) was purchased.[143] The FOP was positioned to ensure alignment of the pixel area borders with FOP edges on one side, against which an LED (KPTD-1608SURCK, Kingbright) emitting at 645 nm was mounted. The top of the LED dome lens was placed to be co-planar with the collection face of the FOP. In this configuration, the LED chip was separated by a distance of

480 µm to the FOP edge. From the technical information provided by the manufacturer, the number of individual fibers in front of the imaging area was estimated to 1.308×10^5. The FOP and LED were held in a 30 mm Thorlabs (Thorlabs Inc., Newton, New Jersey) cage thanks to a homemade dedicated element. Optical grease was used for index matching optimization between the FOP and the CMOS protective glass lid. Finally, silicon treatment was performed to ensure isolation and impermeability of the exposed electronic parts of the device.



(a)



(b)

Fig. 2-9 Photographs of the developed prototype CMOS-based contact imaging system. (a) whole system. Note that silicon treatment was performed on the printed circuit board (PCB) for isolation and impermeability of the exposed electronic parts. (b) Top view of the illumination and imaging area. Dimensions are displayed in millimeters. The CMOS sensitive area delimited by the white dotted line is viewed through the fiber optic plate.

2.3.1.2 Characterization

In this section, optical characterization of the developed prototype is presented. When necessary, tissue-simulating phantoms are used. Manufacturing and characterization of these phantoms is presented in Sec. 2.3.2.1.

Sensor linearity and source stability

The system linearity was measured by taking the average signal over the whole sensor area at constant illumination level and increasing exposure time. Background subtraction was performed for each exposure time. Measured data are shown in Fig. 2-10. The displayed percent linearity represents the deviation from the best linear fit expressed in percent of the sensor dynamic. Note that for better visualization, the points closest to saturation have been left out of range in Fig. 2-10(a) (bottom) and Fig. 2-10(b). The maximum drift from a linear behavior was smaller than 0.6% of sensor dynamic up to 80% of the maximum value (255 ADU). Pixel signals higher than this threshold were disregarded in our processing algorithm.

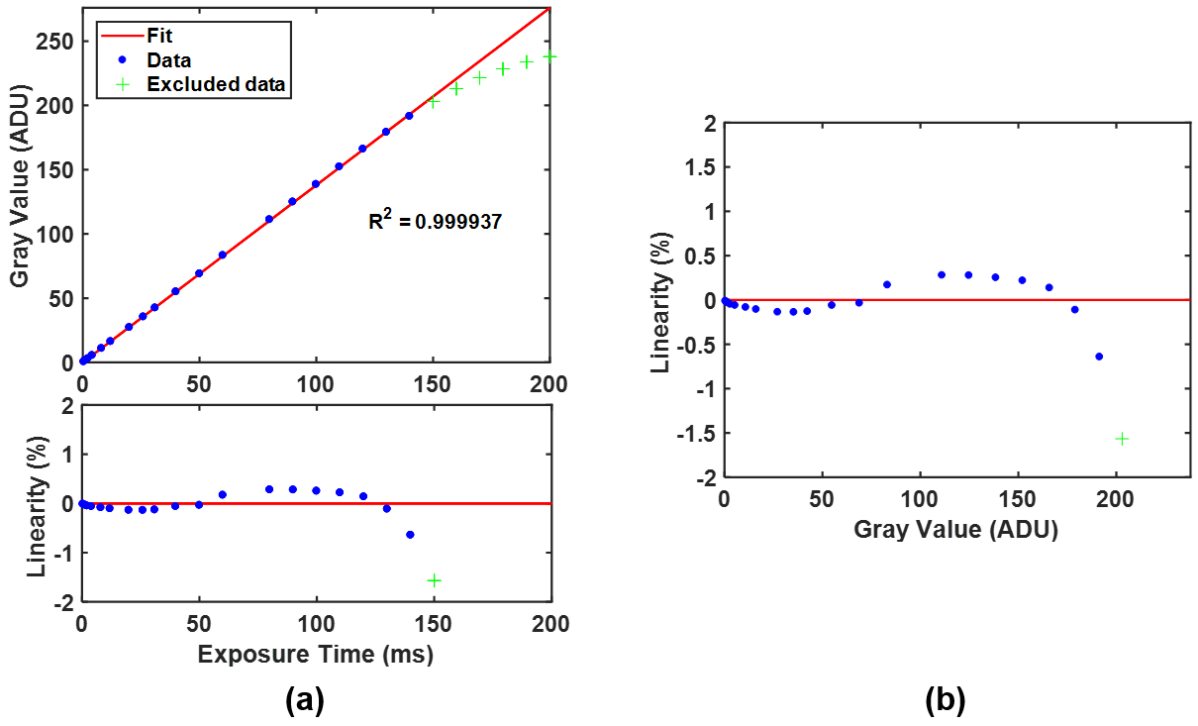


Fig. 2-10 Linearity measurement of the DRS prototype. (a) Measured signal (top) and percent linearity (bottom) as a function of exposure time for a fixed illumination level. (b) Percent linearity as a function of gray level. Measured data are displayed as individual markers while the best linear fit to data (red line) was found using only the blue points and excluding the points close from saturation (green crosses).

For assessment of the source stability, the illumination power out of the LED was monitored over a 1.5h acquisition period using an optical power meter (PM100D, Thorlabs). Over the entire time course of measurement, the LED output power did not drift by more than 0.2% from the nominal value of 240 µW.

Signal-to-noise ratio

For system noise performance characterization, repeated image acquisitions were made on the least favorable phantom, chosen as the one exhibiting the highest μ_a and μ_s'. We calculated the signal-to-noise ratio (SNR) [SNR = 20 log(mean intensity / (standard deviation + dark current))] out of 10 acquisitions for various exposure times. Intensity was averaged over concentric rings surrounding the illumination point, as described in Sec. 2.3.2.2. The dark current was measured for every exposure by taking the mean signal of dark images over the whole sensor area.

Fast decrease of signal-to-noise ratio (SNR) was observed as the radial distance to the source increased. Therefore, acquisition with multiple exposure times was necessary to maintain a sufficient SNR over several millimeters (see Appendix B). Using three to five exposure times separated by a factor close to 10 enabled to achieve SNR ranging from 20 to 35 dB up to 4 mm away from the illumination center.

Flat-field response

Flat-field inhomogeneity was corrected by using a Teflon plate with 10 mm thickness. In order to produce a nearly Lambertian illumination, one face of the Teflon plate was placed against the FOP surface while the other face was illuminated by a distant halogen lamp. In this configuration, ten image acquisitions were made and averaged. After subtraction of background level, the flat-field response of the sensor was obtained (Fig. 2-11). The resulting data was later used as normalization factor to correct from spatial heterogeneities in FOP transmission, especially occurring near edges.

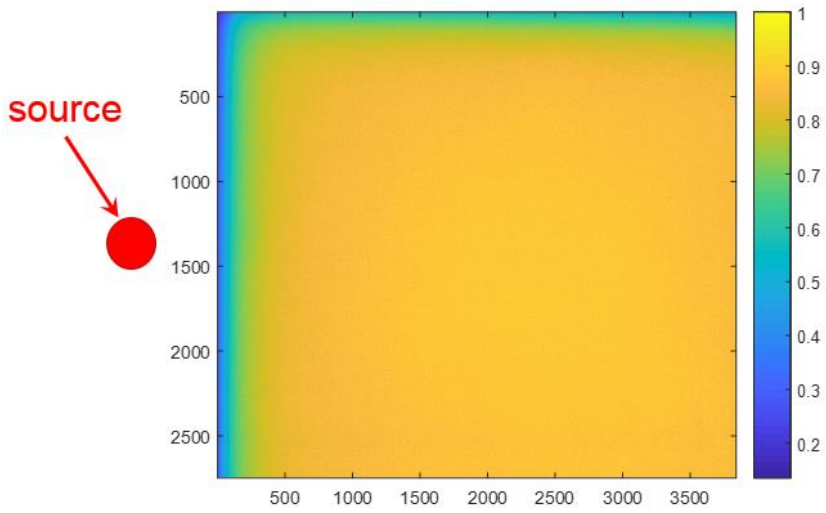


Fig. 2-11 Flat-field image recorded by the srDRS prototype. The source was positioned against the FOP edge on the left side of the image area.

In order to evaluate the inhomogeneity correction, 10 consecutive measurements of the calibration phantom were made without moving the srDRS device. Depending on source-detector separation, the standard deviation between pixels on the same ring for a given measurement after inhomogeneity correction ranged from 3 to 5% of the mean signal. In comparison, the standard deviation between signals from different measurements at the same pixel ranged from 1.5 to 5% of the mean value.

Source profile

Accurate characterization of optical properties necessitates that the source radial intensity profile be accounted for. The source profile was measured using a CMOS camera (UI-1492-LE-M, IDS Imaging) and a 23 mm objective (Xenoplan 1.4/23-0902, Schneider Kreusnach). Following the procedure described in Sec. 2.3.2.2, images were recorded at multiple exposure times and subsequently recombined to measure the radial intensity profile produced by the LED with sufficient signal-to-noise ratio. During phantom measurements, the LED source was immersed in solutions. In an effort to match the experiment conditions as closely as possible, the source intensity profile was measured with the coupling system being immersed in a phantom solution, as described in Fig. 2-12(a). The system was positioned so as the top face of the FOP was coplanar with the phantom surface, the LED being immersed in the solution. The source intensity was measured in the plane of the phantom surface, and the obtained profile (Fig. 2-12(b)) was included in the forward model of light propagation (Sec. 2.3.2.3).

Note that the same phantom was used for measurement of the source profile and calibration of the instrument response (Sec. 2.3.2.3).

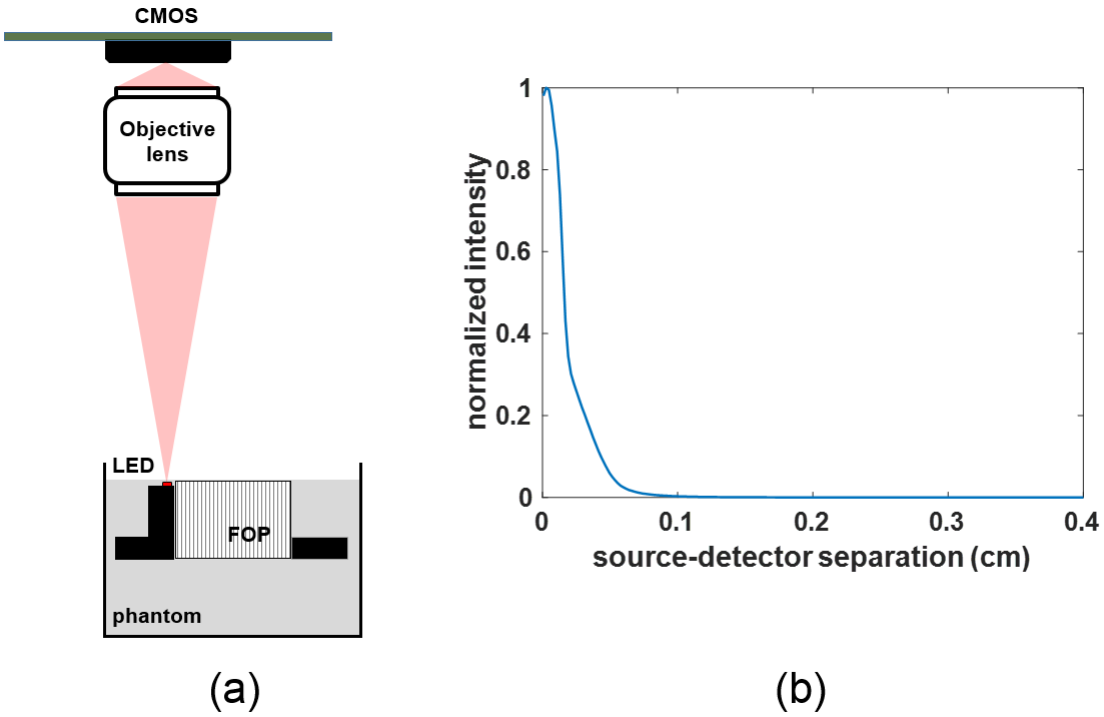


Fig. 2-12 Source profile measurement. (a) Measurement setup. The coupling system was immersed in the calibration phantom so as the surface of the solution and the FOP top face were coplanar. The source intensity in the plane of the FOP top face was measured by a camera. (b) Measured intensity profile.

Edge spread function

Although the FOP transports the image of the tissue surface with high fidelity from on face to another, the final image formed on the CMOS photon sensitive area may be affected by distortions. Indeed, photons propagate freely in the protective glass window and the intermediate air layer before reaching the pixels plane. First, the important index mismatch at the glass-air interface may reduce the SNR. More importantly, considering the high numerical aperture of the FOP (~0.8 as provided by the manufacturer), the final image is blurred compared to the 'true' image of tissue.

Blurring of the diffuse reflectance caused by the CMOS glass window was quantified using the ISO 12333 slanted-edge methodology[146] (SEM), which is a measurement of the Line Spread Function (LSF) of the system at chip level, thereby without need for focusing. The LSF may then be related to the Modulation Transfer Function (MTF) by Fourier transform. The width of the system LSF was thus estimated to ~500µm (see Appendix C), showing an important limitation of the considered prototype toward high contrast imaging.

In order to assess the impact of blurring on measured data, forward model calculations (see Sec. 2.3.2.3) were performed with or without taking account on the blurring effect. Blurring was generated by convolution of the modeled reflectance with a Gaussian function having 500 microns width (see Fig. 2-13). Note that we considered the properties of the phantom having the highest μ_a and μ_s' as the calculated reflectance profile was most sensitive to blurring in this case. Although large discrepancies appeared close to the illumination center, distortions of less than 11% were observed in the SDS range considered in our study. Most of these were limited to separations lower than 1 mm, while at farther distances differences were smaller than 4%.

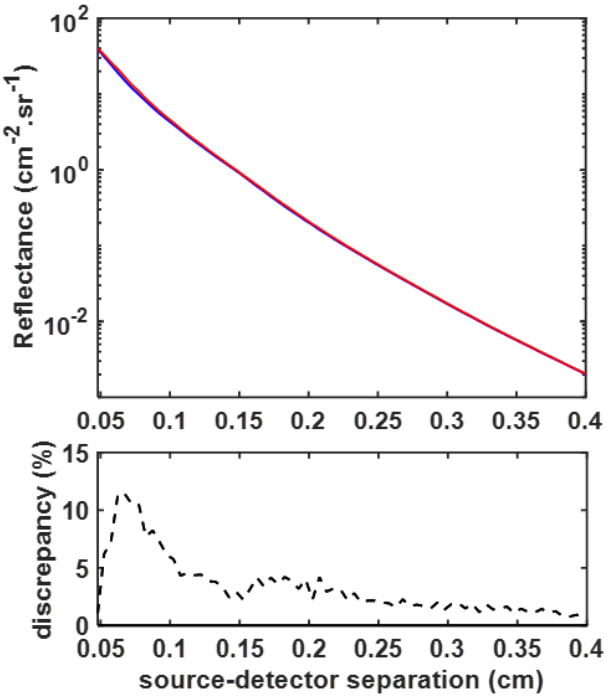


Fig. 2-13 Impact of blurring in diffuse reflectance images. Reflectance profiles were computed using our forward model (Sec. 2.3.2.3). Distortions between calculations taking account on blurring in images (red) or not (blue) are shown (dotted black line).

2.3.2 Experiments and methods

2.3.2.1 Optical phantoms

In order to evaluate the potential of the developed system for the characterization of absorption and scattering properties of tissue, validation experiments were conducted on homogeneous liquid phantoms (Fig. 2-14), following a methodology employed by other authors.[71–74,86,147] Phantoms consisted of solutions of 20% intralipid fat and black india ink (Rotring Inc., Hamburg, Germany) at varying concentrations in distilled water. The

absorbance A of solutions was measured by a spectrophotometer (CARY 300, Agilent) in a 1 centimeter tank, yielding the absorption coefficient $\mu_a = \ln(10) \times A$. Then, various quantities of intralipid fat were added to generate scattering in the medium. Note that the dilution of the ink due to the addition of intralipid was taken into account in the determination of phantom absorption coefficients. For this we applied the following dilution factor: $F = 1 - P/20$, where P is the percentage of intralipid in the phantom, to the absorption coefficient derived from absorbance measurements.

Based on the work of Van Staveren et al.[148], the following formulae were derived to calculate the anisotropy factor g and scattering coefficient μ_s of phantoms:

$$g(\lambda) = 1.1 - 0.58 \times 10^{-3}\lambda \qquad (2.1)$$

$$\mu_s(\lambda) = 2.54 \times 10^{9}\lambda^{-2.4} \times P/10 \qquad (2.2)$$

Where λ is in nanometers and μ_s is in units of cm^{-1}. The additional $P/10$ factor in Eq. (2.2) was used to scale the formula of Van Staveren et al. (derived for a 10%-Intralipid solution) to the percentages of intralipid used in our study.

A set of 15 phantoms, which consisted of three groups of 1, 2 and 3% intralipid concentration, respectively referred to as IL1%, IL2% and IL3%, was fabricated. Each group was composed of five phantoms with varying ink concentration. Corresponding reduced scattering and absorption coefficients ranged from 12.7 cm^{-1} to 38.1 cm^{-1} and 0.31 cm^{-1} to 2.30 cm^{-1}, respectively, spanning values representative of skin properties.[9,11,22,23,149] The expected properties of liquid phantoms are reviewed in Tab. 2-1.

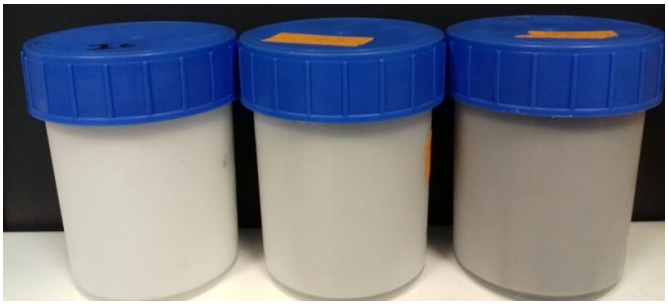


Fig. 2-14 Photograph of liquid tissue-simulating phantoms.

Group	$\mu_a(cm^{-1})$					$\mu_s'(cm^{-1})$
IL 1%	0.33	0,69	1,16	1,63	2,05	12,7
IL 2%	0,31	0,66	1,10	1,94	2,30	25,4
IL 3%	0,37	0,62	1,04	1,46	2,17	38,1

Tab. 2-1 Expected optical properties of tissue-simulating liquid phantoms.

2.3.2.2 Acquisition procedure

Consecutives steps followed during acquisitions are summarized in Fig. 2-15. For each measurement, reflectance images were recorded with the srDRS device using multiple exposure times. Dark images were taken with the same exposure times and subtracted from reflectance images. The resulting images were then normalized by the corresponding exposure time. This set of dark-subtracted and normalized images was employed to produce a single image, herein referred to as 'High Dynamic Range (HDR) image', using a custom algorithm written in Matlab (Mathworks Inc., Natick, Massachusetts). Detailed description and validation of the algorithm are made in Appendix B. The HDR image was composed of pixels from images taken at multiple exposure times in a stepwise manner, going from the longest to the shortest exposure. At each step, pixels with values lower than the saturation limit were kept while saturated pixels were discarded and replaced by the corresponding pixels from the next image (i.e. the one recorded with the nearest lower exposure time). We set the saturation limit to 80% of the sensor dynamic so that pixel values in the HDR image remained within the linear behavior of the camera. Note that for each SDS, signals were extracted only from the image providing the best SNR. This procedure (referred to as dynamic expansion in Fig. 2-15) had to be employed to expand the dynamic range of detection, thereby ensuring sufficient SNR (above 20 dB) up to 4 mm from the source. Depending on phantom properties, three to five different exposure times had to be used, with values ranging from 0.5 ms to 1.2 s. Especially, phantoms with highest absorption and scattering coefficients necessitated additional exposure times compared to phantoms with moderate μ_a and μ_s'. The illumination center was automatically determined through Canny filtering, following a method employed by Foschum et al.[73] Finally, the radial symmetry of illumination was exploited to reduce noise in measured reflectance profiles. Pixel values were averaged over concentric annular areas of 10 pixels thickness around the excitation point. As

rings became larger for increasing SDS, a greater number of pixels were used to calculate the reflectance and thereby the SNR drop (for a given exposure time) was slightly mitigated. This step is referred to as ring averaging in Fig. 2-15.

Following the procedure described before, spatially resolved diffuse reflectance acquisitions were performed on the phantom set. Prior to measurements, phantoms were sonicated for 20 min and left at room temperature for 30 min. During acquisitions, the srDRS device was immersed in phantoms, approximately 5 mm below the surface. Solutions were regularly stirred to prevent from surface layering of intralipid.[150] Five measurements were made for each phantom. Between measurements, the system was removed from phantoms and gently cleaned using ethanol and water.

The acquisition was controlled using a dedicated LabVIEW interface (National Instruments Inc., Austin, Texas).

2.3.2.3 Data processing

Forward model

Theoretical reflectance curves for various optical properties were computed from Monte Carlo (MC) simulations using the algorithm developed at CEA.[125] One million photons were launched in each simulation. A collimated pencil beam vertically incident on a semi-infinite medium with homogeneous optical properties was assumed. We considered a semi-infinite model since phantoms used in this study had homogeneous properties and both depth and width larger than 5 centimeters. The Henyey-Greenstein phase function was used to calculate photon trajectories after scattering events. Following an approach used in previous studies,[71,73] simulated reflectance curves were convolved with the measured source beam profile using the conv2 routine of Matlab (see Appendix A). In Monte Carlo simulations and convolution processes, a radial step size of 50 µm was used.

The obtained reflectance data were stored in a Look-Up Table (LUT). Absorption coefficient values were sampled between 0 and 5 cm^{-1} with 0.02 cm^{-1} step size, while scattering coefficients μ_s ranged from 1 to 300 cm^{-1} with 1 cm^{-1} step size (equivalent to 0.276 to 82.8 cm^{-1} with 0.276 cm^{-1} step size in reduced scattering coefficient μ_s'). The anisotropy factor g was equal to 0.724, as predicted from Mie theory calculations,[30] for all simulations.

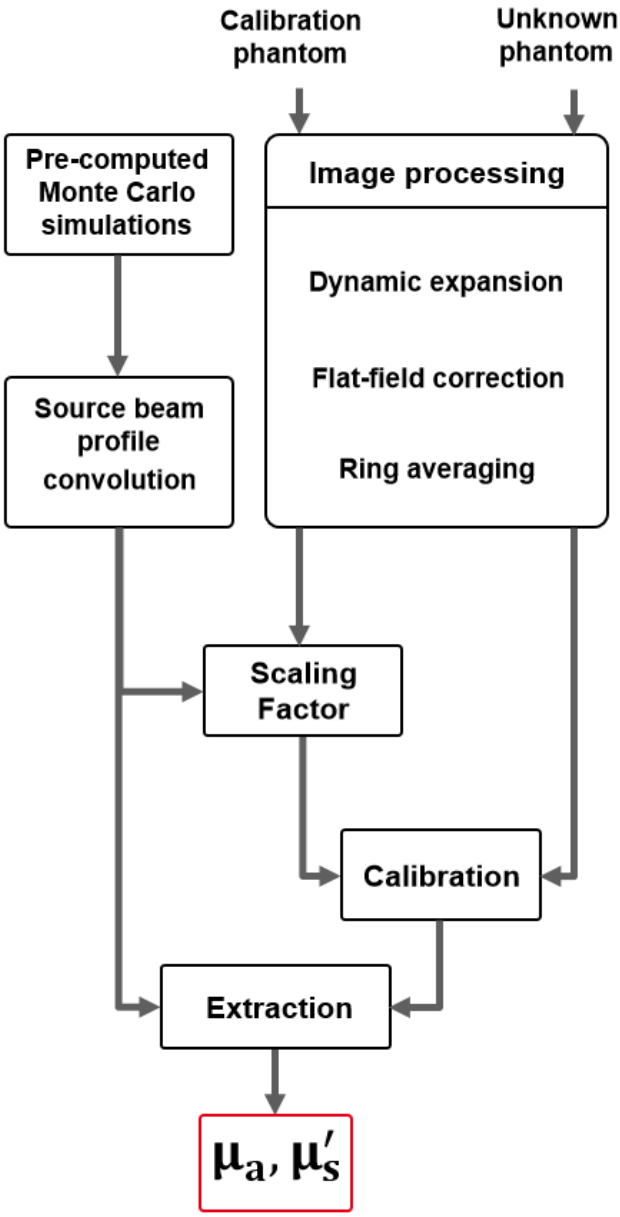


Fig. 2-15 Flowchart of the data processing steps for optical properties quantification. Raw reflectance images were first recorded (image acquisition). Dark images were then recorded and subtracted from reflectance images (background subtraction). This was done at multiple exposure times. The obtained images were recombined to expand the sensor dynamic (dynamic expansion). Then, pixel values were averaged over concentric annular areas surrounding the illumination center to extract the radial profile of raw diffuse reflectance (ring averaging). Theoretical reflectance profiles were derived from Monte Carlo simulations and convoluted with the priory measured source beam profile. Measurement of the calibration phantom diffuse reflectance was used to yield a scaling factor through comparison with theoretical data. The scaling factor was applied to unknown phantoms measurements to convert raw diffuse reflectance profiles into absolute unit. The obtained calibrated reflectance profiles were compared to theoretical data to extract the absorption coefficient (μ_a) and reduced scattering coefficients (μ_s') of phantoms.

Calibration

Calibration of the instrument response must be performed to scale the measured reflectance profiles to MC simulations. Spatially resolved diffuse reflectance measurements were performed on a liquid phantom with known optical properties, herein referred to as *calibration phantom*. We selected the phantom with lowest absorption and medium scattering level among the available phantom set, accordingly with guidelines previously provided by Bender et al.[151] Following an approach used by other authors,[86,152] the following spatially-dependent scaling factor was derived:

$$SF(\rho) = R_{th}\left(\mu_a^{calib}, \mu_s'^{calib}, \rho\right)/R_{meas}^{calib}(\rho) \tag{2.3}$$

where $R_{th}\left(\mu_a^{calib}, \mu_s'^{calib}, \rho\right)$ and $R_{meas}^{calib}(\rho)$ are the simulated and measured reflectance, respectively, of the calibration phantom. This scaling factor was then used to convert the measured reflectance data into absolute unit.

Inverse problem solving

Optical properties extraction was done by searching the best fit between MC-based modeled reflectance and measured data. Reflectance intensities near and far from the source are separated by several orders of magnitude. Consequently, data transformation is necessary to balance the contributions of short and large SDS to fit accuracy.[142,153,154] We considered the following merit functions, which are usually found in the literature:

$$\hat{E}_1(\mu_a, \mu_s') = \sqrt{\sum_{\rho}\left(R_{th}(\mu_a, \mu_s', \rho) - R_{meas}(\mu_a, \mu_s', \rho)\right)^2} \tag{2.4}$$

$$\hat{E}_2(\mu_a, \mu_s') = \sqrt{\sum_{\rho}\left(\ln(R_{th}(\mu_a, \mu_s', \rho)) - \ln\left(R_{meas}(\mu_a, \mu_s', \rho)\right)\right)^2} \tag{2.5}$$

$$\hat{E}_3(\mu_a, \mu_s') = \sqrt{\sum_{\rho}\left(R_{th}(\mu_a, \mu_s', \rho) - R_{meas}(\mu_a, \mu_s', \rho)\right)^2 / R_{meas}(\mu_a, \mu_s', \rho)} \tag{2.6}$$

$$\hat{E}_4(\mu_a, \mu_s') = \sqrt{\sum_{\rho}\left(R_{th}(\mu_a, \mu_s', \rho) - R_{meas}(\mu_a, \mu_s', \rho)\right)^2 / \left(R_{meas}(\mu_a, \mu_s', \rho)\right)^2} \tag{2.7}$$

The properties of the calibration phantom were chosen as initial parameters for the fitting procedure. Linear interpolation of the LUT in the μ_a, μ_s and ρ dimensions was employed. Note that only SDS lower than 4 mm were considered in order to ensure sufficient signal-to-noise ratio (SNR).

Fig. 2-16 illustrates the influence of the merit function on fitting accuracy and sensitivity to optical parameters. Fitting of modeled reflectance to calibrated signals measured on the phantom of group IL2% with highest absorption level was perform using the considered merit functions. It is clear from Fig. 2-16(a) that the use of $\hat{E}_1$ tends to privilege short SDS, which are most strongly sensitive to μ_s', during fitting. This results in poor agreement between fitted and measured curves compared results obtained using $\hat{E}_2, \hat{E}_3$ and $\hat{E}_4$. Among all, $\hat{E}_2$ and $\hat{E}_4$ lead to the best agreement between measured and modeled data, $\hat{E}_4$ providing the closest match between measured and expected properties for the considered phantom. However, both $\hat{E}_2$ and $\hat{E}_4$ were sensitive to the initial parameters for fitting, because of the presence of local minima within the valley of low residuals that can be seen in Fig. 2-16(b). For some phantoms (data not shown), this led to large errors in measured μ_a and μ_s'. Therefore, results presented in Sec. 2.3.3 were obtained using the $\hat{E}_3$ merit function, as it both provided a robust and sufficiently accurate fitting output for all phantoms.

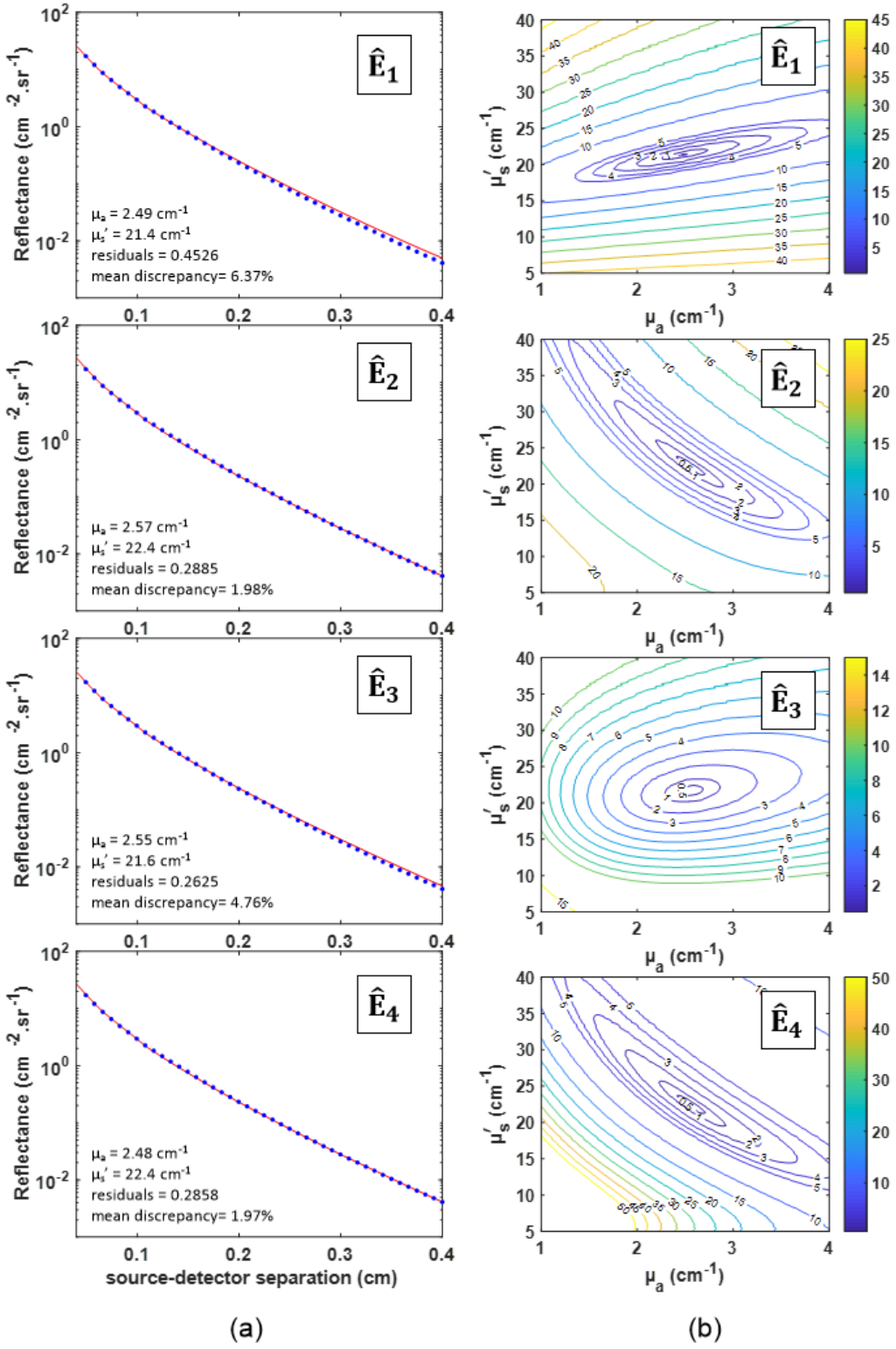


Fig. 2-16 Influence of the merit function on optical properties estimations. (a) Measured (blue dots) and best fits of modeled reflectance (red line). For clarity, only one in five points are shown for the measured data. Estimated properties are given along with the minimum residuals for fit and the discrepancy between measured and fitted data averaged over all SDS. (b) Residuals map obtained for various merit functions.

2.3.3 Results

2.3.3.1 Model fit to data

Measured reflectance profiles versus best fits of modeled reflectance obtained on the whole phantom set are displayed in Fig. 2-17. For clarity, only one in five points are shown for the measured data in the radial dimension. Overall, measured data were well described by our forward model. Mean discrepancies between measured and modeled profiles calculated over all SDS were lower than 6.0%, 2.9% and 3.2% for IL1%, IL2% and IL3%, respectively.

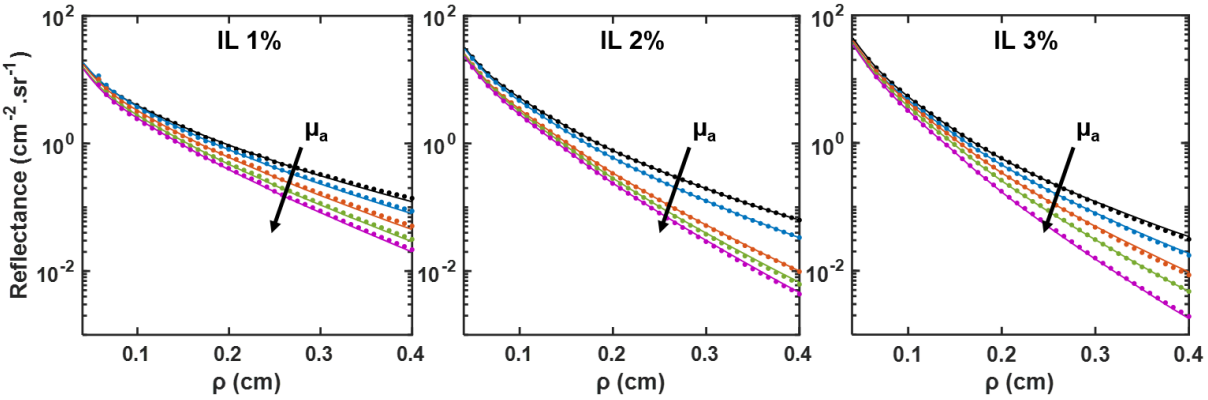


Fig. 2-17 Measured calibrated reflectance of intralipid phantoms (dots) plotted against best fits of theoretical reflectance (solid lines). Measured and fitted data for a given phantom are displayed in the same color. For clarity, only one in five points are plotted for the measured data. Each window shows measured and fitted data for a group of phantoms with same intralipid concentration and varying ink concentration.

2.3.3.2 Optical properties

Measured versus expected μ_a and μ_s' of phantoms are shown in Fig. 2-18. Expected properties were derived from spectrophotometer measurements and Mie theory, as described in Sec. 2.3.2.1, and used as reference values in error calculations. Note that error propagation was not considered in the calculation of absolute error bars, herein corresponding to the standard deviation between properties extracted from different measurements of the same phantom. Percent errors and corresponding error bars represent the absolute errors, respectively error bars, expressed in percent of the expected value for the considered property and phantom. To estimate the overall percent error for optical properties we considered the percent errors (in absolute value) over the whole phantom set and calculated the average. Corresponding intervals were computed as the standard deviation between percent errors (in absolute value) for different phantoms.

Optical parameters were accurately measured, with overall errors of 4.2±3.5% for μ_a and 7.0±4.6% for μ_s'. For μ_a, a correlation coefficient of 0.9915 was calculated between expected and measured values. Fig. 2-18(b) shows slight underestimation of reduced scattering coefficients for highly scattering phantoms. The calculated correlation coefficient was 0.9473. For a fixed intralipid concentration and varying μ_a, minor variations of μ_s' estimates were observed, with standard deviations of 4.9%, 5.7% and 4.0% respectively for IL1%, IL2% and IL3%. We observed that errors in measured μ_s' were closely related to the absorption level of phantoms. For all intralipid concentrations, extracted μ_s' tended to decrease while μ_a increased. This suggests that separation of absorption and scattering influence on measured data was not complete, and some cross-talk remained between parameters.

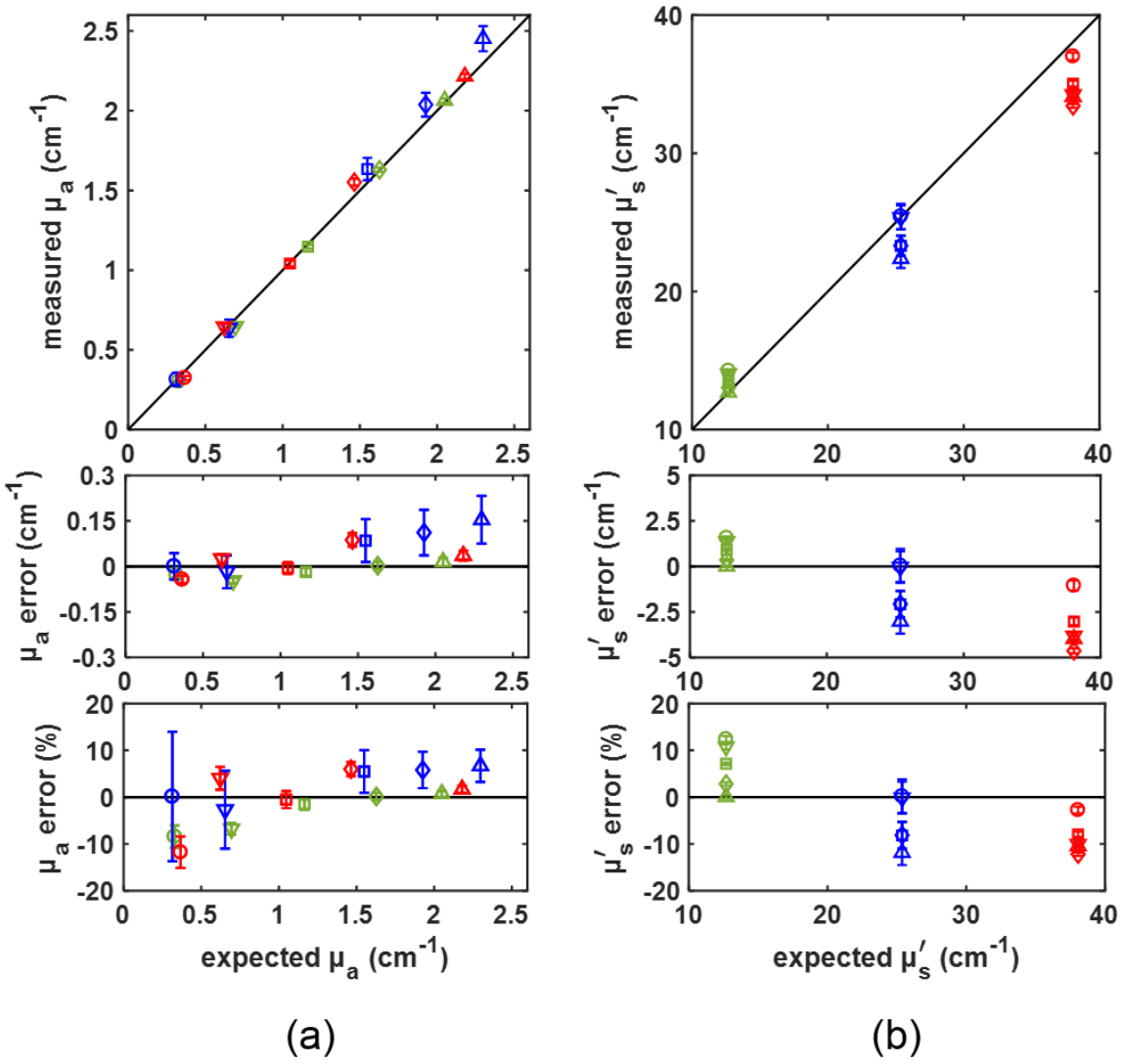


Fig. 2-18 Results of phantom experiments. Measured optical properties for IL1% (green), IL2% (blue) and IL3% (red) are plotted against expected values (black solid line). For each intralipid concentration, different levels of absorption are associated to different markers (from lowest to highest ink concentration: circles, downward-pointing triangles, squares, diamonds, upward-pointing triangles). Absolute values (top), absolute errors (middle) and relative errors (bottom) between measured and expected properties are shown for (a) absorption coefficients μ_a and (b) reduced scattering coefficients μ_s'. Error bars correspond to standard deviations between measurements.

2.3.3.3 Influence of minimal source-detector separation

In order to estimate the influence of the minimal accessible SDS on measured μ_a and μ_s', optical properties extraction was performed over different SDS ranges on three phantoms with varying intralipid concentration. The minimal SDS used for fitting was varied from 480 µm to 2.5 mm. Results are shown in Fig. 2-19. We observed that the yielded optical parameters remain stable up to a minimal SDS of ~800 µm for IL2% and IL3% and ~1.3 mm

for IL1%. Beyond this limit, a brutal increase in measurement error is observed. The influence of the minimal accessible SDS is evident in Fig. 2-20. When short SDS are excluded from the fitting procedure (Fig. 2-20(b)), calculated residuals remain low over a wide range of absorption and scattering parameters combinations, leading to poor estimation of optical properties. Oppositely, the location of the optimal μ_a and μ_s' combination for minimization of the merit function is well-determined when short SDS are included in the fitting procedure (Fig. 2-20(a)). Interestingly, the sensitivity to the accessible SDS range is different between different scattering levels of phantoms. Extrapolating the SDS range toward lower values suggest that a closer proximity between the source and the sensor is unnecessary considering a sample with homogeneous properties.

Overall, these results confirm the relevance of the proposed system architecture and provide an estimate for the minimum SDS to be accessed when implementing a srDRS system for quantitative characterization of absorption and scattering properties.

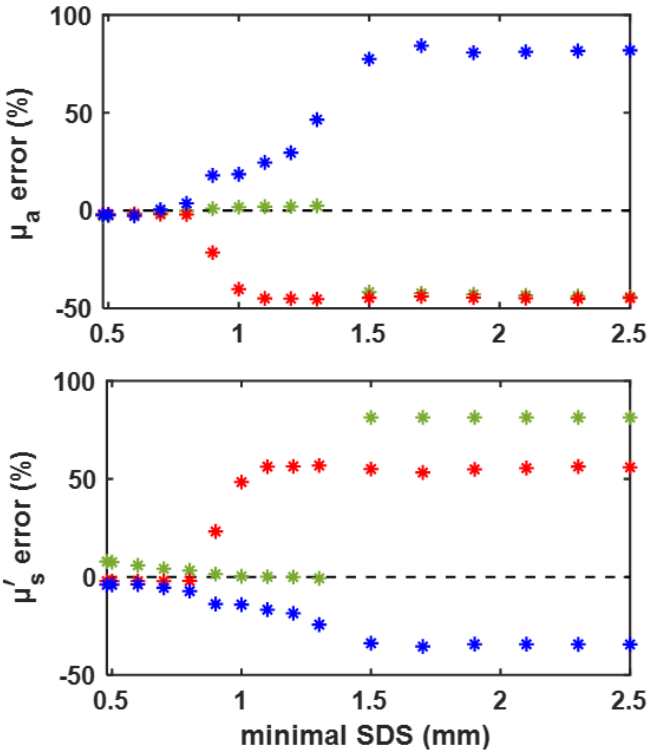


Fig. 2-19 Influence of the minimal accessible SDS on optical properties estimates. Optical properties measurements were made on three phantoms with 1% (green), 2% (blue) and 3% (red) intralipid concentration. The minimum SDS used in the inversion algorithm is varied from 480 µm to 2.5 mm.

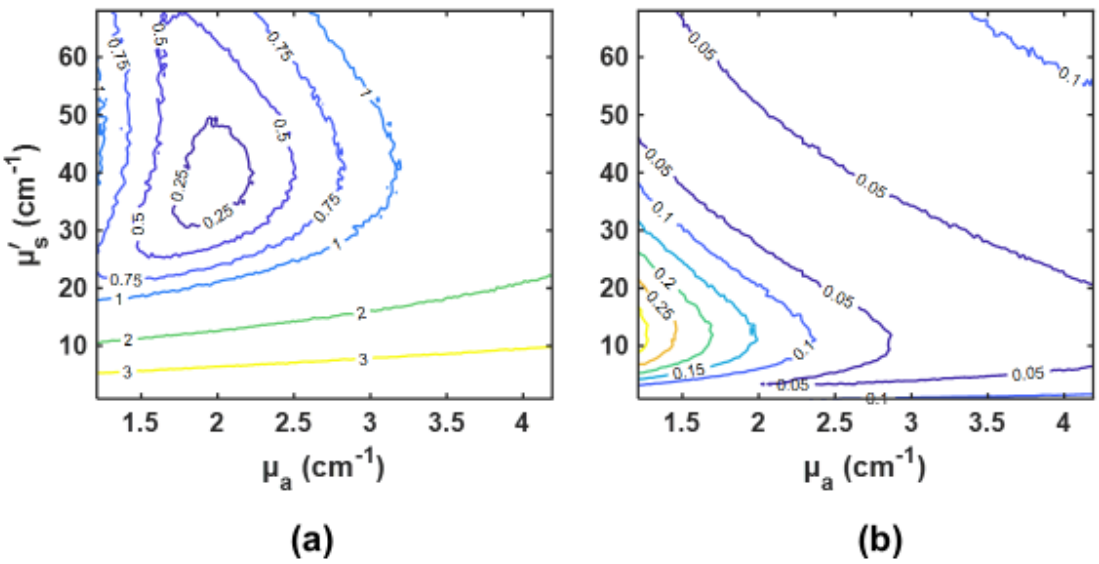


Fig. 2-20 Influence of the minimal source-detector separation on the merit function. The measurement performed on phantom K5 is considered. (a) All SDS lower than 4 mm are used in the calculation. (b) Only SDS between 1.9 and 4 mm are considered.

2.3.4 Discussion

The results obtained from phantom experiments demonstrate the ability of the developed system for accurate quantification of absorption properties of phantoms over the whole range of addressed μ_a. However, Fig. 2-18(b) indicates that accuracy in μ_s' extraction was correlated with the optical properties of measured phantoms. In particular, systematic underestimation of μ_s' was observed for highly scattering phantom. Additionally, the impact of absorption level of phantoms on μ_s' estimates was not completely removed, resulting in slight variations of extracted μ_s' between weakly and highly absorbing phantoms containing the same amount of intralipid (less than 10% overall). These errors were likely due to imperfections of our instrument calibration method. The scaling factor derived in Sec. 2.3.2.3 solely corrects from constant multiplicative effects of the instrument response and does not include influence of the sensor optical transfer function. Furthermore, calibration could only be efficient upon precise knowledge of the source geometry. However, immersion of the srDRS system in intralipid solutions made accurate characterization of the source profile difficult. In our forward model, a planar interface was assumed between the medium and its environment, photons being emitted from the source at this interface. In MC simulations, this interface was placed at the limit between the FOP face and phantoms. Such description was inconsistent with the actual structure of our system. Notably, the presence of the LED dome lens, possible reflections on the FOP side and photon trajectories between the LED chip and

the planar interface were not modeled. In the measurement scheme that was employed for source profile characterization (Sec. 2.3.1.2), our intention was to account for such effects. However, inconsistencies remained between the source profile measurement and the actual conditions of phantom experiments. Notably, the refractive index boundary in the plane of the FOP face was different, as well as the properties of the medium between the LED and this boundary.

It can be noted that the contribution from dependent scattering was not considered in this study. Several authors stressed that the effect of dependent scattering should be accounted for when high concentrations of scatterers are used.[155–157] Further investigation of the influence of dependent scattering should be made in future work.

Because of the limitations listed before, the developed system might show inability to address a wider range of scattering properties (currently from 0.31 cm^{-1} to 2.30 cm^{-1} in absorption and 12.7 cm^{-1} to 38.1 cm^{-1} in reduced scattering). In this case, use of multiple calibration phantoms, as investigated in previous studies,[131,147] could extend the accessible μ_s' range.

A major challenge in current srDRS technology is the analysis of layered tissue with specificity in depth. In skin, epithelium and stroma are the most significant structures (the underlying fat layer is typically too deep to have a significant influence on srDRS signals and is not considered in this study). The separate characterization of these layers may yield critical criteria in a variety of contexts including cancer detection, tissue oxygenation monitoring and drug permeation follow-up. The epithelium thickness varies from 100 to 300 µm, depending on phenotype and location on the body.[6,7] Therefore, the access to both short SDS and high resolution of detection is necessary for accurate characterization of epithelial and stromal layers. Depth-resolution is directly related to lateral resolution and therefore dependent on the apparatus used for collection and detection of photons.

We demonstrated that a multi-pixel sensor used in contact with tissue provided possibility to image diffuse reflectance profiles with high spatial resolution and large FOV (~20mm^2). Moreover, the developed srDRS coupling system provided a way to access short SDS in contact with an unmodified commercial CMOS sensor. In the current version of the system, however, presence of the protective glass window induced blurring of the diffuse reflectance in recorded images. The influence of this effect was estimated. Differences between reflectance profiles affected or not by blurring were lower than 11% on the SDS range

considered in this study. Associated changes in measured optical properties were lower than 2% for all phantoms (data not shown). However, blurring of the diffuse reflectance may limit the ability of the system for the analysis of layered media such as skin, which requires sensitivity to optical properties on reduced footprints. Improvements of the system architecture to address this issue are discussed in the next chapter. Notably, removal of the CMOS glass lid and positioning of the FOP directly on the pixel area is investigated in Chapter 3. In order to further increase the sensitivity of diffuse reflectance spectra to superficial layers, several authors have explored the use of oblique illumination.[48,122,158,159] The proposed architecture is suitable for implementation of such approach.

2.4 Conclusion

A compact design for implementation of spatially resolved diffuse reflectance spectroscopy in contact with tissue has been proposed and evaluated. A prototype instrument, involving an LED source and a commercially available, unmodified CMOS sensor was fabricated. For validation of our approach, a proof-of-concept study was conducted on optical phantoms with controlled properties. Diffuse reflectance imaging was performed with high spatial resolution, large field-of-view (~20 mm^2) and signal-to-noise ratio comparable to that of previously developed instruments.[76,78] A dedicated coupling system involving a Fiber-Optic Plate was developed to provide access to source-detector separations as short as 480 µm. Absorption coefficients (μ_a) and reduced scattering coefficients (μ_s') of phantoms were determined with 4.2% and 7.0% error, respectively, demonstrating the ability of the system for accurate quantification of tissue optical properties. Limitations of this study concerning the modeling of the source geometry and blurring effects that might hinder the potential of the system for the analysis of layered media have been discussed. This work led to the implementation of a wearable system designed for *in vivo* experiments and analysis of layered media. This system is described in Chapter 3.

Chapter 3

Development of a low-cost, wearable srDRS system for skin condition diagnosis: validation study on solid phantoms

This chapter presents the development of a low-cost, wearable srDRS system based on the architecture introduced in Chapter 2 and designed toward *in vivo* applications and analysis of layered media. First, a detailed description of the system is provided (Sec. 3.1). Then validation of the system's performance is made in comparison with a well-established technique, referred to as Spatial Frequency Domain Imaging (SFDI) (Sec. 3.2). For this study, a set of solid tissue-simulating phantoms was developed, as described in Sec. 3.2.1. The work presented in this chapter was conducted jointly with the Photonics Instrumentation for Health group at the Laboratoire des sciences de l'Ingénieur, de l'Informatique et de l'Imagerie (ICube UMR7357) at University of Strasbourg. Collaboration between the CEA and ICube notably concerned the development of a protocol for phantom fabrication and characterization of these phantoms using the srDRS system and the SFDI system developed at ICube, which was considered as a reference instrument.

3.1 Instrument development

3.1.1 Sensor design

An optimized srDRS prototype based on the architecture developed in Chapter 2 was implemented. The design of this new system was specified considering two main goals:

1) Achieve continuous measurement of optical properties for the monitoring of tissue oxygenation *in vivo*.
2) Increase the potential of the system for the analysis of layered media.

In this frame, the work has principally been focused on the miniaturization of the system for attachment on human subjects during *in vivo* measurements and the implementation of multiple sources to obtain the necessary spectral information for oxygenation monitoring. In addition, removal of the CMOS protective glass window was investigated to enhance the contrast in images (see Sec. 3.1.1.3) and a light source with angled illumination was implemented. These two last features aimed at increasing the potential of the system for the analysis of layered media.

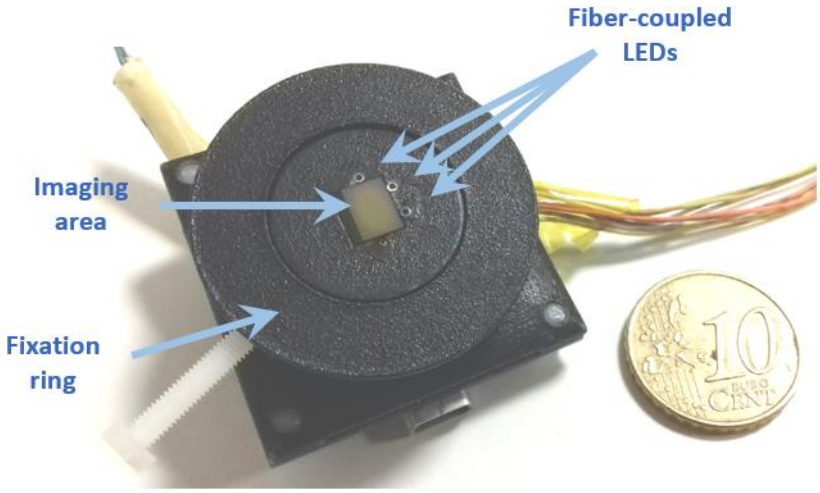


Fig. 3-1 Photograph of the wearable srDRS prototype

A photograph of the fabricated srDRS prototype is shown in Fig. 3-1. A layout of the prototype's structure is given in Fig. 3-2. This system comprises the CMOS camera used previously (UI-1492-LE-M, IDS Imaging, Obersulm, Germany). The camera was coupled to a custom fiber-optic plate (Sec. 3.1.1.3), around which the light sources were placed (Sec. 3.1.1.2). The sources and FOP are hosted in a dedicated packaging module, which is described in the next section.

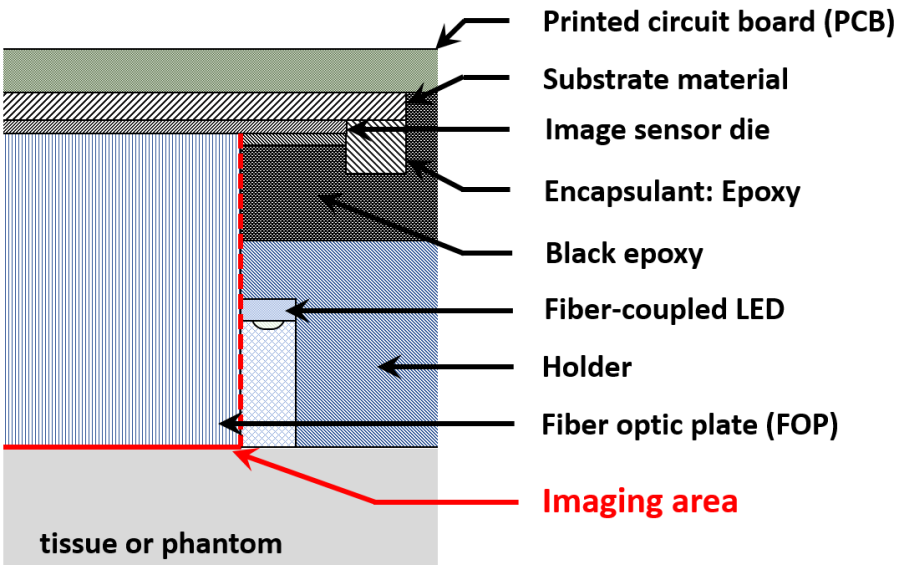


Fig. 3-2 Layout of the wearable srDRS Prototype

3.1.1.1 Packaging module

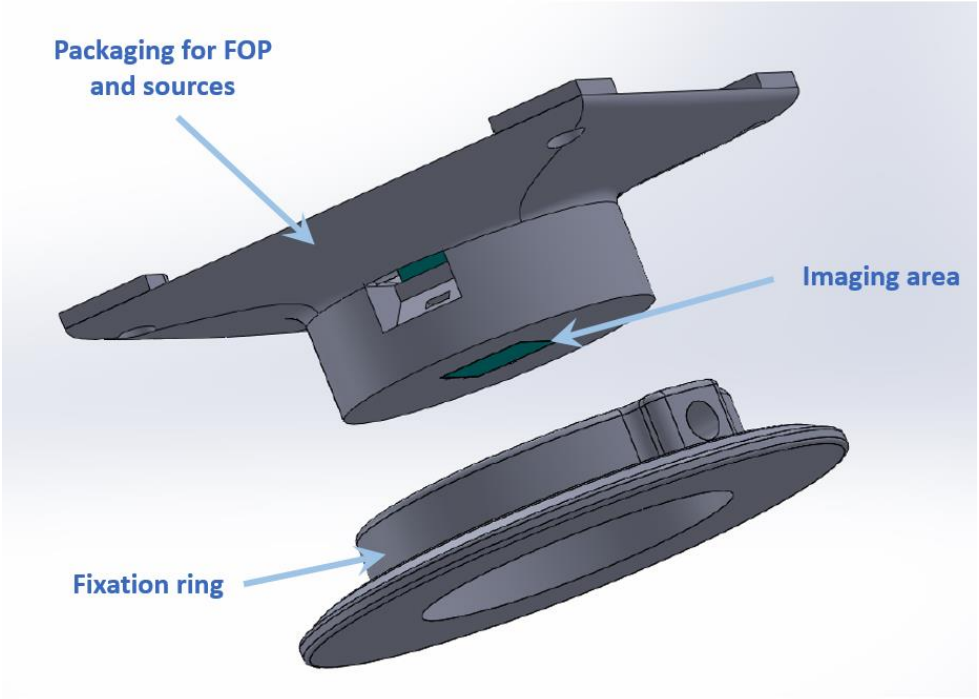


Fig. 3-3 Digital model of the packaging module for the wearable srDRS prototype. The FOP and sources are hosted in a dedicated element. For *in vivo* measurements, this element can be inserted in a custom fixation ring and set with a plastic screw. The fixation ring is priory attached to the tissue at the desired measurement site using standard medical adhesives.

A packaging module was specifically designed for assembly of the different elements of the system. The packaging was 3-D printed in a biocompatible polyamide (PA2200). A central hole corresponding to the imaging area was left free for insertion of the fiber-optic plate (FOP). The module is mounted on the camera using plastic screws at the corners of the PCB. For *in vivo* measurements (see Chapter 4), the packaging module comes with a dedicated fixation ring, which may be attached to the tissue using standard medical adhesive tapes. The device is then inserted through the ring and set with a screw to maintain a constant pressure on the tissue. The outer surface of the packaging was painted in black to limit unwanted reflections at the tissue-exterior interface.

3.1.1.2 Lighting module

Four different light sources were placed around the imaging area. Main characteristics and references of these sources are reported in Tab. 3-1. Surface mounted LEDs were purchased from Kingbright Inc. LEDs with a 1608 packaging were chosen because of their small lateral dimension (0.8 mm), which was required to provide access to sufficiently small SDS. The

LEDs were coupled with custom fiber-optic bundles fabricated at our laboratory. In this manner, we imposed a planar interface between sources and the analyzed medium, with controlled illumination geometry and numerical aperture (NA), thereby facilitating the modeling of source beams in Monte Carlo simulations.

For three sources (lines 1 to 3 of Tab. 3-1), 7 fibers were glued together in a hexagonal geometry. We found that using 7 fibers was necessary to obtain sufficient output power while keeping a small enough source diameter (~600 µm). These sources were then integrated in the packaging module with a vertical illumination angle ($\theta = 0°$).

For the last source (4^{th} line of Tab. 3-1), only one fiber was used. Implementation of this source aimed at optimizing the potential sensitivity of the system to tissue properties at shallow depths toward layered media analysis. Notably, the use of green light and angled illumination ($\theta = 35°$) was chosen to maximize the proportion of detected photons that travel at small tissue depths.[48,122,160] Maximization of the sensitivity of the measured reflectance to shallow depths also requires the use of a thin input beam, motivating our choice for a single fiber coupling. The induced reduction in output power was compensated by the fact that only short SDS (and thereby higher signals) may be considered in this case. A 200 microns fiber core diameter was however necessary for efficient coupling with the LED source.

Remark that each fiber bundle was assembled within a metallic needle having a 1.1 mm diameter. This was necessary to avoid fiber breakage during manipulation by the technician and integration in the packaging module.

For each source, the input current was controlled by an LED current driver (RCD-24-0.70/PL/B, Recom Power, Gmunden, Austria) via a dedicated electronic circuit produced at CEA and LabVIEW interface developed for this study.

Reference	λ (nm)	Δλ/2 (nm)	θ (°)	Bundle geometry	Fiber core diameter (µm)	Fiber NA	Output Power (µW)	Minimal SDS (µm)
KPHD-1608ZGCK	515	35	0		200	0.39	73	760
KPHD-1608SECK-J4-PRV	611	17	0		200	0.39	123	820
KP-1608SRC-PRV	660	20	0		200	0.39	19	690
KPHD-1608ZGCK	515	35	35		200	0.39	17	790

Tab. 3-1 Characteristics of the light sources involved in the wearable srDRS prototype. The output power was measured by an optical power meter (PMD100, Thorlabs Inc.) placed at the output of fiber bundles. The distance of each fiber bundle to the closest FOP side was determined through binocular microscope observations. The minimal SDS for each source was then calculated knowing the position of the FOP sides in the imaging area (see Sec. 3.1.2).

3.1.1.3 FOP-sensor coupling

The CMOS sensor was coupled to a fiber-optic plate (FOP) according to the architecture proposed in Chapter 2. A custom FOP with 6 µm unit fiber core diameter (OS-ST, SZPhoton) was purchased from SZPhoton Inc.[143] Note that this material was equipped with Extra Mural Absorption (EMA) in order to limit light diffusion between adjacent fibers and improve the spatial resolution. The FOP was cut to a 6.4x5.5 mm lateral dimension and 10 mm thickness. This left the possibility to place the light sources on three sides of the imaging area and in close proximity to pixels.

As discussed in Chapter 2, the presence of the protective glass window in front of pixels induces blurring of the diffuse reflectance in images recorded in contact with tissue. Although this effect has a minor impact on measured optical properties for homogeneous media, it may result in a strong limitation when analyzing a layered media such as the skin. Notably, image contrast on small footprints at least of the order of the epithelium thickness (~100-200 microns) may be required if efficient separation of layers influence on the measured signal is

to be achieved. For this reason, removal of the glass lid and positioning of the FOP onto the CMOS photon sensitive area was investigated.

FOP coupling of the CMOS sensor was conducted following guidelines provided by Silfhout and Kachatkou[161]. Permanent bonding of the FOP and sensor was performed using an optical grade epoxy (Opti-tec 5001, Intertronics, Kindlington, United Kingdom). Note that in the choice of epoxy, attention should be paid to the shrinkage coefficient upon curing, which must be sufficiently low to avoid mechanical stresses likely to damage the sensor die.

The procedure for FOP coupling is described in the following. First, the glass lid had to be removed from the sensor. The glass lid is usually glued to the underlying epoxy package protecting the sensor die. For bond breakage, the sensor was subjected to a high temperature (~100°C) air flow. Under this temperature, the epoxy surrounding the glass lid starts to melt and can be extruded progressively down to the basis of the glass layer. When this point is reached, the glass lid can be removed easily using a thin scalpel blade. The next steps of the procedure were conducted in a clean room environment to ensure that the bonding layer and sensor die would remain free from air dust and other unwanted particles. First, the hardener and epoxy parts were mixed by hand in an independent recipient. This step inevitably generates air bubbles. These were removed by placing the mixture in a vacuum container for 15 min. Then, one drop of the mixture was deposited on the sensor die. Because of its low viscosity, the glue rapidly spread over the whole imaging area and wire bonds until it entirely filled the well formed by the surrounding sensor packaging (see Fig. 3-2). At this stage, the FOP could be placed onto the CMOS for coupling. Precise positioning was obtained by using the packaging module described in Sec. 3.1.1.1 priory mounted onto the sensor. The FOP was delicately inserted through the central hole of the module, which was aligned to the imaging area. The epoxy glue ensured protection against mechanical stresses generated during placement of the FOP. The weight of the FOP was then sufficient to obtain a thin bonding layer.[161] In addition to providing a way for precise positioning, the packaging module prevented for lateral movements of the FOP during curing, which would likely result in unwanted heterogeneities of the bonding layer and provoke image distortions. Placement of the FOP may also generate air bubbles in the bonding layer. For this reason, vacuum pumping was performed again for 15 min. The system was then left for 60 min for curing. At the end of the process, bonding of the FOP onto the sensor die was achieved with a thin, clear and homogeneous bonding layer. At this stage however, the FOP may easily be removed by hand and the wire bonds surrounding the imaging area are not efficiently protected. For

further protection, an electronic grade black epoxy (HE70E, Epoxy Technology, Billerica, Massachusetts) was deposited around the FOP and surrounding sensor packaging to ensure a sufficient resistance to mechanical stresses, notably upon removal or mounting of the packaging module. In addition, the black epoxy prevented from stray light illumination of the sensor die between the FOP sides and imaging area borders.

3.1.2 Optical Characterization

The developed srDRS device linearity was measured from images recorded at varying exposure time under constant illumination level and subtracted from corresponding dark images. The mean signal over the entire image was considered. Fig. 3-4 displays the linearity curve of the device, which was calculated as the deviation from the linear best fit in percent of sensor dynamic (256 ADU).

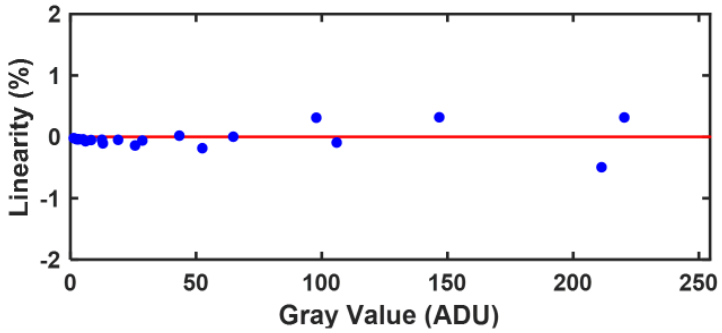


Fig. 3-4 Linearity curve of the wearable srDRS prototype.

The image resolution provided by the developed srDRS system after glass lid removal was evaluated using a USAF-1951 resolution test target (Fig. 3-5). Compared to the prototype presented in Chapter 2, this new implementation increased the spatial resolution of imaging by a factor of 50. Spatial frequencies up to 50.8 lp/mm (group element 5-5), corresponding to 9.8 microns thick lines, could be resolved.

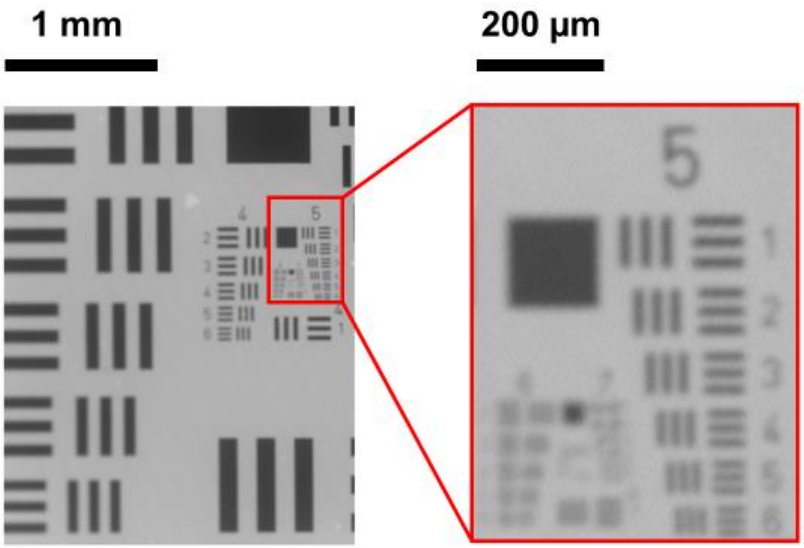


Fig. 3-5 Positive USAF-1951 resolution test target imaged with the wearable srDRS system after glass lid removal.

Following the procedure described in Sec. 2.3.1.2, the flat-field response of the system under Lambertian illumination was characterized, as shown in Fig. 3-6. For comparison, flat-field images recorded before and after removal of the protective glass window are displayed. The obtained images were used for correcting measured reflectance images for flat-field inhomogeneity, as described in Sec. 3.2.2.2. The increase in image resolution obtained after removal of the glass lid is particularly visible at the FOP borders, which are outlined with poor contrast in Fig. 3-7(a) compared to Fig. 3-7(b).

The position of the effective imaging area (limited by the FOP borders) had to be determined to select the correct Region Of Interest (ROI) in raw diffuse reflectance images. Before removal of the glass lid, an image recorded under illumination by a collimated flat beam was used. As shown in Fig. 3-7(a), images recorded with the glass lid were less affected by blurring under collimated illumination, thereby allowing for precise detection of the FOP borders. After removal of the glass lid, the FOP borders could be imaged with high contrast under both collimated and Lambertian illumination. Alternatively to the approach chosen before glass lid removal, we used a Lambertian flat-field image for detection of the FOP borders. In this case, the effect of chamfering, which is usually performed during FOP manufacturing to ensure robustness to shocks, could be observed. Inside the chamfer, fibers arrangement is chaotic and may induce image distortions. Notably, under Lambertian illumination, this results in a clear drop in transmission of light by the FOP. Thus, the limit between the FOP transmissive area and chamfer could be precisely determined, as shown in

Fig. 3-7(b). The position of the sources relatively to the imaging area were then determined through binocular microscope observations of the prototype's top face, in which the fiber bundles, chamfer and FOP transmissive area could be well identified.

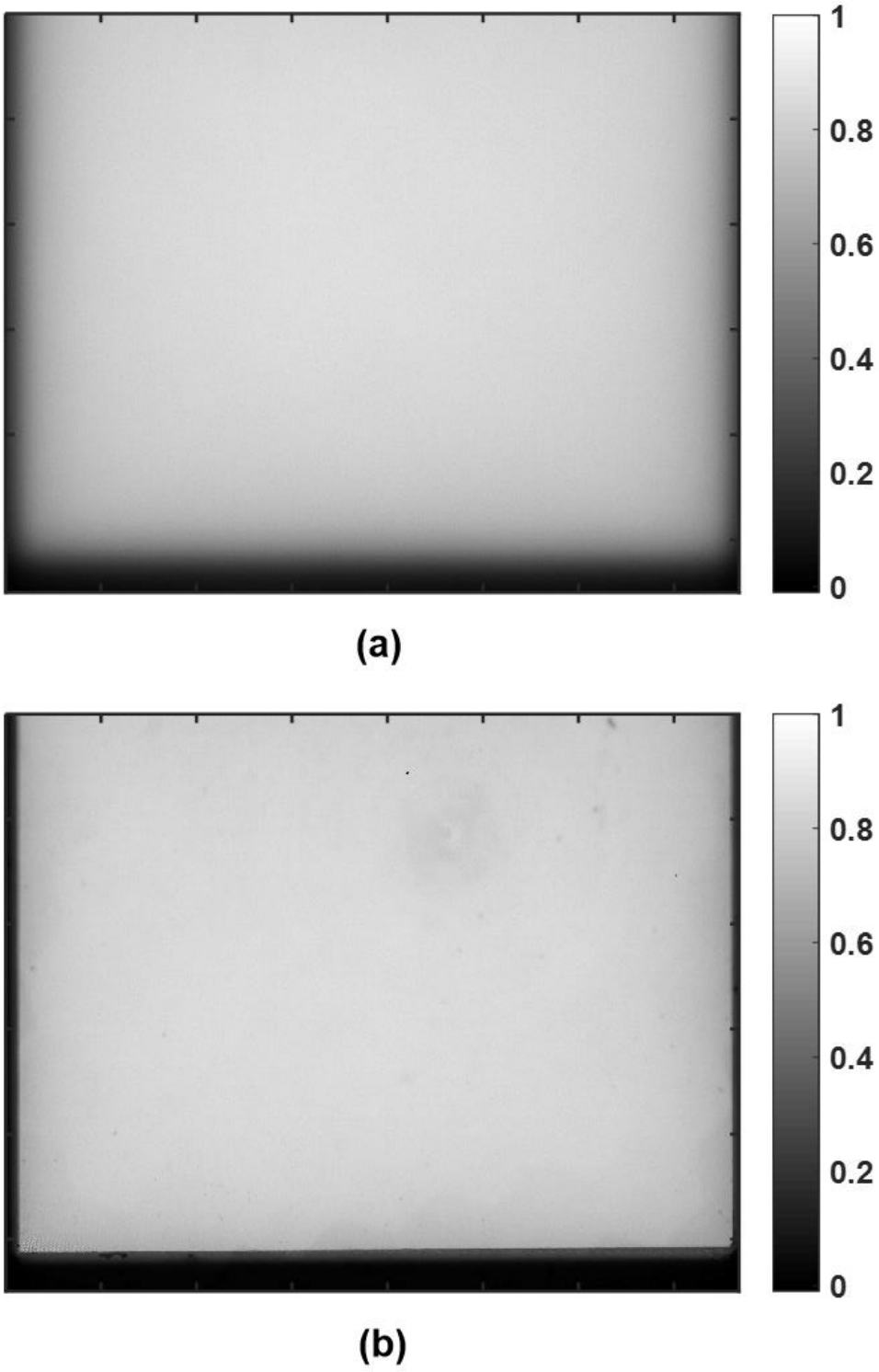


Fig. 3-6 Lambertian flat-field images recorded (a) before and (b) after removal of the protective glass lid.

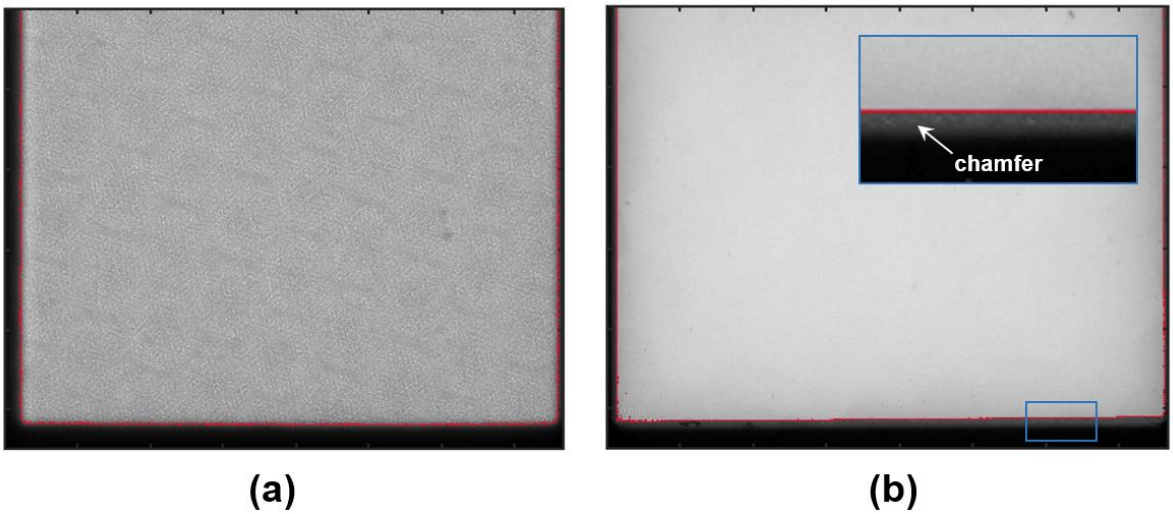


Fig. 3-7 Location of the FOP in the imaging area (a) before and (b) after removal of the protective glass lid. The borders of the FOP are highlighted in red. In (a), collimated illumination was considered to ensure sufficient image contrast at the FOP borders. Remark the regular hexagonal grid, which corresponds to individual fiber bundles assembled during fabrication of the FOP. In (b), Lambertian illumination was used for better visualization of the FOP chamfers, which were excluded in the processing of diffuse reflectance images.

3.2 Phantom validation

The performance of the designed prototype was evaluated for the characterization of optical properties of solid tissue-simulating phantoms. In this section, we first present the development and characterization of these phantoms. Then, evaluation of the wearable srDRS prototype's performance for quantitative characterization of phantom properties is made.

3.2.1 Development of solid phantoms

3.2.1.1 Motivation

A set of solid poly(dimethylsiloxane) (PDMS) phantoms spanning properties representative of human skin has been developed and characterized. We opted for solid phantoms for several reasons. Contrarily to intralipid solutions, this type of phantom can provide a relatively close match to skin in terms of mechanical properties and surface roughness, thereby enabling the study of the influence of coupling between the sensor and tissue. PDMS phantoms conserve stable properties over time and are easily transportable for characterization in various facilities and comparative studies between different systems.[162–164] This was especially necessary to conduct bimodal measurements of phantom properties using

the srDRS system and the reference SFDI system. Finally, PDMS phantoms were chosen because they can be fabricated with a layered structure and rough surface for improved simulation of tissue and characterization of the device's performance.[165]

3.2.1.2 Fabrication

A common protocol for phantom manufacturing was developed jointly between the CEA and ICube. The protocol described here was mainly inspired by a previous protocol established at CEA during the doctoral thesis of Blandine Roig[24] and studies published by Greening et al.[166] and Saager et al.[165] Phantoms with various optical properties (see Fig. 3-9) spanning values representative of skin tissue have been fabricated both at CEA and at ICube.

Fabricated phantoms consist of a mixture of PDMS and curing agent (CA), ethanol-dissolved nigrosin (Ng-EtOH) and titanium dioxide (TiO_2) particles. Absorption in phantoms is modulated by the concentration of nigrosin particles while scattering is generated by the TiO_2 particles. Consecutive steps followed during phantom fabrication are listed and discussed in the next paragraphs:

1) **Preparation of Ng-EtOH solutions**. The desired mass of alcohol soluble nigrosin was sampled and dissolved in ethanol. Note that various concentrations of nigrosin in phantoms were obtained by modulating the concentration of nigrosin in Ng-EtOH solutions while keeping a constant amount of ethanol in the final phantom. Therefore, the contribution of ethanol to phantom absorption remained constant for all phantoms. Although it is easily dissolved in PDMS, an excessive quantity of ethanol may disturb the curing process by generating large amounts of air bubbles. Roig derived an empirical factor of 1/35 between ethanol and PDMS volume not to exceed in order to avoid such issue.[24] In phantoms fabricated for this study, this factor was kept to 1/81.

2) **Preparation of TiO_2-CA solutions.** The desired mass of TiO_2 was sampled and incorporated in a volume of curing agent. In order to break the TiO_2 aggregates, the solutions were subjected to three consecutive cycles of 10 min ultrasonic bath and 1 min hand mixing, accordingly with guidelines provided by Greening et al.[166] At the end of this process, remaining large aggregates were eliminated using a nylon filter with 100 microns mesh. Note that use of smaller meshes was investigated yet could not be achieved due to the high viscosity of the curing agent and poor solubility of

TiO_2 particles. Improvement of this filtration step may be investigated in future work for further reduction of TiO2 aggregates and enhancement of phantoms homogeneity. Remark also that the solutions before filtration rapidly formed new aggregates and may not be conserved for more than a few minutes. After filtration, solutions remained sufficiently homogeneous for a few hours, leaving enough time to complete the fabrication of phantoms.

3) **Mixing.** The desired volume of PDMS was sampled. First, the volume of Ng-EtOH was incorporated in the PDMS and mixed by hand for ~1 min. Then the volume of TiO_2-CA was added. We observed that addition of TiO_2-CA before Ng-EtOH, accordingly to the protocol of Roig,[24] typically resulted in inconsequent absorption levels in phantoms with respect to the amount of Ng-EtOH used. However, further investigation should be made to confirm this trend. In consequence, Ng-EtOH volumes were always incorporated first in phantoms. After addition of the TiO_2-CA volume, hand mixing was performed for at least 5 min until a homogeneous mixture was obtained.

4) **Molding.** Obtained mixtures with various concentrations of TiO_2 particles and nigrosin were poured in separate molds corresponding to each phantom. Molds consisted of 70 mm cylinders placed in glass cups. In order to obtain phantoms with a rough surface, a piece of standard rough paper (Canson®) was priory glued on the bottom of glass cups. Cylinders were maintained with adhesive to prevent from PDMS leakage likely to occur during the degassing step.

5) **Degassing.** Molded phantoms were placed in a vacuum chamber to remove air bubbles formed during the previous steps. Vacuum pumping of the mixtures for 1 hour was sufficient to remove all air bubbles.

6) **Curing.** Eventually, phantoms were left in oven for 2h at 85°C to complete curing. After curing, homogeneous solid phantoms with 70 mm diameter and 15 mm thickness were obtained. The bottom side of phantoms had a rough surface, while the upper face was flat.

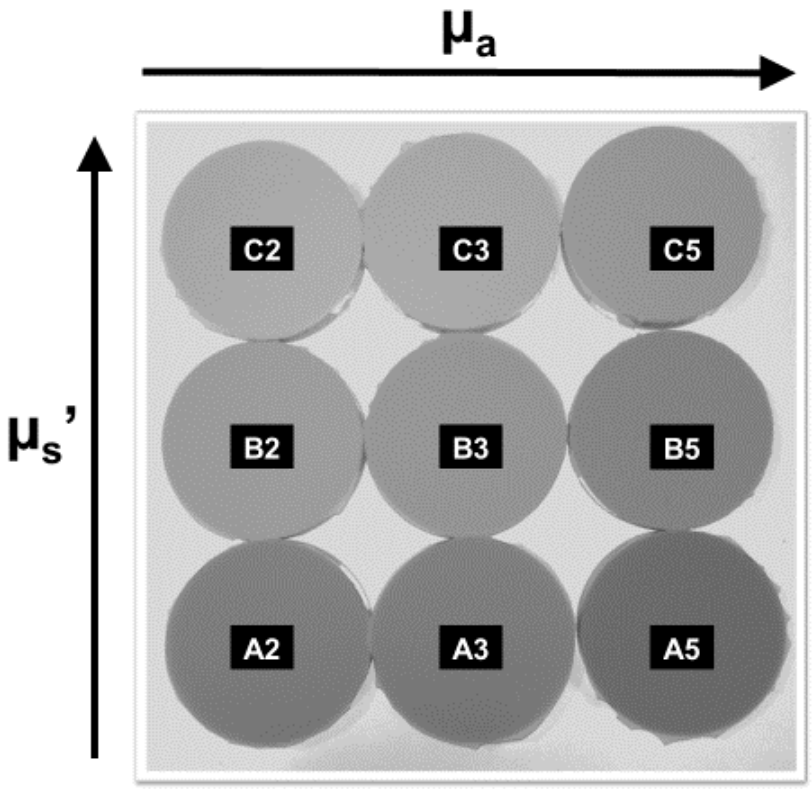


Fig. 3-8 Photograph of manufactured PDMS phantoms.

Following the described protocol, a set of 15 phantoms was fabricated. These were made in groups of 5 phantoms at a time, herein referred to as A, B and C. Each group is composed of phantoms having constant TiO_2 concentration and varying nigrosin concentration. This set of phantoms was completed by a set of 18 phantoms fabricated at ICube. These are divided into two groups herein referred to as D and E. Phantoms of group D were selected to provide a nearly constant μ_a and varying μ_s' as measured through SFDI (Sec. 3.2.1.3), while group E is composed of phantoms having nearly constant μ_s' and varying μ_a. A review of measured phantom properties and corresponding concentrations of TiO_2 and nigrosin is provided in Tab. 3-2.

3.2.1.3 SFDI Characterization

Optical properties of the fabricated phantoms were measured using the SFDI system developed at ICube, which was considered as a reference system for this study. SFDI is a well-established technique providing a quantitative 2-D mapping of optical properties of the analyzed medium.[167] Characterization of phantoms was obtained at 665 nm and 860 nm. Measured absorption and reduced scattering coefficients at 665 nm are shown in Fig. 3-9 and

Tab. 3-2. Overall, extracted properties cover a wide range of values representative of tissue.[9,22,149] Properties are especially thinly sampled in the [0 ;1] cm^{-1} range in absorption and [7 ;20] cm^{-1} range in reduced scattering, which are most representative of light-skinned human subjects and dermal properties. The rest of the phantoms extend this range toward higher levels of absorption and scattering, which may notably be observed in darker skin tones and epithelium.[23,24]

This work may be used in further studies to establish a robust relation between nigrosin and TiO_2 concentrations on one side and the corresponding μ_a and μ_s' of phantoms on the other side.

In the next section, measurement of phantom properties using the developed wearable srDRS device are presented and compared to values obtained from SFDI. Unless stated otherwise, acquisitions were made on the rough face of phantoms. This was notably necessary because of the sensitivity of SFDI to surface specular reflections, which may otherwise have significant impact on measured optical properties.[168]

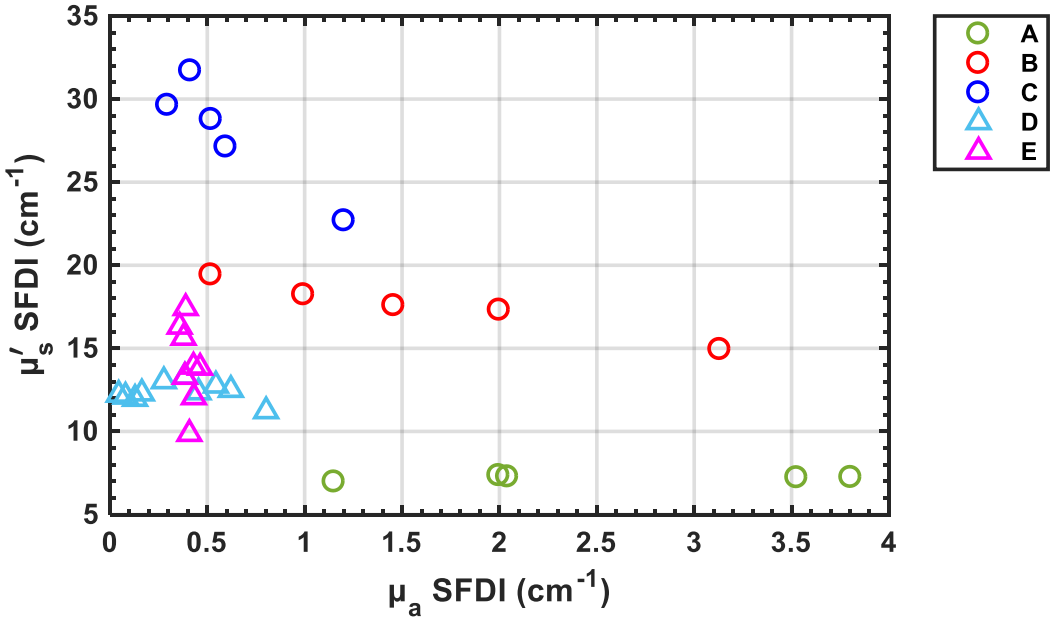


Fig. 3-9 Optical properties of PDMS phantoms measured by SFDI at 665 nm.

Reference	Nigrosin concentration (mg/g)	μ_a (cm^{-1})	TiO_2 concentration (mg/g)	μ_a' (cm^{-1})
A1	0.080	1.15	1.0	6.97
A2	0.239	2.00	1.0	7.35
A3	0.398	2.04	1.0	7.27
A4	0.558	3.53	1.0	7.22
A5	0.717	3.80	1.0	7.23
B1	0.080	0.52	3.0	19.4
B2	0.239	0.99	3.0	18.2
B3	0.557	1.46	3.0	17.6
B4	0.715	2.00	3.0	17.3
B5	1.59	3.13	3.0	14.9
C1	0.08	0.30	5.0	29.6
C2	0.238	0.41	5.0	31.7
C3	0.397	0.52	5.0	28.8
C4	0.555	0.60	5.0	27.1
C5	0.714	1.20	5.0	22.7
D1	0.003	0.05	2.1	12.2
D2	0.003	0.08	1.7	12.1
D3	0.008	0.13	2.1	12.0
D4	0.023	0.16	1.8	12.3
D5	0.017	0.28	2.1	13.0
D6	0.023	0.39	1.8	13.3
D7	0.023	0.46	1.8	12.4

D8	0.023	0.54	1.8	12.8
D9	0.023	0.62	1.8	12.5
D10	0.023	0.80	1.8	11.2
E1	0.017	0.41	1.4	9.9
E2	0.017	0.43	2.1	12.1
E3	0.023	0.39	1.8	13.3
E4	0.023	0.46	1.8	13.8
E5	0.034	0.43	2.1	13.9
E6	0.017	0.38	2.8	15.6
E7	0.017	0.36	2.8	16.3
E8	0.025	0.39	2.8	17.4

Tab. 3-2 Properties of PDMS phantoms measured by SFDI at 665 nm and corresponding TiO_2 and nigrosin concentrations. Note that the given concentrations are those initially targeted and do not take account for variations likely to occur upon filtration and mixing processes.

3.2.2 Materials and Methods

3.2.2.1 Experiments

The optical properties of the fabricated phantoms were measured at 660 nm using the developed wearable srDRS device. The setup used during phantom experiments is described in Fig. 3-10. The system and phantom were placed on a fixed and mobile plate, respectively, inside a Thorlabs cage assembly. A string applied a stable pressure onto the mobile plate. By setting the position of the srDRS device with a fixed wedge, a reproducible pressure level was applied between the device and phantoms. Note that the applied pressure level is also dependent on the phantom thickness. All phantoms fabricated at CEA had the same thickness (15 mm) being slightly larger than the thickness of phantoms fabricated at ICube (10 to 12 mm). For this reason, the sensitivity of measured signals to the position of the wedge was evaluated (Sec. 3.2.3.1).

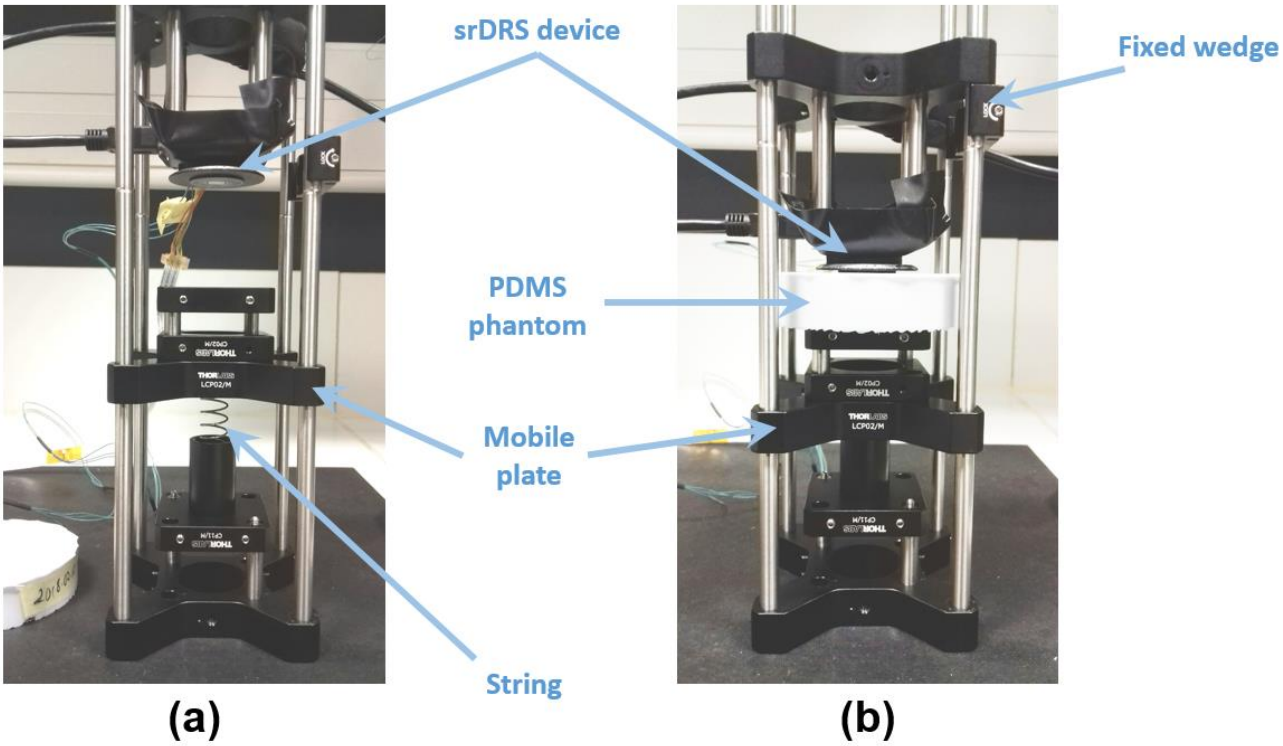


Fig. 3-10 Experimental setup for phantom experiments before (a) and after (b) positioning of the PDMS phantom.

Diffuse reflectance images were recorded on PDMS phantoms using the setup described previously. Several experiment campaigns were made to validate the experimental setup (Sec. 3.2.3.1) and compare the optical properties measured by the srDRS device in different conditions (with and without glass lid protection, on different faces of phantoms) to the reference values provided by SFDI.

During experiments, the acquisition procedure followed the one introduced in Sec. 2.3.2.2. For each phantom, images were recorded at multiple exposure times and subsequently recombined using the dynamic expansion algorithm described in Appendix B. Depending on phantom properties, two to four exposure times were used, with values ranging from 2 ms to 1.2 s. Optical properties were measured at five different positions on the phantom surface and averaged.

3.2.2.2 Data Processing

Forward model

Following the approach described in Sec. 2.3.2.3, theoretical reflectance curves for various optical properties were obtained from Monte Carlo simulations run on GPU. One million

photons were launched in each simulation considering a pencil beam vertically incident on a semi-infinite medium with homogeneous optical properties. The fiber-coupled LED source was modelled by a 600 µm flat beam with 0.39 NA. The numerical aperture of emission was accounted for in pencil beam simulations, and the obtained profiles were convolved by the modeled source profile using the CONV algorithm of Wang et al.[169] implemented in Matlab. A radial step size of 50 µm was used in both MC simulations and convolution process. The Henyey-Greenstein phase function was used for calculation of photon trajectories after scattering events. Note that we considered a medium having anisotropy g=0.8, as was done in the Look-Up Table (LUT) used for SFDI measurements.

Computed MC profiles were stored in a LUT. Absorption coefficient were sampled between 0 and 10 cm^{-1} with 0.02 cm^{-1} step size, while scattering coefficients μ_s ranged from 1 to 400 cm^{-1} with 5 cm^{-1} step size (equivalent to 0.2 to 80 cm^{-1} with 1 cm^{-1} step size for reduced scattering coefficient μ_s'). We verified through numerical computations that the relatively large steps in μ_s' combined with data interpolation did not induce significant changes in calculated profiles compared to a finer μ_s' grid.

Calibration and inverse problem solving

Calibration of the instrument response was performed using the approach described in Sec. 2.3.2.3. Depending on measurement campaigns, two different calibration phantoms were used. Measurements performed at the CEA used phantom B1 as calibration phantom, considering the properties measured by SFDI (0.52 cm^{-1} in absorption and 19.4 cm^{-1} in reduced scattering). Measurements conducted at ICube used an independently characterized PDMS phantom, herein referred to as R1, having μ_a and μ_s' equal to 0.117 cm^{-1} and 10.8 cm^{-1}, respectively. Note that this phantom was also the one used for calibration of the SFDI system.

Optical properties were estimated by searching the best fit between MC-based modeled reflectance and measured data, as described in Sec. 2.3.2.3. For this study, the following merit function was considered:

$$\hat{E}_4(\mu_a, \mu_s') = \sqrt{\sum_{\rho} \left(R_{th}(\mu_a, \mu_s', \rho) - R_{meas}(\mu_a, \mu_s', \rho)\right)^2 / \left(R_{meas}(\mu_a, \mu_s', \rho)\right)^2} \qquad (3\text{-}1)$$

In order to ensure stability of the fitting procedure, calculation of the merit function was done over the entire LUT in a first step. In a second step, the fminsearch routine of Matlab

was used to find the best fit between theoretical and measured data within ±15% of the obtained properties from the first step. Interpolation of the LUT in the μ_a and μ_s' directions was used in the second fitting process. Note that only SDS lower than 3 mm were considered due to insufficient SNR at longer distances for highly scattering and absorbing phantoms.

3.2.3 Results

3.2.3.1 Validation of the experimental setup

In order to validate the measurement setup described in Fig. 3-10, the reproducibility of pressure applied on phantoms was evaluated. Consecutive diffuse reflectance acquisitions were made at the same position on the surface of phantom B1, while pressure was released and applied again between measurements. Fig. 3-11 shows the deviation between measurements as a function of SDS. Measured signals were reproduced within ±0.2% of the mean value for all sources and SDS.

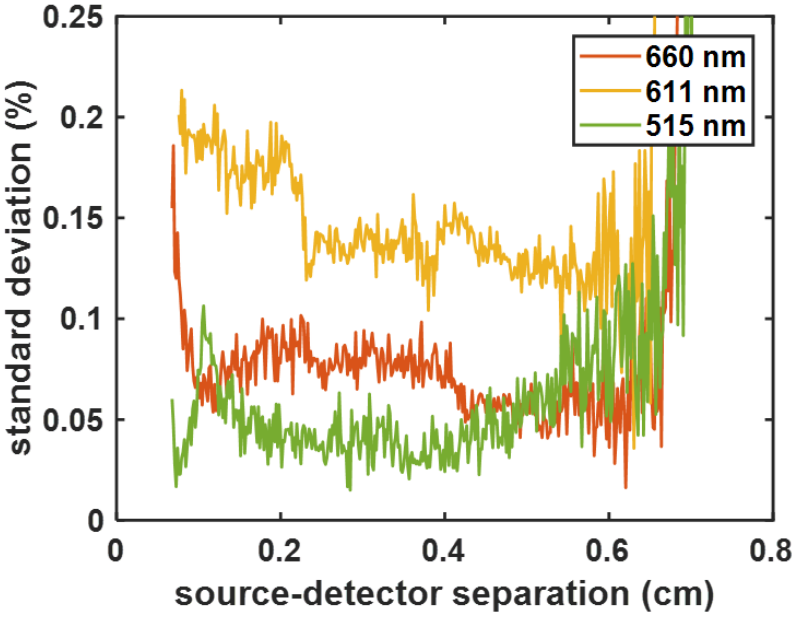


Fig. 3-11 Reproducibility of the pressure applied on phantoms: diffuse reflectance profiles. 5 consecutive acquisitions were made at the same position on the phantom surface. Standard deviations between measured reflectance at the three wavelengths are shown as a function of SDS.

The difference in estimated optical properties between measurements was also evaluated (Fig. 3-12). Deviations lower than 0.5% from the mean value were observed for both μ_a and μ_s', validating the repeatability of pressure applied on phantoms.

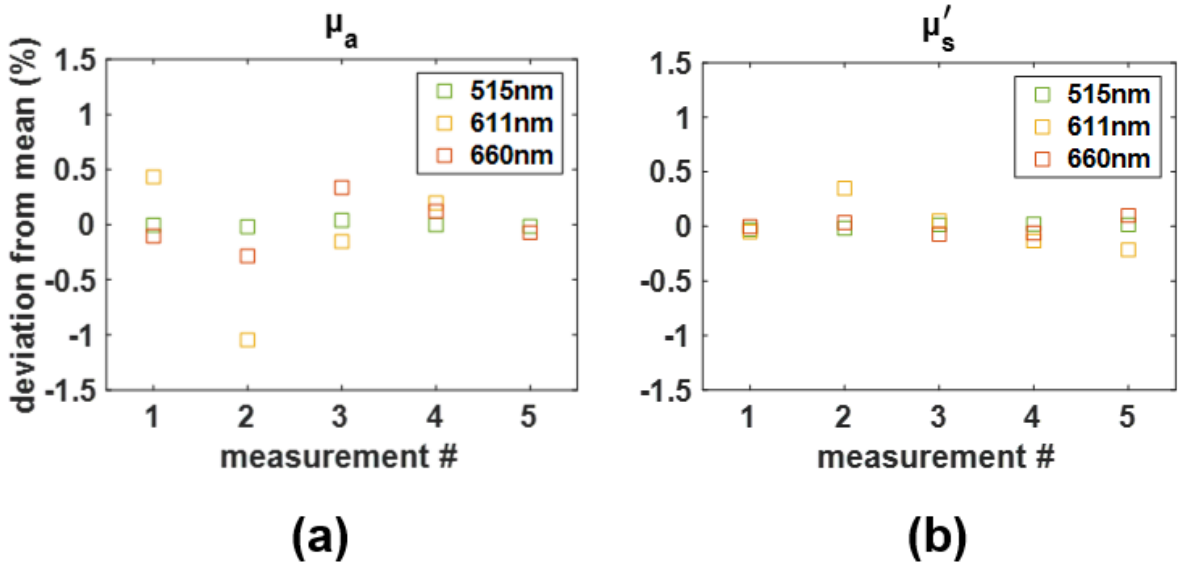


Fig. 3-12 Reproducibility of the pressure applied on phantoms: optical property estimates. 5 consecutive acquisitions were made at the same position on the phantom surface. Standard deviations between measured absorption (a) and scattering (b) coefficients at the three wavelengths are provided.

The impact of the pressure level on measured signals was also investigated. This was notably necessary because of the difference in thickness between phantoms fabricated at CEA and ICube (±5 mm). Several authors demonstrated that the pressure applied by a contact imaging system on tissue during *in vivo* acquisitions has significant impact on measured properties.[170] Although PDMS phantoms exhibit a higher rigidity than skin, the effect of pressure may also have an impact on the optical coupling between the srDRS device and phantoms, and therefore should be quantified. In our setup, the pressure level was determined by the height of the fixed wedge, which was used for positioning of the srDRS device (see Fig. 3-10). Five measurements were made on phantoms B1 and B4. The device was placed at the same position on the phantom surface for all measurements, while the height of the wedge was varied across a 15 mm range centered on the initial position, referred to as P0 (i.e. the one used in all other measurements reported here). Comparison between measured reflectance for different positions of the wedge, and thereby pressure levels, is provided in Fig. 3-13. Observed deviations from P0 remained lower than 1% for all SDS considered for optical properties measurement (below 3 mm). Minor differences were observed in the corresponding measured optical properties (Fig. 3-14).

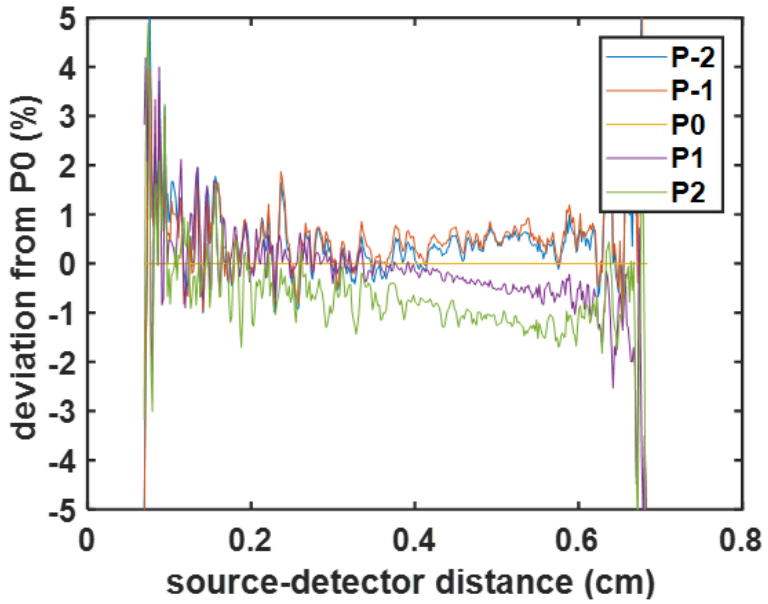


Fig. 3-13 Influence of the wedge position on measured reflectance. Five different wedge heights, referred to as P-2, P-1, P0, P1 and P2, were used. The positions were equally spaced between the maximum (P-2) and minimum (P2) height, corresponding to the lowest and highest pressure levels, respectively. Position P0 is the medium height used for all other measurements reported here.

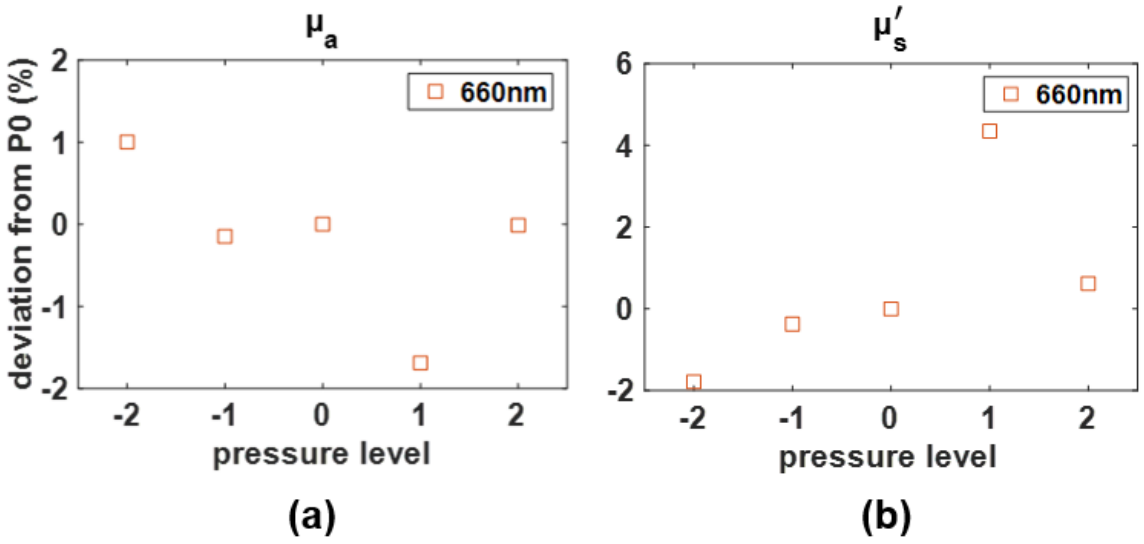


Fig. 3-14 Influence of the wedge position on measured optical properties. Five different wedge heights, referred to as P-2, P-1, P0, P1 and P2, were used. The positions were equally spaced between the maximum (P-2) and minimum (P2) height, corresponding to the lowest and highest pressure levels, respectively. Position P0 is the medium height used for all other measurements reported here.

3.2.3.2 Quantification of optical properties

An acquisition campaign was conducted on the whole phantom set using the srDRS device for quantitative comparison with optical properties measured by SFDI. Phantom R1

was used as calibration phantom for both systems. Note that all phantom properties were measured on the same day with the srDRS device, while SFDI characterization was conducted progressively up to three months before the srDRS measurement campaigns. We thereby considered that phantom properties had kept stable during that time period. Results are show in Fig. 3-15. Error bars were calculated as the standard deviations between different measurements of the same phantom. Close agreement was obtained between SFDI and srDRS systems for the quantification of reduced scattering coefficients, with a calculated correlation coefficient $R^2 = 0.983$. The average relative error in measured μ_s' was 3.3±3.0%. In comparison, large discrepancies reaching up to 300% were observed in μ_a estimates, potentially indicating the presence of uncorrected systematic errors in srDRS measurements. For a given phantom group, qualitative sensitivity to phantom absorption was obtained, yet estimated μ_a were either over or underestimated depending on phantom groups. In particular, we noticed that the relative error in absorption coefficients was constant for a fixed μ_s', which is especially visible for groups A, B and D. Recall that μ_s' values expected from SFDI were not constant between phantoms of group C (Fig. 3-9), which explains that the previous observation does not hold for this group. Further analysis of the relation between the scattering level of phantoms and the relative error in μ_a is made in Sec. 3.2.3.3.

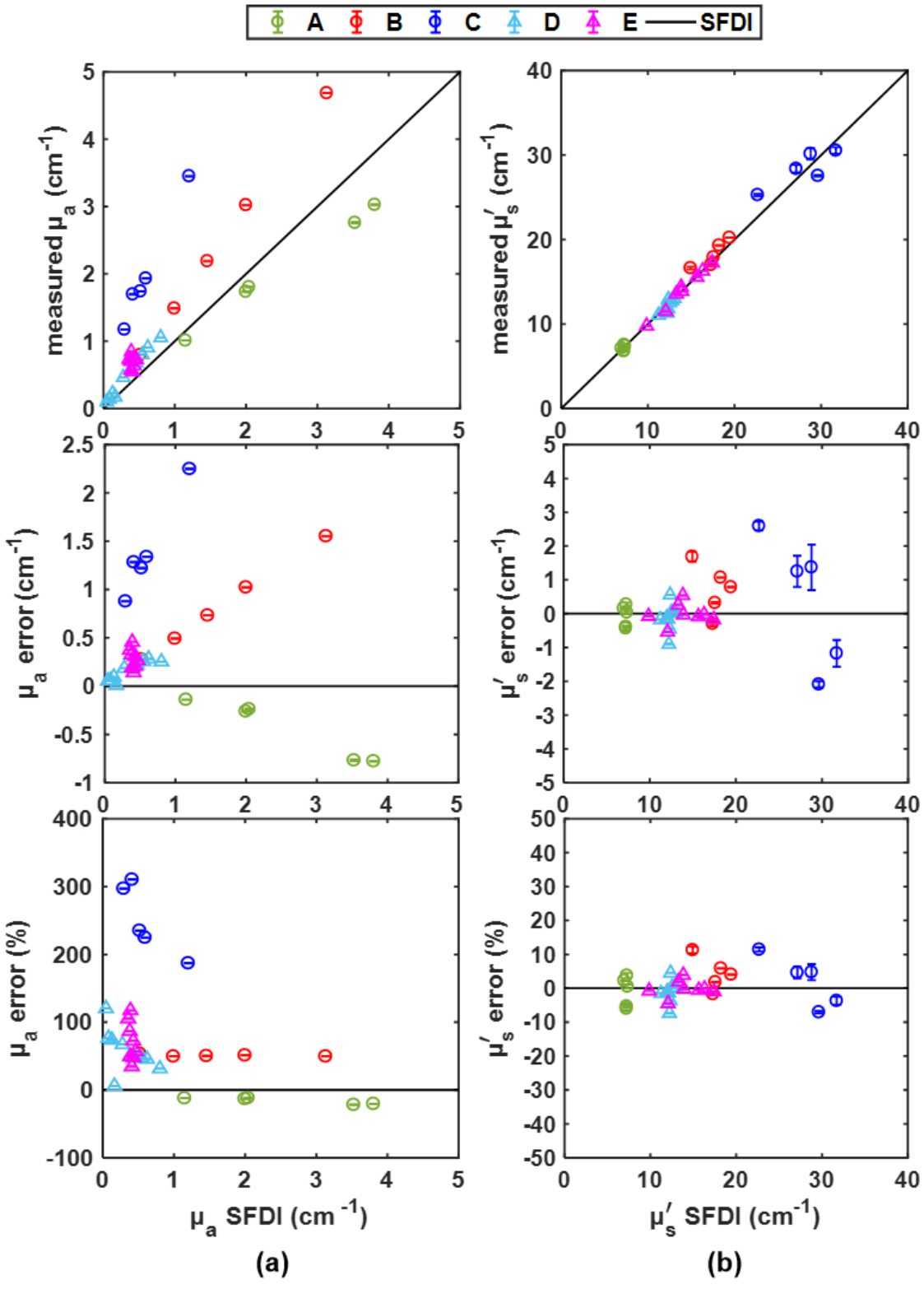


Fig. 3-15 Comparison between optical properties measured with SFDI (black line) and the wearable srDRS system after glass removal. (a) Absorption coefficients. (b) Reduced scattering coefficients. (Top) absolute properties. (Middle) Absolute error. (Bottom) Relative error.

The impact of the considered index coupling condition between the PDMS (having refractive index n = 1.4) and sensor was evaluated. Two conditions were compared, either corresponding to (1) a perfect optical coupling between the PDMS phantom and the FOP (having a refractive index n = 1.5) or (2) the presence of a thin air layer (n = 1) between the phantom and sensor. Corresponding estimates of optical properties are provided in Fig. 3-16. A significant influence of the considered index coupling condition was observed for both optical properties. In particular, condition (1) leads to inaccurate estimation of μ_s' coefficients for highly scattering phantoms. Considering the spatially-dependent sensitivity of the diffuse reflectance to optical properties (see Fig. 2-6), possible errors in the quantification of μ_s' coefficients likely generate errors in measured μ_a. In consequence, condition (2) was used in all calculations of theoretical reflectance. This condition was also preferred as it best corresponds to what should be expected from a physical point of view. Indeed, achieving a perfect optical coupling between the sensor and phantoms was improbable due to the surface rugosity of phantoms.

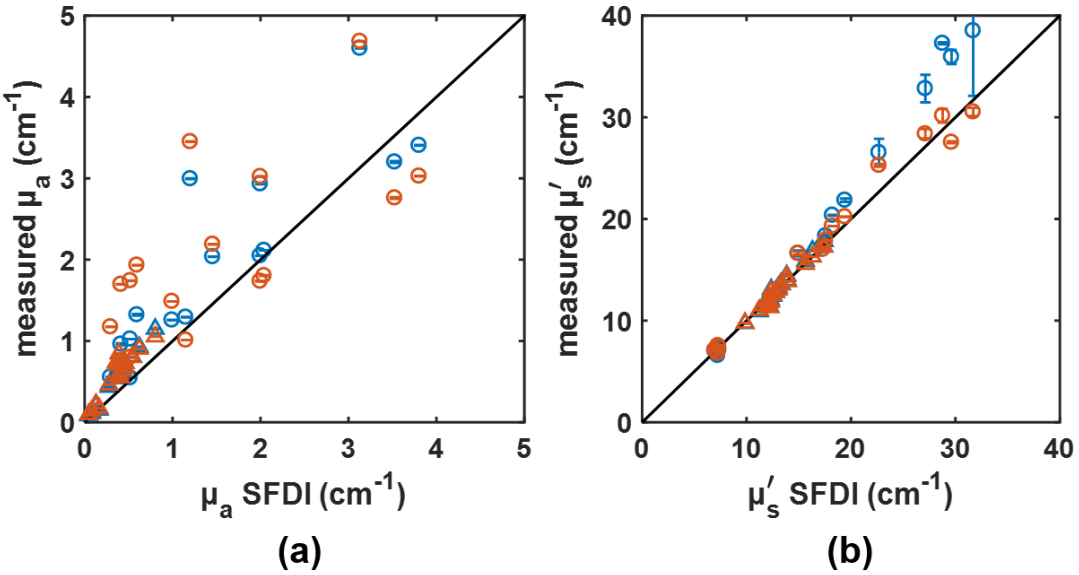


Fig. 3-16 Comparison between two measured absorption (a) and reduced scattering (b) coefficients when considering n = 1 (red) or n = 1.5 (blue) in the exterior medium. The comparison was made on phantoms from groups A, B and C (circles) as well as groups D and E (triangles). Phantom R1 was used for calibration of the instrument.

We considered the possibility that the modifications of the srDRS sensor structure developed in Chapter 2, especially concerning the removal of the protective glass window, might have significant impact on measured properties. Prior to the experiments campaign conducted at ICube on the whole phantom set, srDRS measurements were made on groups A, B and C before and after removal of the glass lid. Note that for this study, phantom B1 was

used for calibration of the system. Estimated properties considering the two sensor structures are shown in Fig. 3-17. Overall, the same disagreement between srDRS and SFDI optical property estimates was observed in both cases. A close match between measured properties before and after removal of the glass window could be seen for groups B and C. However, results show significant discrepancies between the two sensor structures for measured μ_a of group A. For this group, reduced scattering coefficients measured before and after removal of the glass lid did not deviate by more than 1.1 cm^{-1}. Yet, μ_a estimates may show higher sensitivity to measured μ_s' values for low scattering levels, possibly generating larger discrepancies than for other groups. Further acquisitions should be made in future work to conduct an extensive study of the influence of the glass lid on srDRS measurements, which may not be limited to blurring effects.

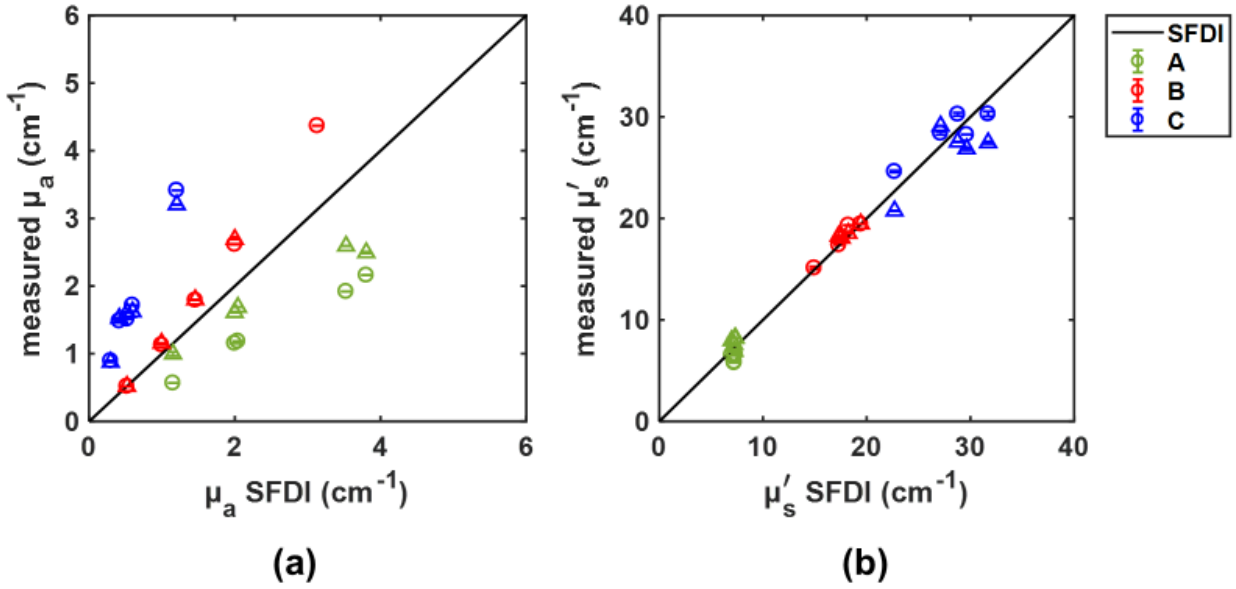


Fig. 3-17 Comparison between optical properties measured with the wearable srDRS device before (upward-pointing triangles) and after (circles) removal of the glass lid. Phantom B1 was used for calibration. Note that phantom B5 was not considered due to poor SNR when employing the srDRS device with glass lid protection.

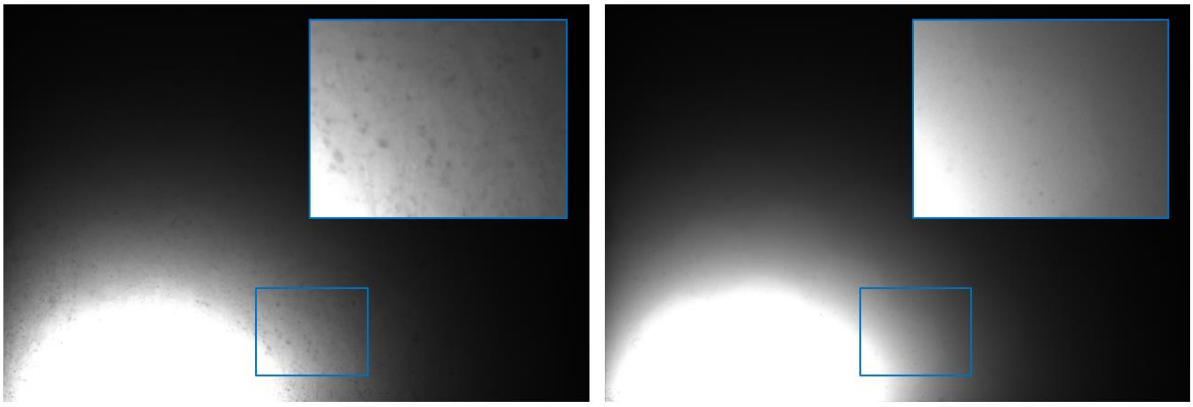


Fig. 3-18 Raw reflectance images of the rough (a) and flat (b) faces of phantom B1.

Additionally, optical properties measured on either the rough or flat face of phantoms were compared. Recall that SFDI measurements were made on the rough surface of phantoms so as to limit specular reflections. In contact srDRS measurements, the surface of the medium induces different optical coupling conditions depending on its rugosity, which may generate errors in measured properties compared to the noncontact modality of SFDI. Besides, aggregates of nigrosin and TiO_2 particles remained due to imperfections of dissolution and mixing processes during phantom fabrication. It is probable that these aggregates migrated toward the rough face of phantoms since this face was molded at the bottom of mixtures. This possibly generated local heterogeneities in phantom properties close to the rough face that were not present on the flat face of phantoms. We determined from binocular microscope observations that these aggregates have a diameter of up to 30 µm for nigrosin and 100 µm for TiO_2. Nigrosin aggregates at the phantom surface are especially visible in images recorded with the wearable srDRS device after removal of the glass lid, as shown in Fig. 3-18. The influence of these heterogeneities, as well as the potential difference in phantom properties between the flat and rough sides due to sedimentation of TiO2 and nigrosin, was thereby investigated. The results are displayed in Fig. 3-19. We observed no major differences (typically less than 10%) between properties measured on different sides of phantoms in comparison with the discrepancies between srDRS and SFDI estimates of absorption coefficients.

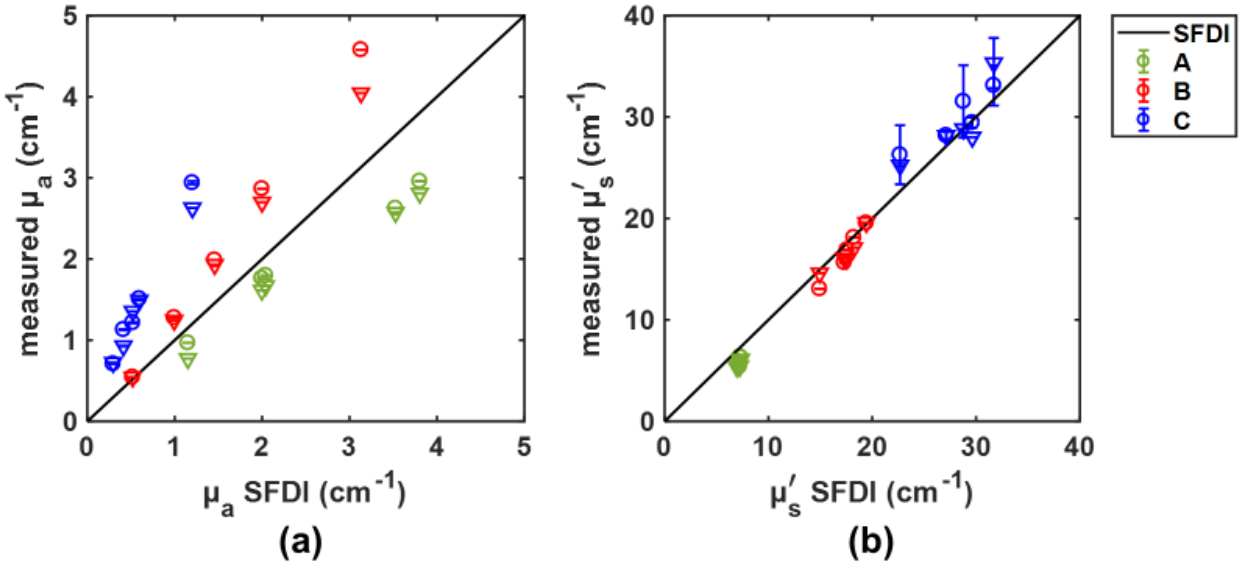


Fig. 3-19 Comparison between measurements performed on the rough (circles) or flat (downward-pointing triangles) surface of phantoms. Phantom B1 was used for calibration of the srDRS device.

3.2.3.3 Scaling of measured absorption coefficients

Fig. 3-15 shows that the relative discrepancy in absorption coefficients measured with the srDRS device and SFDI system was nearly constant for a fixed scattering level of phantoms. Furthermore, results suggest the existence of a linear correlation between observed differences and the scattering coefficient of phantoms, which may be exploited for correction of the measured absorption coefficients. Fig. 3-20 displays the relative error in μ_a as a function of μ_s' estimated by the srDRS device. Linear fitting of this data was performed to extract an empirical scaling relation between initially measured and expected absorption coefficients (Eqs (3-2) and (3-3)). A relatively poor correlation coefficient $R^2 = 0.814$ between measured and fitted data was observed, indicating that measurements were likely affected by other unmodeled biases. However, using the extracted scaling relation on measured μ_a enabled to obtain consistent results between srDRS and SFDI systems for most phantoms. We calculated a correlation coefficient $R^2 = 0.965$ between expected and scaled μ_a, with an average discrepancy of 12.9±14.3%. This scaling method is however sensitive to incorrect estimation of μ_s', which notably explains the remaining large deviations in μ_a for group B, μ_s' estimates being less accurate for this group. Additionally, poor correction of μ_a estimates was obtained at low absorption levels (typically below 0.5 cm^{-1}), for which the linear correlation between relative μ_a errors and measured μ_s' was less evident.

Fig. 3-15 also confirms that errors should be minimal when the scattering coefficients of the calibration phantom and analyzed medium are the same, as has been pointed out by

several authors.[147,151] In fact, the fitted line cuts the horizontal axis close to the μs' value corresponding to the scattering level of the calibration phantom. As a perspective, improvement of the calibration protocol of the developed srDRS systems may be achieved by using a set of multiple calibration phantoms at varying μs'. Alternatively, the proposed scaling method provides a calibration approach based on a single phantom measurement. In future work, its applicability should be established on a larger set of data.

$$a = 11.45; b = -97.03 \tag{3-2}$$

$$\mu_a^{cor} = \frac{\mu_a}{1 + (a \times \mu_s' + b)/100} \tag{3-3}$$

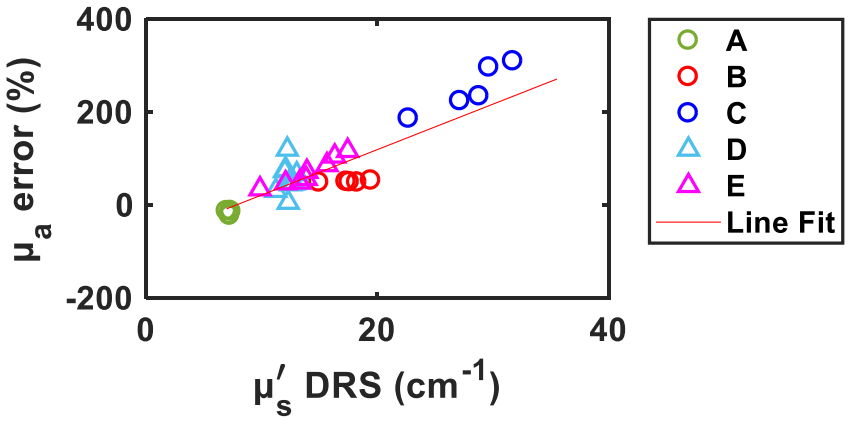


Fig. 3-20 Relation between relative errors in measured μa and reduced scattering coefficients of phantoms. The best linear fit (red line) was calculated.

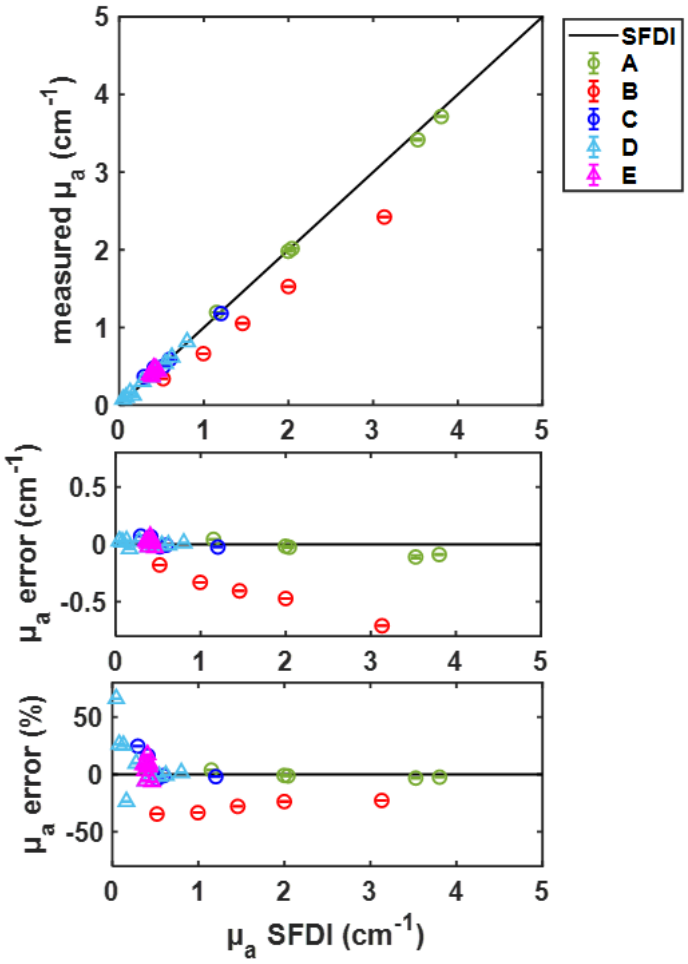


Fig. 3-21 Scaling of absorption coefficients measured with the srDRS device toward expected values. (a) Absolute μ_a. (b) Absolute (top) and relative (bottom) errors between scaled and expected μ_a.

3.2.4 Discussion

Results showed the ability of the wearable srDRS system to provide accurate quantitative μ_s' estimates of tissue-simulating PDMS phantoms characterized by SFDI. Yet, poor correlation was observed between absorption coefficients measured by the two systems, suggesting the existence of important measurement biases that were not accounted for.

Several potential sources of errors have been investigated, including the removal of the glass lid and coupling of the FOP onto the pixels, or the measurement side and surface state of phantoms. For these, no major differences were observed. Comparison between different modeling of sensor-phantom coupling was conducted. Relatively significant differences were observed, highlighting the sensitivity of our method to coupling, notably concerning the measurement of scattering properties. However, none of the proposed approaches provided accurate quantification of phantoms absorption. In future studies, use of a contact gel may be

investigated to ensure control of the sensor-phantom coupling conditions. For this, implementation of the sensor with more robust, antiseptic-resistant materials should be considered.

We noticed that the quantification error in absorption may be related to the difference in scattering levels between the calibration phantom and the analyzed medium, as it was observed in previous studies.[147,151] In order to account for this bias, we analyzed further these discrepancy between SFDI and our system. As a first approximation, a linear modeling of the correlation between relative error in μ_a and μ_s' coefficients of phantoms was considered, which provided the possibility to scale the measured μ_a to the expected values obtained from SFDI. An important decrease in quantification error was observed, yet the poor correlation coefficient between the measured data and linear fit suggests that measurement biases remained that could not be accounted for in this way. Additional experiments should be carried out to confirm the observed trend.

The observed errors were also likely related to limitations of our calibration method. Since instrument calibration was based on a single phantom measurement, instabilities in the calibration measurement may induce large differences in measured optical parameters, especially when considering properties distant from the ones of the calibration phantom (i.e. for high μ_a and μ_s'). Furthermore, the validity of the method depends on accurate characterization of the input beam. In theoretical reflectance calculations, simplifications were made. Notably, the fiber bundle hexagonal geometry and presence of the surrounding reflective needle were not modeled.

Several authors proposed the use of multiple reference phantoms to increase the robustness of instrument calibration and accuracy of measured optical properties.[131,147] Notably, results discussed in Sec. 3.2.3.2 suggest that a set of calibration phantoms with varying μ_s' and constant μ_a (such as group E) may provide a quantification of absorption coefficients consistent with the results obtained from SFDI. Such calibration protocol could be further simplified by exploiting the empirical scaling relation derived in Sec. 3.2.3.3, for which a single calibration phantom measurement is needed. However, derivation of the scaling relation on an extended data set would be necessary to validate this approach. Alternatively, use of a calibration phantom measurement for calculation of the Fourier domain instrument response function (IRF) could be intended, with subsequent deconvolution of measured data. This method may constitute a more robust approach, notably because it compensates for imperfections in the modeling of source beam geometry or

blurring effects. The possibility of applying this approach was investigated by deriving the Fourier domain IRF of the srDRS device from measurements on PDMS phantoms having different scattering levels. Measured IRFs showed large discrepancies, especially at low spatial frequencies (data not shown), which are most sensitive to μ_a.[167] We thereby concluded that possible sources of errors remained which could not be accounted for using such approach.

Limitations of the developed srDRS device in terms of accessible SDS range should also be discussed. Accurate quantification of optical properties requires that the diffuse reflectance be detected at short SDS, as it has been pointed out in Chapter 2. In the present study, only SDS larger than 690 µm could be exploited, possibly generating errors in optical property measurements. The access to shorter SDS was notably limited by the use of a bundle instead of a single fiber to achieve sufficiently efficient optical coupling with the LED source, the necessity of inserting this bundle into a metallic needle and the presence of chamfering (having a thickness of 90 microns) on FOP sides. In order to overcome these limitations, further optimization of the sensor architecture to integrate sources in closer proximity to the imaging area may be intended.

Finally, our study lies upon the characterization of phantom properties by SFDI to validate the performance of the developed srDRS device. However, concerns might be raised by intrinsic differences between the two approaches. Notably, SFDI measurements were based on the use of two spatial frequencies (0 and 0.2 cm^{-1}), possibly leading to inconsistent sensitivity to optical parameters compared with the high resolution imaging method of the srDRS device. Furthermore, quantitative comparison between the contact imaging modality of srDRS and remote imaging approach of SFDI might be hindered by potential effects of sensor-phantom coupling. Additionally, the sensitivity of SFDI to specular reflections, possibly leading to incorrect separation of volume and surface scattering, should be considered.[168]

The present study is overall limited by the current lack of universal referencing procedure of phantom properties, which is why further characterization of these properties using a time-resolved DRS system has been engaged by co-workers at Politecnico di Milano (Milan, Italy).

3.3 Conclusion

The srDRS sensor architecture specified in Chapter 2 was implemented into a wearable, high resolution contact imaging system for measurements of tissue optical properties *in vivo*. In order to overcome the limitations of the previously developed prototype concerning blurring in images, removal of the sensor protective glass window and permanent bonding of the fiber-optic plate with pixels were performed. With this optimized implementation, the spatial resolution of imaging was increased by a factor of 50, enabling the detection of details as sharp as 9.8 µm and thereby providing a high potential for the analysis of layered media. The performance of the system for quantitative characterization of the optical properties of solid homogeneous media was evaluated. In order to conduct this study, a protocol for the manufacturing of PDMS phantoms was developed in collaboration with the laboratoire ICube in Strasbourg. Reference optical properties of these phantoms at 665 nm were obtained from a Spatial Frequency Domain Imaging system developed at ICube and compared with the properties measured using the srDRS prototype at 660 Snm. Results demonstrate the ability of the srDRS device to accurately determine the reduced scattering coefficient of phantoms, with an average error of 3.3±3.0%. However, measured absorption coefficients showed large discrepancies between instruments, possibly indicating the presence of uncorrected systematic errors in srDRS measurements. By noticing a clear correlation between observed errors and scattering levels of phantoms, a scaling relation for correction of measured absorption coefficients was proposed. This empirical calibration method solely relies on srDRS readings and may be used without a priori knowledge of phantom scattering properties. Scaled absorption coefficients showed dramatically improved agreement with expected values, with an average discrepancy of 12.9±14.3% between instruments. Extended studies should be performed for further validation of the system combined with the proposed scaling method, as well as improvement of our calibration protocol.

Chapter 4

Low-cost, wearable srDRS system for skin condition diagnosis: evaluation for *in vivo* tissue oxygenation monitoring

In this chapter, we investigate the potential of our approach for the continuous monitoring of tissue oxygenation toward post-operative assessment of superficial flaps viability. *In vivo* comparative experiments are conducted using the wearable srDRS system presented in Chapter 3 and a real-time SFDI acquisition method, referred to as SSOP (for Single Snapshot of Optical Properties), developed at ICube. The SSOP method has been described in detail by Vervandier et al.[171] Sec. 4.1 provides a brief introduction to the problematic of free tissue transfer. Then, experiments performed with the wearable srDRS device and the SSOP method are described (Sec. 4.2). Finally, results are presented and the potential our approach for the assessment of free flaps viability is discussed (Secs. 4.3 and 4.4).

4.1 Introduction

First introduced in the late 1950s,[172] free tissue transfer is today a common procedure for reconstructive surgery after trauma or cancer. This technique consists in the removal of a tissue portion from a healthy donor site and transfer of this tissue onto an injured receiver site for reconstruction purposes. Survival of the flap lies upon efficient anastomosis of the blood vessels to provide the necessary oxygen and nutrients to the tissue. Although the reliability of free flap surgery has improved over the years, with success rates exceeding 95% in recent reviews,[173,174] vascular occlusion remains a significant risk (6-25% of skin flaps[175,176]). In this eventuality, survival of the compromised flap depends on early detection of the microvascular disorder in order to attempt surgical salvaging procedure with high chances of success. The first 48h of postoperative recovery (corresponding to the interval in which thrombosis happens for 80% of patients[177]) are the most critical and require regular monitoring of the flap viability to maximize the probability of successful flap salvaging.[178] Late detection of flap thrombosis implies a return to the operation room, leading to increased morbidity, recovery time and cost.

Current methods for the monitoring of flaps viability have been reviewed by Smit et al.[179] The most standard of care include clinical assessment of skin color, turgor and temperature. Skin color and turgor assessments are commonly achieved by visual observation and palpation, making them dependent on the experience and subjectivity of the clinician. Another important shortcoming of this approach is its poor reliability when considering superficial flaps with darker skin tones, for which successful and compromised flaps show similar aspects. Alternatively, temperature assessment of the flap is possible but is sensitive

to uncontrolled temperature room, heat produced by the sensor, motion and positioning of the thermometer. These methods however have the advantage to be inexpensive and non-invasive.

Near Infrared Spectroscopy (NIRS) has been well established as an efficient tool to monitor the viability of flaps in both per and post-operative periods.[180] The technique relies on the spectral dependence of light attenuation in the medium to measure the tissue oxygen saturation (StO_2), which is accepted as a relevant metrics to assess the viability of tissue in the region of measurements. NIRS provides quantitative information about the tissue status with high reliability compared to standard techniques and is able to detect flap failure prior to the onset of conventional clinical signs. Another critical advantage is that NIRS is adequate for both superficial and buried flaps monitoring up to 20 mm in depth. However, NIRS still has several limitations, notably related to elevated costs (~20 000$ for current commercial systems) and concerns about the reliability of oxygenation readings in dark pigmented skin.[181]

Current research activities notably concern the reduction of the cost and footprint of NIRS systems to facilitate their use in clinical routine as well as the development of hardware and software tools to provide consistent readings among different phenotypes (age, gender, pigmentation).[182–187] We believe that our approach has significant potential to address these issues. The basic architecture proposed in Chapter 2 may be implemented into low-cost, compact systems providing passive oxygenation monitoring at a high rate and without intervention of the medical staff, thereby optimizing the chances of flap survival while reducing costs and impact on the hospital workflow. Most current wearable sensors measure the pulsed oxygen saturation (SpO_2), which is representative only of the arterial oxygenation. Conversely, a system based on our approach may be sensitive to the total oxygenation of tissue, and thereby provide more reliable identification of the origin of flap failure. Moreover, the high resolution of imaging provided by a multi-pixel sensor may be exploited to address the layer specific tissue analysis, with a potential to correct oxygenation readings from the influence of epidermal pigmentation.

4.2 Materials and methods

4.2.1 Experiments

In order to evaluate the sensitivity of the device to tissue oxygenation changes, an arm cuff occlusion protocol was conducted, as proposed in several studies.[93,188,189] A five minutes venous occlusion of the left arm of a healthy volunteer was performed using an arm cuff set at 80 mmHg pressure. Continuous monitoring of tissue optical properties was carried out on the volar forearm using the srDRS and SSOP systems simultaneously. The volunteer was asked to stay still during the whole procedure, with the arm laid on an optical table in the Field-OF-View (FOV) of the SSOP system. Control of the acquisitions as well as manual pumping and release of the arm cuff were ensured by a secondary operator.

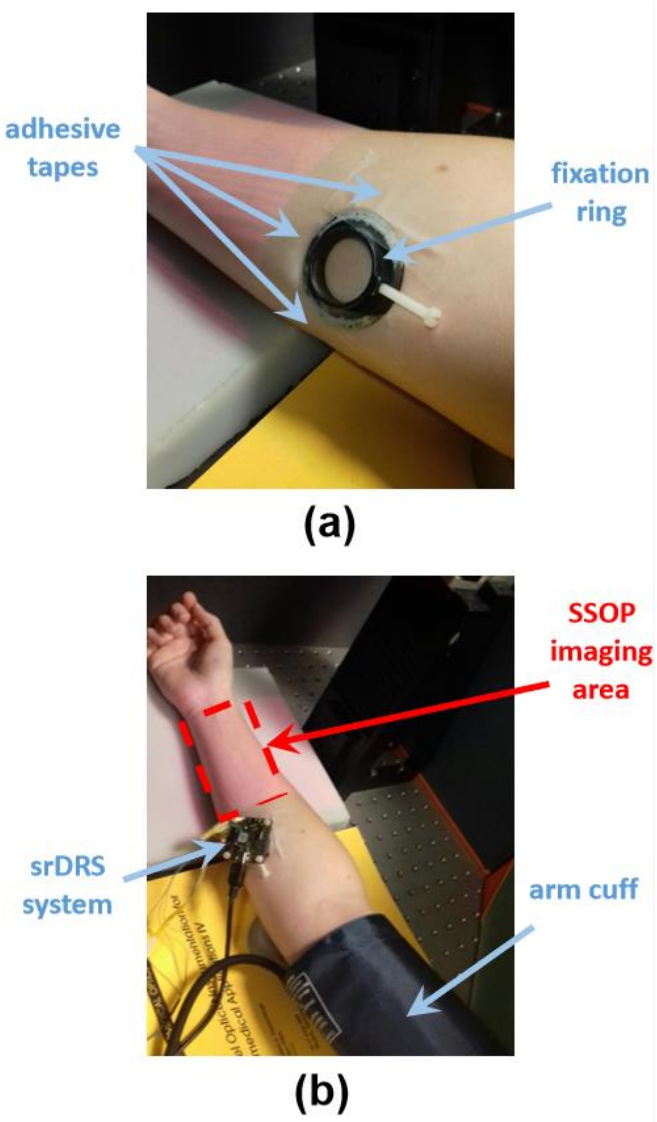


Fig. 4-1 *In vivo* oxygenation measurement. The arm of a healthy volunteer was placed in the FOV of the SSOP system (dotted rectangle). The wearable srDRS system was positioned on the inner forearm outside of the SSOP illumination field to avoid parasite light signals. Attachment of the srDRS system on the arm was performed using a fixation ring and medical adhesive tapes.

Continuous measurement of tissue optical properties was performed using the srDRS device and the SSOP system throughout the occlusion. Diffuse reflectance acquisitions were carried out for about 20 min, starting 6 min before the beginning of the occlusion (*baseline*) and going on for another 6 min after release of pressure (*recovery*).

The srDRS system was placed on the inner forearm of the volunteer using the fixation ring described in Sec. 3.1.1.1. The ring was first placed on the tissue surface (Fig. 4-1(a)). Standard medical adhesive tapes provided a strong attachment of the fixation ring. The srDRS device was then inserted through the ring and set with a screw to ensure a stable level of pressure applied to the tissue during the experiment (Fig. 4-1(b)). Note that the srDRS

system had to be placed away from the SSOP imaging area (about 5 cm) to avoid perturbations caused by the SSOP illumination.

Acquisitions were controlled via a LabVIEW interface. Immediately before the experiment, preparation of the acquisition settings (including LED currents and exposure time sequences) was done by the operator with the device attached to the volunteer. Upon starting the experiment by the operator, automated diffuse reflectance acquisitions were continuously repeated at three wavelengths (515, 611 and 660 nm). Note that only the sources with vertical illumination were used. Sources were turned on sequentially, starting with the 515 nm LED and ending with the 660 nm LED. For each LED, consecutive images were recorded using two exposure times (typically ranging from 1 to 100 ms depending on the considered LED) for SNR optimization. Using this procedure, three wavelengths diffuse reflectance acquisitions were made every 14 s.

Immediately after the experiment, measurements were performed on phantom R1 for calibration of the device. Additionally, a Lambertian flat-field image was recorded using the methodology described in Sec. 3.1.2 for later use in data processing.

4.2.2 Data processing

4.2.2.1 Extraction of optical properties

Processing of diffuse reflectance images recorded by the srDRS system followed the steps detailed in Sec. 3.2.2.2.

Calibration of the srDRS device followed the approach described in Sec. 2.3.2.3. Absorption and reduced scattering coefficients of phantom R1 were only available at 665 and 860 nm. In order to calibrate the srDRS device, properties of this phantom were extrapolated to 660, 611 and 515 nm.

Scattering spectra of TiO2-based PDMS phantoms have been measured by several authors, showing a nearly linear behavior in the [500-900] nm range.[162,165,166] Therefore, linear extrapolation using the values of μ_s' available at 665 and 860 nm was used to calculate the reduced scattering coefficient of the calibration phantom at 511, 615 and 660 nm.

Extrapolation of μ_a coefficients was based on spectra measured with a srDRS fiber-optic probe previously developed at CEA.[89] This approach was preferred to transmission spectrophotometry measurements in nigrosin alcoholic solutions (Ng-EtOH), notably because the latter does not take account on possible changes occurring upon mixing of Ng-EtOH

solutions with PDMS and TiO2. Diffuse reflectance spectra were acquired on a PDMS phantom and scaled to the absorption coefficient of phantom R1 available at 665 nm. Note that probe measurements were made on phantom B1 because of its relatively close properties to the ones of phantom R1 (which was not available at CEA). The measured spectrum was then scaled to the absorption coefficient of phantom R1 at 665 nm using Eq. (4-1):

$$\mu_{a,extrap}(\lambda) = \mu_{a,ref}(665\ nm) \times \left(1 + \frac{\mu_{a,probe}(\lambda) - \mu_{a,probe}(665\ nm)}{\mu_{a,probe}(665\ nm))}\right) \qquad (4\text{-}1)$$

where $\mu_{a,ref}$ is the known absorption coefficient of the calibration phantom at 665 nm (μ_a = 0.117 cm^{-1}), $\mu_{a,probe}$ is the absorption coefficient of phantom B1 as measured by the fiber-optic probe and $\mu_{a,extrap}$ is the extrapolated absorption coefficient of phantom R1. The extrapolated spectrum is shown in Fig. 4-2. Values of extrapolated μ_a and μ_s' of the calibration phantom are provided in Tab. 4-1.

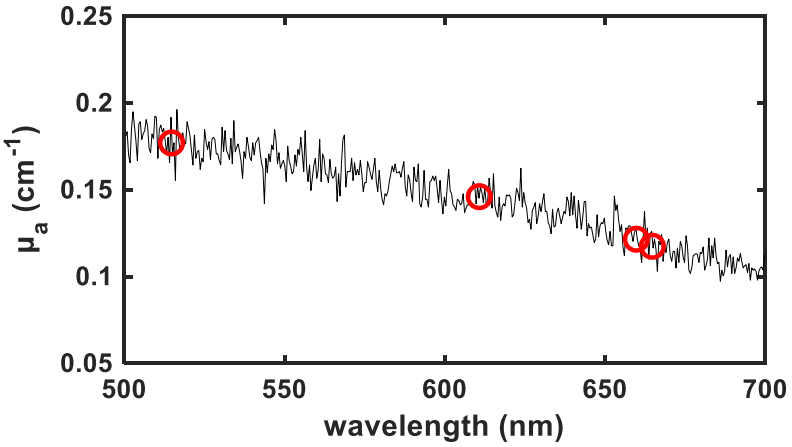


Fig. 4-2 Extrapolation of the calibration phantom absorption coefficient. The black line is the extrapolated absorption spectrum obtained from srDRS fiber-optic probe measurements. Extrapolated μ_a at 515nm, 611nm and 660nm are displayed as red circles along with the known μ_a at 665 nm.

Wavelength (nm)	**515**	**611**	**660**	**665**	**860**
$\boldsymbol{\mu_a(cm^{-1})}$	0.172	0.151	0.123	0.117	0.207
$\boldsymbol{\mu_s'(cm^{-1})}$	13.15	11.66	10.90	10.83	7.80

Tab. 4-1 Properties of the calibration phantom (R1). Properties at 515, 611 and 660 nm were calculated from linear extrapolation for μ_s' and fiber-optic probe measurements for μ_a.

Using the methodology described in Sec. 2.3.2.3, diffuse reflectance measurements on the calibration phantom at 515, 611 and 660 nm were used to calculate the corresponding scaling factors between measured and theoretical profiles. Note that the same LUT was employed for

calibration of the instrument and extraction of skin optical properties, with n=1.4 and g=0.8, as was done for SSOP.

4.2.2.2 Derivation of the tissue oxygen saturation (StO_2)

The measured spectrally resolved optical properties were exploited to measure the relative concentration of oxy and deoxygenated blood in tissue, which is represented by the tissue oxygen saturation (StO_2) according to the following relation:

$$S = \frac{C_{oxy}}{C_{oxy} + C_{deoxy}} = \frac{C_{oxy}}{C_{blood}} \tag{4-2}$$

where S, C_{oxy}, C_{deoxy} and C_{blood} are the StO_2 and concentrations of oxy, deoxy and total blood concentration, respectively. Note that the contribution of other hemoglobin species such as carboxyhemoglobin and methemoglobin has been neglected. Considering only the contribution of blood to skin absorption, the absorption coefficient μ_a of the tissue is expressed as:[9]

$$\mu_a(\lambda) = S \times \mu_{a,oxy}(\lambda) + (1 - S) \times \mu_{a,deoxy}(\lambda) \tag{4-3}$$

with

$$\mu_{a,oxy}(\lambda) = \ln(10)\, C_{blood} \times \varepsilon_{oxy}(\lambda) \tag{4-4}$$

$$\mu_{a,deoxy}(\lambda) = \ln(10)\, C_{blood} \times \varepsilon_{deoxy}(\lambda) \tag{4-5}$$

In Eqs. (4-4) and (4-5), ε_{oxy} and ε_{deoxy} are the tabulated molar extinction coefficients of oxy and deoxyhemoglobin.[190]

Using Eq. (4-3), the tissue oxygenation saturation can be derived from a simple formula based on the difference between absorption coefficients measured at two wavelengths λ_1 and λ_2:

$$S = \frac{\Delta\mu_a - \Delta\mu_{a,deoxy}}{\Delta\mu_{a,oxy} - \Delta\mu_{a,deoxy}} \tag{4-6}$$

Where the operator Δ applies the difference between the considered absorption coefficient at wavelengths λ_1 and λ_2. Absorption coefficients measured by the srDRS device and SSOP method were used to calculate the tissue oxygenation saturation throughout the occlusion. For SSOP, Eq. (4-6) was employed with the measured skin absorption at 665 and 860 nm. For srDRS, absorption coefficients measured at 611 and 660 nm were considered.

A blood volume fraction B of 4% was assumed, in close agreement with values reported by other authors.[191,192] Considering an average mass concentration of hemoglobin in blood of 150 g.L^{-1}, the corresponding blood concentration C_{blood} was equal to 93 µM.[9]

4.3 Results

4.3.1 Measurement repeatability

In order to estimate the repeatability of srDRS measurements *in vivo*, consecutive acquisitions were made on the volar forearm of a volunteer. Between acquisitions, the srDRS device was removed and inserted back in the fixation ring. In order to isolate the effect of the contact between the skin and sensor, the position of the fixation ring was not modified. Results are shown in Fig. 4-3 and Fig. 4-4. The standard deviation between measured reflectance signals did not exceed 3% of the average value over the SDS range considered for optical property calculations. Measured optical properties were however sensitive to different placements of the sensor. The calculated standard deviation between measured optical properties reached 16.6% of the mean value (0.157 cm^{-1}) for μ_a and 2.8% of the mean value (18.7 cm^{-1}) for μ_s'.

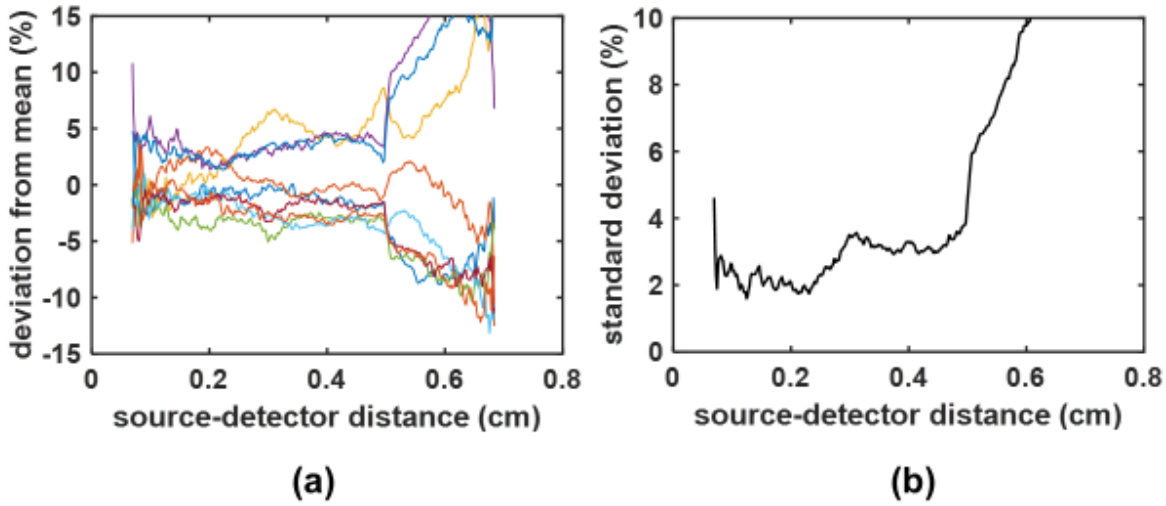


Fig. 4-3 Repeatability of reflectance profiles measured at 660nm. Nine consecutive reflectance measurements were performed. Between measurements, the srDRS device was removed and placed again in the fixation ring. The position of the fixation ring on tissue did not change between acquisitions. (a) Deviation of reflectance signals from the mean value (one color per measurement). (b) Standard deviation between measurements.

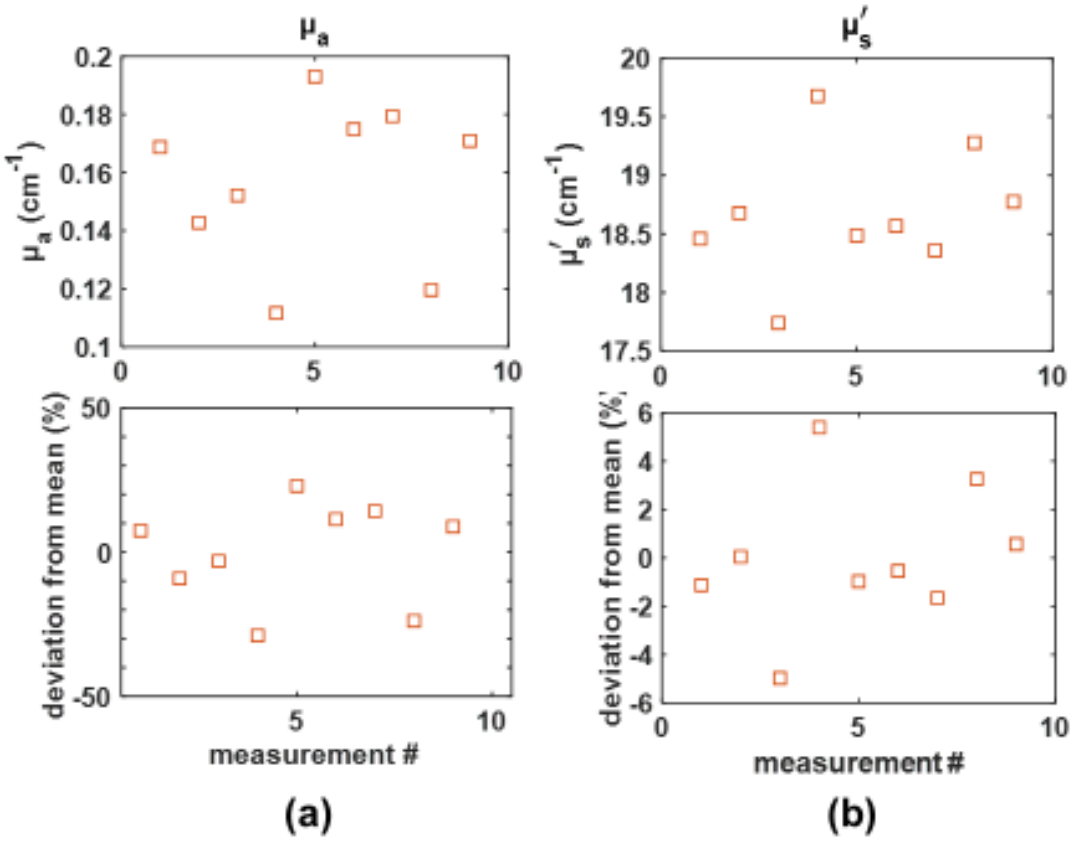


Fig. 4-4 Repeatability of (a) absorption and (b) reduced scattering coefficients measured at 660 nm. Optical properties of tissue were calculated from nine consecutive reflectance measurements were performed. Between measurements, the srDRS device was removed and placed again in the fixation ring. The position of the fixation ring on tissue did not change between acquisitions. Deviation of measured properties from the mean value are provided in (top) absolute and (bottom) relative unit. Phantom R1 was used for calibration of the device.

4.3.2 Optical properties

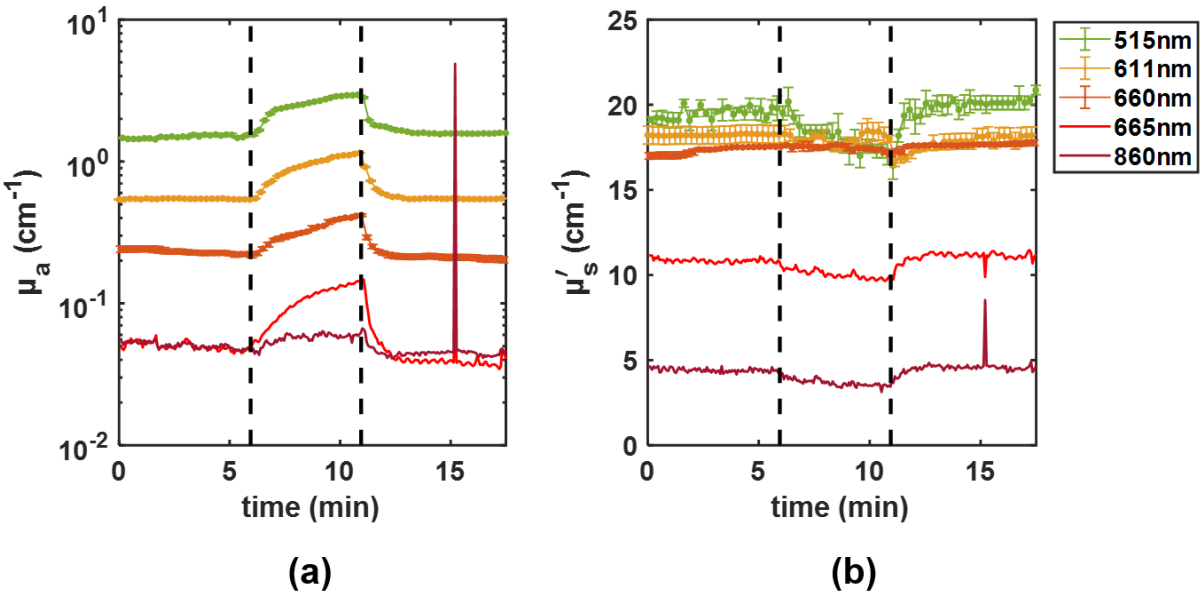


Fig. 4-5 Measured absorption (a) and reduced scattering (b) coefficients. Error bars correspond to standard deviations between properties calculated from different calibration phantom measurements.

Absorption and reduced scattering coefficients measured by the srDRS system and the SSOP method during the occlusion experiment are displayed in Fig. 4-5 and Fig. 4-6. Two-dimensional maps of optical properties were obtained from SSOP. SSOP absorption and reduced scattering coefficients were averaged over a small Region-Of-Interest (ROI) located close to the upper arm and away from most visible heterogeneities, notably veins (see Fig. 4-7). The expected progressive increase in absorption during cuff occlusion was detected at all wavelengths, with a fast return to the baseline values upon cuff release. Oppositely, measured reduced scattering coefficients remained overall stable during the whole experiment, with minor changes (less than 10%) observed during the occlusion.

Results show important inconsistencies between the srDRS and SSOP data at 660 and 665 nm, respectively. The srDRS system typically overestimated the absorption of the medium compared to SSOP, as was observed in phantom experiments (Sec. 3.2), with baseline values of 0.23 cm^{-1} for srDRS and 0.05 cm^{-1} for SSOP. Over the whole FOV of SSOP baseline images (Fig. 4-7) measured μ_a typically varied between 0.01 cm^{-1} to 0.1 cm^{-1} depending on the ROI. After applying the scaling formula derived in Sec. 3.2.3.3 to measured μ_a, a closer agreement was observed between SSOP and srDRS results, the absorption measured with srDRS falling down to 0.11 cm^{-1}. However, measured μ_s' *in vivo* were significantly different between the srDRS system and SSOP. Although the expected

qualitative dependence of μ_s' to wavelength was observed, scattering properties of the tissue measured by srDRS were strongly overestimated compared to SSOP results, conversely to what was observed in phantom experiments.

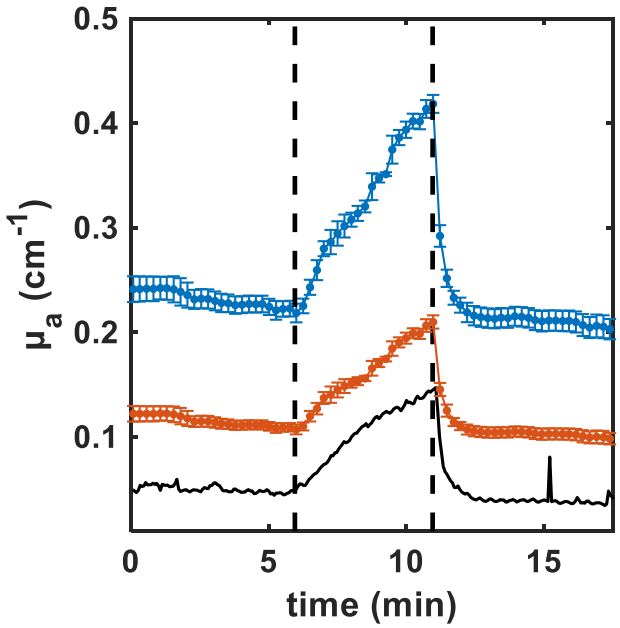


Fig. 4-6 Measured (blue) and scaled (red) μ_a at 660 nm along with the SSOP measurement at 665 nm**.** Error bars correspond to standard deviations between properties calculated from different calibration phantom measurements.

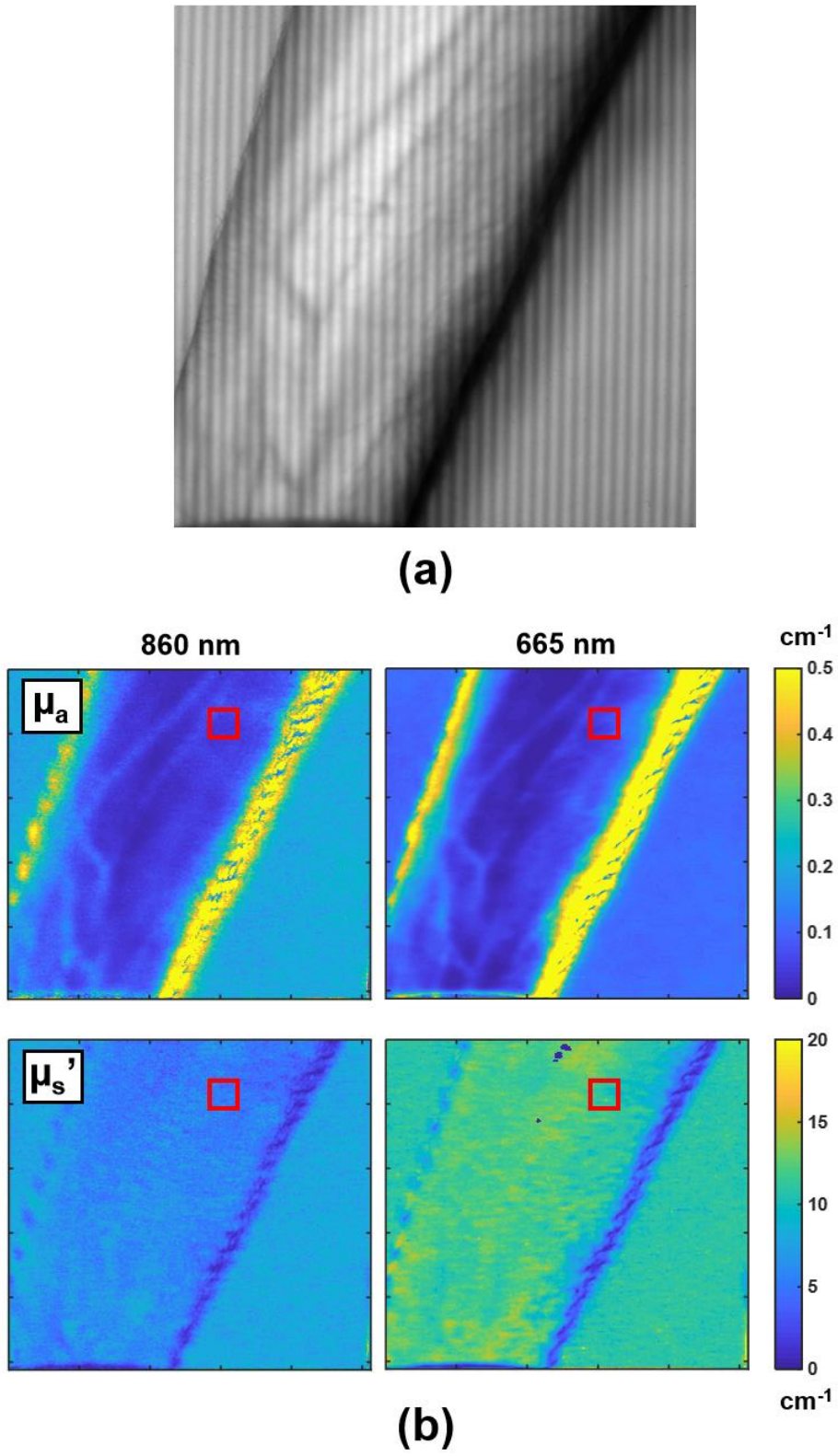


Fig. 4-7 Results from Single Snapshot of Optical Properties (SSOP) at 665 and 860 nm. (a) SSOP raw image. The forearm of the volunteer was illuminated by a sinusoidal light pattern with 0.2 cm^{-1} spatial frequency. (b) Optical properties maps. μ_a and μ_s' values were averaged over the ROI highlighted by the red rectangles.

4.3.3 Tissue oxygen saturation

Measured μ_a were exploited to derive the tissue oxygen saturation as described in Sec. 4.2.2.2. Results are displayed in Fig. 4-8. The occlusion was efficiently detected by the two instruments, with a smooth decrease of StO_2 throughout the occlusion, and quick return to the baseline value upon cuff release. During baseline and recovery, stable readings were obtained with both srDRS and SSOP. However, a continuous drop of StO_2 was observed in srDRS data, reaching up to 7% (relatively to the initial value) at the end of the acquisition. This small, progressive decrease can be understood from the absorption coefficient readings displayed in Fig. 4-5(a). Indeed, a comparable decrease was observed for absorption at 660nm (up to 16% relative variation), while the signal measured at 611nm remained stable (less than 2% relative variation). Conversely, StO_2 readings obtained from SSOP did not show significant change between baseline and recovery (less than 2% relative variation).

Quantitatively, srDRS and SSOP readings exhibit large differences. A baseline saturation of 74% was measured with SSOP, with a maximum decrease to 62% immediately before cuff release. For srDRS, high saturation levels were observed during baseline and recovery, ranging from 90 to 83%, while a large drop was detected during occlusion, saturation levels falling down to 22%. Both relative and absolute StO_2 changes were dramatically larger than changes observed with SSOP, showing strong disagreement between the devices.

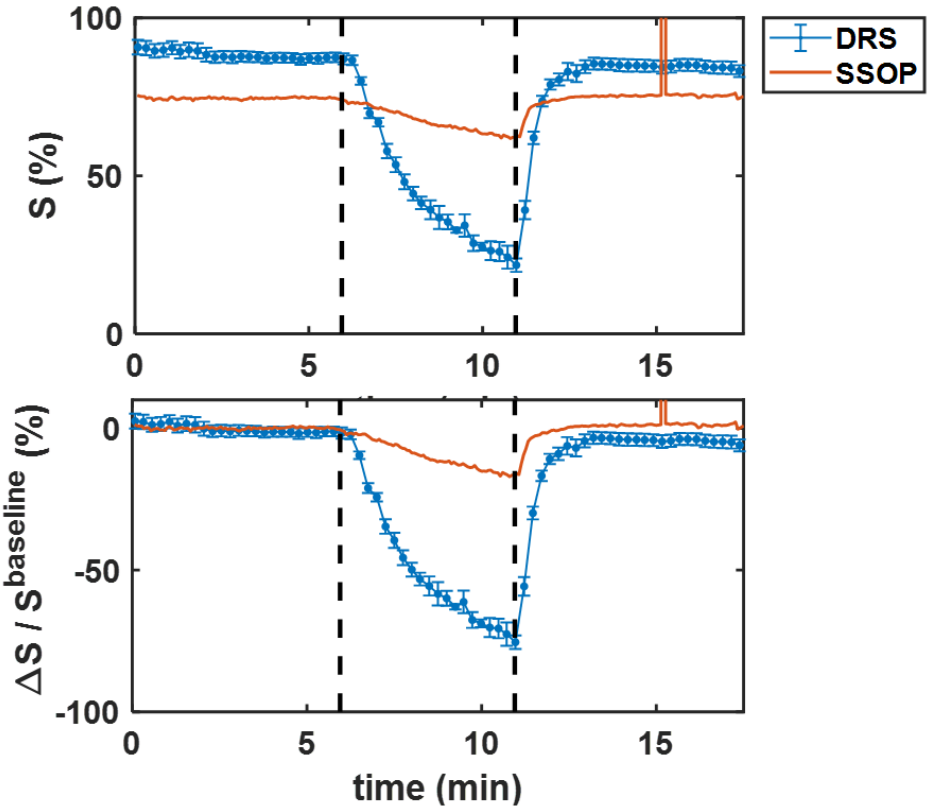


Fig. 4-8 Measured tissue oxygen saturation (StO_2) during the cuff occlusion experiment. Error bars correspond to standard deviations between properties calculated from different calibration phantom measurements. Error bars correspond to the standard deviation between readings obtained using three different measurements of the calibration phantom.

4.4 Discussion

In recent years, the potential of diffuse optical imaging methods to provide physiologically relevant information about the tissue status for diagnosis and therapeutic purposes has been well established. However, the implementation of these techniques into clinical devices remains a challenging task, which is still the object of active research. Translation of a technology into the hospital not only depends on its ability to provide reliable and precise information to the clinician, but also to its potential for efficient integration into the clinical workflow. These requirements have naturally led to the implementation of diffuse optical imaging technologies into handheld or wearable systems based on a contact measurement modalities, facilitating their use in routine clinical practice.[49,60,85,87,88,95,96,127,182–184,193]

In this context, we evaluated the potential of the architecture introduced in Chapter 2 for the monitoring of tissue oxygenation using a wearable contact imaging system. The shortcomings of the contact imaging modality are well-known and principally related to

difficulties in controlling the coupling between the measurement device and tissue and its impact on the measured properties. Notably, several authors reported that measured properties are sensitive to the pressure applied by the sensor on the probed tissue portion due to the induced local changes in the tissue physiology.[170,194,195] The measurement repeatability associated with the developed srDRS device was assessed. Judging by the deviation between optical properties measured upon consecutive removals and placements of the device into the fixation ring, our approach provided a relatively fair reproducibility of measurement conditions. We observed that the estimated reduced scattering coefficient was poorly sensitive to different sensor-tissue couplings. However; measured μ_a varied significantly between measurements. This preliminary study provides an insight of the system's sensitivity to optical properties change in tissue. Further evaluation of the impact of the observed deviations on physiologically relevant parameters should be intended in future work, as well as comparison of these parameters between different body sites.

A comparison between optical properties and tissue oxygenation readings obtained from the developed srDRS device and a reference measurement technique (SSOP) was made by conducting an arm cuff occlusion experiment. Overall, this study demonstrates the ability of the system to provide stable readings *in vivo* and detect qualitative physiological changes. However, large discrepancies were observed between optical properties measured by srDRS and by the SSOP reference system, although estimates from both instruments lie in the range of reported values *in vivo*.[43,59,196–199] Absorption coefficients provided by srDRS were typically overestimated compared to SSOP readings. Using the scaling relation derived in Sec. 3.2.3.3. yielded closer consistency between measured coefficients. Caution should however be taken in further quantitative comparison between measured absorption levels considering the large variation range of μ_a across the SSOP field-of-view. Moreover, effects of contact coupling between the srDRS device and tissue may provoke local changes in tissue properties which are invisible to the noncontact modality of SSOP. Measured scattering coefficients from the two systems showed significant discrepancies as well. These discrepancies may not be explained by the variability of scattering with body site since μ_s' coefficient showed only small variations across SSOP maps. However, quantitative comparison is again made hazardous by the potential effect of contact with tissue.

Reduced scattering coefficients measured by srDRS showed relatively low sensitivity (overall less than 10% changes) to the occlusion compared to the neat change detected in absorption. This may suggest that efficient separation of the contribution of these properties

to measured data was achieved. However, such conclusion should not be made without a more complete validation of the device on controlled media. Although the ability of our system to accurately estimate the reduced scattering coefficients of PDMS phantoms was established at 660 nm, the reliability of μ_s' coefficients measured at 611 nm was not demonstrated. For the same reason, use of the empirical calibration protocol proposed in Sec. 3.2.3.3 to correct the absorption coefficients measured at 611 nm was not intended.

Observed saturation readings demonstrate the ability of the developed srDRS device to detect oxygenation changes in tissue. A low pressure (80 mmHg) arm cuff occlusion was applied on the arm of a healthy volunteer to generate a venous occlusion. The induced smooth saturation decrease was detected by both the srDRS and SSOP systems. Readings obtained from SSOP are consistent with saturation levels observed in previous studies.[42,200] Typical saturation levels reported in these studies fall within the [70-80] % range during baseline, while not falling below 50% during few minutes occlusions, which validates the use of SSOP as a reference instrument in this study. In contrast, saturation levels measured by the srDRS system were different in comparison to the expected values. Potential observed errors in saturation signals are possibly related to the limitations of our system, which have been discussed in Sec. 3.2.4, as well as imperfections of the skin tissue model used in this study. As a preliminary investigation, we chose to use a simple approach for derivation of the tissue saturation based on Eq. (4-6). This equation notably lies upon the assumption that the difference in absorption levels measured at the considered wavelengths ([611; 660] nm for srDRS and [665; 860] nm for SSOP) are exclusively sensitive to the relative concentrations of oxy and deoxygenated blood in tissue, thereby neglecting the possible contribution of background absorption from other molecular species encountered in skin (such as melanin, water, lipids…). Eq. (4-6) holds when the tissue background absorption is either negligible or cancels out in the difference between absorption coefficients measured at the considered wavelengths, making the choice of the source wavelengths critical. Guidelines for optimal wavelengths selection toward tissue hemodynamics measurements have been provided by several authors.[201,202] When employing two sources, wavelengths in the [650-750] nm and [850-950] nm ranges typically provide the best combination for accurate monitoring of tissue oxygenation. However, the selection of sources in our srDRS prototype was primarily motivated by the dimensions and output power of LEDs, as well as low sensitivity of the CMOS camera in the near-infrared domain. Small surface mounted LEDs with a 1608 packaging had be employed to ensure sufficiently close proximity of the illumination center

to the first detection point. This was notably necessary for efficient separation of absorption and scattering influence on measured reflectance profiles, as discussed in Chapter 2. The low availability of LEDs capable of fulfilling this requirement while having sufficient output power and emission wavelength in the [660-850] nm range made the implementation of a fully optimized device difficult. Future work should notably be dedicated to the adaptation of the proposed design to integration of sources with an optimal wavelengths combination. Based on previously published studies,[27,67,93,203] adjustments of our skin model to take account for background absorption by unconsidered molecular species (in particular melanin) having an impact on measured properties may be intended. The development of such model however requires further validation of the system at 611nm and 515nm. Such validation may be carried out through phantom experiments in order to confirm the ability of the device to provide accurate μ_s' estimates at all wavelengths and validate the scaling relation proposed in Chapter 3.

4.5 Conclusion

The potential of our approach for the monitoring of superficial flaps viability during post-operative recovery was evaluated. *In vivo* experiments were conducted on a healthy volunteer to assess the system's performance in terms of repeatability and stability of measured signals as well as sensitivity to physiological changes. A failing flap was emulated by an arm cuff occlusion performed on a healthy volunteer. Optical properties were continuously monitored using the developed srDRS system and a real-time SFDI system used as a reference system. Overall, the ability of the wearable srDRS prototype to provide stable readings upon attachment onto the tissue was demonstrated. Measured properties were however sensitive to different couplings between the sensor and tissue. Average standard deviations between optical properties measured upon different placements of the device were estimated to 16.6% for μ_a and 3% for μ_s'. Signals measured during the occlusion experiment were consistent with the qualitative behavior expected from a venous occlusion. Notably, the progressive decrease in StO_2 upon occlusion and fast return to baseline after pressure release were well detected. However, the srDRS prototype was unable to provide physiologically acceptable saturation readings. Possible reasons for this have been discussed in detail in Sec. 4.4. These may essentially be related to imperfections of the device and calibration protocol. Perspective studies should focus on the modification of the proposed sensor design toward the integration

of an optimized set of sources and better controlled sensor-tissue coupling conditions through the identification of an adequate contact gel and sensor packaging material.

Chapter 5

Summary of results and future directions

5.1 Results summary

Spatially resolved diffuse reflectance spectroscopy is a powerful tool for quantitative tissue analysis using cost-effective and compact systems. Its potential to achieve tissue analysis with layer specificity in contact with the medium has been demonstrated by several authors.[99,204–211] However, the low spatial resolution of current fiber-based and photodiode-base systems limits their ability to detect spatial features of the reflectance on small footprints, thereby diminishing their potential depth-resolution power.

As a way to overcome the shortcomings of current systems, we proposed an innovative srDRS architecture to achieve contact, high resolution imaging of the diffuse reflectance. Only a few studies have reported on the use of compact silicon photodetectors to collect the diffuse reflectance in contact with tissue and with high resolution.[212,213] While these studies relied on the development of custom photodiode arrays, we proposed to implement a system using low-cost, commercially available components including a CMOS image sensor and light-emitting diodes. The limitations of this approach concerning the access to short SDS were identified and an instrumental solution to circumvent these limitations was proposed. This novel srDRS sensor architecture based on the insertion of a fiber-optic plate (FOP) between the sensor and tissue has led to patent filing.

In order to validate the potential of our approach for the quantitative analysis of turbid media, a proof-of-concept study was carried out on homogeneous liquid phantoms. This study confirmed the ability of our system to make accurate quantification of phantoms absorption and reduced scattering coefficients, which were measured with an average error of 4.2±3.5% and 7.0±4.6%, respectively

Based on these developments, a wearable srDRS prototype designed for *in vivo* measurements and analysis of layered media was fabricated. This system comprises a set of fiber-coupled sources at multiple wavelengths for detection of tissue oxygenation changes *in vivo*. One of these sources has been implemented with oblique incidence to enhance the sensitivity of measured reflectance to shallow depths, thereby increasing the potential of the system for layer specific tissue analysis. Additionally, removal of the CMOS protective glass window and bonding of the FOP with the photosensitive area was performed. The resulting system can detect the diffuse reflectance in contact with tissue with spatial resolution as high as 9.8 µm and over a wide range of source-detector separations (approximately 0.7 to 6.5

mm). The development of a dedicated Human-Machine-Interface for control and automation of acquisitions was comprised in this work.

In order to evaluate the performance of our prototype for the analysis of solid materials, a set of PDMS phantoms has been developed. This work was carried out in collaboration with the Laboratoire des sciences de l'Ingénieur, de l'Informatique et de l'Imagerie (ICube), which participated in the specification of the protocol for phantom fabrication and characterization of these phantoms through Spatial Frequency Domain Imaging (SFDI).

Characterization of the developed phantoms was conducted using the SFDI system and srDRS device at 665 nm and 660 nm, respectively. Considering SFDI as a reference approach for phantom characterization, the ability of our sensor to accurately measure the reduced scattering coefficient was demonstrated, with an average error in μ_s' estimates not exceeding 3.3±3.0%. However, large deviations were observed between the two instruments concerning the estimation of absorption coefficients. An empirical calibration method for correction of measured μ_a was proposed and validated. Using this procedure, absorption coefficients could be estimated with an average error of 12.9±14.3% with respect to SFDI reference values.

Finally, *in vivo* evaluation of the developed system for quantitative monitoring of tissue oxygenation was engaged. An arm cuff occlusion experiment was conducted to generate a decrease of oxygen saturation (StO_2) in the tissue. A comparison of results obtained with srDRS and a real-time implementation of SFDI, referred to as Single Snapshot of Optical Properties (SSOP) was made. The ability of the srDRS system to detect tissue desaturation was demonstrated. However, an accurate estimation of StO_2 baseline level and decrease upon occlusion was not reached. Possible reasons for this have been discussed and notably concern the limitations of our calibration protocol and modeling of skin tissue, the sources wavelengths combination considered for derivation of StO_2 and potential unmodeled coupling effects between the sensor and tissue. Future work may notably be dedicated to the adaptation of the system's architecture for implementation of an optimal combination of sources, the improvement of our skin model to account for background absorption from melanin and other species encountered in skin and the use of contact gel for accurate control of sensor-tissue coupling.

5.2 Future directions and perspectives

5.2.1 Analysis of layered media

Perspectives opened by this study notably concern the analysis of layered biological media using a compact, low cost and potentially wearable srDRS system. Assessment of the ability of our approach to achieve this goal should be made in future work.

Preliminary validation of the system's performance necessitates the manufacturing of tissue-simulating media with well-characterized properties. In our study, we relied on a reference measurement system (SFDI) for characterization of PDMS phantoms. Concerns might be raised by this approach, notably because of the non-contact geometry of SFDI compared to our contact measurement modality and the sensitivity of SFDI readings to surface specular reflection.[168] For this reason, independent characterization of the developed phantoms through contact time-resolved DRS has been engaged at a partner institution (Politecnico di Milano, Milan, Italy).

Besides, improvement of our protocol for phantom manufacturing may also be considered. Notably, accurate control of the properties of these phantoms through modulation of TiO_2 and nigrosin concentrations was made difficult possibly by the agglomeration of TiO_2 particles and unknown effect of mixing the two compounds in PDMS. For example, replacement of the TiO2 particles by latex spheres could be considered.[214] For enhanced simulation of skin properties, the use of reconstructed skin models might be investigated.[215]

The manufacturing protocol described in Sec. 3.2.1.2 can be exploited for fabrication of individual phantoms with varying thicknesses and bonding of these to form multi-layer media, for example mimicking the epidermal and stromal layers of skin. Independent characterization of the epithelium and dermis is however a challenging task considering the small thickness of the epidermis. To address this issue, our developments notably comprised the integration of a green light source with angled illumination in the srDRS prototype. We extended the Monte Carlo algorithm to the computation of 3-D reflectance profiles so as to model this source and Look-Up Tables of theoretical reflectance for both vertical and angled illumination in a bi-layer medium have been calculated.[206] In future work, these algorithmic tools may be exploited to specify an adequate inverse model for the analysis of layered tissue. The use of an angled illumination to enhance the sensitivity to shallow tissue layers was proposed by several authors.[206–209,216] The effect of an angled source could be verified (Fig.

5-1 and Fig. 5-2) in simulations and may be validated through phantom experiments in future studies. Based on the architecture proposed here, inclination of both the source and detector to target a specific layer underneath the tissue surface (see Fig. 5-3), as proposed by Nieman et al.[216] may also be explored by using a FOP with angled fibers.[143] Another promising approach proposed by Tseng et al.[217] is founded on the insertion of a diffusive layer with known properties between the sensor and tissue. This approach may also be investigated using the developed prototype.

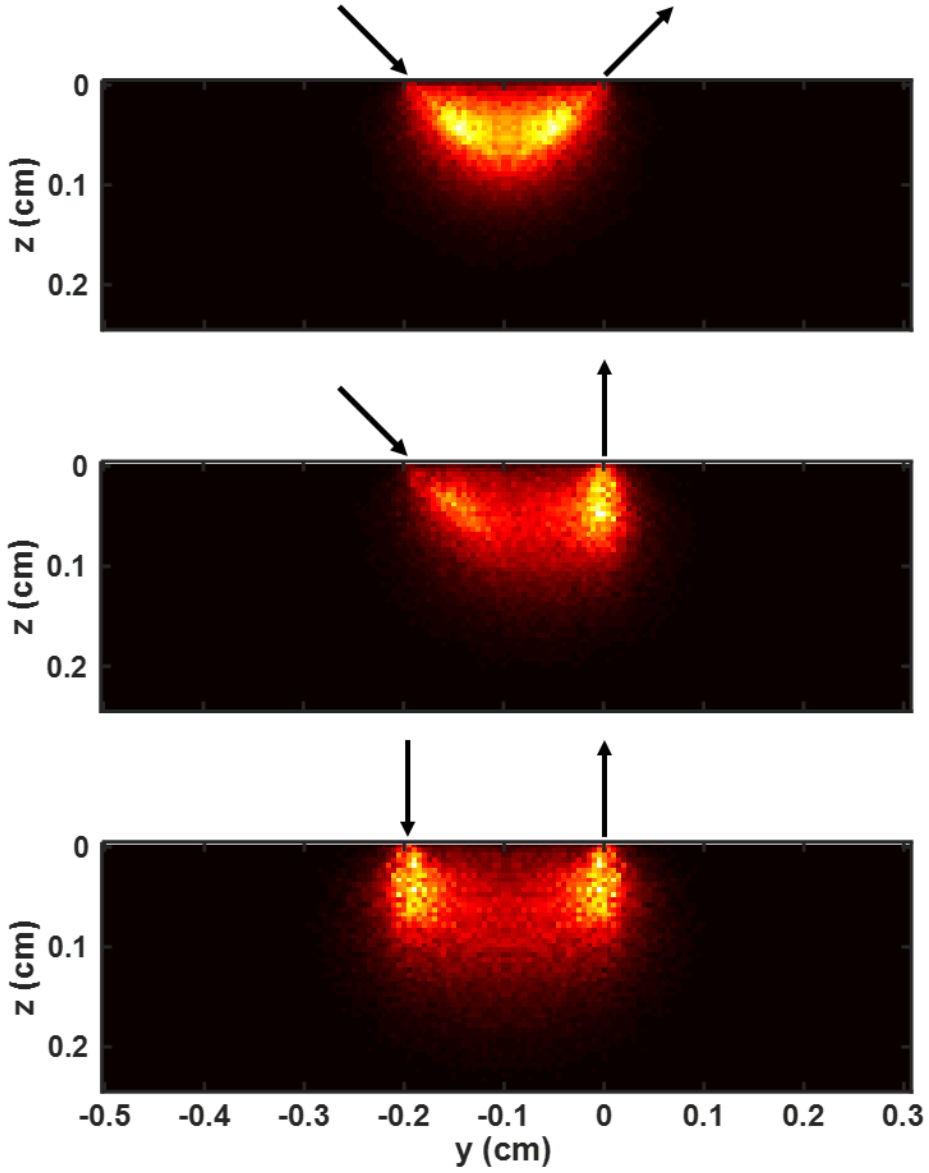


Fig. 5-1 Probability of photon visit as a function of (y,z) location in tissue for a 2 mm SDS and different source-detector combinations. (Top) 45° angled source and detector. (Middle) 45° angled source vertical detector. (Bottom) Vertical source and detector. Arrows show the directions of the source and detection considered in each simulation. Parameters of the simulation were the following: n=1.4; μ_a = 0.02 cm^{-1}; μ_s = 200 cm^{-1}; g=0.8. A flat circular beam with 105 µm width was considered.

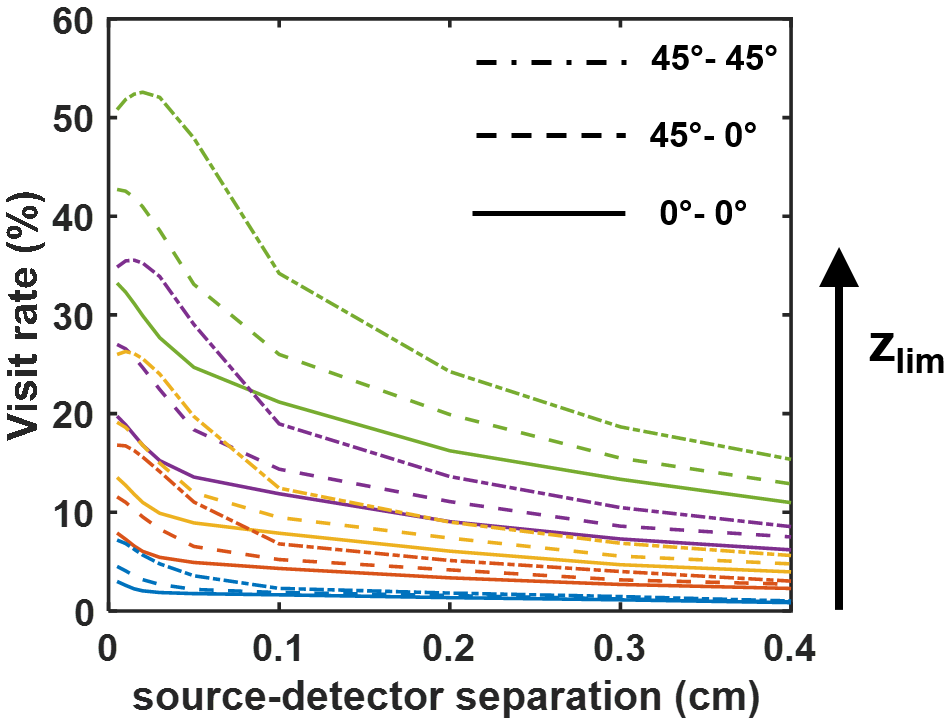


Fig. 5-2 Effect of the source and detector angles on the rate of photon propagation above various depths. The visit rate is defined as the sum of photon probabilities of visit over depths smaller than z_{lim} normalized by the sum of photon probabilities of visit over all depths. In calculations the limit depth z_{lim} was equal to 50 µm (blue), 100 µm (red), 150 µm (orange), 200 µm (purple) and 300 µm (green). Parameters of the computation were the same as in Fig. 5-1. Note the increase in visit rate induced by oblique incidence and the further increase generated by both oblique source and detection.

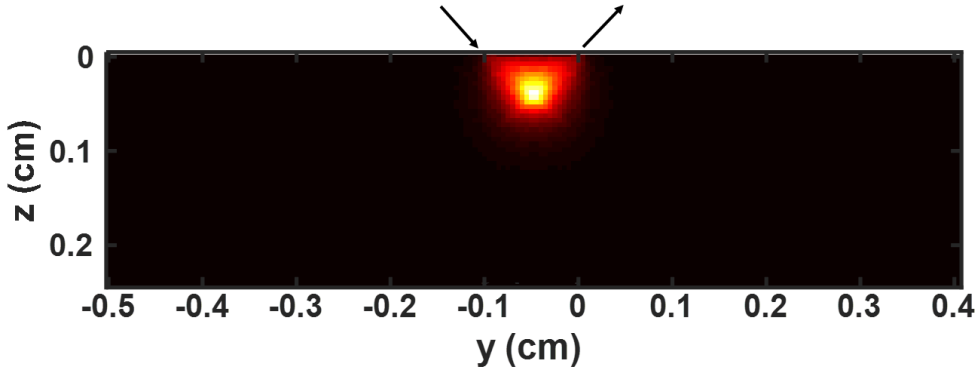


Fig. 5-3 Probability of photon visit as a function of (y,z) location in tissue for a 1 mm and SDS 45° angled source and detector. Photon propagation tends to concentrate in a tissue layer located underneath and slightly away from the surface. This notably explains the decrease in photon visit rate observed in Fig. 5-2 at close proximity to the surface.

The previously mentioned solutions have the advantage to be readily implementable for proof-of-concept studies. However, further miniaturization of srDRS devices and improvement of the system toward layer specific analysis of tissue may be achieved through the development of custom sources and detector arrays. For instance, a micro-electronic chip

comprising LEDs directly integrated within a CMOS-based array of photosensors may be envisioned. Alternatively, an inversed geometry involving a single photodetector combined with an array of LEDs could be proposed. In both cases, bonding of the source-detector array with a fiber-optic plate (FOP), as proposed in this study, may provide both efficient protection upon coupling with the analyzed medium and high resolution of imaging.

This study was focused on the analysis of skin tissue toward diagnostic applications. However, our approach may be relevant for applications in the food and cosmetic industries that require compact, inexpensive and fast characterization tools. The layer-specific analysis of tissue is notably of great interest in the non-destructive assessment of postharvest quality[218,219] and the follow-up of skin permeation by biochemical compounds.[220]

5.2.2 Clinical trial

A clinical protocol involving the developed srDRS prototype has been proposed in collaboration with the Institut National de la Santé et de la Recherche Médicale (Inserm) and the Centre Hospitalier Universitaire (CHU) in Grenoble. The clinical trial is programmed for the spring of 2019 and will involve a panel of healthy volunteers with varying skin types subjected to hypoxic air inhalation. In the last months of the PhD program, time has been dedicated to the preparation of this trial, notably concerning the technical description of the instrument's hardware and software as well as the risk analysis. Results from this trial will provide a valuable set of data that may notably be exploited for the specification of the adequate skin model on the one hand and inverse algorithm on the other hand toward the correction of epithelium influence on StO_2 readings measured in skin.

Conclusion

In recent years, optical imaging methods have proved valuable to assist the clinical in various diagnostic and therapeutic applications *in vivo*. The implementation of these methods into compact, inexpensive tools is of great interest in the current context of strong constraints associated to the management of health care costs and integration of devices into the hospital workflow.

We have introduced and validated an innovative approach for tissue analysis based on the technique known as spatially resolved Diffuse Reflectance Spectroscopy (srDRS). This approach lies upon the use of low-cost and potentially wearable technologies including a high resolution multi-pixel image sensor and light-emitting diodes to achieve diffuse reflectance imaging in contact with tissue. After identifying the main limitations of our approach, a dedicated system architecture was developed and validated on liquid tissue-simulating phantoms. This first proof-of-concept has led to the development of a low-cost, wearable prototype designed for the monitoring of tissue oxygenation *in vivo*. The performances of this device were compared to a state-of-the-art technology, referred to as Spatial Frequency Domain Imaging (SFDI), both on solid tissue-mimicking phantoms and *in vivo*. Notably, the limitations of the developed prototype for the quantification of the optical properties of solid media were identified, and an empirical calibration method accounting for these limitations was proposed. *In vivo* experiments carried out at a partner institution (Laboratoire ICube, CNRS UMR 7357, Strasbourg) demonstrated the ability of the system to detect tissue oxygenation changes induced by a vascular occlusion.

Put together, results confirm the potential of our approach for the accurate quantification of tissue optical properties. This work lays the foundation for the development of inexpensive, compact systems toward *in vivo* tissue diagnostics. In particular, the passive monitoring of tissue oxygenation using a low-cost and wearable device might prove valuable for the improvement of patient management after reconstructive surgery. Furthermore, the developed system has a potential to achieve depth-resolved tissue analysis, which is of great interest in a variety of medical, cosmetic and industrial applications. Several algorithmic and instrumental tools to assess this potential have been set up and may be exploited in future work.

Appendix

A Convolution by the source beam profile

Monte Carlo simulations and analytical formulae of the diffuse reflectance describe the response of the medium to a pencil beam. However, the spatial profile of source intensity may have significant impact on the measured reflectance, especially if short source-detector separations are to be used. In this appendix, we describe the algorithms developed to take account of the source beam profile in the modeling of the diffuse reflectance from tissue.

Wang et al. developed a convolution algorithm to derive the responses to a circular flat beam and Gaussian beam profile to pencil beam Monte Carlo simulations.[169] In order to account for different source beam geometries, a custom convolution algorithm was developed. This algorithm was based on a direct 2-D convolution using the conv2 routine in Matlab.

The convolution script developed by Wang et al. was priory written and used for validation of our own algorithm. Fig. A-1 and Fig. A-2 show the results obtained from both algorithms for a circular flat beam and a Gaussian shaped beam, respectively. In Monte Carlo simulations, the index n, μ_a, μ_s and g were set to 1.4, 1 cm^{-1}, 100 cm^{-1} and 0.8, respectively. For both profiles, a beam with 1 mm width was considered. At the beam's frontier and outside the beam, results obtained with our algorithm are in close agreement with the calculations from Wang et al. At short SDS, our algorithm slightly overestimates the reflectance. This is likely generated by geometrical effects related to the square shaped geometry considered in our algorithm. In particular, augmenting the size of simulated pixels tends to increase the error close to the source. In fact, circular shaped patterns exhibit a squared form as their radius decreases with respect to pixel size. This effect leads to a tradeoff between accuracy of the algorithm and calculation time, since reducing the pixel size increases the number of calculations to be made.

The algorithm of Wang et al. is not affected by this issue since it relies on an analytical formula for the computation of convolution. However, this algorithm is restricted to circular flat and Gaussian profiles.

Improvement of our convolution algorithm is possible yet was not intended. We chose to use a pixel size of 50 microns, which was also the step size considered in Monte Carlo simulations. At short SDS, discrepancies do not exceed 10% and 14% for the circular flat and Gaussian beam, respectively. These short SDS (typically below 500 µm) were however not considered in experiments conducted in our studies.

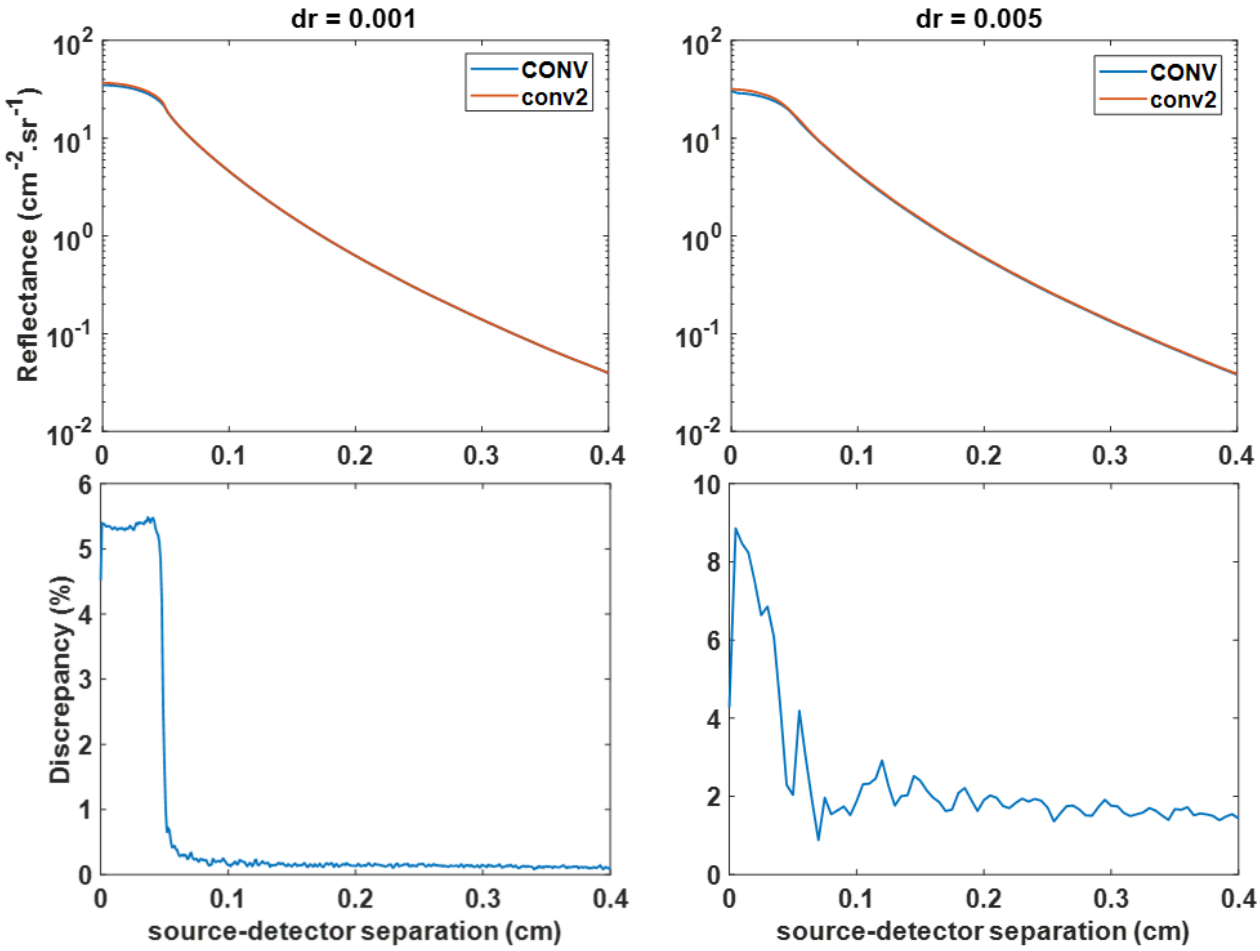


Fig. A-1 Validation of the convolution algorithm for a circular flat beam. A beam having 1mm width was considered. The result obtained from the CONV algorithm of Wang et al. was used as reference. Calculated reflectance profiles are shown for a 10 µm (left) and 50 µm (right) radial step size. (Top) Absolute reflectance calculated with the conv2 routine of Matlab (red) and the CONV algorithm (blue). (Bottom) Relative error between the custom and reference algorithms.

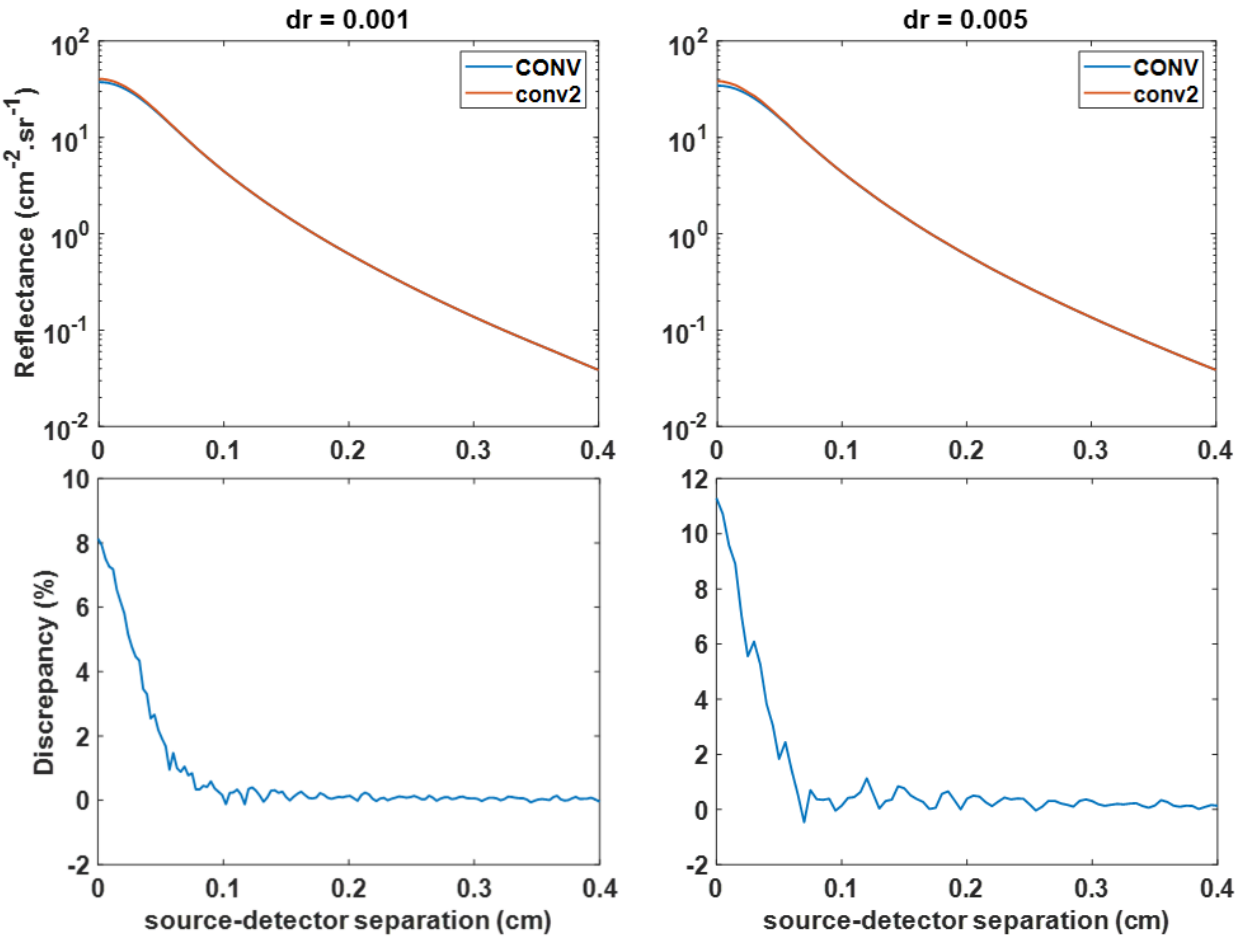


Fig. A-2 Validation of the convolution algorithm for a Gaussian beam. A beam having 1mm width was considered. The result obtained from the CONV algorithm of Wang et al. was used as reference. Calculated reflectance profiles are shown for a 10 µm (left) and 50 µm (right) radial step size. (Top) Absolute reflectance calculated with the conv2 routine of Matlab (red) and the CONV algorithm (blue). (Bottom) Relative error between the custom and reference algorithms.

B Dynamic expansion algorithm

The intensity of measured diffuse reflectance profiles exhibits a fast decrease of several orders of magnitude over a few millimeters range. In order to overcome the limited dynamic range of the CMOS sensor used in our study, an algorithm was developed to expand the dynamic range of detection and achieve diffuse reflectance imaging with sufficient signal-to-noise ratio over the whole sensor area. In this appendix, the principle of the algorithm is detailed and validation on simulated data is presented.

B.1 Principle

B.1.1 Initial data set

In order to expand the dynamic range of measured diffuse reflectance profiles, a set of multiple images of the same sample recorded with increasing exposure times is necessary. Prior background subtraction must be performed using dark images recorded with the same set of exposures. The shortest exposure is chosen so as not to reach the saturation level of the camera. For longer exposures, images comprise a circular area around the illumination point, pixels being saturated up to a certain distance to the source. The diffuse reflectance is detected with higher signal-to-noise ratio compared with images recorded with lower exposure times. An example set of images recorded during diffuse reflectance measurements is displayed in Fig. B-1. Note that at this stage flat-field inhomogeneity of the system are not corrected, resulting in reflectance patterns deformations on the left side of images, along the edge of the fiber-optic plate.

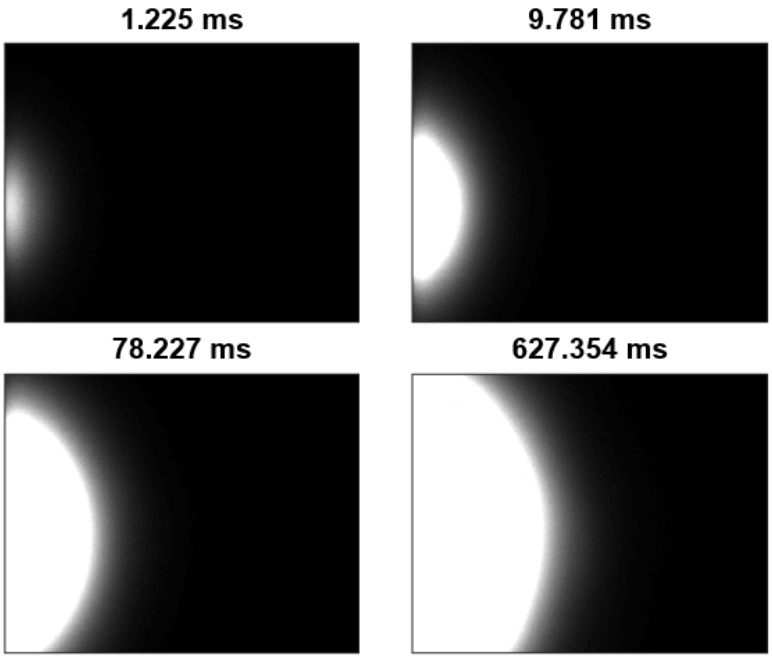


Fig. B-1 Example image set for reconstruction with expanded dynamic.

B.1.2 HDR reconstruction

Consider a set of N diffuse reflectance images priory corrected from the background offset, Im_i, where $i \in [\![1, N]\!]$. Images are recorded with various exposure times T_i so as $T_i > T_{i+1}$.

- Step 0

In the initial step, the HDR image Im_1^{HDR} is built from the image taken with the longest exposure and normalized by the corresponding integration time:

$$Im_1^{HDR} = \frac{Im_1}{T_1} \tag{B.1}$$

- Step i, $i \in [\![1, N-1]\!]$

Following steps consist in building a 2-D mask M_i corresponding to the saturated area in the HDR image $m_{HDR}^{(i)}$:

$$M_i = Im_i^{HDR} \geq m \times \frac{MaxDyn}{T_i} \tag{B.2}$$

and replacing the pixel values in this area by the ones measured in image Im_{i+1}:

$$Im_{i+1}^{HDR} = Im_i^{HDR}\left(M_i^{\complement}\right) \cup \frac{Im_{i+1}(M_i)}{T_{i+1}} \tag{B.3}$$

In order to remain within the linear behavior of the camera sensor, a threshold, m fixed below the saturation level, $MaxDyn$ can be applied. After measurement of the srDRS device linearity, this threshold was set to 80%. Consecutive steps of a reconstruction performed on real data are displayed in Fig. B-2

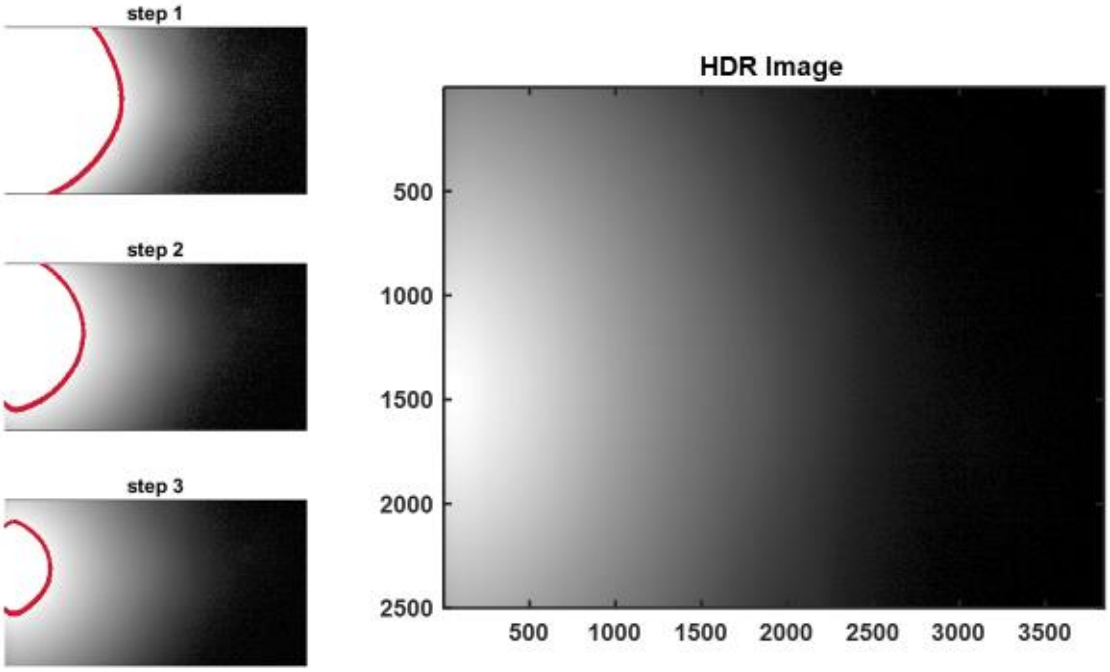


Fig. B-2 HDR image reconstruction. The images obtained after each intermediate step of the algorithm are displayed on the left. The edges of saturation masks are highlighted in red. The final HDR image is shown on the right. Images are displayed in logarithm scale

B.2 Validation

B.2.1 Data simulation

Validation of the algorithm was performed on simulated data. The standard diffusion approximation was used to generate 2-D diffuse reflectance patterns.[107] Optical properties were set to $\frac{n_{in}}{n_{out}} = 1.4$; $\mu_a = 2.5\ cm^{-1}$; $\mu_s' = 35\ cm^{-1}$, n_{in} and n_{out} being the refractive indices of the medium and exterior, respectively.

From this image, 4 images simulating acquisitions at increasing exposure times were built. Saturation of pixels for values above 255 ADU was included. To account for the loss of signal due to dark noise, a uniform background level of 4 ADU was added to each image and subsequently subtracted. Simulated images are shown in Fig. B-3.

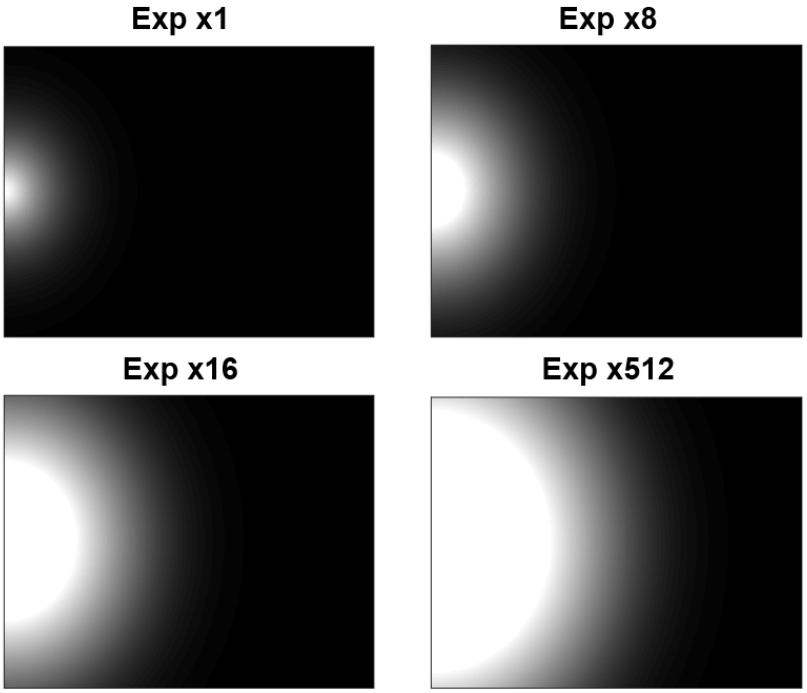


Fig. B-3 Simulated image set.

B.2.2 Results

The simulated image set was used as input to our dynamic expansion algorithm. The linearity threshold was set to 100%. The resulting HDR image was then compared to the initial image, as depicted in Fig. B-4. Relative errors between images were negligible, validating the algorithm performance.

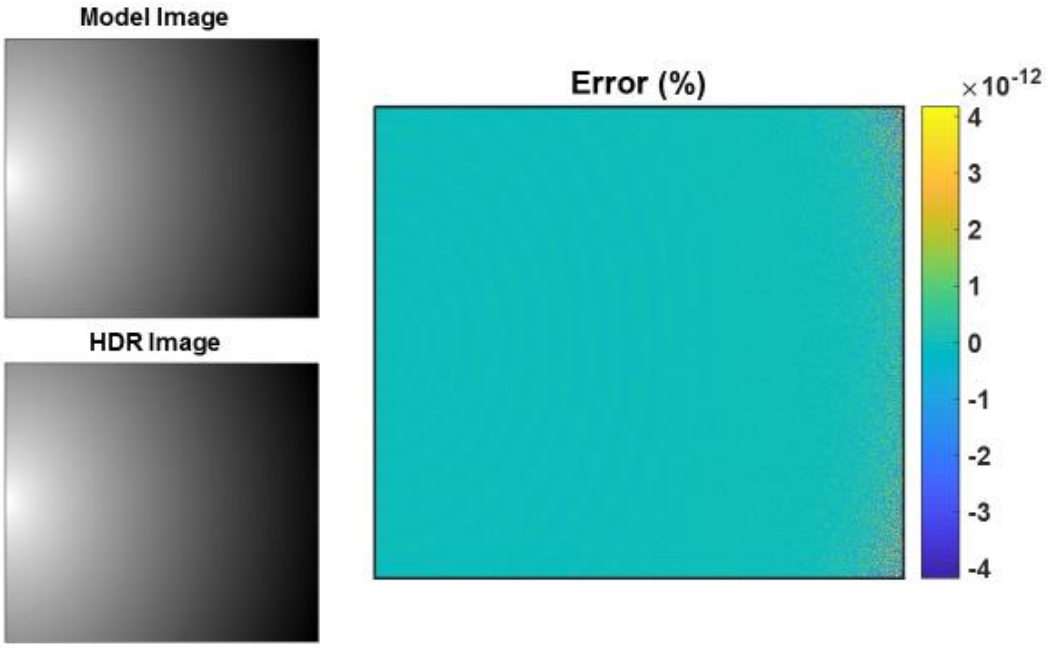


Fig. B-4 Validation of the dynamic expansion algorithm. (Top left) Initial image built from the diffusion approximation. (Bottom left) HDR image obtained from the simulated image set built from the model image. (Right) Relative error between model and HDR images. Images are displayed in logarithm scale.

C Estimation of the blurring effect in contact CMOS-based imaging

Commercial CMOS cameras comprise a glass window in front of the photon sensitive area. This glass lid notably ensures protection of the pixels against shocks and unwanted dust particles. The glass usually has a thickness of about 500 µm. This is an advantage when performing imaging with a focusing lens. Indeed, remaining dusts on the glass surface will affect only poorly the quality of images as they are kept out of focus. In contact imaging modality, the presence of the protective glass window generates blurring of the diffuse reflectance in recorded images due to the unwanted spacing between the imaged sample and pixels.

In order to evaluate the impact of the protective glass lid on images recorded in contact with tissue, we followed an approach inspired by the ISO 12333 slanted-edge methodology[146] (SEM). The SEM provides a measurement of the Line Spread Function (LSF), which may in turn be related to the Modulation Transfer Function (MTF) by Fourier transform. The method records the LSF at chip level without need for focusing and was thereby fully adapted to our problem.

The SEM is based on the imaging of a high contrast edge and calculation of the measured signal as a function of distance to the edge, namely the Edge Spread Function (ESF). By slightly tilting the edge with respect to pixel direction, determination of the ESF with sub-pixel resolution is possible (this was however not intended here considering the broad ESF of the system). The ESF may then be related to the Line Spread Function (LSF) of the system, which relates to the MTF by Fourier transform.

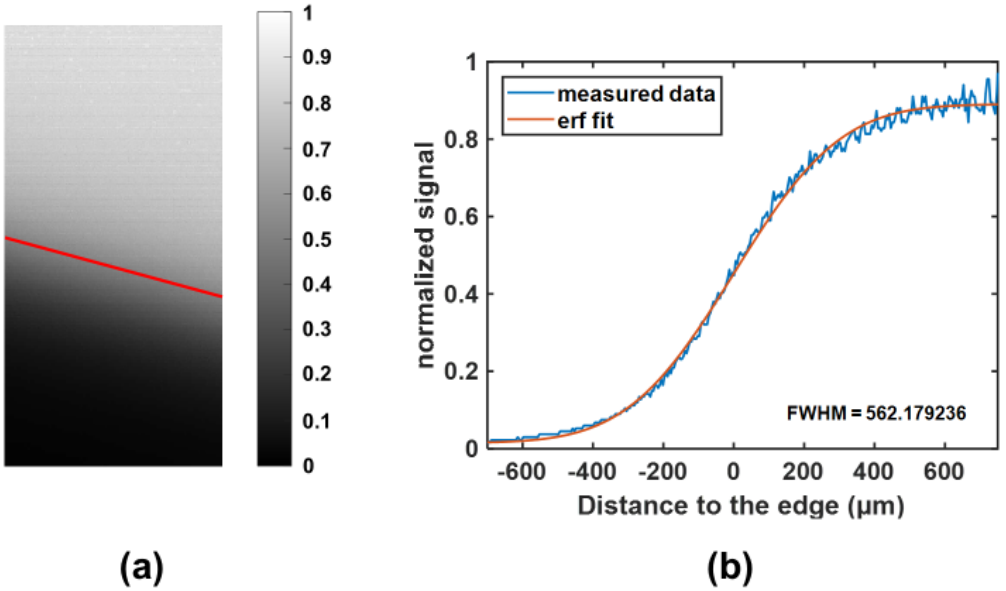


Fig. C-1 Measurement of the srDRS prototype Edge Spread Function (ESF). (a) Region Of Interest (ROI) considered in for ESF calculation in the edge image. The fitted position of the edge is highlighted in red. (b) Measured ESF (blue) and Erf fit (red).

We measured the ESF of the srDRS prototype developed in Chapter 2. A Teflon plate was placed in contact with the FOP top face. A piece of black plastic sheet of 100 µm thickness was priory placed between the FOP and Teflon plate, thereby forming a sharp edge at the FOP surface with a nearly Lambertian illumination background. Ten consecutive images of the edge were recorded, corrected from background and averaged. The position and orientation of the edge were determined by thresholding and line fitting using the curve fitting toolbox of Matlab. The measured signal at each pixel and distance of this pixel to the edge were calculated, thereby yielding the ESF of the system. The measured ESF was then fitted to an Erf function, defined as the response of a system having a Gaussian LSF to an edge:

$$Erf(d) = a + b\int_{-\infty}^{d} \exp(-\frac{r^2}{2\sigma^2})\, dr \tag{C.1}$$

where a and b are arbitrary offset and normalization parameters and d is the distance to the edge. The Full Width at Half Maximum (FWHM) is then obtained using the following relation:

$$FWHM = 2\sqrt{2\ln(2)} \tag{C.2}$$

Results are provided in Fig. C-1. Thereby we found that, modeling the system's response by a Gaussian, the LSF had a FWHM of 562 microns (note that the same definition is used for the FWHM of the LSF and ESF).

Bibliography

1. Wang, L. V. & Wu, H. *Biomedical optics: principles and imaging*. (John Wiley & Sons, 2012).
2. Henyey, L. & Greenstein, J. Diffuse radiation in the galaxy. *Ann. Astrophys.* **3**, 117–137 (1940).
3. Mourant, J. R., Boyer, J., Hielscher, A. H. & Bigio, I. J. Influence of the scattering phase function on light transport measurements in turbid media performed with small source–detector separations. *Opt. Lett.* **21**, 546–548 (1996).
4. Jacques, S. L. & Prahl, S. A. https://omlc.org/classroom/ece532/class3/hg.html.
5. LaPlant, F. Lasers, spectrographs, and detectors. in *Emerging Raman Applications and Techniques in Biomedical and Pharmaceutical Fields* 1–24 (Springer, 2010).
6. Lambert, P. H. & Laurent, P. E. Intradermal vaccine delivery: Will new delivery systems transform vaccine administration? *Vaccine* **26**, 3197–3208 (2008).
7. Flach, C., Zhang, G. & Mendelsohn, R. *In Emerging Raman Applications and Techniques in Biomedical and Pharmaceutical Fields; Matousek P., Morris MD, Eds*. (Springer: New York, 2010).
8. Magnain, C. Modélisation de la couleur de la peau et sa représentation dans les oeuvres d'art. (Université Pierre et Marie Curie Paris 6, 2009).
9. Jacques, S. L. Optical properties of biological tissues: a review. *Phys. Med. Biol.* **58**, R37 (2013).
10. Biswas, T. K. & Luu, T. M. In vivo MR measurement of refractive index, relative water content and T2 relaxation time of various brain lesions with clinical application to discriminate brain lesions. *Internet J. Radiol.* **13**, 1 (2011).
11. Bashkatov, A. N., Genina, E. A. & Tuchin, V. V. Optical properties of skin, subcutaneous, and muscle tissues: a review. *J. Innov. Opt. Health Sci.* **4**, 9–38 (2011).

12. Zonios, G. & Dimou, A. Light scattering spectroscopy of human skin in vivo. *Opt. Express* **17**, 1256–1267 (2009).

13. Ding, H., Lu, J. Q., Wooden, W. A., Kragel, P. J. & Hu, X.-H. Refractive indices of human skin tissues at eight wavelengths and estimated dispersion relations between 300 and 1600 nm. *Phys. Med. Biol.* **51**, 1479 (2006).

14. Igarashi, T., Nishino, K., Nayar, S. K. & others. The appearance of human skin: A survey. *Found. Trends® Comput. Graph. Vis.* **3**, 1–95 (2007).

15. Tearney, G. J. *et al.* Determination of the refractive index of highly scattering human tissue by optical coherence tomography. *Opt Lett* **20**, 2258–2260 (1995).

16. Ding, X.-H., H. .. Lu, J. Q. .. Jacobs, K. M. .. Hu. Determination of refractive indices of porcine skin tissues and intralipid at eight wavelengths between 325 and 1557 nm. *J. Opt. Soc. Am. A Opt. Image Sci. Vis.* **22**, 1151–1157 (2005).

17. Tuchin, V. V. Light scattering study of tissues. *Phys.-Uspekhi* **40**, 495 (1997).

18. Vogel, A. & Venugopalan, V. Mechanisms of pulsed laser ablation of biological tissues. *Chem. Rev.* **103**, 577–644 (2003).

19. Meglinski, I. & Matcher, S. Analysis of the spatial distribution of detector sensitivity in a multilayer randomly inhomogeneous medium with strong light scattering and absorption by the Monte Carlo method. *Opt. Spectrosc.* **91**, 654–659 (2001).

20. Tseng, S. H., Grant, A. & Durkin, A. J. In vivo determination of skin near-infrared optical properties using diffuse optical spectroscopy. *J. Biomed. Opt.* **13**, 014016 (2008).

21. Lisenko, S. & Kugeiko, M. A method of online quantitative interpretation of diffuse reflection profiles of biological tissues. *Opt. Spectrosc.* **114**, 251–259 (2013).

22. Lister, T., Wright, P. A. & Chappell, P. H. Optical properties of human skin. *J. Biomed. Opt.* **17**, 0909011–09090115 (2012).

23. Salomatina, E., Jiang, B., Novak, J. & Yaroslavsky, A. N. Optical properties of normal and cancerous human skin in the visible and near-infrared spectral range. *J. Biomed. Opt.* **11**, 064026 (2006).

24. Roig, B. Caractérisation de tissus cutanés par spectroscopie bimodale : Réflectance Diffuse et Raman. (Université de Reims Champagne Ardenne Physique, spécialité Biophysique, 2015).

25. Jacques, S. L. Origins of tissue optical properties in the UVA, visible, and NIR regions. *OSA TOPS Adv. Opt. Imaging Photon Migr.* **2**, 364–369 (1996).

26. Van Gemert, M., Jacques, S. L., Sterenborg, H. & Star, W. Skin optics. *IEEE Trans. Biomed. Eng.* **36**, 1146–1154 (1989).

27. Jacques, S. L. https://omlc.org/news/jan98/skinoptics.html. (1998).

28. Apelian, C., Harms, F., Thouvenin, O. & Boccara, A. C. Dynamic full field optical coherence tomography: subcellular metabolic contrast revealed in tissues by interferometric signals temporal analysis. *Biomed. Opt. Express* **7**, 1511 (2016).

29. Alex, A. *et al.* 3D optical coherence tomography for clinical diagnosis of nonmelanoma skin cancers. *Imaging Med.* **3**, 653–674 (2011).

30. Grieve, K. *et al.* Ocular Tissue Imaging Using Ultrahigh-Resolution, Full-Field Optical Coherence Tomography. *Investig. Opthalmology Vis. Sci.* **45**, 4126 (2004).

31. Rajadhyaksha, M., Gonzalez, S., Zavislan, J. M., Anderson, R. R. & Webb, R. H. In Vivo Confocal Scanning Laser Microscopy of Human Skin II: Advances in Instrumentation and Comparison With Histology. *J. Invest. Dermatol.* **113**, 293–303 (1999).

32. González, S. & Tannous, Z. Real-time, in vivo confocal reflectance microscopy of basal cell carcinoma. *J. Am. Acad. Dermatol.* **47**, 869–874 (2002).

33. Alvarez-Román, R., Naik, A., Kalia, Y. ., Fessi, H. & Guy, R. . Visualization of skin penetration using confocal laser scanning microscopy. *Eur. J. Pharm. Biopharm.* **58**, 301–316 (2004).

34. Wagner, M., Ivleva, N. P., Haisch, C., Niessner, R. & Horn, H. Combined use of confocal laser scanning microscopy (CLSM) and Raman microscopy (RM): Investigations on EPS – Matrix. *Water Res.* **43**, 63–76 (2009).

35. Oheim, M., Michael, D. J., Geisbauer, M., Madsen, D. & Chow, R. H. Principles of two-photon excitation fluorescence microscopy and other nonlinear imaging approaches. *Adv. Drug Deliv. Rev.* **58**, 788–808 (2006).

36. Weigelin, B., Bakker, G.-J. & Friedl, P. Third harmonic generation microscopy of cells and tissue organization. *J. Cell Sci.* **129**, 245–255 (2016).

37. Cheng, J.-X. & Xie, X. S. Coherent Anti-Stokes Raman Scattering Microscopy: Instrumentation, Theory, and Applications. *J. Phys. Chem. B* **108**, 827–840 (2004).

38. Brancaleon, L. *et al.* In vivo Fluorescence Spectroscopy of Nonmelanoma Skin Cancer. *Photochem. Photobiol.* **73**, 178–183 (2001).

39. Amouroux, M. *et al.* Classification of ultraviolet irradiated mouse skin histological stages by bimodal spectroscopy: multiple excitation autofluorescence and diffuse reflectance. *J. Biomed. Opt.* **14**, 014011 (2009).

40. Stone, N., Baker, R., Rogers, K., Parker, A. W. & Matousek, P. Subsurface probing of calcifications with spatially offset Raman spectroscopy (SORS): future possibilities for the diagnosis of breast cancer. *The Analyst* **132**, 899 (2007).

41. Hallacoglu, B. *et al.* Absolute measurement of cerebral optical coefficients, hemoglobin concentration and oxygen saturation in old and young adults with near-infrared spectroscopy. *J. Biomed. Opt.* **17**, 0814061–0814068 (2012).

42. Gioux, S. *et al.* First-in-human pilot study of a spatial frequency domain oxygenation imaging system. *J. Biomed. Opt.* **16**, 086015–086015 (2011).

43. Saager, R. B., Sharif, A., Kelly, K. M. & Durkin, A. J. In vivo isolation of the effects of melanin from underlying hemodynamics across skin types using spatial frequency domain spectroscopy. *J. Biomed. Opt.* **21**, 057001–057001 (2016).

44. Di Sieno, L. *et al.* Time-resolved diffuse optical tomography for non-invasive flap viability assessment: pre-clinical tests on rats. in *Proc. SPIE* **9538**, 95380N–95380N–7 (2015).

45. Bevilacqua, F. *et al.* In vivo local determination of tissue optical properties: applications to human brain. *Appl. Opt.* **38**, 4939–4950 (1999).

46. Montcel, B., Chabrier, R. & Poulet, P. Time-resolved absorption and hemoglobin concentration difference maps: a method to retrieve depth-related information on cerebral hemodynamics. *Opt. Express* **14**, 12271–12287 (2006).

47. Taroni, P. *et al.* Time-resolved optical mammography between 637 and 985 nm: clinical study on the detection and identification of breast lesions. *Phys. Med. Biol.* **50**, 2469–2488 (2005).

48. Garcia-Uribe, A. *et al.* In-vivo characterization of optical properties of pigmented skin lesions including melanoma using oblique incidence diffuse reflectance spectrometry. *J. Biomed. Opt.* **16**, 020501–020501 (2011).

49. Rajaram, N. *et al.* Design and validation of a clinical instrument for spectral diagnosis of cutaneous malignancy. *Appl. Opt.* **49**, 142–152 (2010).

50. Tromberg, B. J. *et al.* Assessing the future of diffuse optical imaging technologies for breast cancer management. *Med. Phys.* **35**, 2443–2451 (2008).

51. Zonios, G. *et al.* Diffuse Reflectance Spectroscopy of Human Adenomatous Colon Polyps< i> In Vivo</i>. *Appl. Opt.* **38**, 6628–6637 (1999).

52. Rohrbach, D. J. *et al.* Characterization of nonmelanoma skin cancer for light therapy using spatial frequency domain imaging. *Biomed Opt Express* **6**, 1761–1766 (2015).

53. Brown, J. Q. *et al.* Optical Spectral Surveillance of Breast Tissue Landscapes for Detection of Residual Disease in Breast Tumor Margins. *PLOS ONE* **8**, 1–14 (2013).

54. Randeberg, L. L., Roll, E. B., Nilsen, L. T. N., Christensen, T. & Svaasand, L. O. In vivo spectroscopy of jaundiced newborn skin reveals more than a bilirubin index. *Acta Paediatr.* **94**, 65–71

55. Stamatas, G. N. & Kollias, N. In vivo documentation of cutaneous inflammation using spectral imaging. *J. Biomed. Opt.* **12**, 051603–051603 (2007).

56. Stam, B., van Gemert, M. J. C., van Leeuwen, T. G. & Aalders, M. C. G. 3D finite compartment modeling of formation and healing of bruises may identify methods for age determination of bruises. *Med. Biol. Eng. Comput.* **.**, 1–11 (2010).

57. Yudovsky, D., Nouvong, A., Schomacker, K. & Pilon, L. Two-layer optical model of skin for early, non-invasive detection of wound development on the diabetic foot. *BiOS* 755514–755514 (2010).

58. Sunar, U. *et al.* Light-triggered doxorubicin release quantified by spatial frequency domain imaging and diffuse optical spectroscopy. in *Cancer Imaging and Therapy* JW4A–3 (Optical Society of America, 2016).

59. Mazhar, A. *et al.* Spatial frequency domain imaging of port wine stain biochemical composition in response to laser therapy: A pilot study. *Lasers Surg. Med.* **44**, 611–621

60. Planat-Chrétien, A. *et al.* Assessment of the status of onchocerciasis worms with DRS: proposal of a standardized measurement protocol. in *Diffuse Optical Spectroscopy and Imaging VI* 104120I (Optical Society of America, 2017). doi:10.1117/12.2286051

61. Jacques, S. L. Time-resolved reflectance spectroscopy in turbid tissues. *Biomed. Eng. IEEE Trans. On* **36**, 1155–1161 (1989).

62. Montcel, P., B. .. Chabrier, R. .. Poulet. Detection of cortical activation with time-resolved diffuse optical methods. *Appl. Opt.* **44**, 1942–1947 (2005).

63. Liebert, A. *et al.* Evaluation of optical properties of highly scattering media by moments of distributions of times of flight of photons. *Appl. Opt.* **42**, 5785–5792 (2003).

64. Liebert, A. *et al.* Time-resolved multidistance near-infrared spectroscopy of the adult head: intracerebral and extracerebral absorption changes from moments of distribution of times of flight of photons. *Appl. Opt.* **43**, 3037–3047 (2004).

65. Liebert, A. *et al.* Bed-side assessment of cerebral perfusion in stroke patients based on optical monitoring of a dye bolus by time-resolved diffuse reflectance. *Neuroimage* **24**, 426–435 (2005).

66. Contini, D. *et al.* Multi-channel time-resolved system for functional near infrared spectroscopy. *Opt. Express* **14**, 5418–5432 (2006).

67. Yudovsky, D. & Pilon, L. Simple and accurate expressions for diffuse reflectance of semi-infinite and two-layer absorbing and scattering media. *Appl. Opt.* **48**, 6670–6683 (2009).

68. Kienle, A. Determination of the optical properties of semi-infinite turbid media from frequency-domain reflectance close to the source. *Phys Med Biol* **42**, 1801–1819 (1997).

69. David J. Cuccia, B. J. T., Frédéric P. Bevilacqua, Anthony Joseph Durkin, Frederick R. Ayers. Quantitation and mapping of tissue optical properties using modulated imaging. *J. Biomed. Opt.* **14**, 14-14–13 (2009).

70. Giessen, M. van de, Angelo, J. P. & Gioux, S. Real-time, profile-corrected single snapshot imaging of optical properties. *Biomed Opt Express* **6**, 4051–4062 (2015).

71. Pilz, M., Honold, S. & Kienle, A. Determination of the optical properties of turbid media by measurements of the spatially resolved reflectance considering the point-spread function of the camera system. *J. Biomed. Opt.* **13**, 054047–054047 (2008).

72. Kienle, A. *et al.* Spatially resolved absolute diffuse reflectance measurements for noninvasive determination of the optical scattering and absorption coefficients of biological tissue. *Appl. Opt.* **35**, 2304–2314 (1996).

73. Foschum, F., Jäger, M. & Kienle, A. Fully automated spatially resolved reflectance spectrometer for the determination of the absorption and scattering in turbid media. *Rev. Sci. Instrum.* **82**, 103104 (2011).

74. Bolt, R. & Ten Bosch, J. Method for measuring position-dependent volume reflection. *Appl. Opt.* **32**, 4641–4645 (1993).

75. Yudovsky, D., Nguyen, J. Q. M. & Durkin, A. J. In vivo spatial frequency domain spectroscopy of two layer media. *J. Biomed. Opt.* **17**, 107006–107006 (2012).

76. Yu, B. *et al.* Cost-effective diffuse reflectance spectroscopy device for quantifying tissue absorption and scattering in vivo. *J. Biomed. Opt.* **13**, 060505–060505 (2008).

77. Lo, J. Y. *et al.* A strategy for quantitative spectral imaging of tissue absorption and scattering using light emitting diodes and photodiodes. *Opt Express* **17**, 1372–1384 (2009).

78. Senlik, O. & Jokerst, N. M. Concentric Multipixel Silicon Photodiode Array Probes for Spatially Resolved Diffuse Reflectance Spectroscopy. *IEEE J. Sel. Top. Quantum Electron.* **22**, 7–12 (2016).

79. Shokoufi, M. & Golnaraghi, F. Development of a handheld diffuse optical breast cancer assessment probe. *J. Innov. Opt. Health Sci.* **9**, 1650007 (2016).

80. Dhar, S. *et al.* A diffuse reflectance spectral imaging system for tumor margin assessment using custom annular photodiode arrays. *Biomed. Opt. Express* **3**, 3211–3222 (2012).

81. Duun, S. B., Haahr, R. G., Birkelund, K. & Thomsen, E. V. A Ring-shaped photodiode designed for use in a reflectance pulse oximetry sensor in wireless health monitoring applications. *Sens. J. IEEE* **10**, 261–268 (2010).

82. Sun, J. *et al.* Influence of fiber optic probe geometry on the applicability of inverse models of tissue reflectance spectroscopy: computational models and experimental measurements. *Appl. Opt.* **45**, 8152–8162 (2006).

83. Yu, B., Fu, H. L. & Ramanujam, N. Instrument independent diffuse reflectance spectroscopy. *J. Biomed. Opt.* **16**, 011010–011010 (2011).

84. Dam, J. S. *et al.* Fiber-optic probe for noninvasive real-time determination of tissue optical properties at multiple wavelengths. *Appl. Opt.* **40**, 1155–1164 (2001).

85. PLANAT-CHRETIEN, A. *et al.* STOP: a Spectroscopic Tip Optical Probe for skin complexion characterization. in *Biomedical Optics 2016* JM3A.28 (Optical Society of America, 2016).

86. Kim, A., Roy, M., Dadani, F. & Wilson, B. C. A fiberoptic reflectance probe with multiple source-collector separations to increase the dynamic range of derived tissue optical absorption and scattering coefficients. *Opt. Express* **18**, 5580–5594 (2010).

87. Hallacoglu, B., Sassaroli, A., Fantini, S. & Troen, A. M. Cerebral perfusion and oxygenation are impaired by folate deficiency in rat: Absolute measurements with noninvasive near-infrared spectroscopy. *J. Cereb. Blood Flow Metab.* **31**, 1482–1492 (2011).

88. Schwarz, R. A. *et al.* Prospective evaluation of a portable depth-sensitive optical spectroscopy device to identify oral neoplasia. *Biomed Opt Express* **2**, 89–99 (2011).

89. Koenig, A., Roig, B., Le Digabel, J., Josse, G. & Dinten, J.-M. Accessing deep optical properties of skin using diffuse reflectance spectroscopy. in *European Conferences on Biomedical Optics* 95370E–95370E (International Society for Optics and Photonics, 2015).

90. Tseng, S.-H., Hayakawa, C., Tromberg, B. J., Spanier, J. & Durkin, A. J. Quantitative spectroscopy of superficial turbid media. *Opt. Lett.* **30**, 3165–3167 (2005).

91. Andree, S., Helfmann, J. & Gersonde, I. Determination of chromophore concentrations from spatially resolved skin measurements. in *European Conference on Biomedical Optics* (Optical Society of America, 2011).

92. Venugopalan, V., You, J. S. & Tromberg, B. J. Radiative transport in the diffusion approximation: An extension for highly absorbing media and small source-detector separations. *Phys Rev E* **58**, 2395–2407 (1998).

93. Zonios, N., G. .. Bykowski, J. .. Kollias. Skin melanin, hemoglobin, and light scattering properties can be quantitatively assessed in vivo using diffuse reflectance spectroscopy. *J. Invest. Dermatol.* **117**, 1452–1457 (2001).

94. Saager, R. B. *et al.* In vivo measurements of cutaneous melanin across spatial scales: using multiphoton microscopy and spatial frequency domain spectroscopy. *J. Biomed. Opt.* **20**, 066005–066005 (2015).

95. Roig, B. *et al.* Can diffuse reflectance spectroscopy emphasize skin-collagen alterations due to ageing? in *ISBS/SICC 2013* (2013).

96. Koenig, A. *et al.* Diffuse reflectance spectroscopy: a clinical study of tuberculin skin tests reading. in (eds. Wax, A. P. & Backman, V.) 85920S (2013). doi:10.1117/12.2002314

97. Chandrasekhar, S. Stochastic problems in physics and astronomy. *Rev. Mod. Phys.* **15**, 1–89 (1943).

98. Prahl, S. A. Light transport in tissue. (University of Texas at Austin, 1988).

99. Kienle, A. *et al.* Noninvasive determination of the optical properties of two-layered turbid media. *Appl Opt* **37**, 779–791 (1998).

100. Bernice, S. Modeling diffuse reflectance measurements of light scattered by layered tissues. 82

101. Wang, L., Jacques, S. L. & Zheng, L. MCML–Monte Carlo modeling of light transport in multi-layered tissues. *Comput. Methods Programs Biomed.* **47**, 131–146 (1995).

102. Palmer, G. M. & Ramanujam, N. Monte Carlo-based inverse model for calculating tissue optical properties. Part I: Theory and validation on synthetic phantoms. *Appl. Opt.* **45**, 1062–1071 (2006).

103. Liu, Q. & Ramanujam, N. Scaling method for fast Monte Carlo simulation of diffuse reflectance spectra from multilayered turbid media. *J. Opt. Soc. Am. A* **24**, 1011–1025 (2007).

104. Bevilacqua, F. & Depeursinge, C. Monte Carlo study of diffuse reflectance at source–detector separations close to one transport mean free path. *J Opt Soc Am A* **16**, 2935–2945 (1999).

105. Groenhuis, R., Ferwerda, H. A. & Bosch, J. J. T. Scattering and absorption of turbid materials determined from reflection measurements. 1: Theory. *Appl. Opt.* **22**, 2456–2462 (1983).

106. Farrell, T. J., Patterson, M. S. & Wilson, B. A diffusion theory model of spatially resolved, steady-state diffuse reflectance for the noninvasive determination of tissue optical properties in vivo. *Med. Phys.* **19**, 879 (1992).

107. Kienle, A. & Patterson, M. S. Improved solutions of the steady-state and the time-resolved diffusion equations for reflectance from a semi-infinite turbid medium. *J. Opt. Soc. Am. -Opt. Image Sci. Vis.* **14**, 246–254 (Jan).

108. Carp, S. A., Prahl, S. A. & Venugopalan, V. Radiative transport in the delta-P1 approximation: accuracy of fluence rate and optical penetration depth predictions in turbid semi-infinite media. *J. Biomed. Opt.* **9**, 632–647 (2004).

109. Seo, I., Hayakawa, C. K. & Venugopalan, V. Radiative transport in the delta-P1 approximation for semi-infinite turbid media. *Med. Phys.* **35**, 681–693 (2008).

110. Arridge, S. R. Optical tomography in medical imaging. *Inverse Probl.* **15**, R41 (1999).

111. Groenhuis, R., Bosch, J. J. T. & Ferwerda, H. A. Scattering and absorption of turbid materials determined from reflection measurements. 2: Measuring method and calibration. *Appl. Opt.* **22**, 2463–2467 (1983).

112. Star, W. M. Light dosimetry in vivo. *Phys. Med. Biol.* **42**, 763 (1997).

113. Wyman, D. R., Patterson, M. S. & Wilson, B. C. Similarity relations for the interaction parameters in radiation transport. *Appl Opt* **28**, 5243–5249 (1989).

114. Haskell, R. C. *et al.* Boundary conditions for the diffusion equation in radiative transfer. *J. Opt. Soc. Am. A* **11**, 2727–2741 (1994).

115. Gardner, A. R., Kim, A. D. & Venugopalan, V. Radiative transport produced by oblique illumination of turbid media with collimated beams. *Phys. Rev. E* **87**, 063308 (2013).

116. Zemp, R. J. Phase-function corrected diffusion model for diffuse reflectance of a pencil beam obliquely incident on a semi-infinite turbid medium. *J. Biomed. Opt.* **18**, 067005–067005 (2013).

117. Farrell, T. J. & Patterson, M. S. Experimental verification of the effect of refractive index mismatch on the light fluence in a turbid medium. *J. Biomed. Opt.* **6**, 468–473 (2001).

118. Wang, L. V. & Jacques, S. L. Source of error in calculation of optical diffuse reflectance from turbid media using diffusion theory. *Comput. Methods Programs Biomed.* **61**, 163–170 (2000).

119. Hull, E. L. & Foster, T. H. Steady-state reflectance spectroscopy in the P 3 approximation. *JOSA A* **18**, 584–599 (2001).

120. Joseph, J., Wiscombe, W. & Weinman, J. The delta-Eddington approximation for radiative flux transfer. *J. Atmospheric Sci.* **33**, 2452–2459 (1976).

121. Prahl, S. A., Keijzer, M., Jacques, S. L. & Welch, A. J. A Monte Carlo model of light propagation in tissue. *Dosim. Laser Radiat. Med. Biol.* **5**, 102–111 (1989).
122. Liu, Q. & Ramanujam, N. Sequential estimation of optical properties of a two-layered epithelial tissue model from depth-resolved ultraviolet-visible diffuse reflectance spectra. *Appl Opt* **45**, 4776–4790 (2006).
123. Graaff, R. *et al.* Condensed Monte Carlo simulations for the description of light transport. *Appl. Opt.* **32**, 426–434 (1993).
124. Wang, L. & Jacques, S. L. Hybrid model of Monte Carlo simulation and diffusion theory for light reflectance by turbid media. *JOSA A* **10**, 1746–1752 (1993).
125. Poon, W. Rapport de stage: Analyse de la peau par approche multicouche. (2016).
126. Wang, L. https://omlc.org/software/mc/mcml/.
127. Kim, A., Khurana, M., Moriyama, Y. & Wilson, B. C. Quantification of in vivo fluorescence decoupled from the effects of tissue optical properties using fiber-optic spectroscopy measurements. *J. Biomed. Opt.* **15**, 067006-067006-12 (2010).
128. Karin Terstappen, A.-M. K. W., Mart Suurkula, Hakan Hallberg, Marica B. Ericson. Poor correlation between spectrophotometric intracutaneous analysis and histopathology in melanoma and nonmelanoma lesions. *J. Biomed. Opt.* **18**, 18-18–6 (2013).
129. Hunter, R. J., Patterson, M. S., Farrell, T. J. & Hayward, J. E. Haemoglobin oxygenation of a two-layer tissue-simulating phantom from time-resolved reflectance: effect of top layer thickness. *Phys. Med. Biol.* **47**, 193 (2002).
130. Chang, V. T.-C. *et al.* Quantitative physiology of the precancerous cervix in vivo through optical spectroscopy. *Neoplasia* **11**, 325–332 (2009).
131. Zonios, G. & Dimou, A. Modeling diffuse reflectance from semi-infinite turbid media: application to the study of skin optical properties. *Opt. Express* **14**, 8661–8674 (2006).

132. Beiderman, M., Tam, T., Fish, A., Jullien, G. A. & Yadid-Pecht, O. A low-light CMOS contact imager with an emission filter for biosensing applications. *IEEE Trans. Biomed. Circuits Syst.* **2**, 193–203 (2008).

133. Mudraboyina, A. K., Blockstein, L., Luk, C. C., Syed, N. I. & Yadid-Pecht, O. A novel lensless miniature contact imaging system for monitoring calcium changes in live neurons. *IEEE Photonics J.* **6**, 1–15 (2014).

134. Dolci, L. S. *et al.* Point-of-care Parvovirus B19 detection and genotyping based on microfluidics and chemiluminescence contact imaging detection. *BioPhotonics 2011 Int. Workshop On* 1–3 (2011).

135. Singh, R. R., Leng, L., Guenther, A. & Genov, R. A CMOS-microfluidic chemiluminescence contact imaging microsystem. *IEEE J. Solid-State Circuits* **47**, 2822–2833 (2012).

136. Huang, X. *et al.* A dual-mode large-arrayed CMOS ISFET sensor for accurate and high-throughput pH sensing in biomedical diagnosis. *IEEE Trans. Biomed. Eng.* **62**, 2224–2233 (2015).

137. Takehara, H. *et al.* High coupling efficiency contact imaging system having micro light pipe array for a digital enzyme-linked immunosorbent assay. *Biomed. Circuits Syst. Conf. BioCAS 2015 IEEE* 1–4 (2015).

138. Ho, D., Noor, M. O., Krull, U. J., Gulak, G. & Genov, R. CMOS spectrally-multiplexed Fret-on-a-Chip for DNA analysis. *IEEE Trans. Biomed. Circuits Syst.* **7**, 643–654 (2013).

139. Schelkanova, I., Pandya, A., Shah, D., Lilge, L. & Douplik, A. Diffuse reflectance measurements using lensless CMOS imaging chip. *J. Phys. Conf. Ser.* **541**, 012098 (2014).

140. Irina Schelkanova, A. D., Aditya Pandya, Guennadi Saiko, Lidia Nacy, Hannan Babar, Duoaud F. Shah, Lothar Lilge. Spatially resolved, diffuse reflectance imaging for

subsurface pattern visualization toward development of a lensless imaging platform: phantom experiments. *J. Biomed. Opt.* **21**, 21-21–8 (2016).

141. Getman, A. *et al.* Crosstalk, color tint and shading correction for small pixel size image sensor. in *International Image Sensor Workshop* 166–169 (2007).
142. Cen, H., Lu, R. & Dolan, K. Optimization of inverse algorithm for estimating the optical properties of biological materials using spatially-resolved diffuse reflectance. *Inverse Probl. Sci. Eng.* **18**, 853–872 (2010).
143. http://szphoton.com/products/fiber-optic-plate/.
144. Cho, H. S. *et al.* Development of a portable digital radiographic system based on FOP-coupled CMOS image sensor and its performance evaluation. *IEEE Trans. Nucl. Sci.* **52**, 1766–1772 (2005).
145. Bishara, W., Su, T.-W., Coskun, A. F. & Ozcan, A. Lensfree on-chip microscopy over a wide field-of-view using pixel super-resolution. *Opt Express* **18**, 11181–11191 (2010).
146. Estribeau, M. & Magnan, P. Fast MTF measurement of CMOS imagers using ISO 12333 slanted-edge methodology. in **5251**, (2004).
147. Sorgato, V. *et al.* ACA-Pro: calibration protocol for quantitative diffuse reflectance spectroscopy. Validation on contact and noncontact probe-and CCD-based systems. *J. Biomed. Opt.* **21**, 065003–065003 (2016).
148. van Staveren, H. J., Moes, C. J. M., van Marle, J., Prahl, S. A. & van Gemert, M. J. C. Light scattering in Intralipid-10% in the wavelength range of 400–1100 nm. *Appl Opt* **30**, 4507–4514 (1991).
149. Cheong, W. F., Prahl, S. A. & Welch, A. J. A review of the optical properties of biological tissues. *Quantum Electron. IEEE J. Of* **26**, 2166–2185 (1990).
150. Foschum, F. *et al.* Surface layering effect of diluted Intralipid. in (eds. Dehghani, H. & Taroni, P.) 95381A (2015). doi:10.1117/12.2183761

151. Bender, J. E. *et al.* Noninvasive monitoring of tissue hemoglobin using UV-VIS diffuse reflectance spectroscopy: a pilot study. *Opt. Express* **17**, 23396–23409 (2009).

152. Tseng, T. Y., Chen, C. Y., Li, Y. S. & Sung, K. B. Quantification of the optical properties of two-layered turbid media by simultaneously analyzing the spectral and spatial information of steady-state diffuse reflectance spectroscopy. *Biomed. Opt. Express* **2**, 901–914 (2011).

153. Naglič, P., Cugmas, B., Pernuš, F., Likar, B. & Bürmen, M. Extraction of optical properties in the sub-diffuse regime by spatially resolved reflectance spectroscopy. *SPIE BiOS* 97061C–97061C (2016).

154. Rakotomanga, P., Soussen, C. & Blondel, W. C. Influence of cost functions and optimization methods on solving the inverse problem in spatially resolved diffuse reflectance spectroscopy. in *Dynamics and Fluctuations in Biomedical Photonics XIV* **10063**, 100630Y (International Society for Optics and Photonics, 2017).

155. Zaccanti, G., Bianco, S. D. & Martelli, F. Measurements of optical properties of high-density media. *Appl Opt* **42**, 4023–4030 (2003).

156. Nguyen, V. D., Faber, D. J., Pol, E. van der, Leeuwen, T. G. van & Kalkman, J. Dependent and multiple scattering in transmission and backscattering optical coherence tomography. *Opt Express* **21**, 29145–29156 (2013).

157. Aernouts, B., Beers, R. V., Watté, R., Lammertyn, J. & Saeys, W. Dependent scattering in Intralipid® phantoms in the 600-1850 nm range. *Opt Express* **22**, 6086–6098 (2014).

158. Nieman, L., Myakov, A., Aaron, J. & Sokolov, K. Optical sectioning using a fiber probe with an angled illumination-collection geometry: evaluation in engineered tissue phantoms. *Appl. Opt.* **43**, 1308–1319 (2004).

159. Sung, K.-B. & Chen, H.-H. Enhancing the sensitivity to scattering coefficient of the epithelium in a two-layered tissue model by oblique optical fibers: Monte Carlo study. *J. Biomed. Opt.* **17**, 107003–107003 (2012).

160. Nieman, L. T., Jakovljevic, M. & Sokolov, K. Compact beveled fiber optic probe design for enhanced depth discrimination in epithelial tissues. *Opt Express* **17**, 2780–2796 (2009).

161. Silfhout, R. G. van & Kachatkou, A. S. Fibre-optic coupling to high-resolution CCD and CMOS image sensors. *Nucl. Instrum. Methods Phys. Res. Sect. Accel. Spectrometers Detect. Assoc. Equip.* **597**, 266–269 (2008).

162. Kennedy, G. T. *et al.* Solid tissue simulating phantoms having absorption at 970 nm for diffuse optics. *J. Biomed. Opt.* **22**, 076013 (2017).

163. Pogue, B. W. & Patterson, M. S. Review of tissue simulating phantoms for optical spectroscopy, imaging and dosimetry. *J Biomed Opt* **11**, 041102 (2006).

164. de Bruin, D. M. *et al.* Optical phantoms of varying geometry based on thin building blocks with controlled optical properties. *J. Biomed. Opt.* **15**, 025001–025001 (2010).

165. Saager, R. B. *et al.* Multilayer silicone phantoms for the evaluation of quantitative optical techniques in skin imaging. in *BiOS* 756706–756706 (International Society for Optics and Photonics, 2010).

166. Gage J. Greening, T. J. M., Raeef Istfan, Laura M. Higgins, Kartik Balachandran, Darren M. Roblyer, Mark C. Pierce. Characterization of thin poly(dimethylsiloxane)-based tissue-simulating phantoms with tunable reduced scattering and absorption coefficients at visible and near-infrared wavelengths. *J. Biomed. Opt.* **19**, 19-19–14 (2014).

167. Cuccia, D. J., Bevilacqua, F., Durkin, A. J. & Tromberg, B. J. Modulated imaging: quantitative analysis and tomography of turbid media in the spatial-frequency domain. *Opt. Lett.* **30**, 1354–1356 (2005).

168. Nothelfer, S., Bergmann, F., Liemert, A., Reitzle, D. & Kienle, A. Spatial frequency domain imaging using an analytical model for separation of surface and volume scattering. *J. Biomed. Opt.* **24**, 1 (2018).

169. Wang, L., Jacques, S. L. & Zheng, L. CONV - convolution for responses to a finite diameter photon beam incident on multi-layered tissues. *Comput. Methods Programs Biomed.* **54**, 141–150 (1997).

170. Reif, R. *et al.* Analysis of changes in reflectance measurements on biological tissues subjected to different probe pressures. *J. Biomed. Opt.* **13**, 010502–010502 (2008).

171. Vervandier, J. & Gioux, S. Single snapshot imaging of optical properties. *Biomed. Opt. Express* **4**, 2938 (2013).

172. SEIDENBERG, B., ROSENAK, S. S., HURWITT, E. S. & SOM, M. L. Immediate reconstruction of the cervical esophagus by a revascularized isolated jejunal segment. *Ann. Surg.* **149**, 162–171 (1959).

173. Smit, J. M. *et al.* Early reintervention of compromised free flaps improves success rate. *Microsurgery* **27**, 612–616 (2007).

174. Gal, T. J., Jones, K. A. & Valentino, J. Reconstruction of the through-and-through oral cavity defect with the fibula free flap. *Otolaryngol. Neck Surg.* **140**, 519–525 (2009).

175. Yuen, J. C. & Feng, Z. Monitoring Free Flaps Using the Laser Doppler Flowmeter: Five-Year Experience: *Plast. Reconstr. Surg.* **105**, 55–61 (2000).

176. Jones, N. Intraoperative and postoperative monitoring of microsurgical free tissue transfers. *Clin Plast Surg* **19**, 783–797 (1992).

177. Neugan, P. C. Monitoring techniques for the detection of flow failure in the postoperative period. *Microsurgery* **14**, 162–164 (1993).

178. Siemionow, M. & Arslan, E. Ischemia/reperfusion injury: A review in relation to free tissue transfers. *Microsurgery* **24**, 468–475 (2004).

179. Smit, J. M., Zeebregts, C. J., Acosta, R. & Werker, P. M. Advancements in free flap monitoring in the last decade: a critical review. *Plast. Reconstr. Surg.* **125**, 177–185 (2010).

180. Chen, Y., Shen, Z., Shao, Z., Yu, P. & Wu, J. Free flap monitoring using near-infrared spectroscopy: a systemic review. *Ann. Plast. Surg.* **76**, 590–597 (2016).

181. Wassenaar, E. B. & Van den Brand, J. G. H. Reliability of Near-Infrared Spectroscopy in People With Dark Skin Pigmentation. *J. Clin. Monit. Comput.* **19**, 195–199 (2005).

182. Haahr, R. G. *et al.* An Electronic Patch for Wearable Health Monitoring by Reflectance Pulse Oximetry. *Biomed. Circuits Syst. IEEE Trans. On* **6**, 45–53 (2012).

183. Berthelot, M., Yang, G.-Z. & Lo, B. A Self-Calibrated Tissue Viability Sensor for Free Flap Monitoring. *IEEE J. Biomed. Health Inform.* **22**, 5–14 (2018).

184. Futran, N. D., Stack, B. C., Hollenbeak, C. & Scharf, J. E. Green light photoplethysmography monitoring of free flaps. *Arch. Otolaryngol. Neck Surg.* **126**, 659–662 (2000).

185. Yudovsky, D., Nouvong, A., Schomacker, K. & Pilon, L. Two-layer optical model of skin for early, non-invasive detection of wound development on the diabetic foot. *BiOS* 755514–755514 (2010).

186. Yudovsky, D., Nguyen, J. Q. M. & Durkin, A. J. In vivo spatial frequency domain spectroscopy of two layer media. *J. Biomed. Opt.* **17**, 107006–107006 (2012).

187. Saager, R. B., Sharif, A., Kelly, K. M. & Durkin, A. J. In vivo isolation of the effects of melanin from underlying hemodynamics across skin types using spatial frequency domain spectroscopy. *J. Biomed. Opt.* **21**, 057001–057001 (2016).

188. Delpy, D. & Cope, M. Quantification in tissue near–infrared spectroscopy. *Philos. Trans. R. Soc. Lond. B. Biol. Sci.* **352**, 649 (1997).

189. Martelli, F. *et al.* Phantom validation and in vivo application of an inversion procedure for retrieving the optical properties of diffusive layered media from time-resolved reflectance measurements. *Opt. Lett.* **29**, 2037–2039 (2004).

190. Takatani, S. & Graham, M. D. Theoretical analysis of diffuse reflectance from a two-layer tissue model. *IEEE Trans. Biomed. Eng.* 656–664 (1979).

191. Saager, R. B., Truong, A., Durkin, A. J. & Cuccia, D. J. Method for depth-resolved quantitation of optical properties in layered media using spatially modulated quantitative spectroscopy. *J. Biomed. Opt.* **16**, 077002 (2011).

192. Matcher, S. J., Cope, M. & Delpy, D. T. In vivo measurements of the wavelength dependence of tissue-scattering coefficients between 760 and 900 nm measured with time-resolved spectroscopy. *Appl Opt* **36**, 386–396 (1997).

193. Saager, R. B., Dang, A. N., Huang, S. S., Kelly, K. M. & Durkin, A. J. Portable (handheld) clinical device for quantitative spectroscopy of skin, utilizing spatial frequency domain reflectance techniques. *Rev. Sci. Instrum.* **88**, 094302 (2017).

194. Anand, S. & Sujatha, N. Effects of probe placement on tissue oxygenation levels during reflectance measurements for different types of tissues in a clinical setting. *BioPhotonics BioPhotonics 2015 Int. Conf. On* 1–3 (2015).

195. Lim, L., Nichols, B., Rajaram, N. & Tunnell, J. W. Probe pressure effects on human skin diffuse reflectance and fluorescence spectroscopy measurements. *J. Biomed. Opt.* **16**, 011012 (2011).

196. Tseng, S.-H., Hayakawa, C., Spanier, J. & Durkin, A. J. Investigation of a probe design for facilitating the uses of the standard photon diffusion equation at short source-detector separations: Monte Carlo simulations. *J. Biomed. Opt.* **14**, 054043–054043 (2009).

197. Nadeau, K. P., Rice, T. B., Durkin, A. J. & Tromberg, B. J. Multifrequency synthesis and extraction using square wave projection patterns for quantitative tissue imaging. *J. Biomed. Opt.* **20**, 116005–116005 (2015).

198. Gioux, S. *et al.* Three-dimensional surface profile intensity correction for spatially modulated imaging. *J. Biomed. Opt.* **14**, 034045–034045 (2009).

199. Baruch, D. & Abookasis, D. Multimodal optical setup based on spectrometer and cameras combination for biological tissue characterization with spatially modulated illumination. *J. Biomed. Opt.* **22**, 046007 (2017).

200. Yafi, A. *et al.* Postoperative Quantitative Assessment of Reconstructive Tissue Status in a Cutaneous Flap Model Using Spatial Frequency Domain Imaging: *Plast. Reconstr. Surg.* **127**, 117–130 (2011).

201. Amaan Mazhar, B. J. T., Steven Dell, David J. Cuccia, Sylvain Gioux, Anthony J. Durkin, John V. Frangioni. Wavelength optimization for rapid chromophore mapping using spatial frequency domain imaging. *J. Biomed. Opt.* **15**, 15-15–9 (2010).

202. Brendel, B. & Nielsen, T. Selection of optimal wavelengths for spectral reconstruction in diffuse optical tomography. *J. Biomed. Opt.* **14**, 034041 (2009).

203. Meglinski, I. & Matcher, S. Computer simulation of the skin reflectance spectra. *Comput. Methods Programs Biomed.* **70**, 179–186 (2003).

204. Venugopalan, V., You, J. S. & Tromberg, B. J. Radiative transport in the diffusion approximation: An extension for highly absorbing media and small source-detector separations. *Phys Rev E* **58**, 2395–2407 (1998).

205. Tseng, S.-H. & Hou, M.-F. Efficient determination of the epidermal optical properties using a diffusion model–based approach: Monte Carlo studies. *J. Biomed. Opt.* **16**, 087007–087007 (2011).

206. Liu, Q. & Ramanujam, N. Sequential estimation of optical properties of a two-layered epithelial tissue model from depth-resolved ultraviolet-visible diffuse reflectance spectra. *Appl Opt* **45**, 4776–4790 (2006).

207. Arifler, D., Schwarz, R. A., Chang, S. K. & Richards-Kortum, R. Reflectance spectroscopy for diagnosis of epithelial precancer: model-based analysis of fiber-optic probe designs to resolve spectral information from epithelium and stroma. *Appl. Opt.* **44**, 4291–4305 (2005).

208. Nieman, L. T., Jakovljevic, M. & Sokolov, K. Compact beveled fiber optic probe design for enhanced depth discrimination in epithelial tissues. *Opt Express* **17**, 2780–2796 (2009).

209. Sung, K.-B. *et al.* Accurate extraction of optical properties and top layer thickness of two-layered mucosal tissue phantoms from spatially resolved reflectance spectra. *J. Biomed. Opt.* **19**, 077002–077002 (2014).

210. Sharma, M., Hennessy, R., Markey, M. K. & Tunnell, J. W. Verification of a two-layer inverse Monte Carlo absorption model using multiple source-detector separation diffuse reflectance spectroscopy. *Biomed. Opt. Express* **5**, 40 (2014).

211. Zonios, G. & Dimou, A. Simple two-layer reflectance model for biological tissue applications: lower absorbing layer. *Appl Opt* **49**, 5026–5031 (2010).

212. Senlik, O. & Jokerst, N. M. Concentric Multipixel Silicon Photodiode Array Probes for Spatially Resolved Diffuse Reflectance Spectroscopy. *IEEE J. Sel. Top. Quantum Electron.* **22**, 7–12 (2016).

213. Schelkanova, I., Pandya, A., Shah, D., Lilge, L. & Douplik, A. Diffuse reflectance measurements using lensless CMOS imaging chip. *J. Phys. Conf. Ser.* **541**, 012098 (2014).

214. Göbel, G., Kuhn, J. & Fricke, J. Dependent scattering effects in latex-sphere suspensions and scattering powders. *Waves Random Media* **5**, 413–426 (1995).

215. Boelsma, E. *et al.* Characterization and Comparison of Reconstructed Skin Models: Morphological and Immunohistochemical Evaluation. *Acta Derm Venereol* 7

216. Nieman, L., Myakov, A., Aaron, J. & Sokolov, K. Optical sectioning using a fiber probe with an angled illumination-collection geometry: evaluation in engineered tissue phantoms. *Appl. Opt.* **43**, 1308–1319 (2004).

217. Tseng, S.-H., Hayakawa, C., Spanier, J. & Durkin, A. J. Investigation of a probe design for facilitating the uses of the standard photon diffusion equation at short source-detector separations: Monte Carlo simulations. *J. Biomed. Opt.* **14**, 054043–054043 (2009).

218. Giovanelli, G., Sinelli, N., Beghi, R., Guidetti, R. & Casiraghi, E. NIR spectroscopy for the optimization of postharvest apple management. *Postharvest Biol. Technol.* **87**, 13–20 (2014).

219. Bobelyn, E. *et al.* Postharvest quality of apple predicted by NIR-spectroscopy: Study of the effect of biological variability on spectra and model performance. *Postharvest Biol. Technol.* **55**, 133–143 (2010).

220. Sunar, U. *et al.* Light-triggered doxorubicin release quantified by spatial frequency domain imaging and diffuse optical spectroscopy. in *Cancer Imaging and Therapy* JW4A–3 (Optical Society of America, 2016).

Scientific communications

Patent

- **Petitdidier, N.**, Koenig, A., Benhamed, S., « Dispositif de mesure d'un rayonnement rétrodiffusé par un échantillon et procédé de mesure utilisant un tel dispositif » - N° E.N. 17 63097 (2018) **submitted**

Journal Paper

- **Petitdidier, N.**, Koenig, A., Gerbelot, R., Grateau, H., Gioux, S. & Jallon, P., "Contact, high-resolution spatial diffuse reflectance imaging system for skin condition diagnosis", *J. Biomed. Opt.* **23**(11), 115003 (2018). doi:10.1117/1.JBO.23.11.115003

Oral presentations

- **Petitdidier, N.**, Koenig, A., Gerbelot, R., Grateau, H., Gioux, S. & Morales, S., "CMOS-based contact imaging system for skin condition diagnosis by spatially resolved diffuse reflectance spectroscopy", in *Photonics Europe*, (Strasbourg, 25 April 2018)
- **Petitdidier, N.**, Koenig, A., Gerbelot, R., Grateau, H., Gioux, S. & Morales, S., "CMOS-based contact imaging system for spatially resolved diffuse reflectance spectroscopy", in *BIOS*, (San Francisco, 30 January 2018)
- **Petitdidier, N.**, Koenig, A., Gerbelot, R., Grateau, H., Gioux, S. & Dinten, J.-M., "Development of a wearable CMOS-based contact imaging system for real-time skin condition diagnosis." in *European Conferences on Biomedical Optics*, (Munich, 28 July 2017). doi:10.1117/12.2285998

Poster presentations

- **Petitdidier, N.**, Koenig, A., Gerbelot, R., Grateau, H., Gioux, S. & Jallon, P., "Low-cost wearable CMOS-based system for skin condition diagnosis," in *IFSCC Congress* (Munich, 20 September 2018) **invited**

- **Petitdidier, N.**, Koenig, A., Gerbelot, R., Grateau, H., Gioux, S. & Morales, S., "Multi-layer characterization of skin by spatially resolved diffuse reflectance spectroscopy using a CMOS-based contact imaging system," in *Journées Jean-Paul Marty de la Société Française de Cosmétologie* (Paris, 6 December 2017) **best poster award**
- **Petitdidier, N.**, Koenig, A., Gerbelot, R., Grateau, H., Gioux, S. & Morales, S., "Imagerie de réflectance diffuse en contact à l'aide d'un capteur matriciel pour l'analyse de la peau en couches," in *Meeting Annuel de FINYS* (Varennes, 10 October 2017) **best poster award**
- **Petitdidier, N.**, Koenig, A., Hervé, L., Boutet, J., Gerbelot, R., Gioux, S. & Dinten, J.-M., "Utilisation de capteurs matriciels pour le développement d'un instrument de caractérisation de tissus cutanés en couches par spectroscopie de réflectance diffuse," in *1er Meeting Annuel de FINYS* (Dourdan, 3 June 2016)

Nils PETITDIDIER

Système d'imagerie pour la caractérisation en couches de la peau par réflectance diffuse

Résumé

Les travaux effectués au cours de cette thèse concernent le développement d'un instrument à faible coût et porté sur la personne permettant le suivi quantitatif des paramètres physiologiques de la peau *in vivo* et de manière non invasive. L'instrument est fondé sur la technique de Spectroscopie de Réflectance Diffuse résolue spatialement (srDRS). Cette technique fournit une quantification absolue des propriétés optiques endogènes d'absorption et de diffusion du tissu sondé et possède un potentiel pour la caractérisation de ces propriétés en couches de la peau. Afin de maximiser ce potentiel, notre approche repose sur l'utilisation d'un capteur matriciel placé en contact avec le tissu et permettant l'imagerie de réflectance diffuse à haute résolution spatiale. Les travaux présentés ici comprennent la spécification et la validation d'une architecture innovante permettant la mise en œuvre de l'approche proposée, l'implémentation d'un système porté sur la personne et bas coût basé sur cette architecture et l'évaluation des performances de ce système au travers d'expérimentations à la fois sur fantômes de peau et *in vivo*. Les résultats obtenus valident le potentiel de l'instrument développé pour le suivi quantitatif et non-invasif des propriétés de la peau. L'approche proposée est prometteuse pour l'analyse de milieux en couches tels que la peau et ouvre la voie au développement d'une nouvelle génération d'instruments portés sur la personne et bas coûts pour le suivi en continu des propriétés optiques des tissus.

Mots-clés: caractérisation de la peau, propriétés optiques, réflectance diffuse, capteur matriciel, imagerie de contact

Abstract

This work presents the development of a low-cost, wearable instrument for quantitative monitoring of skin physiological parameters toward non-invasive diagnostics *in vivo*. The instrument is based on the spatially resolved Diffuse Reflectance Spectroscopy (srDRS) technique, which provides absolute quantification of absorption and scattering endogenous properties of the probed tissue volume with a potential to discriminate between properties of individual skin layers. In the developed instrument, this potential is maximized by the use of a multi-pixel image sensor to perform contact, high resolution imaging of the diffuse reflectance. This study comprises the specification and validation of a novel srDRS system architecture based on the proposed approach, the implementation of this architecture into a low-cost, wearable device and the evaluation of the device performance both on tissue-simulating phantoms and *in vivo*. Results validate the potential of the instrument for the non-invasive, quantitative monitoring of tissue properties. The described approach is promising for addressing the analysis of layered tissue such as skin and paves the way for the development of low-cost, wearable devices for continuous, passive monitoring of tissue optical properties.

Keywords: skin characterization, optical properties, diffuse reflectance, multi-pixel sensor, contact imaging